Ph.D Thesis

*F*ermi-LAT Study of the Vela Supernova Remnant and X-ray Hotspot in Supernova Remnants RX J1713.7−3946 and W50

Ryota HIGURASHI

Department of Physics
Graduate School of Science
Rikkyo University

Abstract

The origin of cosmic rays is still a lasting mystery in high-energy astronomy. Supernova remnants (SNRs) are considered as the primary accelerators of Galactic cosmic rays with energies less than the "knee" (a few PeV). For revealing the origin, we need to clear the cosmic-ray anomalies, particle acceleration in the astronomical objects, and transportation of the cosmic rays. Positron excess is one of the cosmic-ray anomalies. It represents the anomalous positron excess beyond prediction above ~ 10 GeV. Because of the orbital bending by the interstellar magnetic field, it is not possible to identify the origin from the cosmic-ray measurements. Electromagnetic radiation gives us information on high-energy accelerated particles. Observational evidence of high-energy electrons and protons has been provided by non-thermal X-ray and gamma-ray observations of SNRs. In this thesis, gamma-ray and X-ray data analyses of the three cosmic-ray accelerators are conducted to understand the puzzling positron excess and particle acceleration in these targets.

Since the high-energy electrons lose their energies during propagation, it is difficult to travel more than 1 kpc. Nearby accelerators are candidate sources for the origin of the positron excess. The near distance of the Vela supernova remnant (Vela SNR) makes the SNR one of the most important accelerators for positron excess. Its large apparent diameter makes it difficult to detect gamma-ray emission from the SNR because of the requirement of careful treatment of the Galactic diffuse background and overlapping sources in the line of sight. We succeed in claiming the detection of GeV gamma-ray emission extending over the entire region of the Vela SNR. The large apparent diameter allows us to conduct a spatially resolved analysis and we found the non-uniform distribution in spectra inside the SNR. From the spectral analysis, we detected gamma rays extending to over several hundreds of GeV and it is explained by the inverse-Compton scattering of electrons with the energy of at least several TeV. This finding indicates the presence of very high-energy electrons in the nearby SNR.

Accelerated electrons are observed as cosmic rays when they can travel from SNRs to Earth without significant energy loss. To study the energy dissipation inside SNRs before they escape, RX J1713.7$-$3946 is one of the best targets because of its strong non-thermal synchrotron X-ray emission. Particularly, the northwest rim is a characteristic region where X-ray filaments are observed. In this region, many point-like X-ray sources (hotspots) are apparent in the observed image, but they have been ignored in previous studies. We report, for the first time, a bunch of hotspots is likely associated with the SNR. Using the results of spectral and time-variability analyses, we propose that the hotspots are caused as a consequence of the interactions with the shock waves and compact-dense molecular cores. The accelerated electrons lose their energies by shock-cloud interactions before they escape from the SNR.

To study the acceleration of electrons besides standard SNRs, the SS 433/W50 system is a distinctive target. This system has a microquasar SS 433, and its black hole jets interact with SNR W50 which is expanding around the jets. After the detection of TeV gamma-ray emission with HAWC, the system become one of the notable electron accelerators. X-ray hotspots are detected in the eastern terminal region where the radio continuum has a peak emission. We challenged detecting the gamma-ray emission, and found that the significant emission is not detected from the position of the hotspot. Thus we set upper limits for the first time, considering the debatable results of the previous studies in the GeV gamma-ray band. Using radio, X-ray, and gamma-ray data, we concluded that electrons can be accelerated inside the unique object in addition to standard SNRs.

Based on these results, our findings are summarized as follows. First, the existence of the highly accelerated electrons is indicated by the firm detection of the gamma rays and its detailed analysis from the Vela SNR, suggesting that a nearby SNR can explain the positron excess. Second, the nature of hotspots in RX J1713.7−3946 is uncovered by the detailed X-ray analysis, showing that it is created by the shock-cloud interaction. Lastly, the gamma-ray emission from the hotspot in the putative PeVatron source, SS 433/W50 system, is carefully constrained by using about 12.5-year gamma-ray data, implying that the hotspots in such a complicated system can be of the cosmic-ray accelerator. Our findings and future X-ray and TeV gamma-ray missions will help to estimate the contribution of the nearby SNRs to the cosmic-ray electrons. It may unveil the origin of the positron excess.

Contents

List of Figures

List of Tables

Chapter 1

Introduction

High-energy phenomena in the universe have fascinated us for a long time. Supernovae are one of the high-energy phenomena that have been found in historical records. High-energy astronomy is one of the fields to study such violent phenomena. In the term of astronomy, astronomical messengers are used to study the nature of high-energy objects. Cosmic rays (up to $\sim 10^{20}$ eV) and electromagnetic radiations (from radio to gamma-ray) are often used as messengers. In addition, neutrinos and gravitational waves are new developing messengers. Including these messengers, astronomy is entering a new era of multi-messenger astronomy.

Cosmic rays and high-energy electromagnetic radiation (X rays and gamma rays) are important messengers for observing high-energy phenomena. Cosmic rays were discovered in 1912 by Victor Hess. Since the discovery, the origin of the comic ray is one of the still-lasting mysteries in astronomy though the observations of cosmic rays are developing. Japanese scientists contributed to the early cosmic ray studies such as the identification and precise measurement of the mass of mesons by Yasuo Nishina and their colleague (Nishina, Takeuchi, and Ichimiya, 1937). Baade and Zwicky (1934) proposed the idea of the supernova origin of cosmic rays, considering the large energy output of the explosion. Satio Hayakawa approached the similar supernova origin of cosmic rays, considering the relative abundance of light and heavy nuclei (Hayakawa, 1956). Now, the supernovae and their remnants are the observationally and theoretically prime candidates for the origin of cosmic rays. The flux of comic-ray electrons is less than 1% of all cosmic-ray flux. It made the observation difficult because of the requirement of high background (hadronic cosmic-ray) rejection. In the 1960s, the observational data were reported by several groups like Meyer and Vogt (1961) and Earl (1961). Nishimura et al. (1980) reported the spectrum of cosmic-ray electrons up a few TeV in 1980. In the spectrum, there was no significant feature, implying nearby electron sources, like pulsar and supernova remnant. The electrons lose their energies during the propagation due to synchrotron radiation and inverse Compton scattering. Its energy loss is in proportion to the square of the energy of the electron. For 1 TeV electrons, the timescale of energy loss is $\sim 10^5$ yr and the propagation length is constrained to less than 1 kpc. Shen (1970) first proposed the idea of the effect from nearby electron sources such as the pulsar wind nebula Vela X. This idea is developed by many previous studies, and the Vela supernova remnant (Vela SNR) is one of the prime candidate sources of electrons. Recent accurate measurement of cosmic-ray positron fraction (i.e., $e^+/(e^+ + e^-)$) indicates the anomalous excess of positron above 10 GeV, referred to positron excess. In order to reproduce this excess, the nearby accelerators (e.g., pulsar, pulsar wind nebula, SNR) are considered to be the candidate source of electrons. Other explanations are related to the existence of dark matter, which annihilates or decays into electrons.

Hayakawa also proposed Galactic diffuse gamma rays by the interactions between cosmic rays and interstellar medium through π^0-decay radiation (Hayakawa, 1952). This diffuse gamma-ray emission was confirmed by the observation with the OSO-3 satellite (Kraushaar et al., 1972) and its flux is in agreement with his predicted flux. Later, the gamma-ray observation is developing for the SAS-II, EGRET on board *Compton*, and LAT on board *Fermi* satellites. In the bottom panel of Figure 1.1, the gamma-ray all-sky image observed with the *Fermi*-LAT represents the brighter emission on the Galactic plane where the interstellar mediums are denser and are bombarded by cosmic rays. The *Fermi*-LAT is now working to observe the entire sky, and has detected more than 5000 gamma-ray sources like active galactic nuclei (AGN), pulsars and pulsar wind nebulae, and supernova remnants in the GeV energies. The detection of the characteristic pion-decay feature in the gamma-ray spectra of middle-aged SNRs with the *Fermi*-LAT provides evidence that cosmic-ray protons are accelerated in SNRs (Ackermann et al., 2013). For higher energy gamma rays, the ground-base Imaging Air Cherenkov Telescopes (IACTs) like H.E.S.S., MAGIC, and VERITAS and water Cherenkov like HAWC (High-Altitude Water Cherenkov observatory) are performed to observe the high-energy objects and provides great results. The middle center panel of Figure 1.1 shows the TeV gamma-ray image of SNR RX J1713.7$-$3946 with H.E.S.S.(H.E.S.S. Collaboration et al., 2018b). Recently, HAWC detected significant TeV gamma rays from the jet termination region of the microquasar SS 433 (Abeysekara et al., 2018), as shown in the middle left panel of Figure 1.1.

In contrast to gamma-ray astronomy, B. Rossi and his colleagues found a strong X-ray emission from the direction of Scorpio X-1 (Giacconi et al., 1962). This finding is the beginning of X-ray astronomy. In Japan, Minoru Oda, who is one of the pioneers of X-ray astronomy (and also cosmic-ray astronomy), and his colleagues Miyamoto et al. (1971) revealed the accurate position of Cygnus X-1, which was then predicted to be the first black hole candidate. The position is in good agreement with the results of the Uhuru satellite, which is the first X-ray satellite for scientific observation. In 1979, the first Japanese satellite *Hakucho* was launched. After that launch, Japanese X-ray satellites were constantly launched at intervals between several and about ten years (*Tenma* in 1983, *Ginga* in 1987, *ASCA* in 1993, *Suzaku* in 2005, and *Hitomi* in 2016. The next *XRISM* is going to be launched soon.). Using the *ASCA* satellite, Koyama et al. (1995) detected synchrotron X-ray emission from the

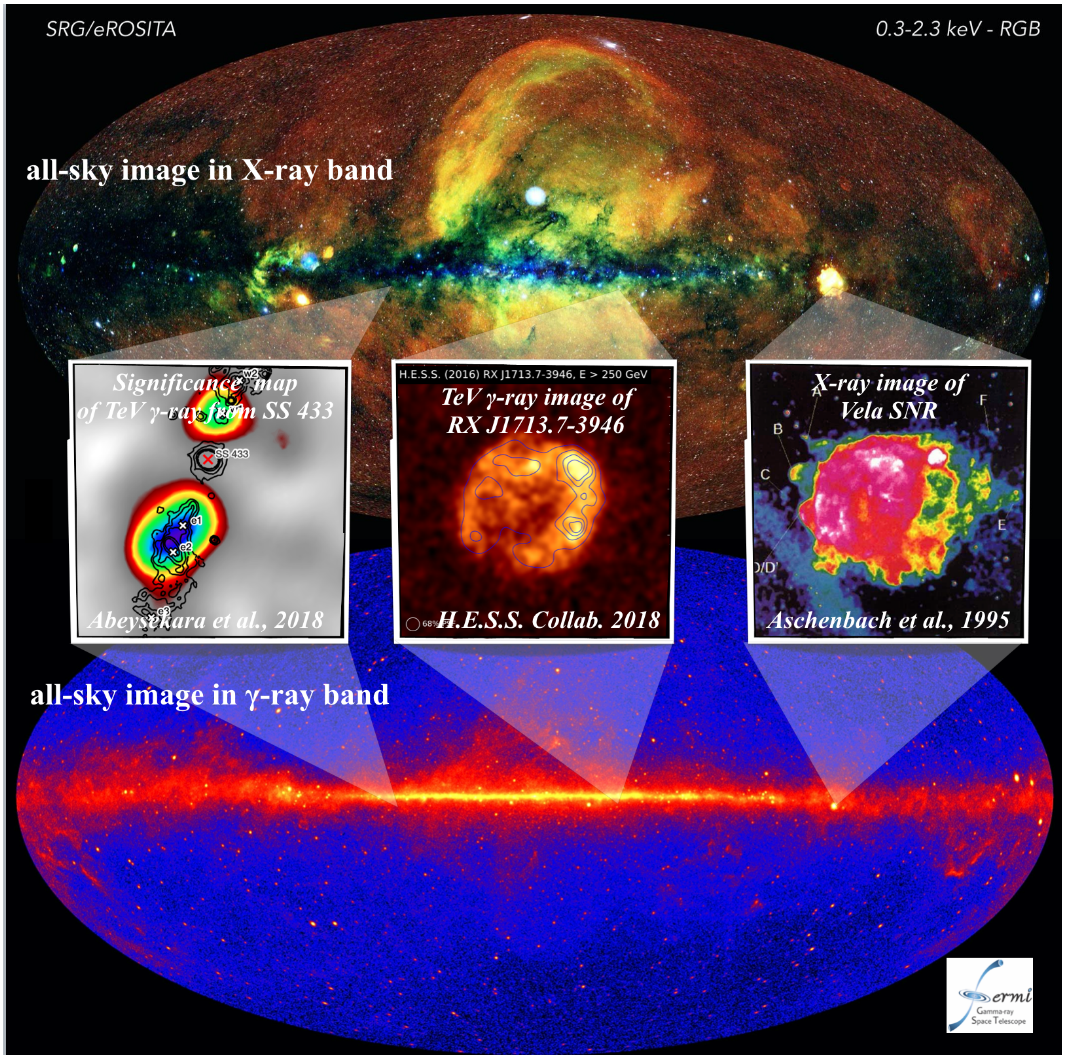

Figure 1.1. (top) All-sky image in X-ray band. (Middle) Significance map of TeV gamma-ray emission from SS433 with HAWC (left). TeV gamma-ray map of the RX J1713.7−3946 observed with H.E.S.S.. X-ray image of the Vela SNR with *ROSAT*. (Bottom) All-sky image in gamma-ray band.

rim of the young supernova remnant SN 1006. It revealed that electrons are accelerated up to TeV energies by the SNR. In addition, the synchrotron X-ray emission was detected from the rim region of the young supernova remnant RX J1713.7−3946 (Koyama et al., 1997; Slane et al., 1999). *Chandra* satellite, launched in 1999, has great spatial resolutions and reveals detailed structures inside SNRs. The observational image with *Chandra* reveals that high-energy electrons are accelerated in the thin filament structures.

In this thesis, particle acceleration of the nearby Vela SNR is analyzed with the *Fermi*-LAT. This object is one of the prime candidates of cosmic-ray electrons and the origin of the positron excess but not yet detected in the gamma-ray band. The analysis revealed the extended gamma-ray emission from the Vela SNR region for the first time, and high-energy electrons with TeV energies are expected from the spectral analysis. In addition, using the great spatial resolution of *Chandra*, a bunch of X-ray hotspots in the northwest rim of RX J1713.7$-$3946 are detected for the first time, and are interpreted to be caused by the shock-cloud interaction. RX J1713.7$-$3946 is one of the very important accelerators of cosmic rays due to its strong non-thermal emissions. However, the gamma-ray radiation mechanism of RX J1713.7$-$3946 is under debate whether it is hadronic (interaction with ambient matter) or leptonic (interaction with low-energy photons). The interpretation of hotspots gives clues to the radiation mechanism. Finally, after the detection of TeV gamma rays with HAWC, particle acceleration of SS 433 is a very hot topic for cosmic-ray acceleration. At the eastern side of SS 433, X-ray hotspots are found with *Chandra* observations. The gamma-ray analysis of the hotspots could not detect the significant emission, but gives accurate upper limits for the first time. Using the radio, X-ray data, and gamma-ray upper limits, electrons are found to be accelerated up to $\sim$ 30 TeV in the X-ray hotspot. The remainder of this thesis is organized as follows. Chapter 2 gives a review of cosmic ray, supernova remnant, particle acceleration, radiation process, and astrophysical objects analyzed in this thesis. In Chapter 3, the information on the instruments used for the analyses is addressed. The motivation of this thesis is summarized in Chapter 4. The analysis of Vela SNR, RX J1713.7$-$3946, and SS 433/W50 system are presented in Chapters 5, 6, and 7, respectively. The summary of this thesis is given in section 8.

Chapter 2

Review

2.1 Cosmic Rays

The origin of cosmic rays has been an unsolved question since their discovery in 1912 by Victor Hess. He measured the strength of ionization in the atmosphere by balloon flight experiments, and concluded that it was caused by extraterrestrial-origin radiation. After the discovery of the cosmic rays, they are found to be very high-energy charged particles by observations and experiments in the early 1900s. Cosmic rays were used in many experiments as a natural source of high-energy particles, leading to the discovery of positrons, muons, kaons, and pions. The physics of high-energy particles is developed in accelerator laboratories on the ground after these technologies are improved. Interests in cosmic rays are shifted to their origin, composition, and transportation in astronomy. Through many theoretical and experimental studies of cosmic rays, their composition and spectrum are being revealed.

2.1.1 Composition of cosmic rays

The composition of cosmic rays is 90% protons, 9% alpha particles, and the rest heavier nuclei, electrons, and so on. Figure 2.1 shows the comparison of the element abundance between the solar system and cosmic rays. The major difference between them appears around Li, Be, B, Sc, Ti, V, Cr, and Mn which are many orders of magnitude abundant in the cosmic rays. This is caused by the spallation reaction of the comic rays during the propagation in the interstellar medium (ISM). The collisions between the ISM and cosmic rays with heavier mass nuclei (particularly C, O, and Fe) produce the lighter-mass cosmic rays. The antiprotons and positrons, which are mostly produced by the interactions between the ISM and cosmic rays, are discovered in cosmic rays. The propagation length of the cosmic rays ($\sim$ 1000 kpc) is derived from the cross-section of the spallation and the fraction of lighter and heavier elements. The long propagation length means the cosmic rays are confined in the Galactic halo by the diffusive propagation. The diffusion coefficient $D(E)$ has a form of:

$$D(E) \sim 10^{28} \left(\frac{E}{10\ \mathrm{GeV}} \right)^{\delta}\ \mathrm{cm^2 s^{-1}}, \tag{2.1}$$

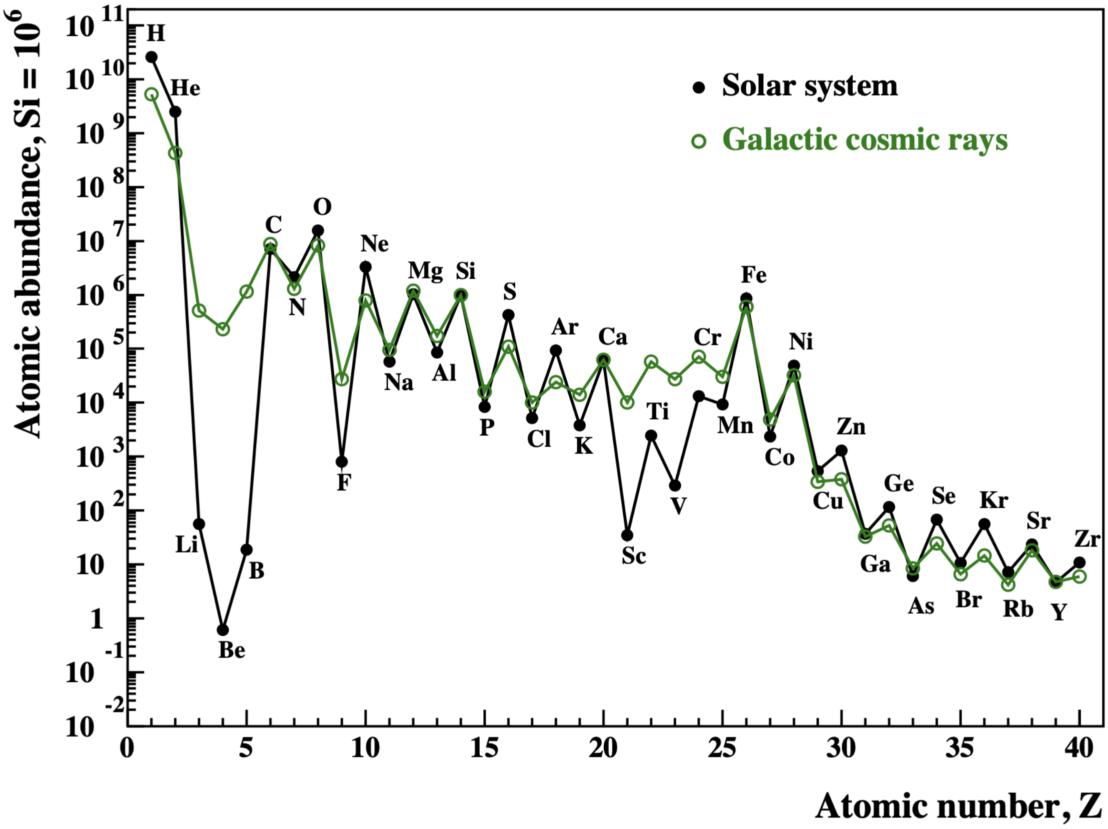

Figure 2.1. Cosmic-ray abundance. Abundances are normalized to become Si $= 10^6$. Green and black plots represent the abundances of the Galactic cosmic rays and solar system, respectively (Tatischeff and Gabici, 2018).

where E denotes energy of a cosmic ray, and δ takes $0.3 - 0.6$ in the various diffusion models. The transportation of cosmic rays is important to reveal the origin of the cosmic rays.

2.1.2 Energy spectrum of cosmic rays

Cosmic rays have relativistic energies that are greater than their masses, and a very small fraction of them reaches $\sim 10^{20}$ eV. The energy density of the cosmic rays in the ISM is ~ 1 eV cm^{-3}, which is comparable to other major energy sources such as magnetic field ($B^2/8\pi \approx 0.25$ eV cm^{-3}, assuming the typical magnetic field of $B = 3$ μG). The energy spectrum of the cosmic rays is shown in Figure 2.2. The spectrum was found to be reproduced by a power-law type spectrum with two clear breaks at $\sim 10^{15}$ and $\sim 10^{18}$ eV, and one cutoff at $\sim 10^{20}$ eV. The breaks at $\sim 3 \times 10^{15}$ eV and $\sim 3 \times 10^{18}$ eV are known as the "knee" and "ankle", respectively. The cosmic rays represent a spectral index of ~ -2.7 below the knee, then the spectrum becomes steep above the knee with the spectral index of ~ -3.2. Above the ankle, the spectrum becomes flat with the index of ~ -2.6. Cosmic rays with energies of less than ~ 10 GeV are influenced by solar activity (so-called solar modulation).

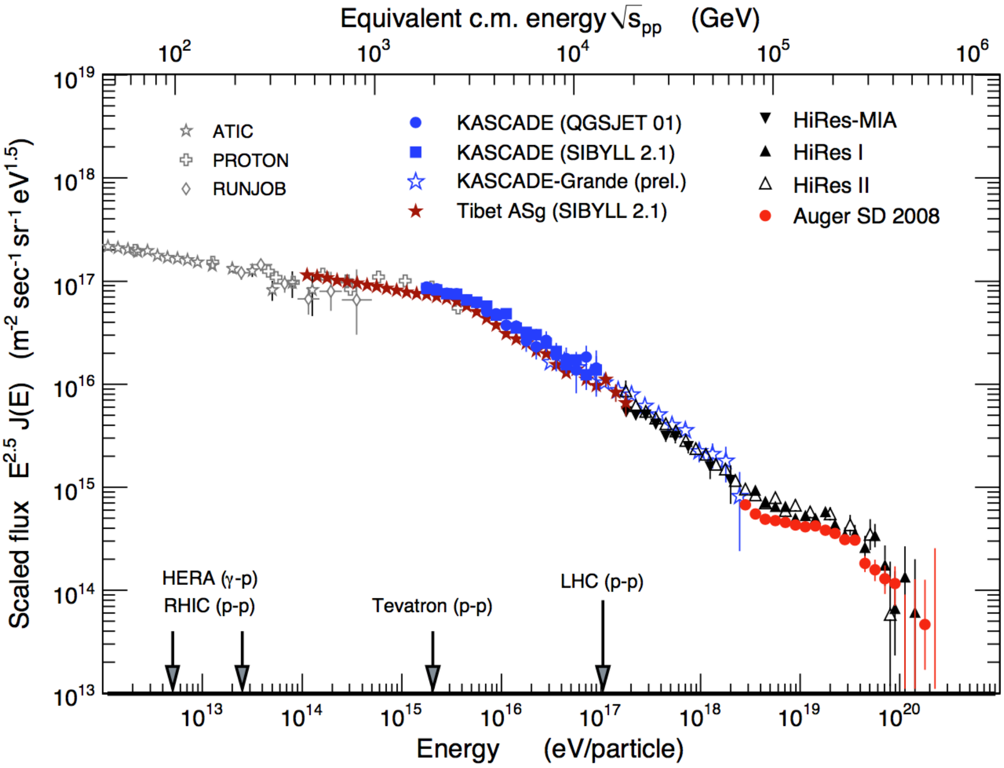

Figure 2.2. Cosmic-ray energy spectrum (Blümer, Engel, and Hörand el, 2009).

Below the knee, the origin of cosmic rays is considered to be in our Galaxy, and is often referred to "Galactic cosmic rays". Above the ankle, the extragalactic origin is considered owing to the larger gyroradius of the particles in the typical magnetic field than the size of the Galaxy.

2.1.3 Recent observational results and anomalies

Recent precise observations have found anomalies that cannot be explained by conventional cosmic-ray models. The positron fraction to the electron and positron in cosmic rays are shown in the top left panel of Figure 2.3. Most of the positrons are considered to be secondarily produced by the interactions between cosmic-ray protons and the ISM. In this case, the positron fraction becomes steeper with higher energies due to the escape from the Galaxy. The observed fraction becomes higher in the energy of greater than ∼ 10 GeV (e.g.: Adriani et al., 2009; Aguilar et al., 2013; Aguilar et al., 2019b), which is called positron excess. The electrons and positrons with energies of 1 TeV can propagate ∼ 1 kpc before losing their energies (Aharonian, Atoyan, and Voelk, 1995; Kobayashi et al., 2004). It indicates that the primarily accelerated electrons and positrons from nearby sources can reach the Earth. A recent study by Ding et al. (2021) shows that a model with a nearby pulsar wind nebula and a supernova remnant is the most favored to explain the recent results

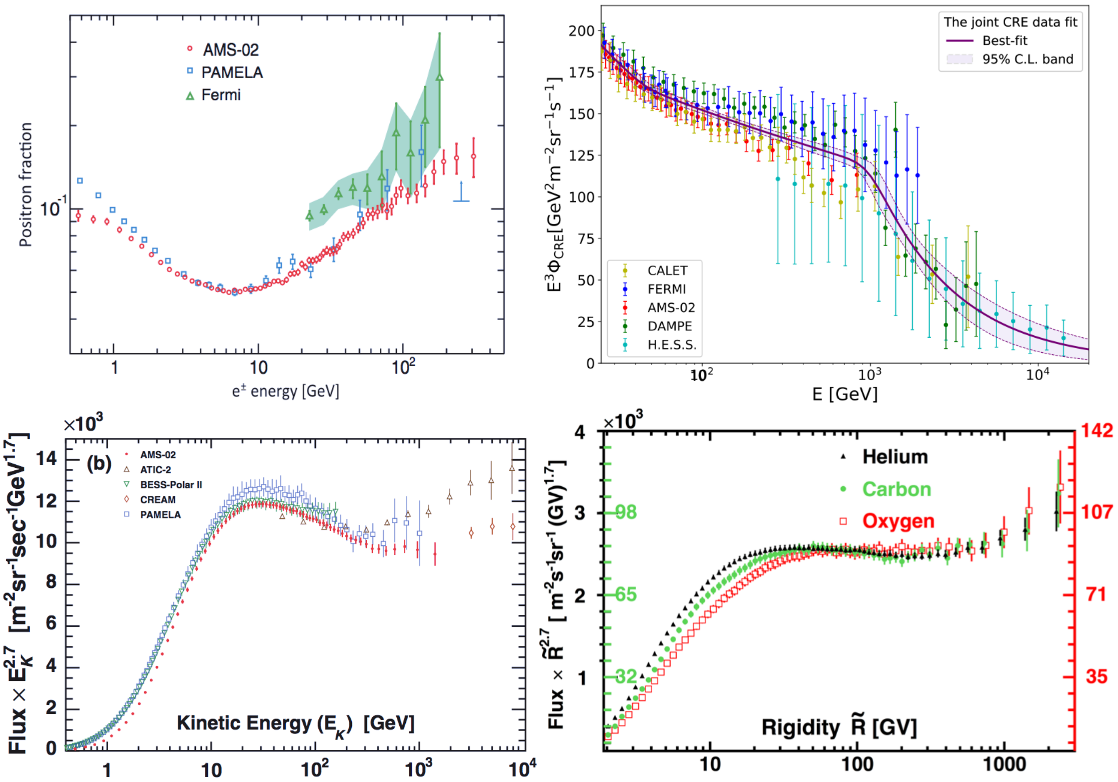

Figure 2.3. (Top left) Positron fraction (Aguilar et al., 2013). (Top right) Cosmic-ray electrons and positrons spectrum (Ding et al., 2021). (Bottom left) Cosmic-ray proton spectrum (Aguilar et al., 2015). (Bottom right) Cosmic-ray spectra of helium, carbon, and oxygen (taken from AMS-02 homepage (`https://ams02.space`) which refers Aguilar et al. (2017) to generate this figure)).

of the positron excess and the softening of the spectrum of the cosmic-ray electrons and positrons at $\sim$ 0.9 TeV (e.g.: Aharonian et al., 2009; DAMPE Collaboration et al., 2017) shown in the top right panel of Figure 2.3.

An unexpected upturning spectrum of cosmic-ray protons has been discovered at an energy of greater than $\sim$ 200 GeV (Aguilar et al., 2015) (see bottom left panel of Figure 2.3). The upturning spectra were also found in the cosmic-ray spectrum of alpha particles, carbon, and oxygen (Aguilar et al., 2017), as shown in the bottom right panel of Figure 2.3. In order to robustly unravel the origin of cosmic rays, it is necessary to explain not only the problems of the accelerator and transport, but also these anomalies discovered by recent observations.

2.1.4 Cosmic-ray electrons and positrons

The analysis of the Vela supernova remnant (Vela SNR) in Chapter 5 in this thesis is related to the cosmic-ray electrons and positrons. Here, I summarized the brief history of observational and theoretical studies of cosmic-ray electrons and positrons.

Balloon-borne detectors were often used for the observations of cosmic rays before using the detectors on satellites. Around 1980, the spectrum of cosmic-ray electrons (electron and positron) reached energy up to $\gtrsim$ 1 TeV (e.g., Nishimura et al.,

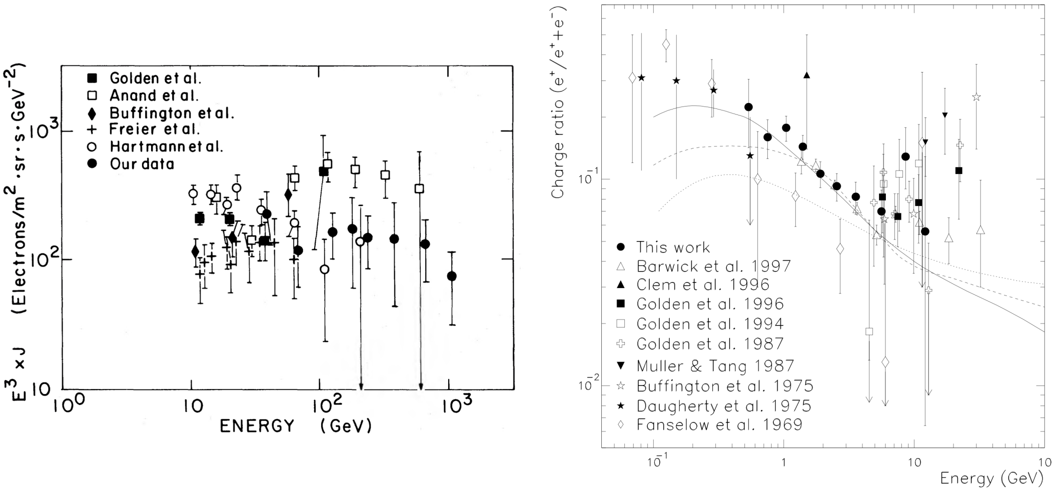

Figure 2.4. (Left) Energy spectrum of primary cosmic-ray electrons (Nishimura et al., 1980). (Right) Positron fraction ($e^+/(e^+ + e^-)$) observed by several groups in the late 1900s (Boezio et al., 2000).

1980), as shown in the left panel of Figure 2.4. The lifetime of cosmic-ray electrons is constrained by the energy loss via the synchrotron radiation and inverse Compton scattering. Observation of cosmic-ray electrons provides us information on the Galactic magnetic field and low-energy photon field in the Galaxy. For an electron with an energy of 1 TeV, the lifetime in the ISM is expected to $\sim 10^5$ years and the corresponding diffusion length is estimated to be several hundreds of parsec. It implies nearby accelerators of electrons located within $\sim$ 1 kpc with an age younger than $\sim 10^5$ years (Nishimura et al., 1980; Aharonian, Atoyan, and Voelk, 1995). Increasing positron fraction ($e^+/(e^+ + e^-)$) above $\sim$ 10 GeV was suggested by several groups (e.g., Golden et al., 1987; Mueller and Tang, 1987) (see the right panel of Figure 2.4) though the observed data still had large uncertainties and robust conclusion whether it is constant or increase with energy was not derived (e.g., Boezio et al., 2000). The fraction could not be explained by the theoretically expected secondary positrons, which were generated by interactions between the cosmic-ray nuclei and ISM during the propagation and its spectrum is expected to decrease with energy. To unveil a certain conclusion, observational data points were needed in a higher energy range. The additional source of high-energy positron was required to explain the positron fraction, if it was true. Nearby SNRs (e.g., Vela SNR, Monogem ring, and Cygnus loop) are considered one of the candidate sources of TeV electrons (e.g., Kobayashi et al., 2004). Nearby pulsars and their pulsar wind nebulae are also discussed as candidate sources of high-energy electrons and positrons (e.g., Aharonian, Atoyan, and Voelk, 1995; Atoyan, Aharonian, and Völk, 1995). For the positron source, the annihilation of weakly interacting massive particles (WIMPs) (e.g., Tylka, 1989), and the special environment conditions (e.g. Aharonian and Atoyan, 1991) were theoretically studied. Since WIMP is considered as one of the dark matter candidates, the positron fraction is an interesting topic not only in cosmic-ray physics

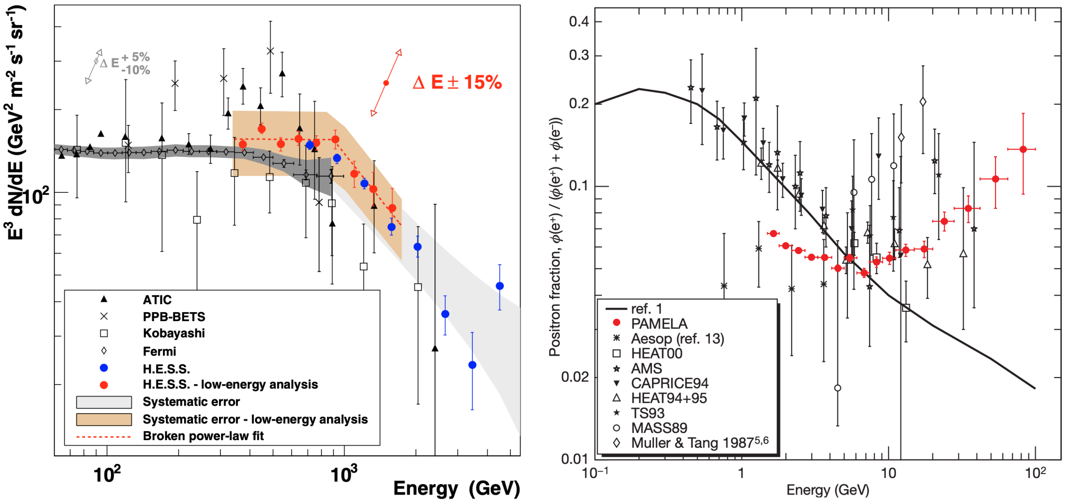

Figure 2.5. (Left) Spectrum of cosmic-ray electrons (Aharonian et al., 2009). (Right) Positron fraction measured with PAMELA(red) and other groups (Adriani et al., 2009).

but also in astronomy.

The new phase of cosmic-ray electrons observation has opened with new generation instruments. In Chang et al. (2008), they detected an excess in the spectrum of the cosmic-ray electrons (electrons and positrons) in the energy range of $300 - 800$ GeV by the observation with the Advanced Thin Ionization Calorimeter (ATIC), as shown in the left panel of Figure 2.5. They considered that the excess could be originated from the annihilation of dark matter particles. For the observation of cosmic-ray electrons, the grand-based and satellite-based gamma-ray telescopes are utilized taking advantage of their great background[1] rejection like H.E.S.S. (Aharonian et al., 2008b; Aharonian et al., 2009) and *Fermi* (Abdo et al., 2009c; Ackermann et al., 2010; Ackermann et al., 2012; Abdollahi et al., 2017). Aharonian et al. (2009) revealed the softening spectrum of cosmic-ray electrons at $\sim$ 0.9 TeV with H.E.S.S. (see red and blue plots in the left panel of Figure 2.5). In contrast to the ATIC experiment (Chang et al., 2008), there is no spectral excess (see Figure 2.5) in the high precision data of cosmic-ray electrons measured with the *Fermi*-LAT (Abdo et al., 2009a). In addition, the PAMELA experiment measured the electrons and there is no clear excess in the spectrum (Adriani et al., 2011). Furthermore, on the results of the Alpha Magnet Spectrometer (AMS)-02 on the International Space Station (ISS), the spectrum of electrons can be described by a single power-law in the energy range of $30.2 - 1000$ GeV, and does not show any distinct features (Aguilar et al., 2014). The Calorimetric Electron Telescope (CALET) on the ISS and Dark Matter Particle Explorer (DAMPE) started observation in 2015. The spectrum of electrons measured by DAMPE confirmed the spectral break at $\sim$ 0.9 TeV with a 6.6σ confidence level (DAMPE Collaboration et al., 2017), which was reported by the H.E.S.S. observations

---

[1] In this sentence, the background means the cosmic-ray electrons and positrons unlike other missions because they become the major background for their gamma-ray observations.

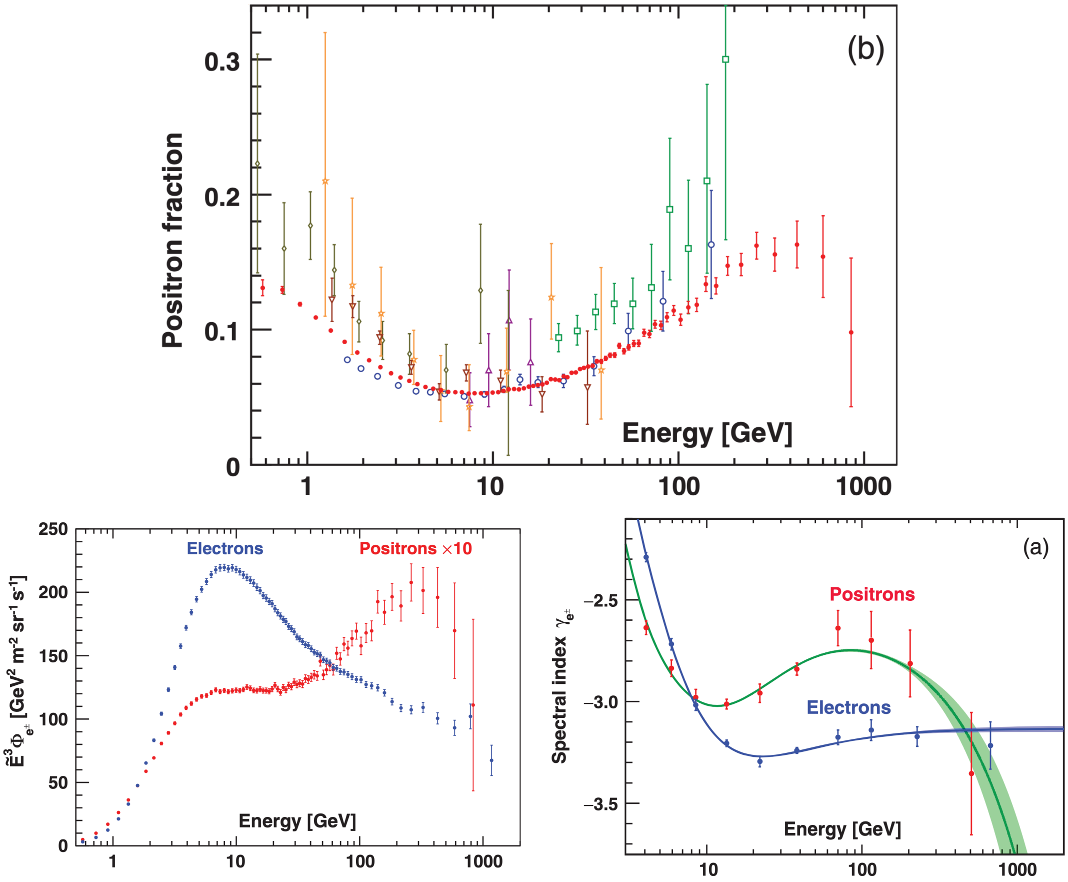

Figure 2.6. (Top) Positron fraction above 200 GeV with AMS-02 (red). Other plot represents the measured fraction by different groups (Aguilar et al., 2019b). (Bottom) Each spectrum of electron and positron (left). Positron spectrum is multiplied by 10. Spectral index of electron and positron at each energy bin (right) (Aguilar et al., 2019a).

in Aharonian et al. (2009). The spectrum was well described by a broken power-law function. The spectral indices were ~ 3.1 and ~ 3.9 below and above the break energy, respectively. The CALET measured the spectrum of electrons up to a few TeV, and the spectrum indicated the flux suppression like H.E.S.S. and DAMPE. But they could not conclude the existence of a statistically significant break (Adriani et al., 2017; Adriani et al., 2018). The spectra measured by CALET and DAMPE are shown in the top right panel of Figure 2.3. Ding et al. (2021) reported the existence of a significant break at ~ 1 TeV with a 13.3σ confidence level, using the precise data measured by several groups. They found consistent spectral indices with those of DAMPE results (DAMPE Collaboration et al., 2017).

In the context of positron fraction which was suggested to be increased with energy above 10 GeV (see the right panel of Figure 2.4), the Payload for Antimatter Matter Exploration and Light-nuclei Astrophysics (PAMELA) experiment measured the positrons precisely, and found the positron fraction increase with energy above ~ 10 GeV (Adriani et al., 2009; Adriani et al., 2013). The results of the *Fermi*-LAT measurement (see top left panel of Figure 2.3) support the increasing fraction with energy (Ackermann et al., 2012). Then, the AMS-02 on the ISS confirmed the results of PAMELA (Aguilar et al., 2013), as shown in the top left panel of Figure 2.3. Long observation with ASM-02 extends the data point of the positron fraction up to ~ 1 TeV (Aguilar et al., 2019a). The fraction above $200-300$ GeV seems not to be extended with energy like that of $10-100$ GeV. This is caused by a steep drop-off at ~ 285 GeV in the positron spectrum, as shown in the bottom left panel of Figure 2.6 (Aguilar et al., 2019b). In contrast, the spectrum of electrons does not have a cut-off[2] at a 5σ confidence level below 1.9 TeV(Aguilar et al., 2019a). In spite of the smooth power-law spectrum of electrons, the deep measurement of the AMS-02 reported interesting spectra hardening above ~ 42 GeV, suggesting nearby electron sources. It is difficult to explain the positron excess by secondary positrons created by interactions between cosmic-ray nuclei and the ISM. At least a (or a few) positron sources are observationally required to reproduce the fraction.

There are a lot of previous studies, that theoretically discuss a candidate source to explain the positron excess and softening spectrum of cosmic-ray electrons. The explanations are roughly classified into three types: 1) nearby astronomical source, 2) improved propagation model, and 3) annihilations of dark matter particles.

Nearby pulsars and their pulsar wind nebulae, and supernova remnants are often considered as candidate astrophysical sources. For example, the effect of the famous pulsar Geminga (age: ~342 kyr and distance: ~250 pc) and Monogem (age: ~110 kyr and distance: ~288 pc) was theoretically expected in Linden and Profumo (2013) because of their favored distance and age. The HAWC observation detected spatially extended TeV gamma-ray emission at the location of their pulsars (Abeysekara et al., 2017), as shown in Figure 2.7. They calculated the particle diffusion to explain the extended emission, and concluded these pulsars are unlikely to be the origin of the positron excess. However, this extended emission around Geminga and Monogem pulsars made the theoretical approach with astrophysical sources a hotter topic. Using the different diffusion processes such as different diffusion coefficient, energy-independent diffusion coefficient, and two-zone diffusion, many theoretical studies were performed to reproduce the positron excess (e.g. Hooper et al., 2017; Profumo et al., 2018; Tang and Piran, 2019). For Vela pulsar and its pulsar wind nebula Vela X, Huang et al. (2018) proposed the inefficient cosmic-ray diffuse around Vela X by using the observed multi-wavelength data and cosmic-ray data. The inefficiency could be caused by the turbulence inside the Vela SNR, which expands around Vela X. Nearby SNRs (like the Vela SNR, Monogem ring, and Cygnus loop) are also considered as the candidate astrophysical source of positrons (also electrons). SNR can generate positrons through interactions between accelerated nuclei and ambient matter, then accelerated by the shock waves or escape from the SNR (some of them emit electromagnetic radiation). Using different assumptions such as nearby SNR, nearby SNR plus other distant SNRs, and nearby SNR interacting with Molecular cloud, there are many theoretical studies to interpret the positron

---

[2] Below ~ 10 GeV, the measured data has time variability due to the solar modulation.

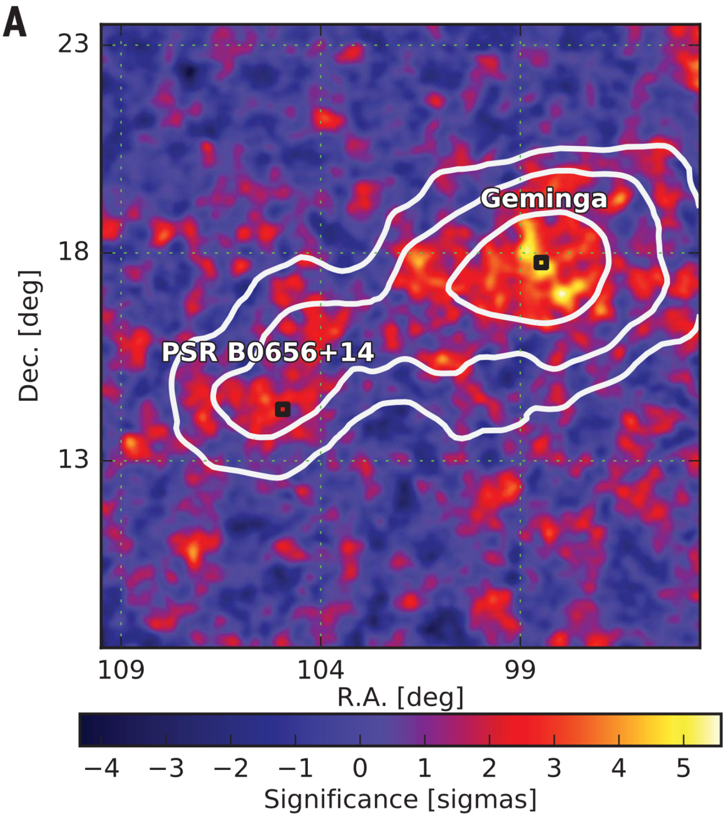

Figure 2.7. HAWC significance map (1 − 50 TeV) in the region of Geminga and Monogem pulsars with contours of 5σ, 7σ, and 10σ confidence levels (Abeysekara et al., 2017).

excess (e.g., Mertsch and Sarkar, 2014; Tomassetti and Donato, 2015; Liu et al., 2017; Kachelrieß, Neronov, and Semikoz, 2018). The combination of SNR and pulsar (and its pulsar wind nebula) is also considered for an explanation of the excess (e.g., Ding et al., 2021). In this case, SNR plays a source of only electrons or both electrons and positrons.

Using the results of the precise cosmic-ray antiproton measurement, the sophisticated cosmic-ray diffusion can reproduce the positron excess and softening spectrum of electrons (e.g., Blum, Katz, and Waxman, 2013; Cowsik, Burch, and Madziwa-Nussinov, 2014; Lipari, 2017). In this case, the positrons are produced via interactions between comic rays and ISM during the propagation. Their diffusion models are needed to be validated with future observational data at higher energy.

Annihilation of dark matter particles into positrons in the vicinity of Earth has also a possibility to explain the origin of the positron excess. There are a lot of studies to interpret the excess with dark matter (e.g., Kopp, 2013; Chen, Chiang, and Nomura, 2015; Bai, Berger, and Lu, 2018). But the required annihilation rate of $\sim 10^{-23}$ cm^{3}s^{-1} is about two to three orders of magnitude higher than that of the annihilation predicted by the simple dark matter model. In addition, the observed antiproton spectrum is consistent with a model of secondary produced by the cosmic-ray protons during their propagation. It constrains the dark matter not to annihilate into a hadronic channel. In order to explain the origin of the positron excess by dark matter, candidate particles are satisfied with these observational requirements.

2.2 Supernova Remnant (SNR)

Supernovae are explosions with an enormous amount of kinetic energy ($\sim 10^{51}$ erg) occurring in the final stages of stellar evolution. They are classified into two types: thermonuclear supernovae (or type Ia supernovae) and core-collapse supernovae, based on the explosion mechanism. Type Ia supernovae are triggered by the thermonuclear explosions of white dwarfs which have accreted mass from a companion star in a binary system (Single Degenerate channel). Another scenario of type Ia supernovae is a merger of two white dwarfs (Double Degenerate channel). The core-collapse supernovae are triggered by the core collapses of the massive stars ($> 8\,\mathrm{M}_\odot$) after consuming out of their nuclear fuel. The collapsed core remained as a central compact object (CCO), such as a neutron star or black hole. In Figure 2.8, examples of type Ia and core-collapse supernova remnants (SNRs) are shown.

After a supernova explosion, materials which were consisted of the star before the supernova, are ejected and expanded into space. This astronomical object is named the supernova remnant (SNR). It emits electromagnetic radiation for $\sim 10^6$ years and has a size of several hundreds of parsecs at the end of its evolution. SNRs play multiple roles in galaxies (e.g., heating the ISM, chemical evolution of the galaxy, inducing star formation by compressing interstellar clouds, and dispersing metals synthesized inside stars and during the supernovae into space.) Among those roles, this thesis focuses on particle acceleration by SNR[3].

2.2.1 Energy contents of cosmic rays and supernova remnant

SNRs are considered as one of the candidate accelerators of the Galactic cosmic rays, whose idea was proposed by Baade and Zwicky (1934) and Ginzburg and Syrovatsky (1961). In the following, the amount of energy required for Galactic cosmic rays is simply compared to the amount of energy released by an SNR. The escape time of Galactic cosmic rays from the Galaxy is $\tau_{\mathrm{esc}} \sim 10^7$ years which is derived from the ratio of cosmic-ray boron and carbon (B/C). From the energy density of cosmic rays $U_{\mathrm{CR}} \sim 1$ eV cm^{-3} and the volume of the Galaxy V_{gal}, the necessary power to maintain the energy density of Galactic cosmic rays is estimated to be

$$\dot{E}_{\mathrm{CR}} \sim \frac{U_{\mathrm{CR}} V_{\mathrm{gal}}}{\tau_{\mathrm{esc}}} \sim 10^{41}\ \mathrm{erg\ s^{-1}}. \tag{2.2}$$

The power provided by supernova explosions is

$$\dot{E}_{\mathrm{SN}} \sim \frac{E_{\mathrm{SN}}}{\tau_{\mathrm{SN}}} \sim 10^{42}\ \mathrm{erg\ s^{-1}}, \tag{2.3}$$

where $E_{\mathrm{SN}} \sim 10^{51}$ erg and $\tau_{\mathrm{SN}} \sim 1/(30 - 100)$ year^{-1} are the kinetic energy released in a supernova explosion and the rate of supernova, respectively. From Equations

---

[3] The other physics and evolution of SNR are summarized in Vink (2020).

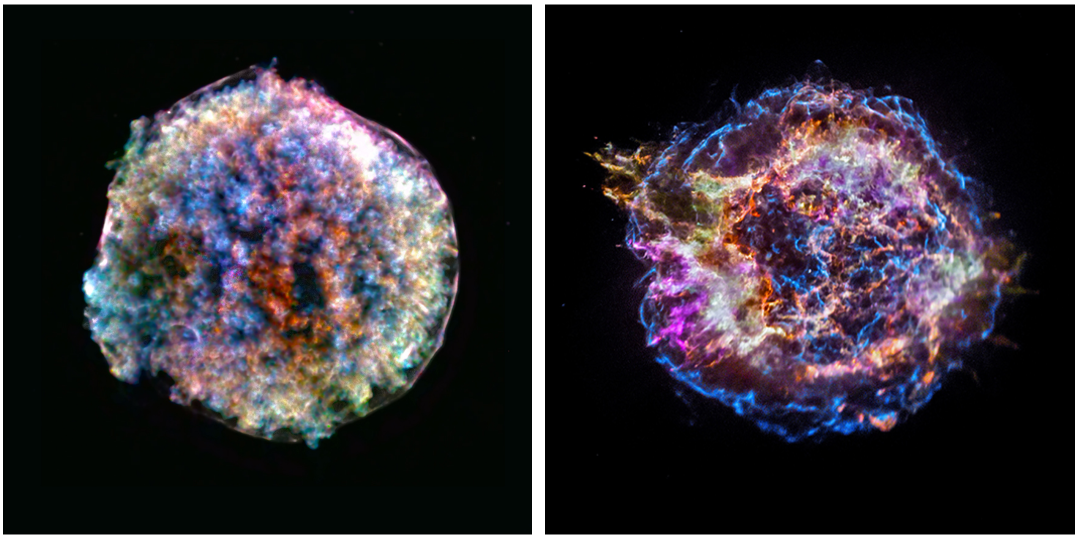

Figure 2.8. (Left) X-ray image of a type Ia SNR named Tycho's SNR. (Right) X-ray image of a core-collapsed SNR named Cassiopeia A. (taken from Chandra X-ray Center (CXC) https://chandra.harvard.edu/)

2.2 and 2.3, SNRs can supply the energy required for Galactic cosmic rays by transferring about 10% of the kinetic energy released in a supernova explosion for the acceleration of cosmic rays.

2.2.2 Electromagnetic radiation by high-energy particles

Direct observations of cosmic rays are unable to identify the accelerator due to the orbital bending by the interstellar magnetic field. The information of accelerated particles by SNRs is indirectly obtained by using electromagnetic radiation. SNRs have been observed in multi-wavelength radiation from radio to TeV gamma-ray bands. High-energy particles radiate multi-wavelength radiation by interacting with the magnetic field, ISM, and photon field.

Radio synchrotron radiations were discovered at the locations of SNRs around the 1950s. They indicate that electrons are accelerated to energies on the order of GeV from the relation between synchrotron frequency ν_{synch} and electron energy E_{e} of $\nu_{\mathrm{synch}} \approx 15(B/10\ \mu\mathrm{G})(E_{\mathrm{e}}/1\ \mathrm{GeV})^2$ MHz. From the perspective of the accelerator of Galactic cosmic rays, the particles would be expected to have energies in the range of 10^{12} to $\lesssim 10^{15}$ eV. In 1995, Koyama et al. (1995) first discovered electrons with energies of the TeV regime in SN 1006 by detecting the synchrotron X-ray emission with the Japanese X-ray satellite ASCA (Advanced Satellite for Cosmology and Astrophysics). The ASCA observation found the limbs are dominated by synchrotron emission, while the central region is dominated by thermal emission (see Figure 2.9). In the limb region, the shock wave is expanding into the ISM and transfers the kinetic energy released by a supernova explosion into particle acceleration. After the discovery of synchrotron X-ray emission from SN 1006, non-thermal X-ray emissions are observed from limb regions of many young SNRs, such as RX J1713.7−3946 and

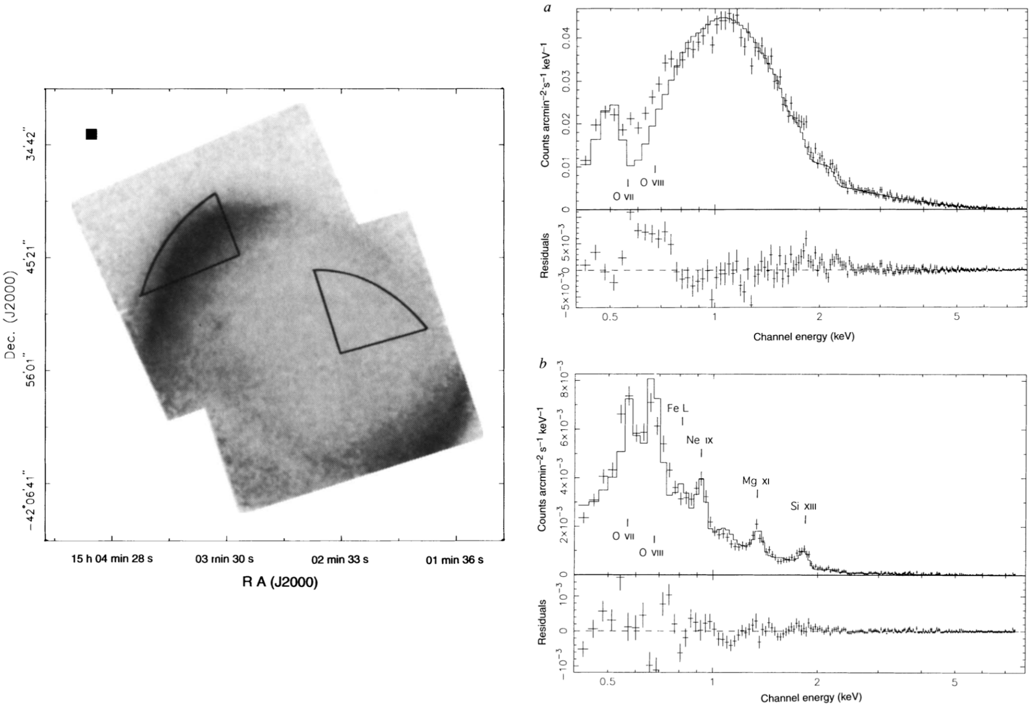

Figure 2.9. (Left) X-ray image of SN 1006 with ASCA. (Right) X-ray spectra extracted from limb (top) and central (bottom) regions (Koyama et al., 1995).

Vela Junior (see Reynolds, 2008, for review). As shown in Figure 2.8, the non-thermal X-ray filaments are observed in the limb region of many SNRs using the high angular resolution of the *Chandra* satellite. The synchrotron emissions from radio to X rays revealed the existence of accelerated electrons (leptonic cosmic rays) inside the SNRs.

Cosmic rays observed on Earth are mainly high-energy atomic nuclei (hadronic cosmic rays). Detection of π^0-decay gamma rays, which are byproducts of the interaction of hadronic cosmic rays with the ISM, provides evidence for the existence of hadronic cosmic rays. It became possible to observe the gamma-ray sky as the technology of gamma-ray observation developed in the late 20th century. In the 2000s, TeV gamma-ray emissions from SNRs were confirmed with Imaging Atmospheric Cherenkov Telescopes (IACTs) on the ground such as H.E.S.S, MAGIC, and VERITAS telescopes (e.g.: Aharonian et al., 2004; Aharonian et al., 2005), implying the high-energy particles accelerated up to TeV band. In GeV gamma-ray band, the EGRET on board *Compton* Gamma-Ray Observatory has made great results such as all-sky surveys and the detection of gamma-ray emission from SNR regions (e.g., Hartman et al., 1999). The Large Area Telescope (LAT) on board *Fermi*, which has much better performance than the EGRET, has taken over all-sky observations of GeV gamma-ray sky. Many SNRs have been established as gamma-ray sources by these observations (see Funk, 2015, for review). High-energy protons were firmly discovered from several middle-aged SNRs by detecting the gamma-ray spectrum

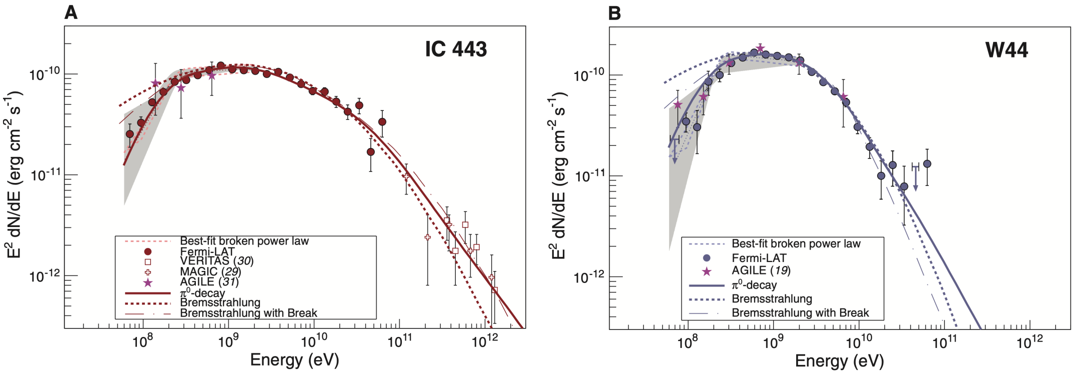

Figure 2.10. Gamma-ray spectra of IC 443 (left) and W44 (right). Both spectra show characteristic pion bump at a few hundreds of GeV, indicating the high-energy protons radiate gamma rays via π^0-decay process (Ackermann et al., 2013).

with a characteristic cut-off around a few hundreds MeV radiated by the π^0-decay process (Ackermann et al., 2013; Jogler and Funk, 2016), as shown in Figure 2.10. The gamma-ray spectrum of very young SNR Cassiopeia A (see Figure 2.11) was also found to be explained by the π^0-decay process (Ahnen et al., 2017; Abeysekara et al., 2020). The spectrum in the high-energy band can be described by a power law with an exponential cut-off at $\sim 2.3-3.5$ TeV. The corresponding cut-off energy of the proton spectrum is $\sim 6-12$ TeV, though the proton acceleration up to PeV is feasible in the young SNR because of the high shock speed. Recently, Fang et al. (2022) suggest the evidence of protons accelerated up to ~ 1 PeV from middle-aged SNR G106.3+2.7. Since this SNR is detected from many TeV gamma-ray observations (VERITAS: Acciari et al. (2009), HAWC: Albert et al. (2020), LHAASO: Cao et al. (2021), and Tibet ASγ: Tibet ASγ Collaboration et al. (2021)), it is considered one of the candidate accelerators of PeV particles but the radiation mechanism had been under debate (i.e., leptonic or hadronic). Using the GeV gamma-ray data, Fang et al. (2022) constrained the mechanism deeper and found that the leptonic scenario is inconsistent with multi-wavelength data.

Although the evidence of accelerated electrons and protons are discovered in several SNRs, the radiation processes of gamma-ray emission in many SNRs are still controversial: whether they are emitted by high-energy electrons (leptonic scenario) or protons (hadronic scenario). Magnetic field and interaction with the ISM (e.g., molecular cloud and HI gas) are important to constrain the gamma-ray radiation mechanism. The strength of the magnetic field can constrain the leptonic emission, like synchrotron and inverse-Compton radiations, and it can be expected by comparing the synchrotron and inverse-Compton emissions. The interactions between the ISM and SNR also constrain the hadronic emission by using the number density of target matter and spatial correlation. It is important to approach the dominant radiation mechanism using multi-wavelength electromagnetic radiations as well as developing messenger like neutrinos.

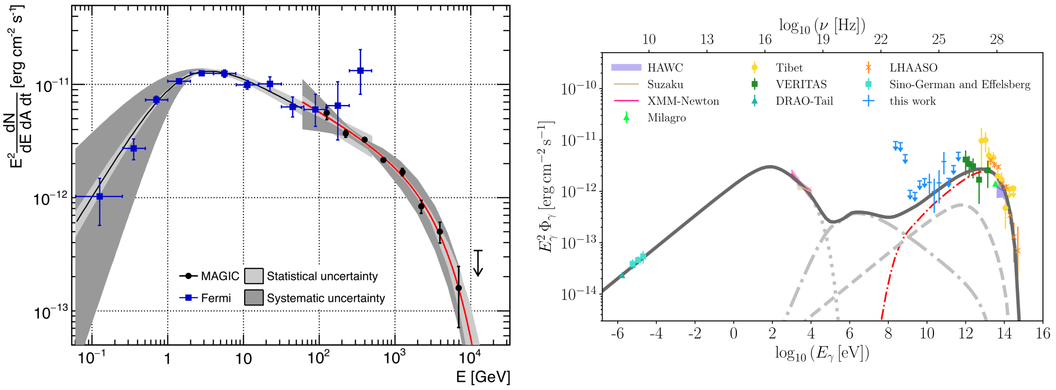

Figure 2.11. (Left) Gamma-ray spectrum of SNR Cassiopeia A with *Fermi*-LAT and MAGIC telescope (Ahnen et al., 2017). (Right) Multi-wavelength spectrum (from radio to gamma-ray band) of SNR G106.3+2.6. Red line represents the π^0-decay gamma-ray emission. Gray lines represent synchrotron (dotted), bremsstrahlung (dash-dotted), and inverse-Compton scattering (dashed) (Fang et al., 2022).

2.2.3 Unsolved issues of SNRs as Galactic cosmic-ray accelerators

The bulk of Galactic cosmic rays is considered to be accelerated by SNRs and it is supported by discoveries of accelerated high-energy electrons and protons. There are remaining problems to be solved before SNRs are established as accelerators of Galactic cosmic rays. The major problems that need to be satisfied as accelerators of Galactic cosmic rays are addressed here.

-Maximum energy that can be accelerated by SNRs. There is only one evidence of hadronic particles accelerated up to the knee energy (a few PeV) because of the cutoffs at several TeV in the gamma-ray spectra of many observed SNRs. The candidate SNR G106.3+2.7 even requires the proton spectrum with an index of ~ 1.73, which is harder than that predicted by the standard acceleration mechanism (Fang et al., 2022). Observational studies on the maximum energy are being conducted in parallel with theoretical studies using telescopes (e.g.: Tibet ASγ and LHAASO) that can detect more energetic gamma rays than previous TeV gamma-ray telescopes. It is expected that evidence of protons accelerated to PeV are found from many SNRs with these new TeV gamma-ray telescopes, like G106.3+2.7. Since the magnetic field is important for the acceleration and energy loss of particles, to constrain the strength of the magnetic field can develop the discussion of the maximum energies of SNRs.

-Injection into the acceleration process and the escape from the process. The seed particles injected into the acceleration process are unclear. The mechanism of injection and the characteristics of seed particles are needed to be clear. The escape from the acceleration region is also an unsolved problem. The higher energy particles are considered to escape faster because the gyro radius of high-energy particles becomes larger than the size of SNRs. The escape problem is also related to the maximum energy of accelerated particles. The escape of high-energy particles can be studied by gamma-ray analysis from molecular clouds in the vicinity of SNRs (Aharonian et al., 2008a; Hanabata et al., 2014; Uchiyama et al., 2012).

-Cosmic-ray anomalies discovered by recent precise observations. Cosmic-ray anomalies (e.g.: positron excess and spectral hardening of protons) need to be uncovered. Nearby accelerators are important with regard to the positron excess and the spectral break of electrons and positrons (shown at the top left and right panels in Figure 2.3). SNRs are also the candidate accelerators of these anomalies.

2.2.4 Compact objects playing the role of cosmic-ray accelerators

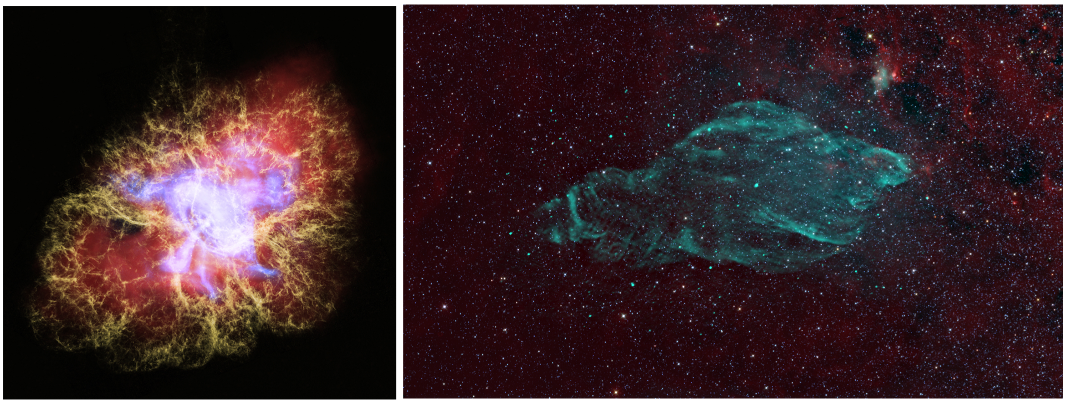

Figure 2.12. Left: Composite image of Crab Nebula. Red, yellow, and blue colors represent the infrared, optical, and X-ray images, respectively. Crab pulsar is located at the center of Crab Nebula. (take from CXC `https://chandra.harvard.edu/`.) Right: Composite image of microquasar SS 433/W50 system. Green and red colors represent radio and infrared background emission, respectively. (taken from NRAO `https://www.nrao.edu/`.)

After a core-collapse supernova explosion, a compact star (neutron star or black hole) has remained inside the SNR. The neutron star pulsating in the multi-wavelength band is called "pulsar". It is rapidly rotating (pulse period$\sim 0.1 - 10$ s) and has a strong magnetic field ($B \sim 10^{12}$ G). The particles are accelerated and generated the magnetosphere around the neutron star. The dipole field breaks up when the velocity of the magnetic field and trapped particles exceed the speed of light for a certain radius. Outside the radius, particles (electrons and positrons) are escaping from the magnetosphere with relativistic bulk velocity (pulsar wind) until the pressure of the wind equals external pressure at the termination shock. The particles are shock-heated and accelerated at the termination shock (i.e., termination shock converts a part of the kinetic energy of bulk motion into the energy of accelerated particles.). The outside region beyond the termination shock is called "pulsar wind nebula", where accelerated electrons and positrons emit synchrotron radiation and inverse Compton radiation in the multi-wavelength band. In the pulsar wind nebula, the presence of very high-energy particles is confirmed by the spectrum with a cutoff at several hundreds of TeV. In the left panel of Figure 2.12, Crab pulsar and its pulsar wind nebula is shown as an example of pulsar and pulsar wind nebula.

The compact star occasionally forms a binary system with a relativistic jet during its evolution. The binary with the jet is called "Microquasar". It is also one of the cosmic-ray accelerators; the synchrotron radio emissions radiated by accelerated electrons are detected from many X-ray binaries. Only three X-ray binary are confirmed as gamma-ray sources (i.e., Cygnus X-1, Cygnus X-3, and SS 433). The gamma-ray emission via inverse Compton scattering can be observed in the acceleration region (inside the jet or shocks created by the jet propagation) if high-photon fields are provided by the accretion disk, companion star, and the jet itself as well. Recently, very high-energy photons (in TeV gamma-ray range) are detected from the SS 433/W50 system with HAWC (Abeysekara et al., 2018). Its detection makes this system one of the most notable accelerators of cosmic rays. Following the detection in TeV band, studies of particle acceleration in this system have been actively performed in GeV gamma-ray band (Xing et al., 2019; Sun et al., 2019; Rasul et al., 2019; Li et al., 2020; Fang, Charles, and Blandford, 2020). In the right panel of Figure 2.12, the radio image of the SS 433/W50 system is shown.

2.3 Particle Acceleration

Some kinetic energy released in a supernova explosion is converted to particle acceleration via shock waves (Axford, Leer, and Skadron, 1977; Krymskii, 1977; Bell, 1978; Blandford and Ostriker, 1978). The theoretical model is usually referred to as diffusive shock acceleration (DSA). In this section, the acceleration of particles via DSA is briefly derived, and the timescale and maximum energy of the acceleration are estimated.

2.3.1 Shock wave induced by a supernova explosion

A supernova explosion ejects the stellar materials, and the ejecta expands in the ISM. The initial velocity of the ejecta ($V_{\rm ej}$) is expected as

$$V_{\rm ej} = 10000 \left(\frac{E_{\rm SN}}{10^{51}\ {\rm erg}}\right)^{1/2} \left(\frac{M_{\rm ej}}{1\ {\rm M}_\odot}\right)^{-1/2} \ {\rm km\ s^{-1}}, \tag{2.4}$$

where $E_{\rm SN}$ and $M_{\rm ej}$ denote the kinetic energy released in a supernova explosion and the ejecta mass in the units of the solar mass, respectively. The sound speed c_s in the ISM is described as

$$c_s = \sqrt{\gamma_g \frac{k_B T}{m_p}} \approx 11 \left(\frac{T}{10^4\ {\rm K}}\right)^{-1/2} \ {\rm km\ s^{-1}}, \tag{2.5}$$

where γ_g, k_B, T, and m_p denote the adiabatic index, Boltzmann constant, temperature of the ISM, and proton mass, respectively. Shock waves are induced as the ejecta expands at speeds faster than the sound speed in ISM. From Equations 2.4 and 2.5, the Mach number of ejecta is

$$M_s = \frac{V_{\rm ej}}{c_s} \approx 900 \left(\frac{E_{\rm SN}}{10^{51}\ {\rm erg}}\right)^{1/2} \left(\frac{M_{\rm ej}}{1\ {\rm M}_\odot}\right)^{-1/2} \left(\frac{T}{10^4\ {\rm K}}\right)^{-1/2}. \tag{2.6}$$

Shock waves of SNRs hold the speed of thousands of km s^{-1} for more than thousands of years. The particles are accelerated at the shock waves in SNRs via DSA.

2.3.2 Rankine-Hugoniot jump conditions

In shock waves, the physical quantities are changed discontinuously. From the conservation laws of mass, momentum, and energy flux, the density (ρ), pressure (p), and temperature (T) between the upstream and downstream of shock have jump

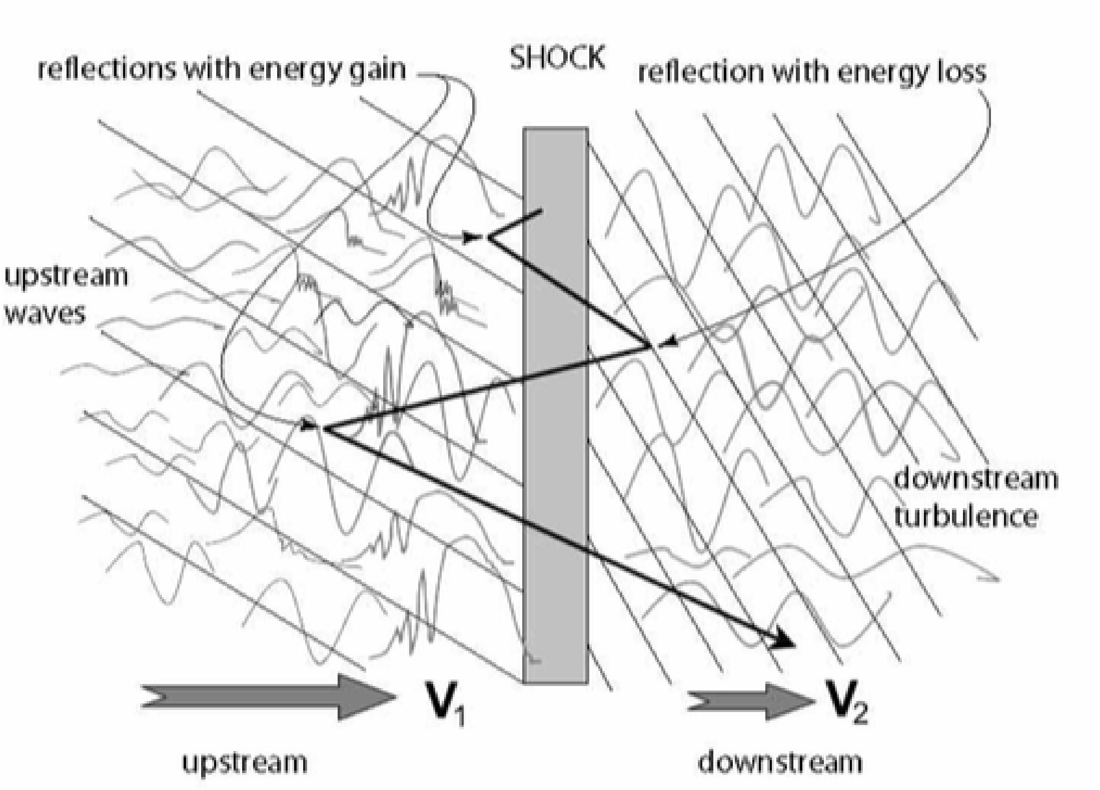

Figure 2.13. Schematic picture of both upstream and downstream in the rest frame of shock wave. Upstream and downstream regions are un-shocked and shocked regions, respectively (Treumann and Jaroschek, 2008).

conditions (so-called Rankine-Hugoniot jump conditions), which are expressed as:

$$\frac{\rho_2}{\rho_1} = \frac{V_1}{V_2} = \frac{(\gamma_g+1)M_s^2}{(\gamma_g-1)M_s^2+2} \approx 4, \tag{2.7}$$

$$\frac{p_2}{p_1} = \frac{2\gamma_g M_s^2-(\gamma_g-1)}{\gamma_g+1} \propto M_s^2, \tag{2.8}$$

$$\frac{T_2}{T_1} = \frac{p_2\rho_1}{p_1\rho_2} = \frac{\left[2\gamma_g M_s^2-(\gamma_g-1)\right]\left[(\gamma_g-1)M_s^2+2\right]}{(\gamma_g+1)^2M_s^2} \propto M_s^2, \tag{2.9}$$

where subscript 1 and 2 are the labels of quantities in the unshocked region (upstream) and shocked region (downstream), respectively. The last terms are derived from the assumption of the $\gamma_g = 5/3$ and $M_s \gg 1$ (strong shock).

2.3.3 Diffusive shock acceleration (DSA)

The charged particles cross and recross the shock owing to the reflections by magnetic-field irregularities. The basic idea of diffusive shock acceleration is that the particles gain energies in this cycle. The accelerated particles have a spectrum of power-law type with a spectral index of ~ 2, which is consistent with the spectrum of the Galactic cosmic rays[4].

Let us consider the energy gain of a particle with energy E_1 in upstream and cross the shock. The energy of the particle in downstream (E_2) is given by a Lorenz transformation:

$$E_2 = E_1 \left(1 - \frac{V_1 - V_2}{c} \cos\theta_1\right), \tag{2.10}$$

where V_1, V_2, and c denote the velocities of the upstream and downstream, and speed of light, respectively. θ_1 is the angle between the shock normal vector and velocity vector of the particle. The particle across the shock into the downstream is randomly reflected to the upstream via irregularity of magnetic field. The energy of the particle returned into the upstream is given by inverse-Lorenz transformation:

$$E_1' = E_2 \left(1 + \frac{V_1 - V_2}{c} \cos\theta_2\right). \tag{2.11}$$

Here, θ_2 is the angle between the shock normal vector and velocity vector of the particle. The energy gain in one cycle is derived from Equations 2.10 and 2.11 as:

$$\frac{\Delta E_1}{E_1} = \frac{E_1' - E_1}{E_1} \approx \frac{V_1 - V_2}{c} \left(\cos\theta_1 - \cos\theta_2\right). \tag{2.12}$$

By averaging the angles, the energy gain can be described as

$$\frac{\Delta E_1}{E_1} \approx \frac{4}{3}\frac{(V_1 - V_2)}{c} = \frac{4}{3}\frac{V}{c}. \tag{2.13}$$

The particles are needed to cross the shock many times in order to be accelerated up to the energy of cosmic rays. After k cycles, the energy E of a particle with initial energy E_0 is given by

$$E = E_0 \left(1 + \frac{4V}{3c}\right)^k \sim E_0 \exp\left(\frac{4V}{3c}k\right). \tag{2.14}$$

The average flux of particles across the shock from the upstream to the downstream is $f_1 = nc/4$, while the flux of particles advected away and escaped from the shock is $f_2 = nV_2$, where n denotes the number density of the particle. After one cycle, the probability of particles being escaped from the acceleration cycle is written as $f_2/f_1 = 4V_2/c$. After the k cycle, the number of particles (N) being remained in the acceleration cycle is given as

$$N = N_0 P^k, \tag{2.15}$$

where N_0 and $P = 1 - 4V_2/c$ are the initial number of particles and the probability of particles remained after one cycle, respectively. With Equations 2.14 and 2.15, k is

---

[4] The spectrum gets steeper during the propagation in the Galaxy (the spectral index becomes larger by the original index $+(0.3 - 0.6)$).

eliminated by

$$\frac{\ln(N/N_0)}{\ln(E/E_0)} = \frac{\ln P}{V_1/c} \tag{2.16}$$

resulting in

$$\frac{dN}{dE} \propto E^{\ln P/(4V/3c)-1} = E^{-\frac{\sigma+2}{\sigma-1}}. \tag{2.17}$$

In the case of a strong shock, the spectral index of 2 is derived by the compression ratio $\sigma = 4$.

2.3.4 Acceleration timescale

The timescale needed for particles to be accelerated strongly depends on the shock velocity. The average time that a particle spends in the upstream and downstream of the shock to complete one cycle is given by

$$\Delta t = \frac{4}{c}\left(\frac{D_1}{V_1} + \frac{D_2}{V_2}\right), \tag{2.18}$$

where D_1 and D_2 denote the diffusion coefficient of the upstream and downstream, respectively. Using Equations 2.12 and 2.18, the acceleration timescale is written as

$$\tau_{\rm acc} = \frac{E}{\Delta E/\Delta t} = \frac{3}{V}\left(\frac{D_1(E)}{V_1} + \frac{D_2(E)}{V_2}\right). \tag{2.19}$$

In general, the diffusion coefficient around SNR is often parameterized as $D = \eta r_g c/3$, where $\eta \geq 1$ and $r_g = E/ZqB = 3.3 \times 10^{15}(E/10\,\mathrm{TeV})(B/10\,\mu\mathrm{G})^{-1}(Z/1)^{-1}$ cm denote the Bohm factor and gyroradius of the particle. In the extreme case with $\eta = 1$, the effective mean free path can be as small as gyroradius of particle. Assuming $D_1 = D_2$, the acceleration timescale becomes

$$\tau_{\rm acc} = \frac{20}{3}\frac{cE}{V_{\rm sh}^2 ZqB}\eta \approx 5.2 \times 10^3 \eta \left(\frac{E}{100\,\mathrm{TeV}}\right)\left(\frac{B}{10\,\mu\mathrm{G}}\right)^{-1}\left(\frac{V_{\rm sh}}{2000\,\mathrm{km\,s^{-1}}}\right)^{-2} \text{years} \tag{2.20}$$

where $V_{\rm sh}$ denotes the shock speed, and in the last term $Z = 1$ (e.g.: proton and electron) is assumed. The acceleration timescale indicates that the higher shock speed results in the shorter time needed for the particle to be accelerated. The stronger magnetic field also results in a shorter acceleration time. The young SNRs with high-speed shock waves can effectively accelerate particles.

2.3.5 Maximum energy

From Equation 2.20, a very young SNR with the age ($\tau_{\rm age}$) of serval hundreds of years is unable to accelerate the particle up to 100 TeV in the magnetic field of 10 μG because of $\tau_{\rm age} < \tau_{\rm acc}$. The maximum energy of a particle obtained in an SNR is constrained by the age of the SNR, and written as

$$E_{\mathrm{max(age)}} = \frac{3}{20}\frac{V_{\mathrm{sh}}^2 ZqB}{c}\tau_{\mathrm{age}}\eta^{-1} \sim 19\eta^{-1}\left(\frac{\tau_{\mathrm{age}}}{10^3\ \mathrm{yr}}\right)\left(\frac{V_{\mathrm{sh}}}{2000\ \mathrm{km\ s^{-1}}}\right)^2\left(\frac{B}{10\ \mu\mathrm{G}}\right)\ \mathrm{TeV}. \tag{2.21}$$

The high-energy particle has a diffusion length of D_1/V_{sh} in the upstream region. If the diffusion length is small, the particle is confined around shock and accelerated via DSA. If it becomes larger, the particle escape from the acceleration cycle. Assuming the ℓ as the distance from the shock in the upstream, the maximum energy constrained by escaping of particles ($D_1/V_{\mathrm{sh}} \sim \ell$) is given by

$$E_{\mathrm{max(esc)}} = \frac{3Zq}{4c}\ell V_{\mathrm{sh}}B\eta^{-1} \sim 48\eta^{-1}\left(\frac{V_{\mathrm{sh}}}{2000\ \mathrm{km\ s^{-1}}}\right)\left(\frac{\ell}{1\ \mathrm{pc}}\right)\left(\frac{B}{10\ \mu\mathrm{G}}\right)\ \mathrm{TeV}. \tag{2.22}$$

From Equations 2.21 and 2.22,

$$\frac{E_{\mathrm{max(loss)}}}{E_{\mathrm{max(age)}}} = 5\frac{\ell}{V_{\mathrm{sh}}\tau_{\mathrm{age}}}, \tag{2.23}$$

which implies that in the case of $\ell \gg V_{\mathrm{sh}}\tau_{\mathrm{age}}$ (early phase of SNR evolution) the maximum energy is constrained by age limit. In the case of $\ell \ll V_{\mathrm{sh}}\tau_{\mathrm{age}}$ the maximum energy is constrained by particle escape.

As described subsequent section (Section 2.4), the high-energy particles lose their energy through non-thermal radiations. Very high-energy electrons particularly lose energy rapidly and effectively (less than the age of a young SNR) by synchrotron radiation (details are given in Section 2.4.1). The maximum energy of electrons constrained by the synchrotron radiation loss is expected to be $\tau_{\mathrm{acc}} = \tau_{\mathrm{synch}}$, and given by

$$E_{\mathrm{max(loss)}} \sim 48\eta^{-\frac{1}{2}}\left(\frac{B}{10\ \mu\mathrm{G}}\right)^{-\frac{1}{2}}\left(\frac{V_{\mathrm{sh}}}{2000\ \mathrm{km\ s^{-1}}}\right)\ \mathrm{TeV}. \tag{2.24}$$

The minimum energy among the $E_{\mathrm{max(age)}}$, $E_{\mathrm{max(esc)}}$, and $E_{\mathrm{max(loss)}}$ is the attainable maximum energy in SNR. It depends on the age, shock speed, and magnetic field, which indicates the evolution of SNR and amplification of magnetic field are crucial to determining the maximum energy.

2.4 Radiative Processes

High-energy particles emit electromagnetic radiation from radio to the TeV gamma-ray band by interaction with the magnetic field (synchrotron radiation), low-energy photon field (inverse Compton scattering), and the ISM (neutral pion (π^0) decay). It allows us to indirectly investigate the particle acceleration occurred in SNRs. The radiation is called non-thermal radiation in contrast to thermal radiation which originated from electrons and ions heated by shocks. An example of non-thermal radiations emitted by SNRs is shown in Figure 2.14. In this figure, a power-law with an exponential cutoff model is assumed as:

$$\frac{dN_i}{dE_i} \propto E_i^{-s_i} \exp\left(\frac{E_i}{E_c}\right), \tag{2.25}$$

where the subscript $i = e$ or p denotes the particle spectra of electrons and protons. s_i and E_c, which are the spectral index and cutoff energy, are assumed to be 2 and 30 TeV, respectively.In this section, each radiation process is summarized in the subsequent subsections, and the details could be found e.g., in Rybicki and Lightman (1986), Longair (2011), Kelner, Aharonian, and Bugayov (2006), and Kafexhiu et al. (2014).

2.4.1 Synchrotron radiation

Synchrotron radiation is emitted by the relativistic charged particles gyrating in the magnetic field. The synchrotron radiation from SNRs is efficiently emitted by electrons because of its light mass. The radiation could be widely detected from radio to the X-ray band (see Figure 2.14). Hereafter when synchrotron radiation is referred to, it is considered to be emitted by electrons.

The power of synchrotron radiation emitted by a single electron is given by

$$P_{\rm synch} = -\left(\frac{dE_e}{dt}\right)_{\rm synch} = \frac{3}{4}\sigma_{\rm T} c \gamma_e^2 U_B, \tag{2.26}$$

where $\sigma_T = 8\pi r_0^2/3$ (where $r_0 = e^2/m_e c^2$), γ_e, and $U_B = B^2/8\pi$ denote the Thomson cross-section, Lorentz factor of the electron, and energy density of the magnetic field. Because of the beaming effect, the synchrotron radiation is concentrated within the narrow angle ($\sim 1/\gamma_e$) directed to the movement. The synchrotron spectrum by a single electron is written as

$$P(\omega) = \frac{\sqrt{3}}{2\pi}\frac{e^3 B \sin\alpha}{m_e c^2} F\left(\frac{\omega}{\omega_c}\right), \tag{2.27}$$

where α denotes the pitch angle. ω_c is the critical frequency defined as

$$\omega_c = \frac{3\gamma_e^2 e B \sin\alpha}{2 m_e c}. \tag{2.28}$$

The function F is described as

$$F(x) \equiv x \int_x^\infty K_{\frac{5}{3}}(\xi) d\xi \tag{2.29}$$

with modified Bessel function of $K_{\frac{5}{3}}$. The function has a peak roughly at $x = \omega/\omega_c = 0.29$, which indicates the maximum power is reached at $\omega = 0.29\omega_c$. This frequency is often used as the typical frequency of synchrotron radiation from an electron. The corresponding energy of synchrotron emission is given by

$$\varepsilon = 0.29\hbar\omega_c \approx 1.6 \left(\frac{B}{10\ \mu\mathrm{G}}\right) \left(\frac{E_e}{100\ \mathrm{TeV}}\right)^2 \mathrm{keV}. \tag{2.30}$$

It represents that the typical electron energy of synchrotron radio emission is about an order of GeV, whereas the typical electron energy of synchrotron X-ray emission is about an oder of TeV.

Owing to DSA, the electrons are expected to have a power-law type spectrum in SNRs. The synchrotron spectrum from the electrons with the energy distribution of power-law type ($dN_e/dE_e \propto E_e^{-s}$) is given by

$$P_{tot}(\omega) \propto \int_0^\infty P(\omega) dN_e \propto \omega^{-(s-1)/2}. \tag{2.31}$$

The synchrotron spectrum also has a power-law type spectrum with the index of $(s-1)/2$. In the X-ray and gamma-ray bands, the spectrum is commonly expressed with luminosity density in units of photons per second per energy. In this expression, the spectral index become $(s+1)/2$.

From Equation 2.26, the cooling timescale in which an electron loses a substantial fraction of the energy is given by

$$\tau_{\mathrm{synch}} \equiv \frac{E_e}{dE_e/dt} \approx 12 \left(\frac{E_e}{1\ \mathrm{TeV}}\right)^{-1} \left(\frac{B}{1\ \mathrm{mG}}\right)^{-2} \mathrm{years}, \tag{2.32}$$

which means that in a strong magnetic field, electrons with TeV-scale energy lose their energies in several years. It also implies that electrons with higher energies lose the energies faster. This cooling timescale of electron arise a spectral break in the electron spectrum at the energy of

$$E_{\mathrm{break}} \approx 1.25 \left(\frac{B}{100\ \mu\mathrm{G}}\right)^{-2} \left(\frac{t}{1000\ \mathrm{yr}}\right)^{-1} \mathrm{TeV}. \tag{2.33}$$

2.4.2 Inverse Compton scattering

High-energy electrons emit gamma rays via up-scattering of low-energy photons to higher energy, which is called inverse Compton scattering (see Figure 2.14).

It is one of the principal gamma-ray processes in high-energy astrophysics. If high-energy electrons exit, the inverse Compton scattering works almost everywhere because of the presence of cosmic microwave background. The inverse Compton scattering of protons is suppressed by a factor of $(m_e/m_p)^4$. Hereafter when inverse Compton scattering is referred to, it is considered to be emitted by electrons.

In the Thomson regime ($\gamma_e\varepsilon \ll m_ec^2$), the up-scattered photon gains the energy of $\sim \gamma_e^2\varepsilon$. The power of inverse Compton scattering is described as

$$P_{\rm IC} = -\left(\frac{dE_e}{dt}\right) = \frac{4}{3}\sigma_{\rm T}c\gamma_e^2U_{ph}, \tag{2.34}$$

where U_{ph} denotes the energy density of the seed photon field. Compared between Equation 2.26 and Equation 2.34, the only difference is the replacement of energy density of magnetic field to target photon field. The ratio is given by

$$\frac{P_{\rm synch}}{P_{\rm IC}} = \frac{U_B}{U_{ph}}. \tag{2.35}$$

The ratio decided the dominant radiation process of high-energy electrons, and it is used to estimate the strength of magnetic field from the observed synchrotron radiation and inverse Compton scattering.

The total cross section of Inverse Compton scattering is described in the Klein-Nishina formula as

$$\sigma_{\rm KN} = \sigma_{\rm T}\frac{1}{x}\left\{\left[1-\frac{2(x+1)}{x^2}\right]\ln(2x+1)+\frac{1}{2}+\frac{4}{x}-\frac{1}{2(2x+1)^2}\right\}, \tag{2.36}$$

with $x = h\nu/m_ec^2$ (see e.g.: Jones (1968) and Blumenthal and Gould (1970) for more details). In the Thomson regime ($\gamma_e\varepsilon \ll m_ec^2$), the cross-section reduces to $\sigma_{\rm KN} \approx \sigma_{\rm T}$. While in the Klein-Nishina regime, the cross-section becomes

$$\sigma_{\rm KN} = \frac{3}{8}\sigma_{\rm T}\frac{1}{x}\left(\ln 2x + \frac{1}{2}\right), \tag{2.37}$$

implying that the cross-section decreases roughly as x^{-1} at high energy. The typical photon energy up-scattered by high-energy electron is given by

$$\varepsilon_{\rm IC} = 5\left(\frac{\varepsilon}{10^{-3}\ {\rm eV}}\right)\left(\frac{E_e}{1\ {\rm TeV}}\right)^2\ {\rm GeV}. \tag{2.38}$$

The spectrum of the inverse Compton scattering by electrons with power-law spectrum ($dN_e/dE_e \propto E_e^{-s}$) has also a power-law type spectrum with the index of $(s+1)/2$ in the Thomson regime, as well as the synchrotron spectrum. In the Klein-Nishina regime, the spectrum of the Inverse Compton scattering becomes steeper with the index of $s+1$.

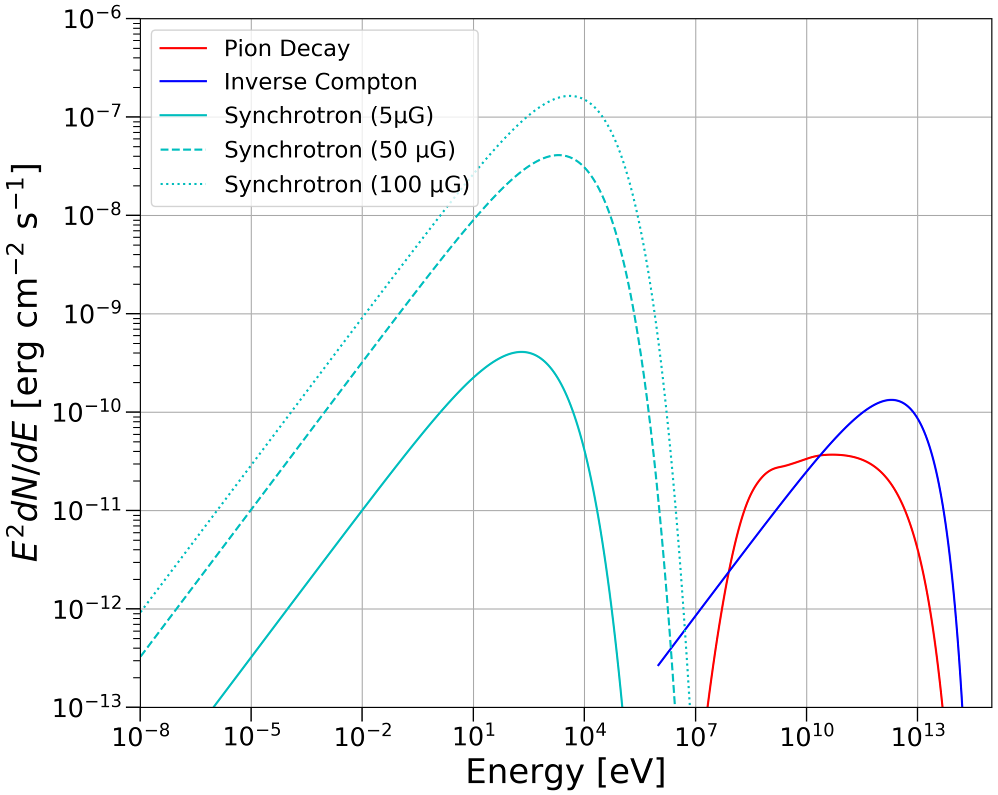

Figure 2.14. Example of energy spectra of non-thermal radiations assuming electrons and protons have spectrum of a power-law with a cutoff model in which spectral index and cutoff energy are 2 and 30 TeV, respectively. Cosmic microwave background (CMB) is assumed to be the seed photon of the inverse Compton scattering. A number density of 1 cm^{-3} is assumed as the density of target matter of the pion decay and Bremsstrahlung.

From Equation 2.34, the cooling timescale in which an electron loses the substantial fraction of the energy is given by

$$\tau_{\mathrm{IC}} \equiv \frac{E_e}{dE_e/dt} \approx 3 \times 10^8 \left(\frac{U_{ph}}{1\ \mathrm{eV\ cm^{-3}}}\right)^{-1} \left(\frac{E_e}{1\ \mathrm{GeV}}\right)^{-1} \mathrm{years}, \tag{2.39}$$

which means the higher the energy of an electron, the faster the cooling time.

2.4.3 Neutral pion (π^0) decay

Neutral pion decay, which is also one of the effective processes emitting gamma rays, arises from the interactions between high-energy nucleon and the ISM (pp interaction). In contrast to the aforementioned radiative processes, this radiative process originates and provides information from the hadronic component of cosmic rays, which are the main component of cosmic rays. When the relativistic protons (and also nuclei) inelastically collide with the ISM, the neutral pion (π^0) is produced and immediately decays into two gamma rays in a short time (the mean lifetime of π^0 is $\sim 8.4 \times 10^{-17}$ s). The gamma-ray energy of this process is approximately 67.5 MeV in the rest frame of π^0 because the rest mass of π^0 is $\sim$ 135 MeV.

The fraction of the energy of proton converted to gamma rays is approximately 17%. The steep rise of the spectrum of π^0 decay in the E^2dN/dE representation (like Figure 2.14) around 300 MeV is caused by the threshold of π^0 production and often referred to as the "pion bump". This characteristic spectral feature is used to investigate the presence of the hadronic cosmic rays in gamma-ray observation.

The cross-section of the pp interaction is approximated by

$$\sigma_{\text{pp}}(E_p) \approx 30 \left[0.95 + 0.06 \ln \left(\frac{E_p - m_p c^2}{1\ \text{GeV}}\right)\right] \text{mb}, \tag{2.40}$$

where E_p is the energy of the proton. The π^0 and produced gamma-ray emissivities are respectively described as

$$\begin{aligned} P_{\pi^0,\text{pp}}(E_{\pi^0}) &= 4\pi n \int_{E_{p,\text{th}}}^{\infty} \sigma_{\text{pp}}(E_p) N_p dE_p, & (2.41) \\ P_{\pi^0,\gamma}(E_\gamma) &= 2 \int_{E_{\text{min}}}^{\infty} \frac{P_{\pi^0,pp}(E_{\pi^0})}{\sqrt{E_{\pi^0}^2 - m_{\pi^0}^2 c^4}} dE_{\pi^0}. & (2.42) \end{aligned}$$

Here $E_{p,\text{th}}$ is the threshold energy to produce π^0 given by $2m_{\pi^0}c^2(1 + m_{\pi^0}/4m_p) \approx$ 280 MeV. n and N_p denote the number density of target matter and energy distribution of proton, respectively. E_{min} is represented by $\varepsilon + m_{\pi^0}^2 c^4/4\varepsilon$ with the energy of gamma ray produced by π^0 decay.

The gamma-ray spectrum emitted by high-energy protons with a power-law type spectrum ($dN_p/dE \propto E_p^{-s}$) has a power-law type spectrum with an index of s above $\sim$ 1 GeV, though various convolutions are involved to calculate the gamma-ray spectrum. The cooling timescale of a proton by π^0 decay radiation is given by

$$\tau_{\text{pp}} \sim 5.3 \times 10^7 \left(\frac{n}{1\ \text{cm}^{-3}}\right)^{-1} \text{years}, \tag{2.43}$$

assuming the cross-section of 40 mb at a high-energy proton. The timescale means the protons lose their energies faster as the denser target matter.

2.5 Vela Supernova Remnant (Vela SNR)

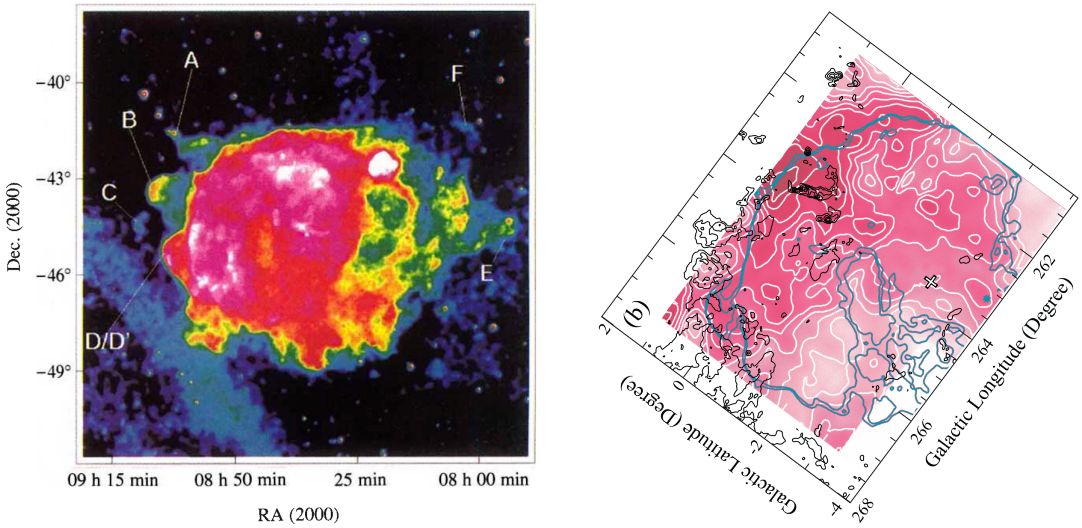

Figure 2.15. Left: X-ray ($0.1 - 2.4$ keV) image of Vela SNR observed by *ROSAT* (Aschenbach, Egger, and Trümper, 1995). Right: Distribution of the ISM in the Vela SNR region in Galactic coordinate (Moriguchi et al., 2001). Color and white contour represent the HI intensity integrated between $2.5 - 5.0$ km s^{-1}. Black contour shows the ^{12}CO intensity integrated between $1 - 4.0$ km s^{-1}. X-ray brightness distribution is represented by cyan contour.

The Vela supernova remnant (Vela SNR) is one of the closest SNRs to the Earth. The distance of 287^{+19}_{-17} pc was derived from the VLBI parallax measurement of Vela pulsar (Dodson et al., 2003), which was created by the same supernova explosion of Vela SNR. The age of the SNR was estimated as $\sim$ 11 kyr from the characteristic age of Vela pulsar. Due to its proximity, the Vela SNR has a large apparent diameter of $\sim 8^\circ$ (Aschenbach, Egger, and Trümper, 1995) shown in the left panel of Figure 2.15, making it an appropriate target for analyzing the detailed internal structure of a middle-aged SNR. Because of its large apparent size, the patch of the sky occupied by the Vela SNR contains other sources such as the SNRs Puppis A and Vela Junior (Vela Jr.). Furthermore, the emission generated in the Vela pulsar wind nebula (PWN) contaminates the emission from the Vela SNR itself. Interaction with molecular clouds and HI gas have been reported in the northeast region of the SNR (Moriguchi et al., 2001; Dubner et al., 1998) as shown in the right panel of Figure 2.15.

The Vela SNR area has a complex structure in the radio continuum. Three regions with enhanced brightness temperature are defined as the Vela X, Vela Y, and Vela Z. Vela Y and Vela Z are blended and considered to be the synchrotron emission accelerated electrons by the Vela SNR, while Vela X, which is the brightest among them, is a PWN powered by Vela pulsar.

In the X-ray sky, the Vela SNR is one of the brightest sources. The *ROSAT* observations shows that the thermal X-ray emission dominates the entire SNR, and the northeast region is brighter than the southwest region (Aschenbach, Egger, and Trümper, 1995; Lu and Aschenbach, 2000). The left panel of Figure 2.15 represents the X-ray image of the SNR observed by *ROSAT*. The asymmetry of the brightness distribution is considered to be caused by the density gradient of the ISM (Sushch, Hnatyk, and Neronov, 2011). The northeast region has a larger density than the southwest region because of the wind bubble created by the Wolf-Rayet star in the γ^2Velorum system. The morphology of Vela X, which extends in the southwest direction of Vela pulsar, is also considered to be the consequence of this asymmetric density distribution (Slane et al., 2018). Aschenbach, Egger, and Trümper (1995) detected six fragmented X-ray source outside the Vela SNR, as shown in the left panel of Figure 2.15 by A$-$F. They are considered to be ejecta of the SNR and referred to be "shrapnel" or "bullet". An overabundance of Si, which is produced in the deep layers of stars, compared with solar abundance is found in the shrapnel A Miyata et al. (2001) and Katsuda and Tsunemi (2006). At the shrapnel D, Katsuda and Tsunemi (2005) also found overabundances of O, Ne, and Mg than the solar abundance. A similar pattern of overabundance in O, Ne, and Mg is confirmed in the shrapnel B (Yamaguchi and Katsuda, 2009). These overabundances supports the ejecta origin shrapnels. Vela pulsar and its PWN Vela X, as well as SNRs Puppis A and Vela Jr., are the X-ray and gamma-ray sources located in the Vela SNR region in the line of sight, as shown in Figure 2.16. The age of $1700 - 4300$ years and 4450 ± 750 years, while the distance of ~ 750 pc and ~ 2.2 kpc are estimated for Vela Jr. and Puppis A, respectively (Katsuda, Tsunemi, and Mori, 2008; Becker et al., 2012; Reynoso et al., 2003). The X-ray emission from the Vela Jr. is dominated by synchrotron X-ray emission (Slane et al., 2001) like RX J1713.7$-$3946. In contrast, the X-ray emission from the Puppis A is thermal origin, i.e., shock-heated ISM (Hwang, Flanagan, and Petre, 2005) and the SN ejecta (Hwang, Petre, and Flanagan, 2008; Katsuda et al., 2008; Katsuda et al., 2010). These SNRs exist beyond the Vela SNR in the line of sight.

In the gamma-ray sky, several sources are detected in the Vela SNR region. Vela pulsar is the brightest steady GeV gamma-ray source, with a spectral cutoff of several GeV (Abdo et al., 2009a; Abdo et al., 2010d). In addition, Vela X and Vela Jr were detected from the GeV gamma-ray band (Vela X: Abdo et al. (2010a), Grondin et al. (2013), and Tibaldo et al. (2018); Vela Jr: Tanaka et al. (2011)) to TeV gamma-ray band (Vela X: Aharonian et al. (2006b) and Abramowski et al. (2012); Vela Jr.: Aharonian et al. (2005), Aharonian et al. (2007a), and H.E.S.S. Collaboration et al. (2018a)) in the line of sight. Puppis A has been detected in the GeV gamma-ray band (Hewitt et al., 2012; Xin et al., 2017), but no yet in the TeV gamma-ray band (H. E. S. S. Collaboration et al., 2015). Figure 2.16 shows the GeV and TeV gamma-ray images and broad band spectra of these gamma-ray sources. The radiation mechanism of Vela X is considered to be inverse Compton scattering of electrons and positrons. For Puppis A, π^0-decay gamma-ray process is favored to reproduce the broad-band spectrum (Xin et al., 2017), and it was supported by the interaction with ISM (Dubner and Arnal, 1988; Reynoso et al., 1995; Dubner et al., 2013). In contrast, the gamma-ray

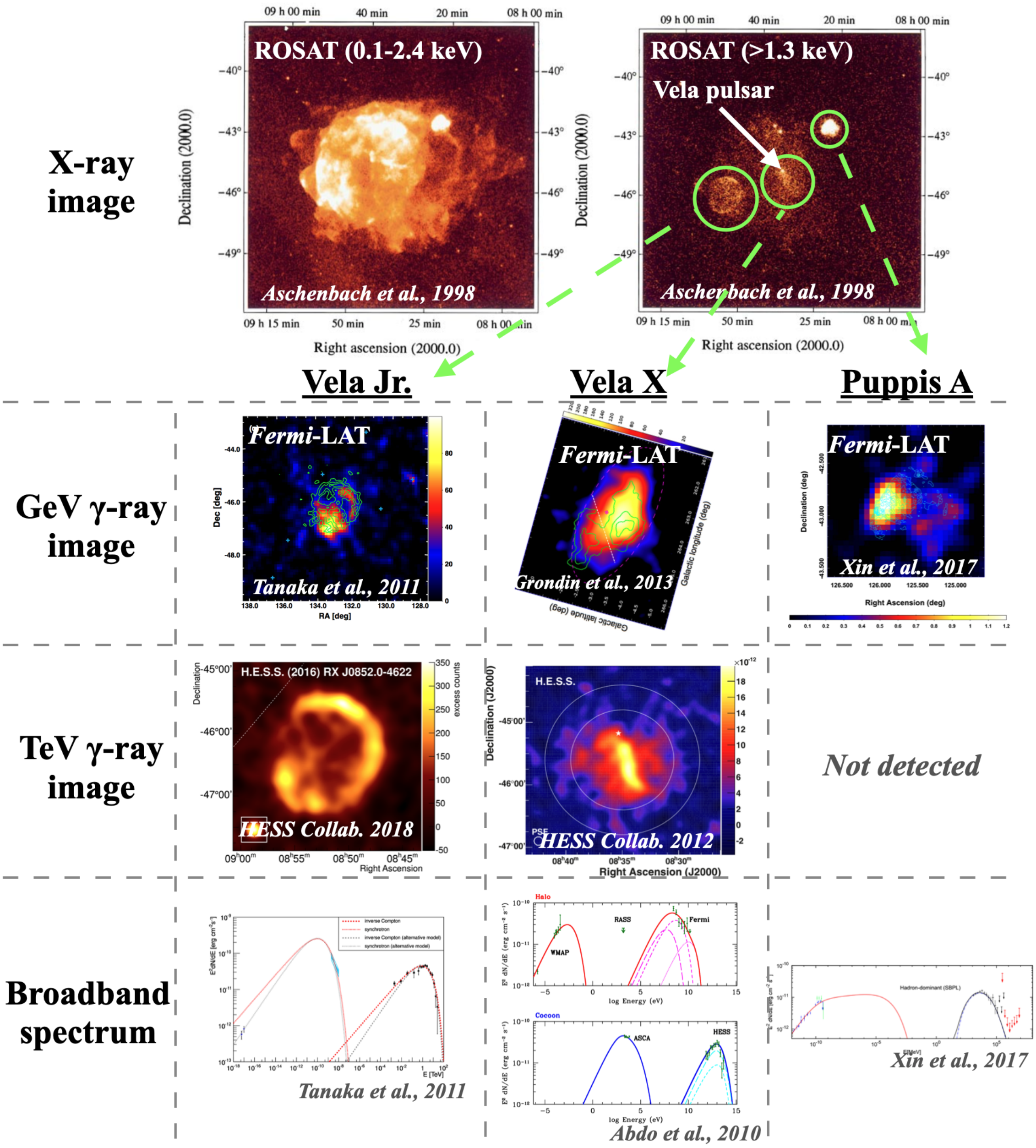

Figure 2.16. Summary of famous sources in the Vela SNR region. From top, X-ray, GeV gamma-ray, TeV gamma-ray images of Vela Jr (left), Vela X (center), Puppis A(right) are shown. At bottom, broad-band spectrum of each source are represented. (The X-ray image is taken from Aschenbach (1998). The gamma-ray images of Vela Jr, Vela X, and Puppis A are taken from Tanaka et al. (2011), Grondin et al. (2013), and Xin et al. (2017), respectively. The TeV gamma-ray images of Vela Jr. and Vela X are taken from H.E.S.S. Collaboration et al. (2018a) and Abdo et al. (2010a), respectively. The broad-band spectrum of Vela Jr., Vela X, and Puppis A are taken from Tanaka et al. (2011), Abdo et al. (2010a), and Xin et al. (2017), respectively.)

mechanism of Vela Jr. is under debate because the modeling of broad-band spectrum shows the both Inverse Compton scattering and π^0-decay radiation can explain the spectrum (H.E.S.S. Collaboration et al., 2018a).

Gamma-ray emission from the Vela SNR has not been reported, in spite of many observational analyses of the gamma-ray sources (Vela pulsar, Vela X, Vela Jr., and Puppis A) in the Vela SNR region. These extended gamma-ray source makes the detection of the Vela SNR difficult in addition to the effect of very bright Vela pulsar. In contrast, the *Fermi*-LAT has detected the GeV gamma-ray emissions from many "middle-aged" SNRs, e.g., IC443 (Abdo et al., 2010c; Ackermann et al., 2013), W44 (Abdo et al., 2010b; Ackermann et al., 2013), W51C(Abdo et al., 2009b; Jogler and Funk, 2016), and Cygnus Loop (Katagiri et al., 2011). These middle-aged SNRs typically have a steep spectrum with a break at a few to a few tens of GeV. Cygnus Loop, for example, is one of the closest SNRs like the Vela SNR. Its distance and age is estimated to be 540^{+100}_{-80} (Blair, Sankrit, and Raymond, 2005) and $\sim 2 \times 10^4$ years (Miyata et al., 1994), respectively. In Katagiri et al. (2011) and Tutone et al. (2021), the spatially resolved analyses (with surprisingly four regions[5]) were performed taking advantage of its near distance. Considering the closer distance of the Vela SNR than Cygnus Loop, more detailed spatially resolved analysis can be conducted to analyze the spectral distribution inside the SNR.

Due to the close distance of the Vela SNR, electrons and positrons may reach the Earth without significant energy attenuation. Such a nearby source may explain the softening of the spectrum of electrons and positrons at $\sim$ 0.9 TeV(Aharonian et al., 2009; DAMPE Collaboration et al., 2017) and the excess of the cosmic-ray positrons(Adriani et al., 2009; Aguilar et al., 2013; Aguilar et al., 2019b) (see also section 2.1.3 and 2.1.4). Owing to the favored distance and age of the source, the Vela SNR is listed as one of the possible candidate sources (Aharonian, Atoyan, and Voelk, 1995; Kobayashi et al., 2004; Ding et al., 2021).

---

[5] Spatially resolved analysis with *Fermi*-LATis difficult because of its large PSF (see Section 3.1). Only nearby diffuse objects allow us to perform spatially resolved analysis.

2.6 SNR RX J1713.7−3946

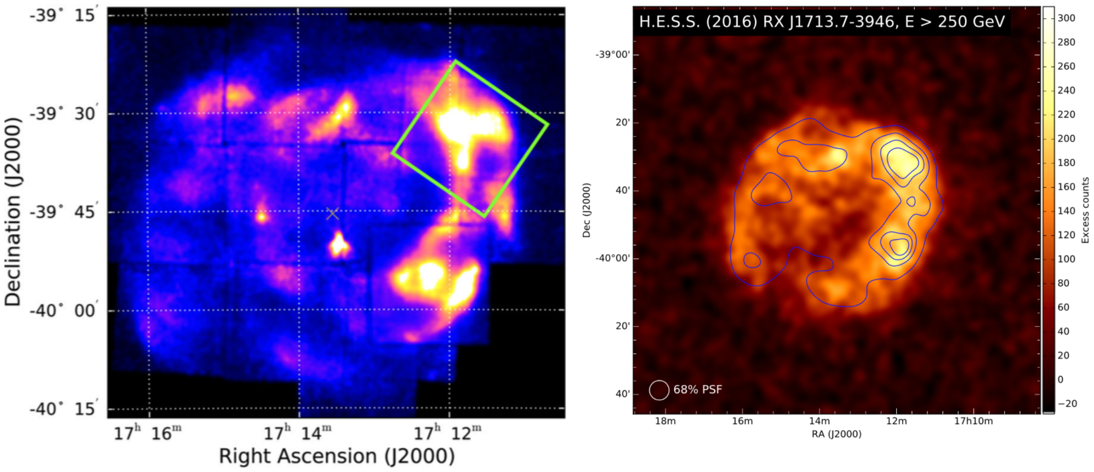

Figure 2.17. Left: X-ray (0.5−10 keV) image of RX J1713.7−3946 observed by the *Suzaku* XIS (Tsuji and Uchiyama, 2016). Right: TeV gamma-ray images (above 250 GeV) of the SNR observed by H.E.S.S. (H.E.S.S. Collaboration et al., 2018b).

The shell-type SNR RX J1713.7−3946 (also known as G347.3−0.5) was first discovered by the *ROSAT* All-Sky Survey (Pfeffermann and Aschenbach, 1996). The distance was estimated to be ∼ 1 kpc by tracing the CO lines from the associated molecular clouds (Fukui et al., 2003). Its association with one of the historical SNRs, namely SN 393, has been discussed (Wang, Qu, and Chen, 1997; Fesen et al., 2012). The SN 393 was discovered in the direction of the tail of Scorpio, where RX J1713.7−3946 resides in the direction. Recent measurements of the forward shock velocity suggested the SN-SNR association, supporting the SNR age of ∼ 1600 yr (Tsuji and Uchiyama, 2016; Acero et al., 2017a). RX J1713.7−3946 is one of the best-studied objects for investigating particle acceleration because of its strong non-thermal X-ray and gamma-ray emissions. Figure 2.17 shows the X-ray and TeV gamma-ray image of RX J1713.7−3946 observed by *Suzaku* and H.E.S.S. respectively. The contour overlaid in the TeV gamma-ray image shows the X-ray flux distribution. The morphology of RX J1713.7−3946 in X-ray image is similar to that in TeV gamma-ray image.

The X-ray emission of RX J1713.7−3946 is dominated by non-thermal radiation, i.e., synchrotron radiation that is emitted by very high-energy electrons accelerated in the SNR shock via DSA (e.g.: Koyama et al., 1997; Slane et al., 1999; Uchiyama, Aharonian, and Takahashi, 2003; Cassam-Chenaï et al., 2004; Hiraga et al., 2005; Takahashi et al., 2008; Tanaka et al., 2008). The acceleration efficiency was found to be the maximum rate (Bohm limit: Bohm factor $\eta \sim 1$) based on the X-ray Observations (Uchiyama et al., 2007; Tanaka et al., 2008; Tsuji and Uchiyama, 2016). Katsuda et al. (2015) detected thermal X-ray components in the inner region. They inferred that the thermal line emission originates from the ejecta heated by the reverse shock, and the mass of the progenitor is estimated to be $\lesssim 20\ M_\odot$ by the composition of its ejecta. In the shell region, complex filamentary structures have been revealed by *Chandra* with its superb angular resolution (Uchiyama, Aharonian, and Takahashi, 2003; Lazendic et al., 2004). Okuno et al. (2018) recently presented the spatially resolved spectroscopy of the SNR with *Chandra*. They showed that the filamentary structures in the southeast regions have harder spectra ($\Gamma \sim 2.0$) than the surrounding regions, whereas those in the southwest have relatively soft spectra ($\Gamma \sim 2.7$) because of the deceleration of shock waves which are interacting with the clumpy interstellar medium (ISM) produced by the stellar wind of the massive progenitor star. Recently, NuSTAR observations of the northwest rim obtained a spatially resolved X-ray image in the $10 - 20$ keV energy band (Tsuji et al., 2019, including R. Higurashi). The X-ray morphology is roughly in agreement with the soft-band images of previous works.

RX J1713.7−3946 is known as a strong GeV−TeV gamma-ray emitter (Aharonian et al., 2006a; Aharonian et al., 2007b), but the radiation mechanism has been a matter of debate(e.g.: Uchiyama, Aharonian, and Takahashi, 2003; Aharonian et al., 2006a; Tanaka et al., 2008; Ellison et al., 2010; Zirakashvili and Aharonian, 2010; Abdo et al., 2011; Fukui et al., 2012; Inoue et al., 2012; Sano et al., 2013; Gabici and Aharonian, 2014; H.E.S.S. Collaboration et al., 2018b; Celli et al., 2019). The spatial coincidence between the non-thermal X rays and the TeV gamma rays may imply that the parent particles responsible for these two emissions are identical, i.e., electrons. The leptonic radiation also seems to be favored with the *Fermi*-LAT (Abdo et al., 2011). The observed photon index ($\Gamma = 1.5 \pm 0.1$) in the bandpass of *Fermi*-LAT is reconciled with the IC gamma rays radiated from the electron population with a spectral index of 2, which is expected from standard acceleration via DSA. Note that simple modeling with a unique population of electrons fails to reproduce the multiwavelength spectrum (H.E.S.S. Collaboration et al., 2018b). It has recently been shown that the observed GeV−TeV gamma-ray spectrum can be reproduced by the hadronic scenario as well (Inoue et al., 2012; Gabici and Aharonian, 2014; Celli et al., 2019). Because RX J1713.7−3946 is located in a complex region in the Galactic Plane, target materials exist to produce π^0-decay gamma-rays through the proton-proton interactions. Although deeper H.E.S.S. observations with a total live time of 164 hr have been conducted, the mechanism of the gamma-ray radiation remains ambiguous (H.E.S.S. Collaboration et al., 2018b). There are several ways to distinguish the gamma-ray origin, such as by the detection of synchrotron emission from a secondary electron produced by the decay of a charged pion in the proton-proton interaction (Huang et al., 2020) or by accurate observation around 100 TeV with the Cherenkov Telescope Array (CTA) because the Klein-Nishina effect would suppress the leptonic emission component (Acero et al., 2017b). The confirmation of the hadronic component would also come from observations of neutrinos, with large volume instruments such as KM3NeT (Ambrogi, Celli, and Aharonian, 2018).

RX J1713.7−3946 is located in the complex environment of ambient molecular clouds (Fukui et al., 2003; Fukui et al., 2012). The progenitor star is expected to have

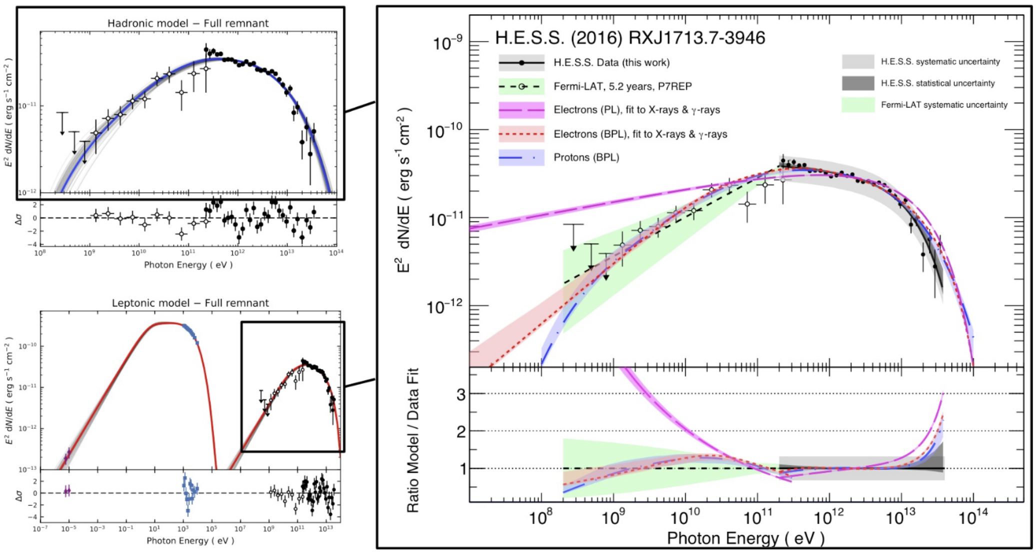

Figure 2.18. Spectral energy distribution of RX J1713.7−3946 (H.E.S.S. Collaboration et al., 2018b). Top left panel shows the reproduced hadronic gamma-ray emission. In contrast, bottom left panel shows the reproduced leptonic gamma-ray emission and also radio to X-ray emission.

exploded in a cavity wall produced by the stellar wind from the massive progenitor star. In this case, dense materials, such as molecular clumps and molecular cores, could have survived against the wind. Here we refer to a "clump" as a denser part inside a molecular cloud with a number density of $10^3 - 10^4$ cm^{-3} and a typical size of 0.1 pc, and a "core" as a much denser part inside the clump with a number density of $10^5 - 10^7$ cm^{-3} and a typical size of 0.01 pc. The medium with a lower density is thought to be swept up before the supernova explosion. This results in complex surroundings which have some molecular clumps and cores inside the wind-blown cavity, as mentioned in Slane et al. (1999), Inoue et al. (2012), and Katsuda et al. (2015). The left panel of Figure 2.19 shows a schematic image of the circumstellar environment before the supernova explosion. After the supernova explosion, the shock wave expands into the wind-blown cavity and interacts with the survived clumpy medium (molecular clumps and cores).

Shock-cloud interactions in such complex circumstances have been studied with magnetohydrodynamical (MHD) simulations. Inoue et al. (2012) showed that the magnetic field is amplified up to 1 mG in a small region ($\sim$ 0.05 pc), resulting from the SNR shock propagating within the clumpy environment. Recently, Celli et al. (2019) showed that magnetic field amplification occurs at a thin region with a size of $\sim$ 0.05 pc at the surface of the molecular clump.

Observations have been in agreement with the picture of shock-cloud interaction in RX J1713.7−3946 (Fukui et al., 2003; Fukui et al., 2012; Moriguchi et al., 2005; Sano et al., 2010; Sano et al., 2013). Using observations with *Suzaku*, Sano et al. (2015) reported a parsec-scale correlation between the intensities of the nonthermal X-ray

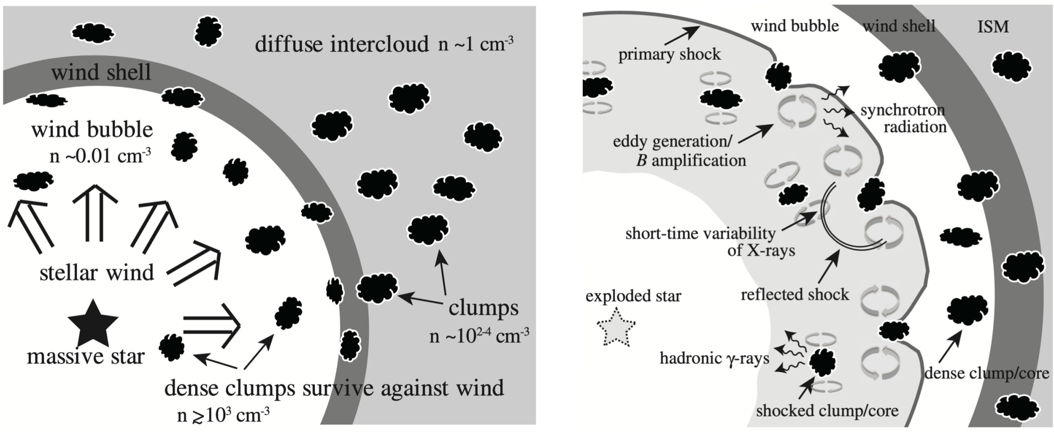

Figure 2.19. Left: Schematic image of the wind-brown circumstellar medium before supernova expansion. Dense part of molecular cloud are survived against the stellar wind, and clumpy circumstellar medium is distributed around the progenitor star. Right: Schematic image of shock-cloud interaction around RX J1713.7−3946. Clumpy ISM interacts with shock and results in e.g., amplification of magnetic field and reflected shock (Inoue et al., 2012).

emission and the molecular clumps. They also found an anticorrelation between the X-ray radiation and the molecular clumps on a subparsec scale. This suggested that the synchrotron X-ray intensity is indeed strong in the surroundings of the clumps where the magnetic field is expected to be enhanced. Okuno et al. (2018) showed a similar anticorrelation between molecular clumps and the photon indices of the X-ray spectra with *Chandra*. The presence of a magnetic field with $B \sim 1$ mG was reported in small knot-like regions in the northwest shell of RX J1713.7−3946, inferred from the detection of year-scale variability caused by a balance between the synchrotron emission and the acceleration (Uchiyama et al., 2007).

2.7 W50/SS433 System

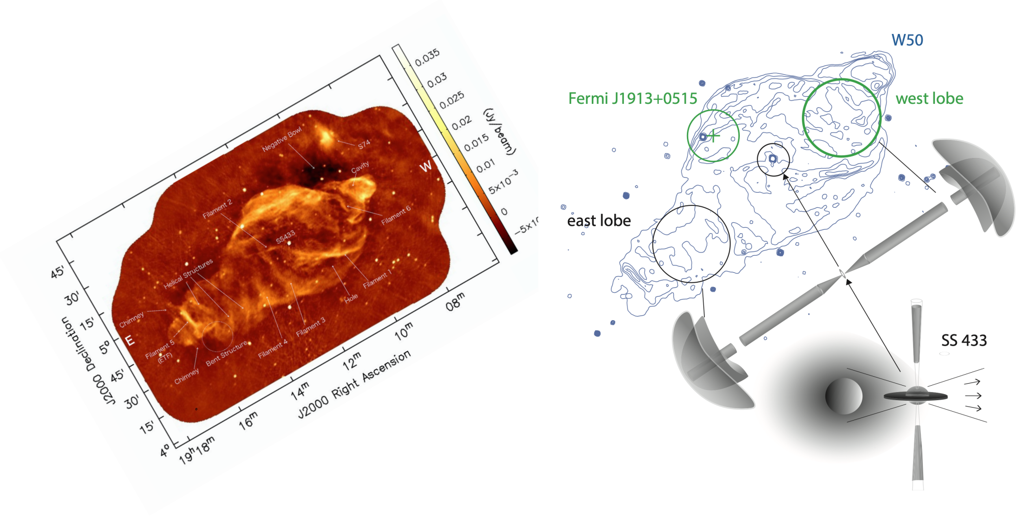

Figure 2.20. Left: Radio image (1.4 GHz) of microquasar SS 433/W50 system (Sakemi et al., 2021). Right: schematic image of SS 433/W50 system (Bordas, 2020).

The microquasar SS 433 is located at a distance of ~ 5.5 kpc, and roughly on the Galactic plane $(l = 39.7°, b = -2.2°)$ surrounded by radio nebula W50 (most likely SNR) as shown in the left panel of Figure 2.20. Here, l and b denote the Galactic longitude and latitude, respectively. SS 433 is an X-ray binary that consists of a compact object (probably a black hole) with a mass of $10 - 20$ $M_\odot$ and a supergiant star with a mass of 20 $M_\odot$. The accretion gas is fed onto the compact object from the supergiant star at a rate of 10^{-4} $M_\odot$ year^{-1}. This very high transferring rate is one of the characteristics of SS 433 among other X-ray binaries. Another characteristic property of SS 433 is a baryonic jet with a speed of $0.26c$, where c represents the speed of light. The kinetic energy of the jet is enormous ($(0.2 - 5) \times 10^{39}$ erg s^{-1}), but only a small fraction of $\sim 0.01\%$ is emitted in X-ray radiation.

The radio nebula W50 (a.k.a., "Manatee nebula") is considered to be created via core-collapse supernova explosion. As shown in Figure 2.20, the morphology of W50 is elongated to the east and west directions along the jet direction of SS 433. It implies that the circular shape of the SNR has been changed by the ram pressure from the jet. The extended X-ray emission has been observed with many X-ray satellites, such as *Einstein, ASCA, and ROSAT*. The distribution in the X-ray band is represented in the left panel of Figure 2.21 by solid black contours. The bright X-ray regions are defined as e1, e2, and e3 in the east side, and w1 and w2 in the west side. The locations of the bright regions are shown in the left panel of Figure 2.21 by white crosses. Yamauchi, Kawai, and Aoki (1994) reported the non-thermal X-ray emission with *ASCA* observations of the eastern jet. The *XMM-Newton* observations support the non-thermal radiation at the eastern jet region.

Recent Observations with HAWC revealed the presence of TeV gamma rays with energies of at least 25 TeV far from the center (see left panel of Figure 2.21) where the

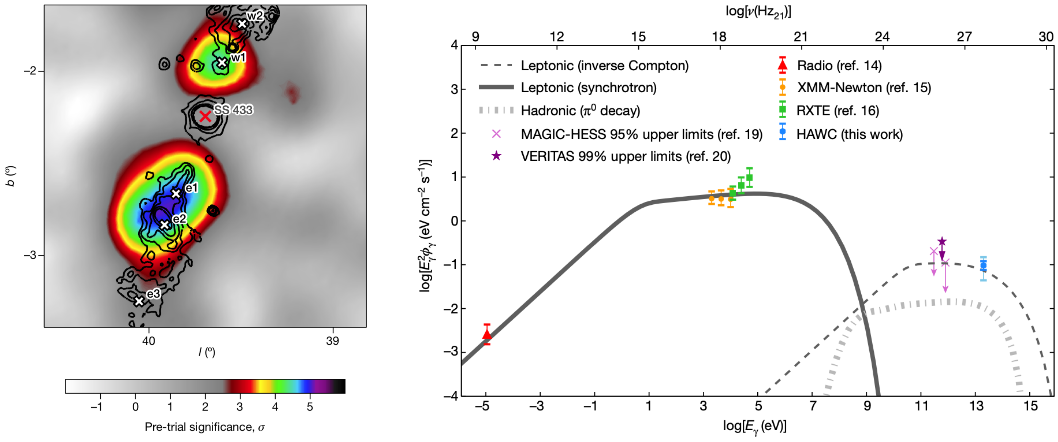

Figure 2.21. Left:TeV gamma-ray image of SS 433/W50 system. Color scale represents the statistical significance of TeV gamma-ray emission. White crosses represent the bright X-ray regions and red cross is the location of central binary. Black solid contour shows the X-ray emission of the system. Right: Broadband spectral energy distribution of eastern region e1 (Abeysekara et al., 2018).

jets are formed (Abeysekara et al., 2018). The spectral point given by the HAWC observation constrained the radiation mechanism of multi-wavelength emission from radio to gamma rays. As shown in the right panel of Figure 2.21, the broadband emission is consistent with synchrotron and inverse Compton radiations with a single population of electrons with energies of at least up to hundreds of TeV. The HAWC detection makes the particle acceleration in this system a very hot topic. After the detection of TeV gamma rays, GeV gamma-ray studies were actively performed and found the GeV gamma-ray emission from the system (Xing et al., 2019; Sun et al., 2019; Rasul et al., 2019; Li et al., 2020; Fang, Charles, and Blandford, 2020). The GeV gamma-ray observation is important to discuss the distribution of high-energy particles and radiation mechanism. However, the subsequent GeV gamma-ray studies are controversial: the results of morphology and spectral analysis are different from each other. For example, Xing et al. (2019) presented the GeV gamma-ray image in which the west side of the system is bright. In contrast, Sun et al. (2019) show the GeV gamma-ray image in which the entire system is bright and the size is comparable to that of W50. The spectral results in Sun et al. (2019), Rasul et al. (2019), and Xing et al. (2019) show a very steep spectrum and extended up to ~ 1 GeV (e.g., Xing et al. (2019) reported the photon index of ~ 6). While in Li et al. (2020), the spectrum has a photon index of ~ 2.3 (see Figure 2.22). In these analyses, the inconsistencies are caused by their setup, i.e., how to treat the gamma-ray sources Fermi J1913+0515 and west excess located in the W50/SS 433 system and also nearby pulsar PSR J1907+0602 (see Figure 2.22). It is necessary to analyze the GeV gamma-ray data of the system taking into account these uncertainties.

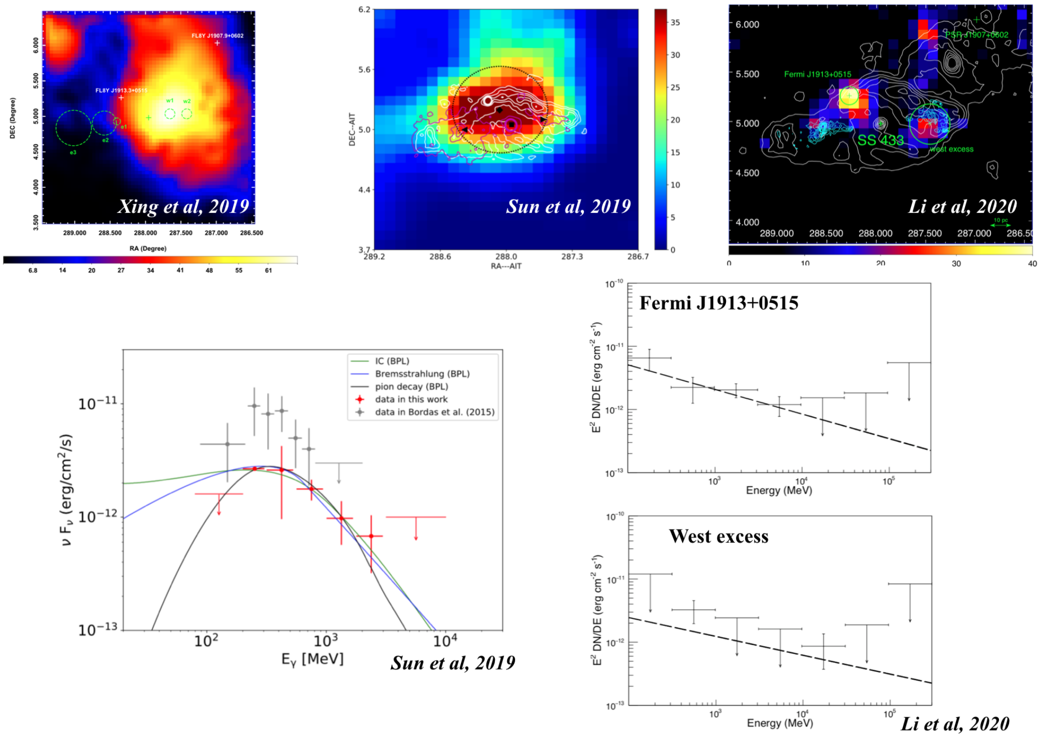

Figure 2.22. (Top row) Gamma-ray image of the region of W50/SS 433 system, taken by previous studies (left: Xing et al. (2019), middle: Sun et al. (2019), and right: Li et al. (2020). (Bottom row) GeV gamma-ray spectra of the system reported in Sun et al. (2019) (left) and Li et al. (2020) (right).

Chapter 3

Instruments

In this thesis, the analyses are based on observational data with *Fermi* and *Chandra* satellites. The *Fermi* observed the GeV gamma-ray sky and provide the image and spectroscopy of GeV gamma rays, and the *Chandra* provide the soft X-ray image and spectroscopy with energies less than ~ 10 keV The properties and performance of the *Fermi* and *Chandra* are briefly summarized in this chapter. In the section of *Fermi*, the basic analysis method is also addressed because the analysis of *Fermi* data is complicated. It will be helpful to understand the gamma-ray analysis with *Fermi* in the subsequent chapters.

3.1 *Fermi* Gamma-ray Space Telescope

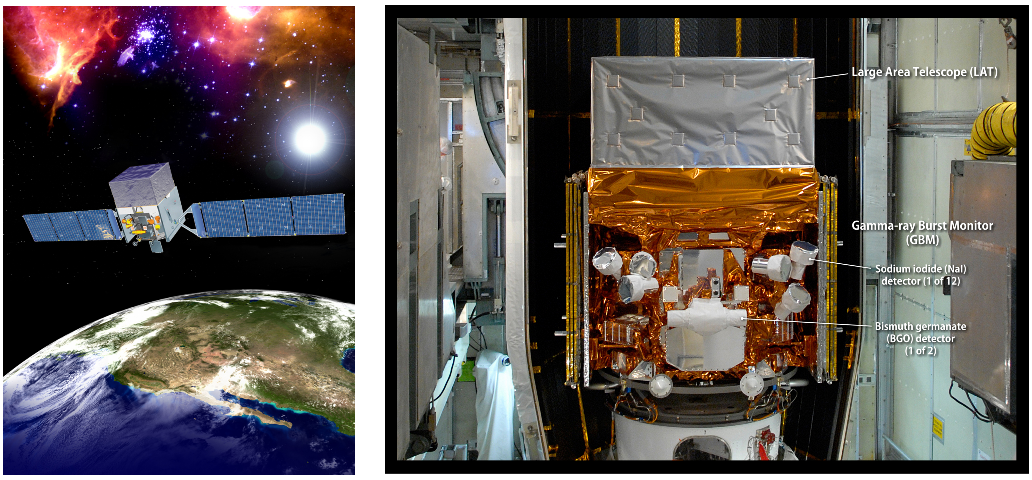

Figure 3.1. Left:Artificial image of *Fermi* surveying the gamma-ray sky orbiting around Earth. Right: Side view of *Fermi* with its detectors (GBM and LAT). (Taken from `https://www.nasa.gov/`)

Fermi Gamma-ray Telescope has been observing the gamma-ray sky since it was launched in 2008 with grateful contributions from many institutes in the United States, France, German, Japan, Italy, and Sweden. Two detectors, the Large Area Telescope (LAT) and Gamma-ray Burst Monitor (GBM), are on board *Fermi* to explore the high-energy phenomena in the universe (e.g., supernova remnant, active

Table 3.1: Comparison of the LAT performance with EGRET.

Quantity	LAT	EGRET
Energy Range	20 MeV − 1000 GeV	20 MeV − 30 GeV
Peak Effective Area	> 8000 cm^2	1500 cm^2
Field of View	> 2 sr	0.5 sr
Angular Resolution[1]	$< 3.5°$(100 MeV) 0.15° (> 10 GeV)	5.8° (100 MeV)
Energy Resolution[2]	<10%	10%
Deadtime per Event	$<$ 100 ¯s	100 ms
Source Location Determination[3]	$< 0.5'$	$15'$
Point Source Sensitivity[4]	$< 6 \times 10^{-9}$ cm^{-2}s^{-1}	$\sim 10^7$ cm^{-2}s^{-1}

[1] 68% contamination angle of a single photon entering on-axis.

[2] 1σ energy resolution entering on-axis.

[3] 1σ radius for a source with the flux of 10^{-7} cm^{-2}s^{-1} (>100 MeV) and located on high $|b|$

[4] >100 MeV, at high $|b|$, for the exposure of one year, photon index -2

galaxies, dark matter, gamma-ray burst, pulsar). The LAT, which is a primary detector of *Fermi*, detects gamma rays in the energy range of 20 MeV − 1 TeV with a wide field of view. The entire sky is surveyed in every 3 hours (2 orbits) owing to the wide field of view. The LAT has the best performance in GeV gamma-ray observation, and the comparison with the former GeV gamma-ray detector EGRET on board *Compton* is summarized in Table 3.1. The GRB is a complementary detector, and has sensitive to X rays and gamma rays in the energy of 8 keV − 30 MeV. It has a larger field of view than that of the LAT (see right panel of Figure 3.1 and the direction of attached detectors of GBM), and observes the entire direction of the sky without the direction of the Earth. When a gamma-ray burst is detected, it sends a signal to the LAT immediately for analyzing the area in detail.

Fermi has surveyed with energies of more than seven decades with the very large field of view. In the subsequent section, basic information of the LAT, whose data was analyzed in this thesis, is summarized. More detailed information is available in Atwood et al. (2009).

3.1.1 Large Area Telescope (LAT)

Detectors composing the LAT

The LAT is a pair-conversion telescope with trackers and calorimeters to determine the direction and energy of incident gamma rays, and also has anti-coincident detectors which provide a veto for incident cosmic rays. The schematic diagram of the LAT is represented in Figure 3.1. The LAT is designed to measure gamma rays in the energy range of 20 MeV to above 300 GeV with good precision. As shown in the left panel of Figure 3.2, the LAT is composed of 4×4 towers, and each tower consists of a tracker and calorimeter.

The incident gamma ray produces electron-positron pair in the tracker system and the direction of the gamma ray is reconstructed by detecting its trajectory with silicon strip detectors in the tracker. The tracker system has 16 planes of high-Z material (tungsten) to convert the incident gamma ray to electron-positron pair. The converter planes are interleaved with x-y pair silicon strip detectors. 2 planes of x-y pair silicon strip detectors without converter are arranged below the 16 layers. The passage of charged particles is recorded by reconstructing the (x,y) positions detected with silicon strip detectors. The first 12 converter layers have a thin tungsten foil to achieve a good point spread function (PSF) for low-energy gamma rays. The low-energy gamma ray suffers the multiple scattering, and the reconstructed trajectory has a large uncertainty. The last 4 converter layers have a thick tungsten foil to maximize the effective area for high-energy gamma rays. It is one of the most complex LAT design trades. Events are classified as Front (first 12 thin layers) or Back (last 4 thick layers) events depending on the converted layers.

The energy of the incident gamma ray is measured from the energy deposition of the electromagnetic showers, which results from electron-positron pairs, at the bottom of each tower. Each calorimeter equipped below a tracker system is composed of 96 CsI scintillation bars with 8 layers. 12 bars are used to make one layer, and each layer is aligned 90° with respect to above and below layers consisting of x-y arrays. The array enables us to reconstruct electromagnetic shower three dimensionally. The schematic image of the calorimeter is represented in the right panel of Figure 3.2.

The LAT has anti-coincident detectors (ACDs) which provide a veto for incident cosmic rays (charged particles). The ACDs cover the 4×4 towers, and remove the background event by detecting the charged particles using plastic scintillator tiles as shown in the left panel of Figure 3.2. A gamma-ray candidate event is rejected, when the event hits an ACD tile on the passage of incident direction.

Performance of the LAT

The LAT performance is basically determined by the hardware design of the LAT, algorithms of the event reconstruction, and algorithms of the event selection. The instrumental response function (IRF) is used in the analysis of LAT data to characterize the total LAT performance. IRF is improved gradually by the on-orbit observations since *Fermi* was launched. The effective area, energy resolution, and PSF of the latest IRF are shown in Figure 3.3. The effective area is maximized in the energy range of $1-1000$ GeV because of the requirement for the observation of GeV gamma rays. The energy resolution is minimized in the energy range of $1-1000$ GeV due to the same requirement. The energy loss in the tracker causes a large uncertainty of energy for low-energy gamma rays. The energy leakage from the calorimeter causes a large energy uncertainty for high-energy gamma rays as well. The PSF improves as the energy of incident gamma rays increases. Low-energy gamma rays suffer multiple scattering in trackers, resulting in the larger uncertainty of incident angle reconstructed by the trajectories.

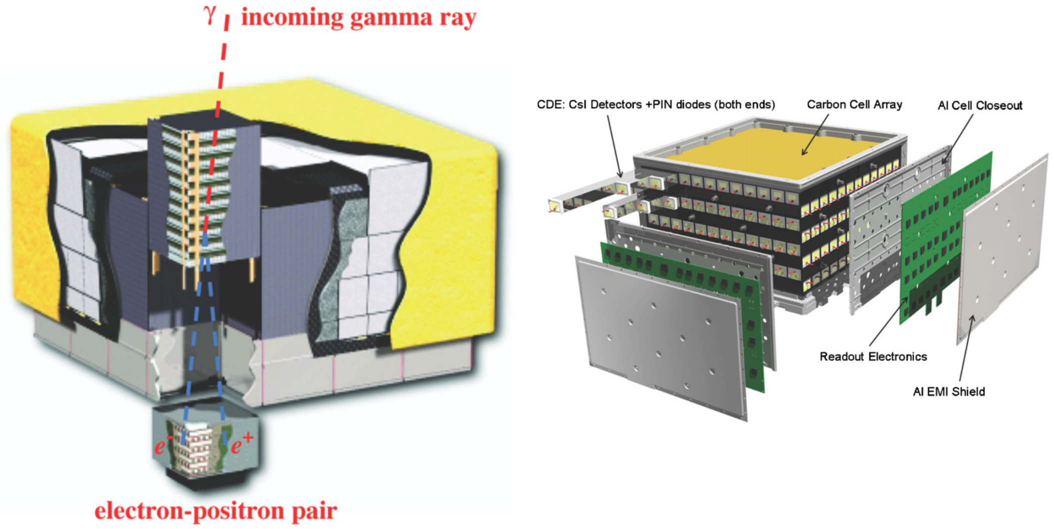

Figure 3.2. Left: Schematic diagram of the LAT (Atwood et al., 2009). 16 towers consisted with the tracker and calorimeter are arranged 4×4 array, and covered by tiles of the anti-coincident detector overlaid by yellow sheet. Right:Schematic diagram of the LAT calorimeter (Atwood et al., 2009).

3.1.2 Basic analysis method of LAT data

The analysis method of the LAT data is complicated; thus briefly addressed here. The gamma-ray all-sky image observed by the LAT is shown in the bottom panel of Figure 1.1. Because of interactions between the ISM and cosmic rays, the Galactic plane is very bright and become one of the dominant diffuse backgrounds for the analysis of each gamma-ray source. Interactions of cosmic rays with the ISM produce gamma rays through the π^0-decay process, which is predicted by Hayakawa (1952). Cosmic-ray electrons also radiate gamma rays by the interaction with the ISM and the low-energy interstellar radiation field (ISRF) through Bremsstrahlung and the inverse Compton scattering, respectively. Because of the large PSF and low-counting statistics for gamma-ray observation, the Galactic diffuse background is desired to be accurately modeled. The Galactic diffuse background is highly anisotropic; it becomes stronger as the absolute value of Galactic latitude ($|b|$) is smaller. In particular, it needs to be accurate at low Galactic latitude, otherwise, the detection of the sources located on the Galactic plane becomes challenging. The latest ISM observations of CO (tracer of H_2) (Dame, Hartmann, and Thaddeus, 2001), H_{I} (HI4PI Collaboration et al., 2016), and infrared dust map (Planck Collaboration et al., 2016) are used to trace the interstellar gas components. To trace the IC component, the numerical code `GALPROP`[1] is used for calculating the cosmic-ray propagation. The other large-scale structures, such as the *Fermi* bubble and Loop I, are modeled by the "patch" components based on the positive residual gamma-ray intensity.

---

[1] `https://galprop.stanford.edu`

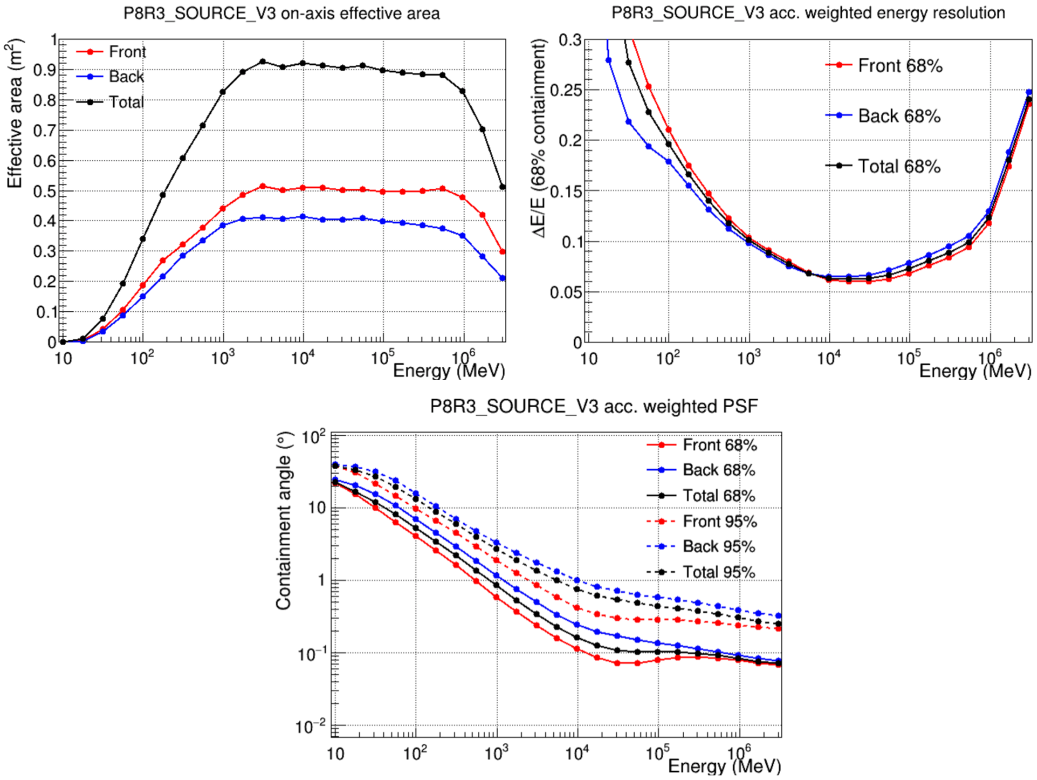

Figure 3.3. Top left: effective area of the LAT in the energy range of $10 - 3 \times 10^6$ MeV. Top right: energy resolution of the LAT in the same energy range. Bottom: point spread function of the LAT in the same energy range. (taken from `https://www.slac.stanford.edu/exp/glast/groups/canda/lat_Performance.htm`)

The isotropic diffuse emission is the diffuse background caused by emissions of unresolved extra-galactic sources. Its model also includes the residual charged particles background which was triggered and misclassified as gamma rays by the LAT. Since this residual component depends on the IRFs, a suitable model is prepared for each IRF.

In the all-sky image shown in the bottom panel of Figure 1.1, emissions from many gamma-ray sources are included along with the diffuse background emissions. The gamma-ray sources detected by the LAT are listed in the gamma-ray source catalog (e.g., the 4FGL catalog is summarized in Abdollahi et al., 2020; Ballet et al., 2020). More than 5000 sources have been detected, and they are concentrated on the Galactic plane as shown in Figure 3.4. Most of the Galactic sources are located on the Galactic plane, in contrast, many extra-galactic sources (e.g., AGNs) have been detected at high $|b|$.

Because of the large PSF of the LAT in a low-energy band (see the bottom image of Figure 3.3), the gamma rays from each source are distributed within several degrees. If some sources are located within the size of the PSF, the gamma-ray emissions are blended with each other. The emission from the position of a certain analyzing source is contaminated by other nearby sources. Thus, the analysis is needed

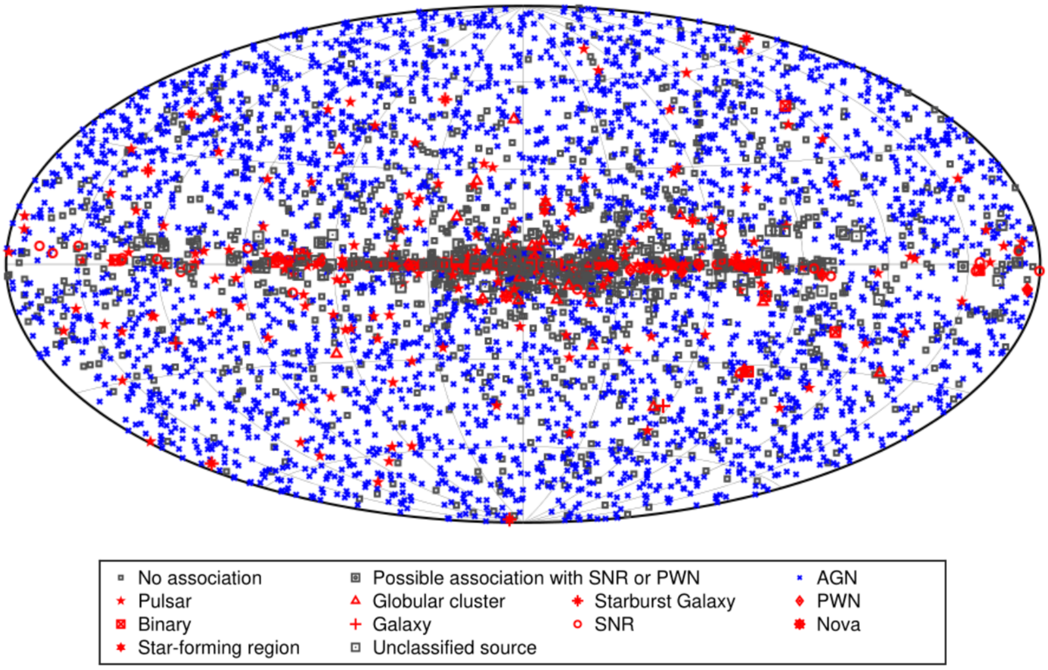

Figure 3.4. Positions and classifications of GeV gamma-ray sources listed in the GeV gamma-ray source catalog (Abdollahi et al., 2020).

to model the large region of interest (ROI), e.g.: 20° × 20°. In the ROI, the gamma-ray emissions could be classified into the emission from gamma-ray source and diffuse background (Galactic diffuse emission and isotropic diffuse emission). The Galactic and isotropic diffuse background models are provided by the *Fermi* science support center[2]. The model of each gamma-ray source is available from the gamma-ray source catalog. Using the diffuse background models and source models, the spectral parameters in the ROI are fitted to maximize the likelihood between models and observed data. The spectral parameters of an analyzed source are derived from the best-fit model. In this fitting procedure, the maximum-likelihood method is adopted (Mattox et al., 1996). The likelihood is given by

$$\mathcal{L} = \prod_i \frac{m_i^{n_i} e^{-m_i}}{n_i!}, \tag{3.1}$$

where m_i and n_i denote the predicted gamma-ray counts in the model and observed gamma-ray counts, respectively. In the likelihood, the probability distribution is described by the Poisson distribution. In practice, the fitting command `gtlike` in the analysis software for the LAT data is constructed to maximize the logarithm of likelihood ($\ln \mathcal{L}$).

A likelihood ratio test is employed to compare two opposing hypotheses and derives the significance (e.g., detection or non-detection of a source, and power-law

---

[2] https://fermi.gsfc.nasa.gov/ssc/data/access/lat/BackgroundModels.html

spectrum or power-law with a break spectrum). The test statistics (TS) is written as

$$TS = -2\left(\ln \mathcal{L}_0 - \ln \mathcal{L}_1\right), \tag{3.2}$$

where $\mathcal{L}_0$ and $\mathcal{L}_1$ denote the likelihood of the null hypothesis and the tested hypnosis, respectively. If the null hypothesis and tested hypothesis are nested and have a degree of freedom (d.o.f) of a and b, the TS asymptotically approaches a χ^2 distribution with a d.o.f. of $(b-a)$[3]. For example, a significance of a point source detection with a fixed position is given by $\sqrt{TS}$. In the analysis of LAT data, the TS value is commonly used to represent the significance.

For an analysis of an extended source, a spatial template is used to express the size and spatial distribution of the source. It is desirable to use a template that has the size and distribution of actual GeV gamma-ray emission. In many cases, the template is created by assuming a simple uniform distribution or other wavelength profile (e.g., radio, X-ray, and TeV gamma ray). Since the result could be affected by the assuming template, it is needed to carefully choose the template for the analysis. There are two types templates of spatial map template (2D: two sky coordinates) and map cube template (3D: two sky coordinates and one energy axis). A spatial map template assumes that a spatial profile holds in the entire analyzing energy range, and it is often used in the analysis of extended sources. In contrast, the map cube template has an axis of energy. It can express the spatial profile of the source in each energy band. Since it is difficult to investigate GeV gamma-ray spectra for each area inside the extended source because of the large PSF of the LAT, this type of template is used to express the large-scale gamma-ray emission, such as Galactic diffuse emission.

---

[3] This is called Wilks theorem.

3.2 *Chandra* X-ray Observatory

The *Chandra* X-ray observatory is one of NASA's Great Observatories (the others are the Hubble Space Telescope, Compton Gamma-Ray Observatory, and Spitzer Space Telescope.) It was launched and deployed by space shuttle Colombia in 1999, and is in an elliptical orbit with an orbital period of 63.5 hours. *Chandra* consists of an X-ray telescope and X-ray spectrometers. A schematic diagram of *Chandra* is represented in Figure 3.5. The X-ray telescope named High Resolution Mirror Assembly (HRMA) is needed to be exquisitely shaped and aligned nearly parallel to incident X rays. On the focal plane, the Science Instrument Module (SIM) is placed to detect X rays collected by HRMA. The SIM contains 4 detectors named Advanced CCD Imaging Spectrometer (ACIS), High Resolution Camera (HRC), Low Energy Transmission Grating (LEMG), and High Energy Transmission Grating (HETG).

3.2.1 High Resolution Mirror Assembly (HRMA)

The X-ray telescope of *Chandra*, HRMA, consists of a nested set of four paraboloid-hyperboloid (Wolter-I type) X-ray mirrors. The left panel of Figure 3.6 represents the schematic diagram of HRMA. The diameter and focal length of HRMA are 1.2 m and 10 m, respectively. HRMA is composed of the smoothest and cleanest mirrors ever made, and the aperture is twice larger than that of the former *Einstein* observatory. With the mirrors and large aperture, *Chandra* achieved an unprecedented angular resolution of $0.5''$. This angular resolution makes *Chandra* one of the most powerful X-ray observatories to date. It is possible to distinguish individual X-ray sources even in crowded regions, and to analyze the detailed structure of extended X-ray sources.

3.2.2 Advanced CCD Imaging Spectrometer (ACIS)

ACIS acquires the high-resolution image and moderate resolution spectrum at the same time. The higher resolution spectrum is also obtained using HETG and LETG. The ACIS is composed of 10 CCD chips, each of which has 1024×1024 pixels ($8.3' \times 8.3'$). The arrays of the CCD chips are shown in the right panel of Figure 3.6. In this figure, the 2×2 array is ACIS-I and the 1×6 array is ACIS-S. Besides obtaining the image, ACIS-S is also used for the readout of the grating spectrum. In ACIS-S, there are two back-illuminated chips in the ACIS-S array, while the others are front-illuminated chips. Up to 6 CCD chips are enabled to operate simultaneously.

The performance of ACIS with HRMA is shown in Figure 3.7. The effective area of the front-illuminated chip is larger than the back-illuminated chip in the energy above $\sim$ 5 keV and vice versa, as shown in the left panel of Figure 3.7. The PSF of *Chandra* is indicated by encircled power radius, as shown in the middle panel of Figure 3.7. The right panel of Figure 3.7 shows encircled energy radius of X rays with

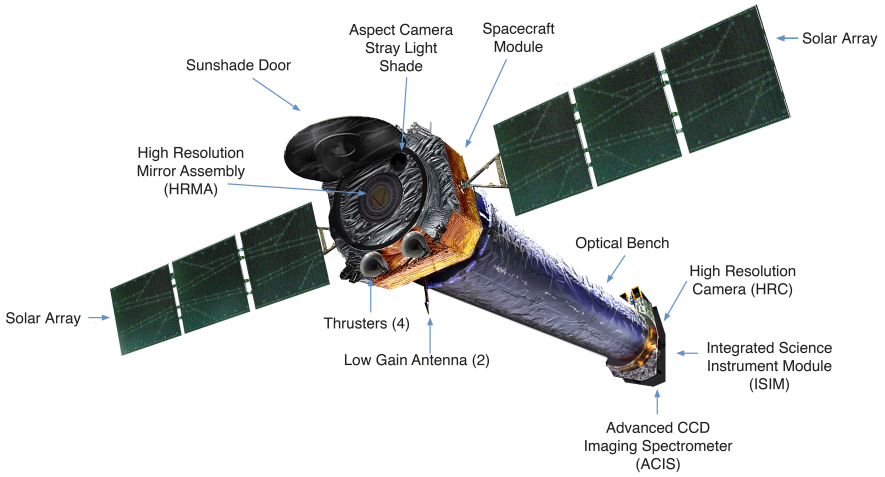

Figure 3.5. Schematic diagram of *Chandra* (taken from Chandra X-ray Center: CXC https://chandra.harvard.edu/).

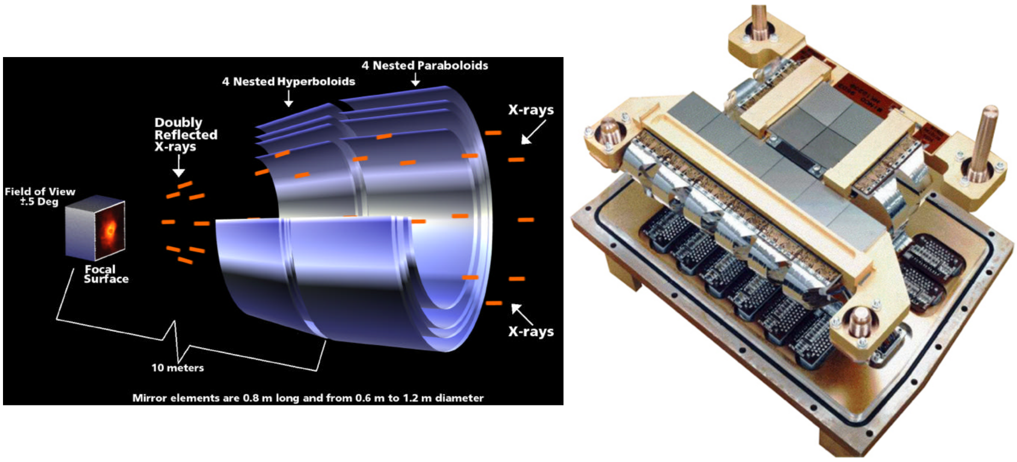

Figure 3.6. Left:Schematic picture of HRMA and incident X rays reflected to focal plane. Right: Real picture of ACIS-I (2 × 2 array) and ACIS-S (1 × 6 array). (taken from Chandra X-ray Center: CXC https://chandra.harvard.edu/).

low-energy (1.49 keV) and high-energy (6.40 keV). It implies that the PSF of *Chandra* becomes larger as the energy of incident X rays increases. The PSF also becomes larger as the distance from the on-axis position. The observed data with ACIS was analyzed in this thesis.

3.2.3 High Resolution Camera (HRC)

HRC comprises two microchannel plate (MCP) imaging detectors: the HRC-I and HRC-S. The HRC-I is designed for wide-field imaging (filed of view: FOV $\sim 30 \times 30$ arcmin^2), while HRC-S is also designed for a readout of LETG (FOV 6×99 arcmin^2).

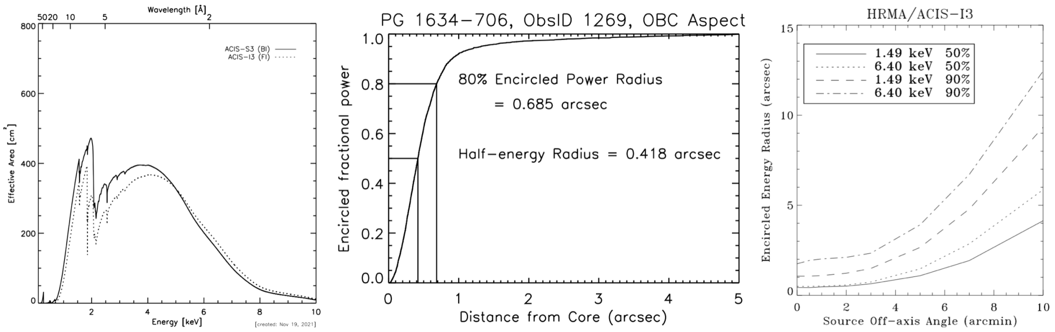

Figure 3.7. Left: Effective area of front-illuminated (FI) and back-illuminated (BI) chips. Middle: On-axis encircled fractional power (i.e, PSF of *Chandra*). Right: Encircled energy radius (i.e., PSF of *Chandra* for low and high energy X rays). (taken from CXC)

3.2.4 Transmission Grating (LETG, HETG)

The transmission grating spectroscopy provides a high-resolution spectrum in the energy range of 0.08 − 10 keV. The LETG and HETG cover the low energy (0.08- − 0.2 keV) and high-energy (0.4 − 10 keV) bands, respectively. The energy resolution ($E/\Delta E$) is 1000 and more than 1000 for HETG and LETG, respectively.

Chapter 4

Motivation of This Thesis

This chapter briefly summarizes the motivations for the analyses in the subsequent chapters. The detailed information of each analyzed object is given in Section 2.5−2.7. The detailed results and discussions are given in Chapter 5−7

Since the precise measurement of cosmic-ray electrons (electron and positron) reveals the anomalous positron excess beyond prediction, nearby astronomical objects are very important sources of the cosmic-ray electron and positron. The Vela SNR is one of the nearest SNRs from Earth located at a distance of $\sim$ 290 pc. Its close distance makes the SNR one of the prime candidates for the source of electrons. The motivation of the work in Chapter 5 is to estimate how high energy the electrons are accelerated to and how much amount of total energy they gain by using the GeV gamma-ray data with the *Fermi*-LAT. However, the Vela SNR has not yet been detected in the gamma-ray band. In this work, extended gamma-ray emission from the Vela SNR region is significantly detected for the first time. In addition, a spatially resolved analysis reveals that the spectra are not uniform over the SNR. Efficient acceleration of multi-TeV electrons is suggested from the spectral analysis, and the spectrum appears to extend into TeV energies.

RX J1713.7−3946, which is one of the important accelerators, is studied with multi-wavelength observations in particularly X-ray and gamma-ray bands. Although the gamma-ray emission from the SNR is detected from GeV to TeV band, the radiation mechanism is a matter of debate. The hard GeV gamma-ray emission (photon index: $\sim$ 1.5) suggests that the inverse Compton scattering of high-energy electrons is dominant. Theoretically, this hard emission could be reproduced by assuming a clumpy ISM (i.e., hadronic scenario), and the evidence of the molecular clumps is provided by the radio observations. Since the synchrotron X-ray emission is discovered in the SNR, electrons are considered to be accelerated to TeV energies. In the X-ray image of RX J1713.7−3946 northwest rim, there seem to be many point-like X-ray sources (hotspots). The motivation of the work in Chapter 6 is to unveil the origin of the hotspots. In this work, a bunch of hotspots is detected from the northwest rim of RX J1713.7−3946 for the first time. The hotspots are interpreted to be caused by interactions between the shock waves and compact-dense molecular core. One of the aspects of this interpretation includes the hadronic gamma-ray emission. This idea provides a new suggestion for the shock-cloud interaction, and clues for the gamma-ray radiation mechanism.

Since the TeV gamma-ray detection from the SS 433/W50 system by HAWC, this system becomes one of the hottest accelerators. Recently, many studies were conducted in the GeV gamma-ray band, but the results differ depending on the groups. Using the good angular resolution of *Chandra*, the two bright X-ray hotspots[1] are detected at the eastern ear of the system. In the radio band, the brightness distribution has a peak at the position of the X-ray hotspots. The motivation of the work in Chapter 7 is to analyze the properties of the hotspots in the gamma-ray band and reveal the nature of the particle acceleration. Since the results of previous studies in the GeV band were controversial, the analysis was performed considering the reasons of the different results. Using the multi-wavelength data, electrons are found to be accelerated up to $\sim$ 30 TeV at the position of hotspots.

---

[1] In the term of *hotspot*, it just means the bright and compact source. It is not obvious whether the origin of the hotspots in this system has the same origin as hotspots in the northwest rim of RX J1713.7$-$3946.

Chapter 5

Discovery of Extended GeV Gamma-ray Emission from the Region of the Vela Supernova Remnant with *Fermi*-LAT

5.1 Overview

We report the detection of ≥ 1 GeV gamma-ray emission extending over the entire region of the Vela supernova remnant (Vela SNR) using the *Fermi* Large Area Telescope. One of the nearest SNRs at a distance of only $\sim$ 287 pc, it is a possible source of the puzzling "positron excess" of cosmic-ray positron at energies above 10 GeV. The large extent of the gamma-ray emission allows us to perform a spatially resolved analysis for 50 regions with a unit are of $1^\circ \times 1^\circ$. The photon flux of each region in the $1 - 500$ GeV band is in the range of $(0.2 - 3.5) \times 10^{-9}$ cm^{-2}s^{-1}, and the northeast regions show relatively higher fluxes than those of the southwest regions. The total energy flux of the entire region is $(2.07 \pm 0.12) \times 10^{-10}$ erg cm^{-2}s^{-1}, corresponding to a luminosity of $(2.04 \pm 0.12) \times 10^{33}$ erg s^{-1}. The observed photon index Γ of each region differs widely from 1.5 to 3.0, and the spectra with harder indices ($\Gamma \lesssim 2.0$) are found in $\sim$33% of the southwest regions. The hard gamma-ray emission of the southwest regions is interpreted as the inverse-Compton scattering of electrons with a maximum energy of at a few TeV. Efficient acceleration of multi-TeV electrons suggests that the primary source of the electrons (and positrons) in the southwest part is the pulsar wind nebula, Vela X.

5.2 Observation and Data Reduction

We analyzed the LAT data from nearly 12 years of observation(August 8, 2008 to August 17, 2020 for off-pulse phase data, and August 4, 2008 to August 24, 2020 for all phase data). We used Fermitools version 2.0.8[1] with the P8R3_SOURCE_V3

---

[1] available from the LAT Science Support Center `https://fermi.gsfc.nasa.gov/ssc/`

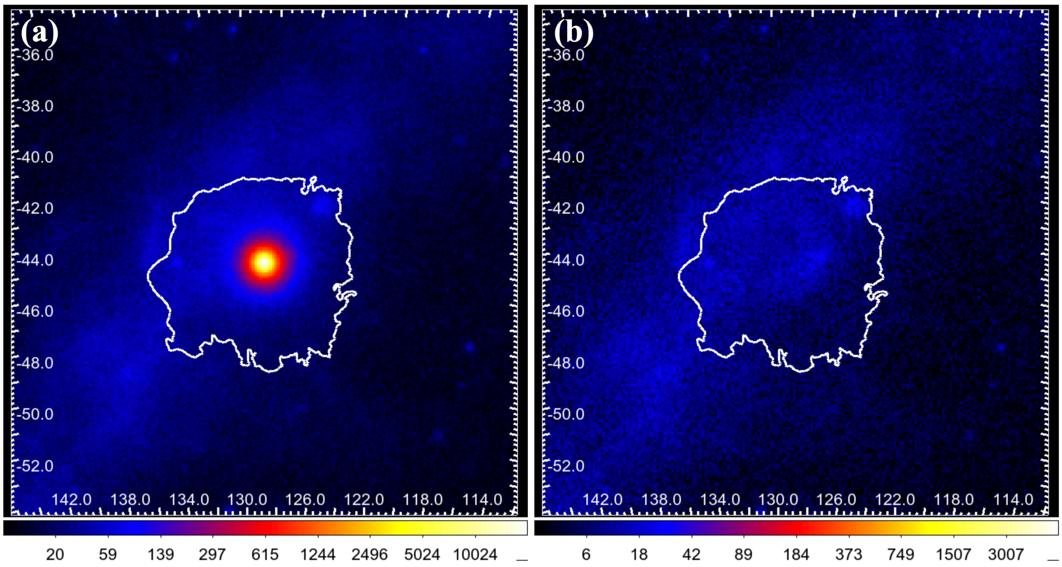

Figure 5.1. Count map of the ROI in the energy range of $1 - 1000$ GeV created by using the all phase data and off-pulse phase data presented in the left (a) and right (b) panels, respectively. The color scale is log-scale to represent the dimmer emission relative to the Vela pulsar. A white curve represents the outline of the Vela SNR in X-ray band.

instrumental response functions (IRFs). Events were extracted within a $20^\circ \times 20^\circ$ region of interest (ROI) centered at the position of Vela pulsar ((RA, Dec)=$(128^\circ.84,\ -45^\circ.176)$) with the energy of $1 - 1000$ GeV. To reduce the contamination from the Earth limb, only the events with zenith angle $< 90^\circ$ were used for the analysis. The binned maximum likelihood method of `gtlike` implemented in Fermitools was used to extract the spectral information. Figure 5.1 (a) shows a raw count map of the ROI in the energy range of $1 - 1000$ GeV.

Vela pulsar, which is the brightest steady GeV gamma-ray source, is located at the center of the ROI. As shown in Figure 5.1 (a), the emission from Vela pulsar stands out at the center of the ROI. The off-pulse phase data was analyzed to reduce the effect of the pulsar. For this purpose, we used the `TEMPO2` package[2] (Hobbs, Edwards, and Manchester, 2006) for the phase-gating analysis (Ray et al., 2011). To assign phase to each LAT photon, we used an ephemeris for the Vela pulsar prepared for the upcoming third pulsar catalog following the procedure given in FERMI-LAT Collaboration et al. (2022). The off-pulse window was selected as the pulse phase between 0.7 and 1.0 following the analysis of Vela X in Abdo et al. (2010a). Figure 5.2 shows a folded light curve of the counts within a radius of 1° from Vela pulsar in the energy range of $1 - 1000$ GeV. The off-pulse window is represented by a gray hatch. A count map created by using the off-pulse phase data is show in Figure 5.1 (b). Count maps around Vela pulsar is also compared in Figure 5.2. These maps shows the effect from the pulsar is clearly decreased by using the off-pulse phase data.

---

[2] `https://www.atnf.csiro.au/research/pulsar/tempo2/`

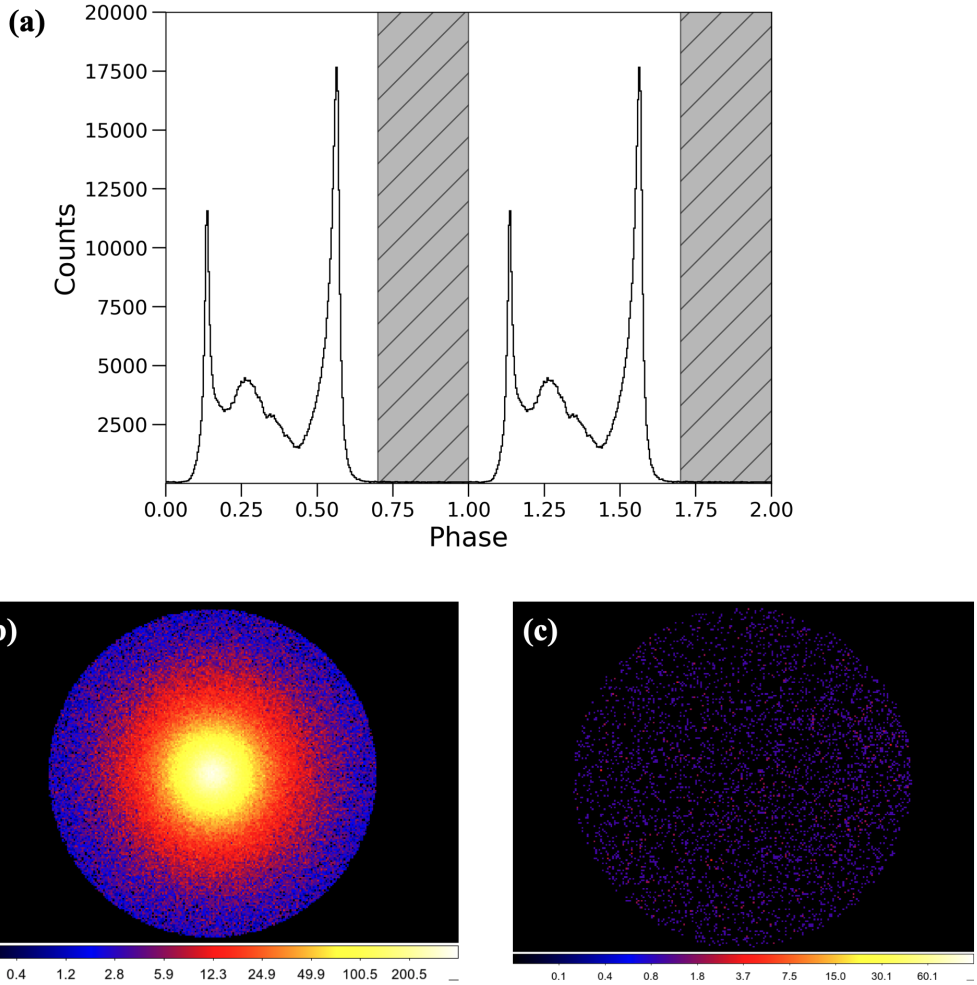

Figure 5.2. (a) Folded light curve of Vela pulsar in the $1 - 1000$ GeV energy range using the events within 1° from the pulsar. The off-pulse window used for the analysis is shown by the gray hatch. Count map within the 1° from Vela pulsar in the energy range of $1 - 1000$ GeV created by using the all phase data and off-pulse phase data presented in the bottom left (b) and right (c) panels, respectively. Each pixel has a size of $0\overset{\circ}{.}01 \times 0\overset{\circ}{.}01$ in the panel (b) and (c).

The gamma-ray sources listed in the 4FGL-DR2 catalog (Ballet et al., 2020; Abdollahi et al., 2020) within 18° of the center of the ROI were included in the background model. Extended sources Puppis A and Vela Junior (Vela Jr.) were modeled with uniform disk templates with radii 0.44° and 0.98°, respectively, in the same way as the catalog. The spatial template for Vela X was generated using the smoothed brightness map of the TeV emission ($0.75 - 70$ TeV) from the H.E.S.S. observations (Abramowski et al., 2012), whose size is comparable to that of radio emission. In addition, an extended gamma-ray source near Vela X, FGES J0830.3-−4453, reported in the Fermi Galactic Extended Source (FGES) catalog (Ackermann et al., 2017), was added to the model with a uniform disk template with a radius of 0.22°. This source was confirmed by Tibaldo et al. (2018). The diffuse Galactic ("gll_iem_v07.fits") and isotropic ("iso_P8R3_SOURCE_V3_v1.txt") emission models were adopted background model. During the spectral fits, the spectral parameters of the sources with a significance of more than 7σ located within 7° from the center of the ROI were left free unless otherwise noted. The normalization of the Galactic and isotropic diffuse emission models was also left free.

5.3 Analysis and Results

5.3.1 Extended emission from the Vela SNR region

We performed a binned maximum likelihood fit of the data using our background model. In order to accurately model the Vela SNR region, normalization of the spectral parameters are left free for the sources with a significance of less than 7σ and within 7° from the center of the ROI, in addition to the aforementioned conditions. In the analysis of the off-pulse data, we excluded Vela pulsar from the background model in the subsequent analysis because of the lack of significant emissions. Figure 5.3 (a) shows a map of residual counts after subtracting the best-fit background model. A positive excess (marked in red) can be seen over the area of Vela SNR indicating that the model is insufficient to reproduce the LAT gamma-ray data in the ROI. The size of the excess is a radius of $\sim 4°$, comparable to the size of Vela SNR.

A uniform disk template with a radius of 4° centered at the position of the X-ray Vela SNR was added to our model assuming a power-law type spectrum. When fitting the data with the new source, we obtained $TS = 235$ for 2 additional free parameters by comparing the likelihoods with and without the new source, thus confirming spatially extended excess emission in the Vela SNR region. Figure 5.3 (b) shows the residual count map obtained when using the model with an additional disk template. The residual counts inside Vela SNR became smaller but with remaining residuals in the northeast region in Figure 5.3 (b) suggesting that the extended emission is not uniform, but is brighter in the northeast region than the southwest.

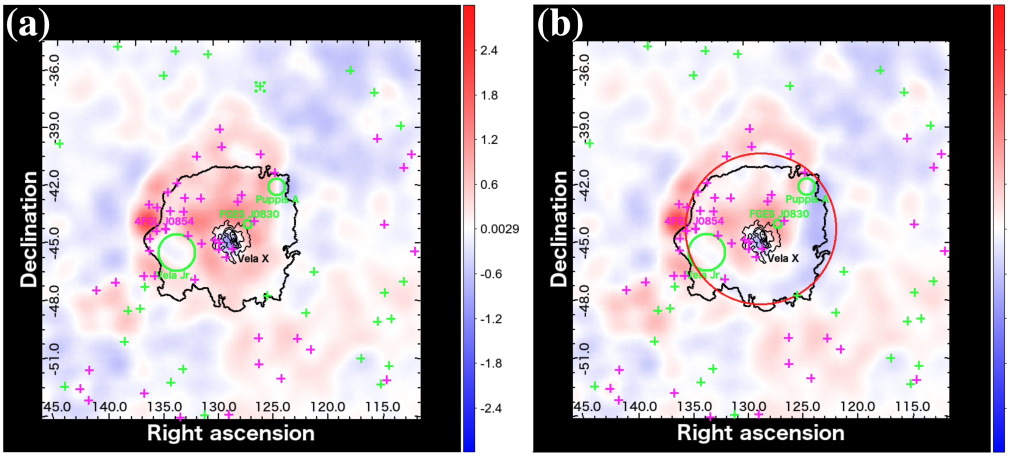

Figure 5.3. Maps of the residual counts in the region of Vela SNR in the energy range $1 - 1000$ GeV. A Gaussian smoothing with a radius of 1° was applied to both maps. Green crosses represent the identified gamma-ray sources while magenta crosses represent the unassociated sources in the 4FGL-DR2 catalog. Green circles represent the position of Vela Jr., FGES J0830.3−4453, and Puppis A from left to right, respectively. Black contours show the outer boundary of Vela SNR in the X-ray band and the TeV gamma-ray emission of Vela X near the center of the maps. (a) Residual map when fitting the ROI with sources included in the gamma-ray source catalogs. (b) Residual map when fitting the ROI with sources included in the gamma-ray source catalogs and a uniform disk template with a radius of 4°. The Red circle represents the size and location of the disk template.

The uniform disk template with a radius of 4° is used to derive the significance of the extended excess emission from the region of Vela SNR. From the residual map shown in Figure 5.3, excess emission still remains outside the Vela SNR. The TS values against the model with the radius of 4° was investigated by changing the radius of the uniform disk template as shown in Figure 5.4. The profile implies that the radius of 4.6° is preferred over radius of 4° at TS=15. However, we intended to show the extended excess emission at the position of the well-known X-ray emitting region in this section. The area with the radius of 4.6° is almost covered by the small grid regions and analyzed in Section 5.3.2.

The gamma-ray point sources in the catalog are represented by crosses in Figure 5.3. The magenta crosses indicate unassociated sources listed in the 4FGL-DR2 catalog[3]. In Table 5.1, unassociated sources within 7° from the center of the ROI are summarized. Unassociated sources are not distributed uniformly over the ROI. They are concentrated in the northeast and central regions of Vela SNR. Figure 5.5 shows the radial profile of the number densities of unassociated sources from the center of the ROI. One can see high densities of unassociated sources inside Vela SNR within a radius of $\sim$ 4°. The density of the unassociated sources within a radius of $\sim$ 4° was ~ 0.4 degree^{-2} (20 sources), whereas it was ~ 0.1 degree^{-2} (16 sources, eight

---

[3] We define unassociated sources as those no entry in the column for the association name (assoc_name) in the 4FGL-DR2 catalog.

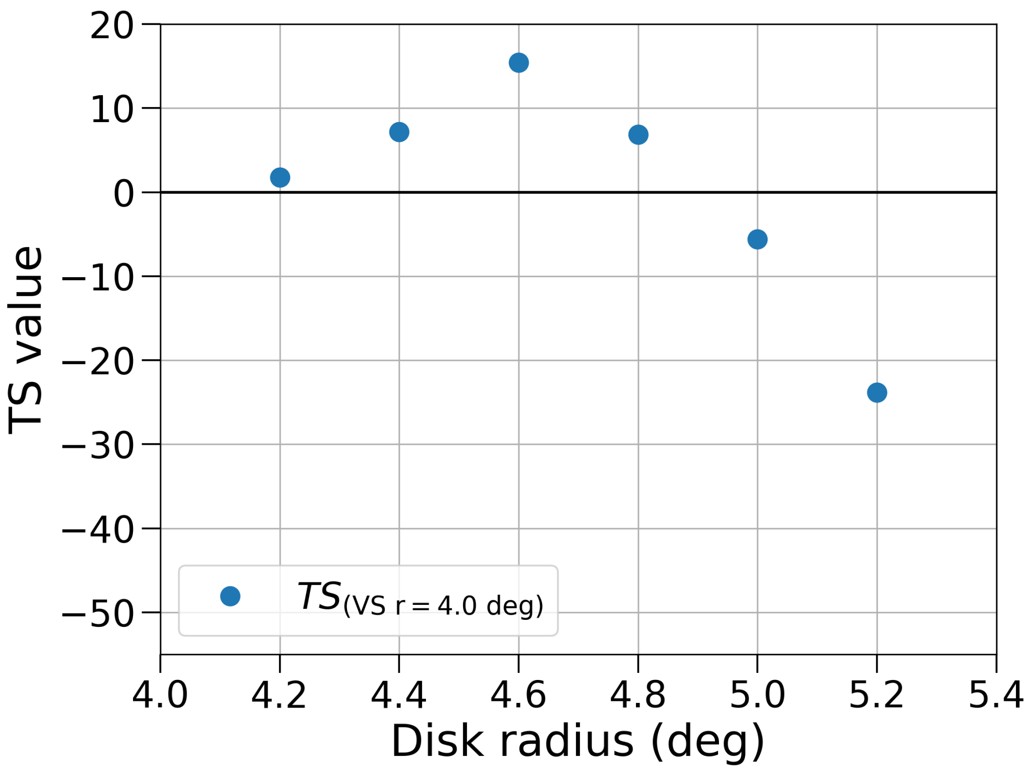

Figure 5.4. Profile of TS values to the model of a disk template with a radius of 4° obtained by changing the radius in 0°.2 steps at the position of Vela SNR.

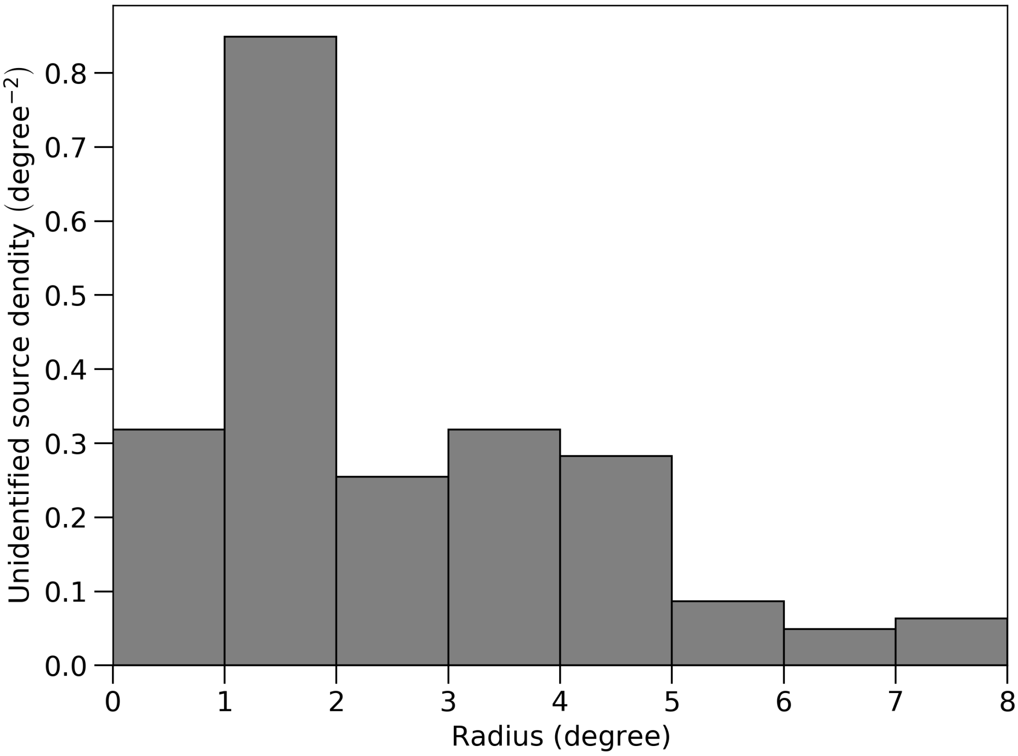

Figure 5.5. Radial profile of the unassociated sources density from the center of the ROI. A large number of unassociated sources are distributed within a radius of $\sim 4^\circ$ where Vela SNR is located.

of which are located within a radius between 4° and 5°) inside an annulus region with inner and outer radii of 4° and 8°, respectively. If the density of the unassociated sources inside Vela SNR is typical for the ROI, approximately 60 unassociated sources would be located inside the annulus region. We also compare the number densities of the unassociated sources within two regions on both sides of Vela SNR. The regions are circles with radii of 4° located on the same Galactic latitude of Vela SNR and 11° away from the center of the ROI((A: $l = 274^\circ.6, b = -2^\circ.8$) and (B: $l = 252^\circ.5, b = -2^\circ.8$)). The density of the circular region closer to the Galactic center (east side: A) was $\sim$ 0.1 degree^{-2} (five sources), and there was no unassociated sources on the other circular region (west side: B). These results imply that the number density of unassociated sources inside Vela SNR is abnormally high. Multiple unassociated sources in the catalog inside Vela SNR are likely to be placed to reproduced the emission from a spatially extended sources in this region. In the following analysis, we exclude the unassociated sources inside the Vela SNR from our background model, assuming that the majority of these are surrogate for the extended emission of the SNR. However, we retain 4FGL J0854.8−4505, which has the highest flux and detection significance among the unassociated sources inside the Vela SNR region and which clearly stands out as a point-like source.

It notes that the highest number density in the radial profile between 1° and 2° in Figure 5.5 was caused by the position of Vela X in the 4FGL-DR2 catalog. The position is shifted to the northwestern direction of Vela X observed in other bands (e.g., radio and TeV gamma-ray band), as shown in Figure 5.6. This is because the west side of Vela X was found to be bright in the previous study with the LAT (e.g., Abdo et al., 2010a; Grondin et al., 2013). A recent study in GeV gamma-ray band revealed the emission is extended similar to that of the radio band (Tibaldo et al., 2018). This caused the remained residual emission in the eastern side of Vela X in GeV gamma-ray band, and multiple unassociated sources are placed on the position of eastern side of Vela X to reproduce the residual emissions. These sources are located in a small area with radii between 1° and 2°, resulting in the highest number density in the radial profile.

5.3.2 Spatially resolved analysis

The above analysis demonstrates the presence of the spatially extended gamma-ray emission and hence the presence of the high-energy particles accelerated in the Vela SNR. Both the residuals and the concentration of unassociated sources in the northeast region (see Figure 5.3 (b)) suggest that it is brighter than the southwest portion of the remnant. This asymmetry was also observed in the X-ray band, shown in Figure 5.7. Sushch, Hnatyk, and Neronov (2011) reported that the asymmetry is caused by the density distribution of the gas inside Vela SNR. Interactions between Vela SNR and the ISM have also been reported in the northeast region (Moriguchi et al., 2001; Dubner et al., 1998). These previous results indicate that the different mechanisms of gamma-ray radiation dominate from region to region because of the

Table 5.1: Unassociated sources within 7° from the center of the ROI

Name	Position (RA, Dec)	Detection Significance (σ)	Distance (arcmin)	Inside/Outside
4FGL J0838.8-4552c	(129°.7229, −45°.8674)	3.7004	55.945	Inside
4FGL J0834.9-4612	(128°.7368, −46°.2096)	6.0274	62.139	Inside
4FGL J0840.3-4544	(130°.0803, −45°.7351)	4.8711	62.404	Inside
4FGL J0839.1-4613c	(129°.7962, −46°.2262)	6.4778	74.897	Inside
4FGL J0828.4-4444	(127°.105, −44°.7362)	9.5455	77.848	Inside
4FGL J0836.8-4638	(129°.2014, −46°.6472)	6.9717	89.623	Inside
4FGL J0833.3-4342c	(128°.3398, −43°.7136)	5.8110	90.221	Inside
4FGL J0844.2-4554c	(131°.0655, −45°.914)	6.0253	103.846	Inside
4FGL J0832.2-4322c	(128°.0633, −43°.3672)	4.5387	113.415	Inside
4FGL J0844.1-4330	(131°.0335, −43°.515)	6.9955	137.363	Inside
4FGL J0848.2-4527	(132°.0722, −45°.4656)	7.2535	137.872	Inside
4FGL J0849.2-4410c	(132°.3217, −44°.1819)	4.1350	160.448	Inside
4FGL J0848.8-4328	(132°.2109, −43°.4731)	11.1457	177.456	Inside
4FGL J0846.6-4747	(131°.6711, −47°.7913)	4.8065	195.930	Inside
4FGL J0853.1-4407	(133°.2972, −44°.128)	7.2485	200.743	Inside
4FGL J0854.8-4504	(133°.7035, −45°.0722)	32.5249	206.379	Inside
4FGL J0850.8-4239	(132°.7154, −42°.6652)	8.8174	225.543	Inside
4FGL J0822.8-4207	(125°.7178, −42°.1298)	5.2959	227.247	Outside
4FGL J0853.6-4306	(133°.4193, −43°.112)	10.9413	233.139	Inside
4FGL J0857.7-4507	(134°.4336, −45°.1205)	4.6277	237.101	Inside
4FGL J0857.0-4353c	(134°.2597, −43°.8935)	4.1660	244.584	Outside
4FGL J0844.9-4117	(131°.2473, −41°.2962)	10.6714	255.615	Outside
4FGL J0827.0-4111c	(126°.768, −41°.1858)	4.1409	255.822	Outside
4FGL J0859.8-4530c	(134°.9591, −45°.5039)	5.8605	259.172	Inside
4FGL J0837.8-4048c	(129°.4748, −40°.8118)	5.4945	263.374	Outside
4FGL J0900.2-4608	(135°.0508, −46°.1347)	4.8955	267.080	Inside
4FGL J0859.3-4342	(134°.8271, −43°.7125)	14.9002	271.404	Outside
4FGL J0859.2-4729	(134°.8042, −47°.4883)	16.2353	283.621	Outside
4FGL J0902.5-4727	(135°.6393, −47°.4536)	5.1607	313.387	Outside
4FGL J0838.4-3952	(129°.6142, −39°.8762)	5.8813	319.868	Outside
4FGL J0826.1-5053	(126°.5257, −50°.8991)	12.1866	355.564	Outside
4FGL J0911.6-4738c	(137°.9166, −47°.6403)	6.1461	403.646	Outside
4FGL J0813.1-5049	(123°.2868, −50°.8241)	4.7810	405.168	Outside

Note– The detection significance and position are referred from the 4FGL-DR2 catalog. Distance from the center of the ROI is represented in fourth column. The last column represents the location of each source inside or outside of the analysis region of the Vela SNR.

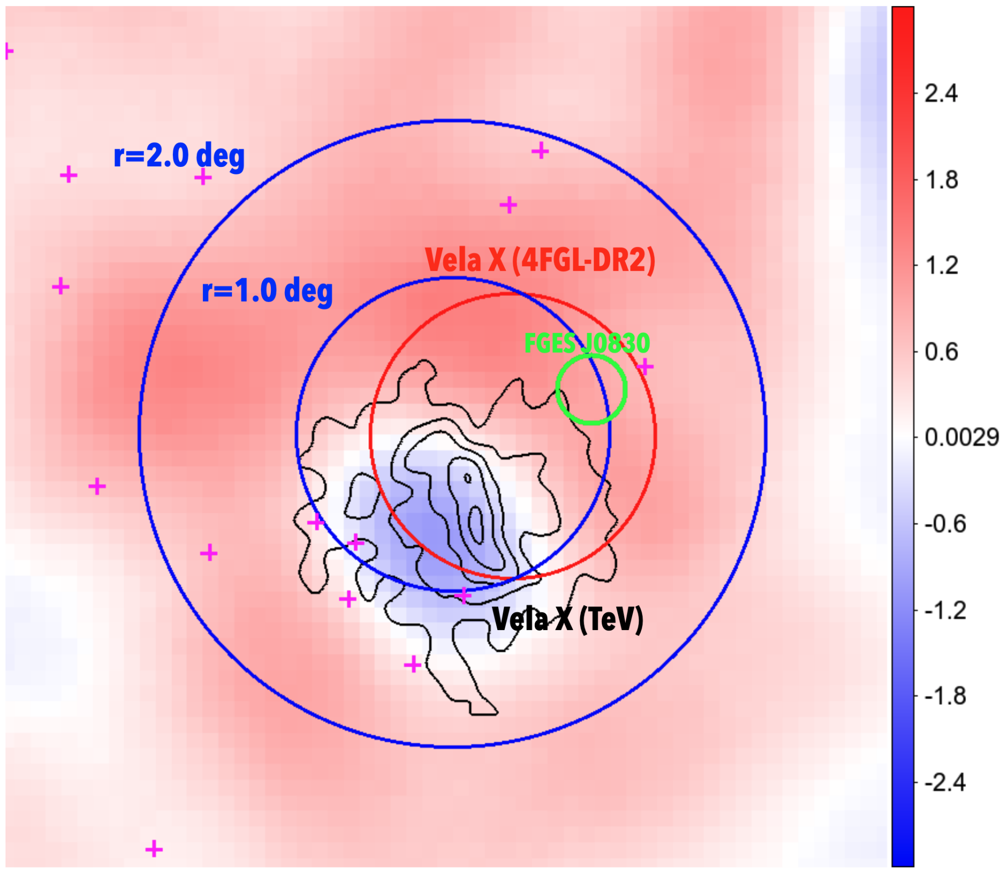

Figure 5.6. Position of Vela X in the 4FGL-DR2 catalog (red circle) and TeV gamma-ray band (black contour). Radii from the center of the ROI are represented by blue circles. Unassociated sources are shown by magenta crosses.

different environments inside the SNR. The large angular diameter of the SNR allowed us to investigate the dominant radiation mechanism in each grid region by performing a spatially resolved analysis of the Vela SNR region.

Spectral analysis by small square grids

The region of Vela SNR was divided into $1^\circ \times 1^\circ$ regions and selected for analysis the 50 grid regions which have a ROSAT count rate in excess of 10^4 s^{-1}. The grid regions that satisfying this criterion are shown in Figure 5.7. In order to analyze the spectra from each grid region, a uniform square template was added to the model at the position of each grid region assuming a power-law type spectrum. We performed a maximum likelihood fit to the gamma-ray data during the off-pulse phase interval of the Vela pulsar. For the regions which show a weak signal, the fit was also performed for the complete data sed (i.e., ignoring the Vela pulsar phase). During these fits, grid regions with TS<4 in both analyses were excluded from the model because they did not emit significant GeV gamma-ray emissions and affected the convergence of the fitting. The spectral parameters of the grid regions with TS<4 in the off-pulse phase analysis and TS>4 in the all-phase analysis were fixed to the best-fit values of the all-phase analysis.

Figure 5.8 shows the results of the TS, photon index, and flux in the energy range of $1-500$ GeV for each grid region. The white crosses in Figure 5.8 represent grid regions with a TS of less than four and are excluded from the model. These regions coincide with the dim area in the X rays (see Figure 5.7), except for the regions of Vela Jr. and Puppis A. The map of the photon index exhibits a trend of softer spectra in the northeast region than in the southwest region. The flux map exhibits a similar trend; the northeast region is brighter than the southwest region. Figure 5.9 shows the scatter plot for the photon index and flux. The northeast regions (marked by red points) were brighter and had softer spectra than the southwest regions (marked by blue points). In this plot, the grid regions were divided into two groups depending on whether the Galactic latitude was more or less than $-2\overset{\circ}{.}3$. The latitude is shown by the white solid line, and the northeast and southwest regions are represented by the magenta and cyan square regions, respectively, in Figure 5.7. These trends indicate that the spectrum and brightness are not uniform across Vela SNR. The results and the classifications of each grid region are summarized in Table 5.2. For the Galactic and isotropic diffuse emission models, we found normalization of 0.953 ± 0.004 and 1.22 ± 0.07 in our ROI, respectively.

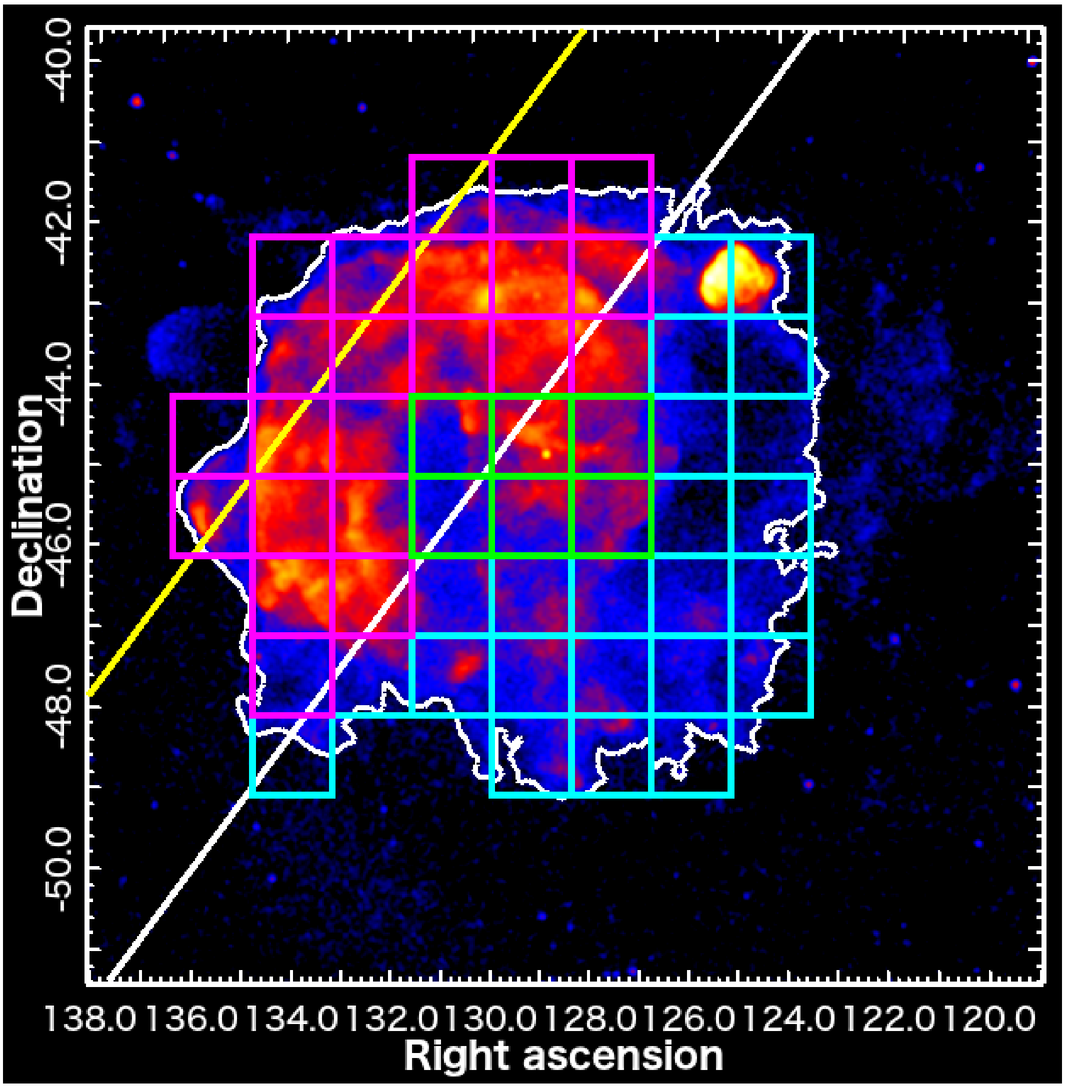

Figure 5.7. *ROSAT* soft X-ray (0.1−2.4 keV) image of the Vela SNR. X-ray image with an energy of 0.1 − 2.4 keV observed by *ROSAT*. White contour shows the outer boundary of the Vela SNR. Grid regions with a count rate of more than 10^4 s^{-1} are overlaid. The size of each square region is 1° × 1°. Magenta and cyan represent the northeast and southwest regions, respectively, when the Vela SNR is divided into the two regions. Green square regions represent the regions excluded due to possible contamination from the Vela X. Yellow and white thick lines represents the Galactic latitude of 0° and $-2.^{\circ}3$, respectively.

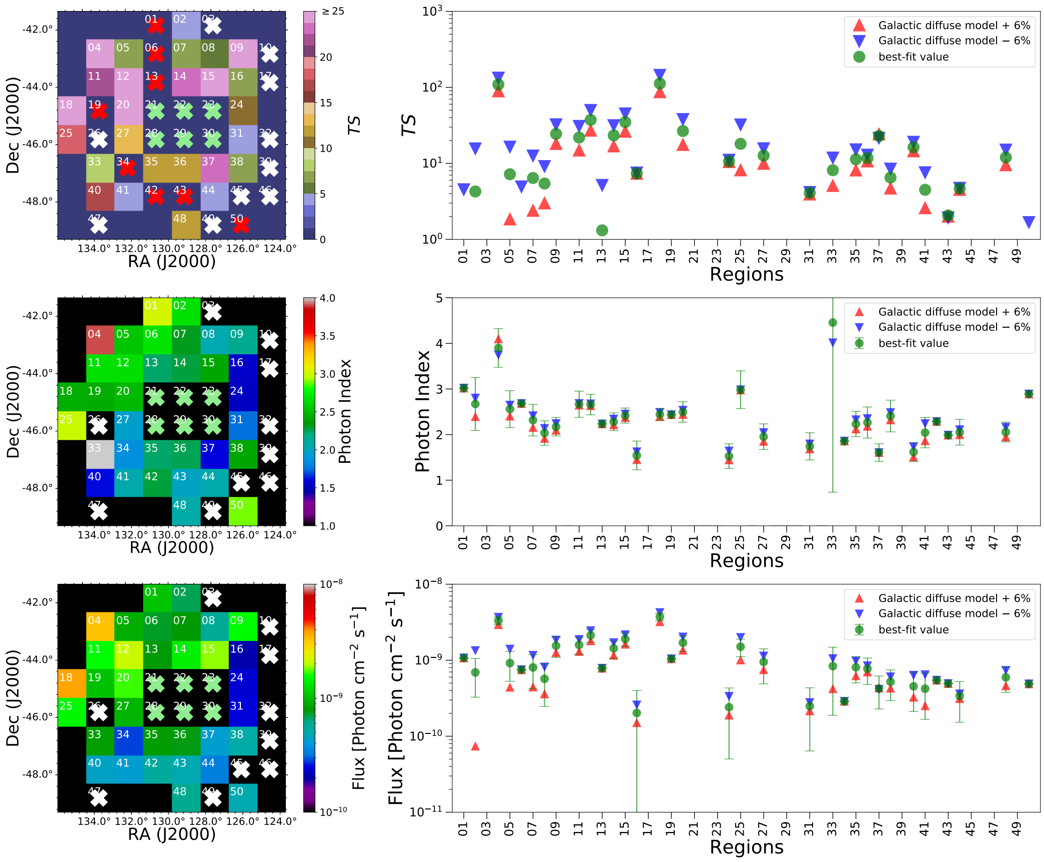

Figure 5.8. Results of TS, photon index, and flux in the energy range of $1 - 500$GeV obtained by spatially resolved analysis are shown from top to bottom, respectively. These maps and plots are shown in the left and right panels. White crosses in the maps indicate grid regions with the TS less than 4 and removed from the model. Red crosses in the map of TS indicate grid regions with the TS more than 4 in the analysis of all phase data, and less than 4 in that of off-pulse phase data. Spectral parameters of the grid regions with red crosses are fixed to the results of all phase analysis. Green crosses represent the regions excluded due to possible contamination from the Vela X. Red and blue ponits show the best-fit values when the normalization of the Galactic diffuse model was artificially changed by ±6% to quantify the effect of the uncertainty of the model.

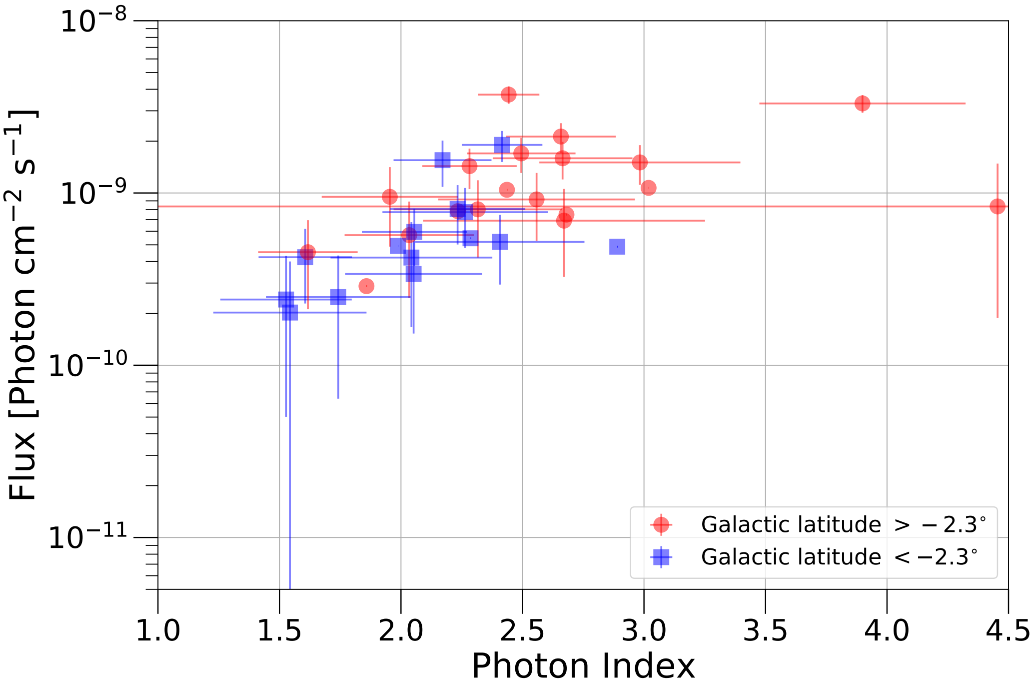

Figure 5.9. Diagram of the photon index and flux of grid regions. The red and blue plots indicate that the Galactic latitude of the grid region is more or less than $-2.^\circ3$, respectively. Plots without error bars represent the grid regions with spectral parameters fixed to the results of all phase data analysis.

Table 5.2: Results of the spectral analysis of grid regions.

Source name	Center Position (α [$J2000$], δ [$J2000$])	Flux ($1-500$ GeV) (10^{-9} photon cm^{-2}s^{-1})	Photon Index	TS	Northeast (NE) or Southwest (SW)
Grid reg 01	(130.4,-42.0)	1.07 (fixed)	3.02 (fixed)	0.0	NE
Grid reg 02	(129.0,-42.0)	$0.69 \pm 0.36^{+0.65}_{-0.62}$	$2.67 \pm 0.58^{+0.13}_{-0.28}$	4.3	NE
Grid reg 03	(127.7,-42.0)	–	–	–	–
Grid reg 04	(133.1,-42.9)	$3.31 \pm 0.39^{+0.37}_{-0.38}$	$3.90 \pm 0.42^{+0.20}_{-0.15}$	109.0	NE
Grid reg 05	(131.8,-42.9)	$0.92 \pm 0.39^{+0.48}_{-0.48}$	$2.56 \pm 0.40^{+0.09}_{-0.15}$	7.2	NE
Grid reg 06	(130.4,-43.0)	0.75 (fixed)	2.68 (fixed)	0.1	NE
Grid reg 07	(129.1,-43.0)	$0.80 \pm 0.38^{+0.36}_{-0.36}$	$2.32 \pm 0.35^{+0.10}_{-0.16}$	6.4	NE
Grid reg 08	(127.7,-43.0)	$0.57 \pm 0.32^{+0.25}_{-0.21}$	$2.03 \pm 0.27^{+0.10}_{-0.12}$	5.4	NE
Grid reg 09	(126.3,-43.0)	$1.55 \pm 0.47^{+0.29}_{-0.29}$	$2.17 \pm 0.20^{+0.07}_{-0.08}$	24.4	SW
Grid reg 10	(125.0,-42.9)	–	–	–	–
Grid reg 11	(133.2,-43.9)	$1.59 \pm 0.39^{+0.29}_{-0.29}$	$2.67 \pm 0.29^{+0.02}_{-0.02}$	21.9	NE
Grid reg 12	(131.8,-43.9)	$2.13 \pm 0.41^{+0.32}_{-0.33}$	$2.66 \pm 0.23^{+0.02}_{-0.03}$	37.3	NE
Grid reg 13	(130.5,-44.0)	0.78 (fixed)	2.23 (fixed)	1.3	NE
Grid reg 14	(129.1,-44.0)	$1.43 \pm 0.38^{+0.27}_{-0.27}$	$2.28 \pm 0.19^{+0.06}_{-0.07}$	23.3	NE
Grid reg 15	(127.7,-44.0)	$1.90 \pm 0.39^{+0.26}_{-0.28}$	$2.42 \pm 0.17^{+0.03}_{-0.04}$	34.9	SW
Grid reg 16	(126.3,-44.0)	$0.20 \pm 0.20^{+0.06}_{-0.05}$	$1.54 \pm 0.32^{+0.08}_{-0.09}$	7.4	SW
Grid reg 17	(124.9,-43.9)	–	–	–	–
Grid reg 18	(134.7,-44.8)	$3.72 \pm 0.44^{+0.51}_{-0.52}$	$2.44 \pm 0.13^{+0.04}_{-0.05}$	112.1	NE
Grid reg 19	(133.3,-44.9)	1.04 (fixed)	2.44 (fixed)	0.0	NE
Grid reg 20	(131.9,-44.9)	$1.70 \pm 0.39^{+0.33}_{-0.34}$	$2.50 \pm 0.22^{+0.04}_{-0.06}$	26.6	NE
Grid reg 21	(130.5,-45.0)	$0.57 \pm 0.30^{+0.19}_{-0.16}$	$1.90 \pm 0.23^{+0.09}_{-0.09}$	7.7	X
Grid reg 22	(129.1,-45.0)	$2.09 \pm 0.54^{+0.14}_{-0.17}$	$3.23 \pm 0.49^{+0.04}_{-0.03}$	35.1	X
Grid reg 23	(127.7,-45.0)	$5.56 \pm 0.68^{+0.16}_{-0.19}$	$2.28 \pm 0.08^{+0.01}_{-0.01}$	261.8	X
Grid reg 24	(126.2,-45.0)	$0.24 \pm 0.19^{+0.09}_{-0.05}$	$1.53 \pm 0.27^{+0.11}_{-0.08}$	10.6	SW
Grid reg 25	(134.8,-45.8)	$1.50 \pm 0.39^{+0.49}_{-0.50}$	$2.98 \pm 0.41^{+0.01}_{-0.01}$	18.1	NE
Grid reg 26	(133.4,-45.9)	–	–	–	–
Grid reg 27	(132.0,-45.9)	$0.95 \pm 0.46^{+0.19}_{-0.20}$	$1.95 \pm 0.28^{+0.09}_{-0.10}$	12.7	NE
Grid reg 28	(130.5,-46.0)	$2.88 \pm 0.39^{+0.15}_{-0.16}$	$2.29 \pm 0.11^{+0.02}_{-0.02}$	96.1	X
Grid reg 29	(129.1,-46.0)	$2.01 \pm 0.83^{+0.08}_{-0.10}$	$2.31 \pm 0.25^{+0.01}_{-0.01}$	37.4	X

Source name	Center Position (α [$J2000$], δ [$J2000$])	Flux ($1-500$ GeV) (10^{-9} photon cm^{-2}s^{-1})	Photon Index	TS	Northeast (NE) or Southwest (SW)
Grid reg 30	(127.6,-46.0)	$1.49 \pm 0.41^{+0.11}_{-0.12}$	$2.06 \pm 0.16^{+0.03}_{-0.03}$	35.2	X
Grid reg 31	(126.2,-46.0)	$0.25 \pm 0.18^{+0.03}_{-0.03}$	$1.74 \pm 0.30^{+0.05}_{-0.06}$	4.1	SW
Grid reg 32	(124.8,-45.9)	–	–	–	–
Grid reg 33	(133.5,-46.9)	$0.84 \pm 0.65^{+0.22}_{-0.41}$	$4.46 \pm 3.72^{+5.54}_{-0.44}$	8.1	NE
Grid reg 34	(132.0,-46.9)	0.29 (fixed)	1.86 (fixed)	0.0	SW
Grid reg 35	(130.6,-47.0)	$0.81 \pm 0.30^{+0.17}_{-0.18}$	$2.23 \pm 0.28^{+0.09}_{-0.11}$	11.3	SW
Grid reg 36	(129.1,-47.0)	$0.77 \pm 0.29^{+0.07}_{-0.07}$	$2.26 \pm 0.34^{+0.09}_{-0.08}$	11.7	SW
Grid reg 37	(127.6,-47.0)	$0.42 \pm 0.20^{+0.01}_{-0.01}$	$1.61 \pm 0.19^{+0.00}_{-0.00}$	22.9	SW
Grid reg 38	(126.2,-47.0)	$0.52 \pm 0.23^{+0.08}_{-0.09}$	$2.41 \pm 0.35^{+0.08}_{-0.09}$	6.5	SW
Grid reg 39	(124.7,-46.9)	–	–	–	–
Grid reg 40	(133.6,-47.9)	$0.45 \pm 0.24^{+0.18}_{-0.13}$	$1.62 \pm 0.20^{+0.12}_{-0.11}$	16.3	NE
Grid reg 41	(132.1,-47.9)	$0.42 \pm 0.26^{+0.22}_{-0.17}$	$2.04 \pm 0.33^{+0.20}_{-0.18}$	4.5	SW
Grid reg 42	(130.6,-48.0)	0.55 (fixed)	2.29 (fixed)	0.0	SW
Grid reg 43	(129.1,-48.0)	0.49 (fixed)	1.99 (fixed)	2.1	SW
Grid reg 44	(127.6,-48.0)	$0.34 \pm 0.19^{+0.02}_{-0.03}$	$2.05 \pm 0.28^{+0.06}_{-0.06}$	4.7	SW
Grid reg 45	(126.1,-48.0)	–	–	–	–
Grid reg 46	(124.6,-47.9)	–	–	–	–
Grid reg 47	(133.7,-48.9)	–	–	–	–
Grid reg 48	(129.1,-49.0)	$0.59 \pm 0.22^{+0.14}_{-0.13}$	$2.06 \pm 0.22^{+0.10}_{-0.11}$	12.0	SW
Grid reg 49	(127.6,-49.0)	–	–	–	–
Grid reg 50	(126.1,-48.9)	0.49 (fixed)	2.89 (fixed)	0.0	SW

Note- The first and second errors in the column of the flux and photon index represent the statistic and the systematic errors, respectively. The systematic errors are estimated by artificially changing the normalization of the Galactic diffuse model by 6%. The grid regions with a TS of less than four in both the all-phase and off-pulse phases are indicated by "–" and are removed from the model. The regions with a TS of less than four in the off-pulse phase analysis were fixed to the results of the all-phase analysis if the TS was more than four in the all-phase analysis. In the last column, grid regions are classified as northeast (NE) when the Galactic latitude of the center of the grid region is more than -2.3°, and southwest (SW) when it is less than -2.3°. The classification of "X" in the last column represents the grid regions overlapping Vela X, and are considered as the background sources in this work.

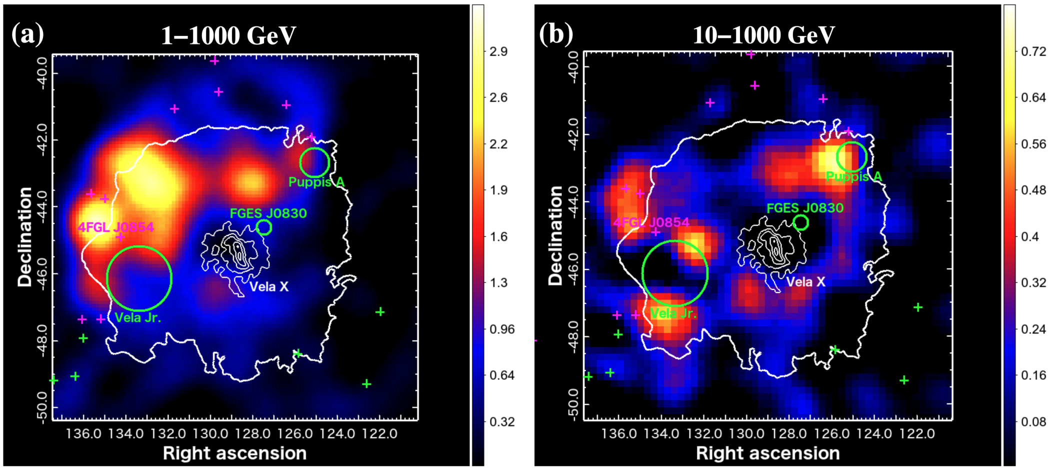

Figure 5.10. Gamma-ray count maps around Vela SNR in the energy ranges of $1 - 1000$GeV and $10 - 1000$GeV after subtraction of the background emission. Pixel sizes of (a) and (b) are $0.^\circ1 \times 0.^\circ1$ and $0.^\circ2 \times 0.^\circ2$, respectively. A Gaussian smoothing with a radius of 1° was applied to both maps. Contours and regions by crosses and circles are the same as those in Figure 5.3.

The origin (Vela X or Vela SNR) is uncertain for gamma rays detected from the region of the Vela SNR overlapping with the Vela X (i.e., Grid reg 21, 22, 23, 28, 29, and 30) The template of TeV emission for Vela X yields the highest likelihood value relative to radio and uniform disk templates created by referring to Tibaldo et al. (2018), in which GeV gamma-ray emission from Vela X is analyzed in detail. The TS values against the template with TeV emission profile are -7.0 and -63.2 for radio and uniform disk templates, respectively. The best template of Vela X is beyond scope of this work. The impact of the Vela X template is seen in the grid regions overlapping with Vela X where relatively high flux are observed. If contamination from Vela X is dominant in these grid regions, the regions do not represent the gamma-ray emission from Vela SNR. We excluded these grid regions from the analysis region of the Vela SNR. Count maps were generated around Vela SNR after subtracting the best-fit background emission, as shown in Figure 5.10.

Since Vela SNR is located on the Galactic plane as shown in Figure 5.7, we considered the systematic errors caused by the uncertainty of the Galactic diffuse emission model. We artificially changed the normalization of the Galactic diffuse emission model by ±6% (Abdo et al., 2009b). The estimated systematic errors of the spectral parameters are listed in Table 5.2. The uncertainty of the spectral parameters is shown in Figure 5.8. The Galactic diffuse emission might still be contaminated in the grid regions of the northeast region. In this work, we systematically analyzed the emission from the region of Vela SNR defined based on X-ray observations. We leave it a future work to analyze whether the excess emission in the northeast (inside and outside the SNR, in Figure 5.3 (b)) may be partially due to Galactic background not well modeled in Galactic diffuse model (gll_iem_v07.fits).

The northeast and southwest regions

The analysis of the grid regions revealed a spatial trend of the photon index and flux in the northeast and southwest regions, and in this section we performed a spectral analysis of these regions, which we define simply as being divided by a parallel at Galactic latitude $2\overset{\circ}{.}3$. The magenta and cyan regions in Figure 5.7 show which grid points are assigned to the northeast and southwest region, respectively. The flux of each grid region indicated that the brightness distribution was not uniform inside Vela SNR. The photon indices of the grid regions indicated that the brightness distribution changes depending on the energy bands. For the template of each region, we used a map cube template which is 3-dimensional map (2 sky coordinates and 1 energy). In the energy axis, the template consisted of flux maps of grid regions in 12 logarithmically spaced band from 1 to 500 GeV. The flux maps, which have shapes of the magenta and cyan regions for the northeast and southwest regions of Figure 5.7, respectively, were created by using the results of the spatially resolved analysis. The flux of each grid region in the each energy band was calculated from the best-fit power-law spectrum. Since these flux maps in the direction of the energy axis have information on the spectral index, each flux map was normalized to 1 independently to evaluate spectral indices of the northeast and southwest regions. In this way, the map cube template has a brightness distribution corresponding to each energy band. For the map cube templates of both regions, the spectral form of a power-law type is assumed.

We obtained the fluxes $f_{\rm NE} = (2.7 \pm 0.1) \times 10^{-8}$ cm^{-2}s^{-1} and $f_{\rm SW} = (1.1 \pm 0.1) \times 10^{-8}$ cm^{-2}s^{-1} in the energy range of $1 - 500$ GeV, and the photo indices $\Gamma_{\rm NE} = 2.56 \pm 0.06$ and $\Gamma_{\rm SW} = 2.06 \pm 0.05$ from the northeast and southwest regions, respectively. The energy fluxes in the energy range of $1{-}500$ GeV were $(1.14 \pm 0.08) \times 10^{-10}$ erg cm^{-2}s^{-1} and $(0.95 \pm 0.09) \times 10^{-10}$ erg cm^{-2}s^{-1} for the northeast and southwest regions, respectively. Assuming the distance of 287 pc, the corresponding luminosities were $(1.13 \pm 0.08) \times 10^{33}$ erg s^{-1} and $(0.94 \pm 0.09) \times 10^{33}$ erg s^{-1} for the northeast and southwest regions, respectively. The best-fit models are shown in Figure 5.11 by solid lines. The best-fit spectra show that the southwest region has a harder spectrum than the northeast region, as expected from the spatially resolved analysis with the grid regions.

The spectral energy distribution (SED) of both regions are also generated by performing the maximum likelihood fits in six logarithmically spaced band from 1 to 500 GeV. During each fit, the normalization of the sources overlapping on Vela SNR in the line of sight and also the Galactic and isotropic diffuse emission models were left free. The SEDs of both the northeast and southwest regions are shown in Figure 5.11 by red and blue plots, respectively. It is suggested that the spectrum of the entire Vela SNR is dominated by the gamma-ray emission from the northeast region in the low-energy band.

We verified on our results by varying the models of Vela Jr. and Puppis A, and adding a random fraction of unassociated sources inside the SNR to the background

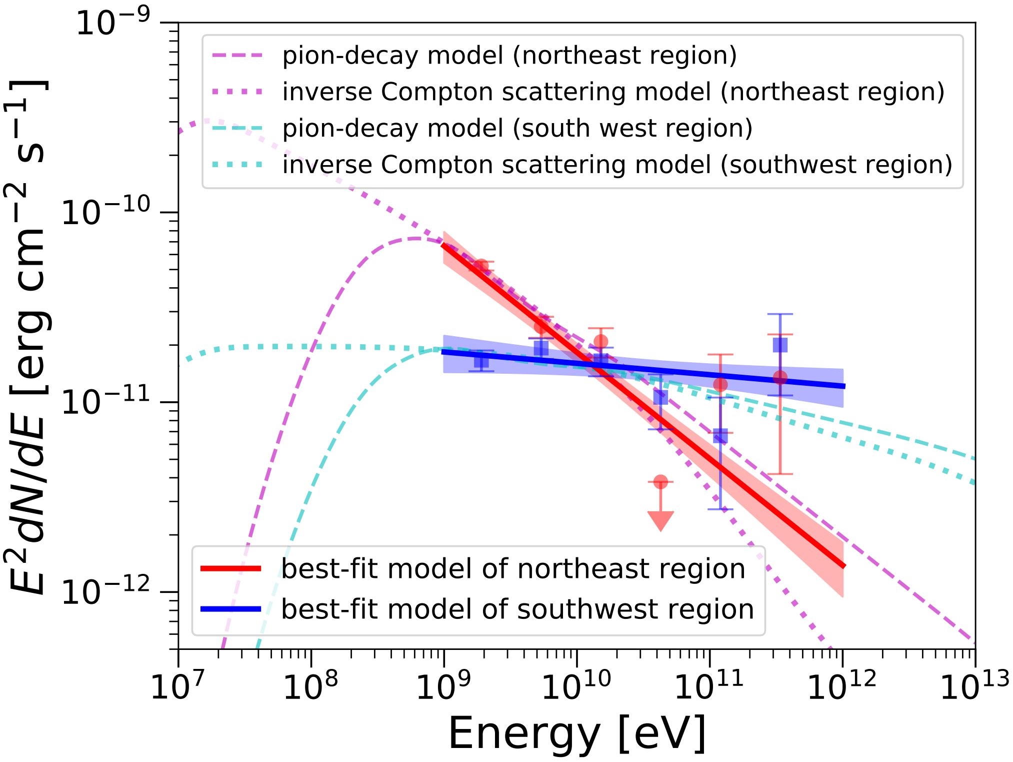

Figure 5.11. Spectral energy distributions (SEDs) of the northeast and southwest regions with six bins in the energy range of $1-500$ GeV. Statistical uncertainties are shown by error bars. Where the detection of each bin is not significant (TS<4), an upper limit is shown at the 95% confidence level. Red and blue solid lines represent the best-fit power-law model of the northeast and southwest regions, respectively. Hatches show the statistical uncertainties of the best-fit models. Cyan and magenta lines show the results of modeling of gamma-ray radiation mechanisms in the northeast and southwest regions, respectively. Pion-decay and inverse Compton scattering models are represented by dashed and dotted lines, respectively.

model. The impact of the template size of Vela Jr. and Puppis A was examined by changing the size by $\pm 3\sigma$ errors of their size listed in the FGES catalog (Ackermann et al., 2017). The impact of the uniform distribution template of Vela Jr, and Puppis A was examined by changing the uniform disk template to X-ray distribution for Puppis A and TeV gamma-ray distribution for Vela Jr. (H.E.S.S. Collaboration et al., 2018a). The spectral parameters and SEDs of the northeast and southwest regions show consistent results with the aforementioned results though the parameters of the grid regions overlapping these extended sources are influenced. At the position of these extended sources, the gamma-ray image shown in Figure 5.10 could be affected by the impact of the templates. To test the impact of exclusion of all unassociated sources, the same analysis were performed with 10 different background model, in which randomly chosen unassociated sources remained inside the SNR to make the number density of 0.1 degree^{-1} that is comparable to those of around Vela SNR. The spectral parameters and SEDs of both regions are consistent with the average results of these ten trials. The results of these tests are shown in Figure 5.12.

5.3.3 Spectral analysis of the entire Vela SNR

We performed a spectral analysis of the entire Vela SNR in the energy range of 1- $-$ 1000 GeV using the same procedure as used for the spectral analysis of the. northeast and southwest regions. We obtained the flux $f = (3.7 \pm 0.2) \times 10^{-8}\ \text{cm}^{-2}\ \text{s}^{-1}$ in the energy range of $1 - 500$ GeV and photon index $\Gamma = 2.34 \pm 0.04$. The energy flux and luminosity (assuming the distance of 287 pc) integrated between 1 and 500 GeV were $(2.07 \pm 0.12) \times 10^{-10}\ \text{erg cm}^{-2}\text{s}^{-1}$ and $(2.04 \pm 0.12) \times 10^{33}\ \text{erg s}^{-1}$, respectively. The best-fit model is indicated by black solid line in Figure 5.13. We generated the SED by performing maximum likelihood fits in 12 logarithmically spaced bands from 1 to 500 GeV (shown in Figure 5.13 by black plots).

In Figure 5.13, the SED plots have larger values that those of the best-fit model in the energies greater than $\sim$ 100 GeV. This suggests that Vela SNR has a harder spectrum in the high-energy band. We performed a spectral analysis in the energy range of $100 - 1000$ GeV. The normalization of the sources overlapping with Vela SNR and normalization of the Galactic and isotropic diffuse emission models were left free. The spectral parameters of the other sources were fixed to the best-fit values of the $1 - 1000$ GeV fit because of the poor statistics in the high-energy band. We obtained the TS=47.9 and the photon index $\Gamma = 1.5 \pm 0.4$. The flux integrated between 100 and 500 GeV was $(1.4 \pm 0.4) \times 10^{-10}\ \text{cm}^{-2}\text{s}^{-1}$. The best-fit spectrum is shown in Figure 5.13 by the light-gray dashed line. This hard gamma-ray spectrum could not originate from Vela X because of the exclusion of the Vela X region from the template for Vela SNR. There is a possibility of contamination from the TeV gamma-ray source Vela Jr. We investigated this using a template in which the Vela Jr. region was excluded. In this case, we obtained a spectrum with a photo index of 1.5 ± 0.4 and the flux of $(1.3 \pm 0.4) \times 10^{-10}\ \text{cm}^{-2}\text{s}^{-1}$ in the energy range of $100 - 500$ GeV. This

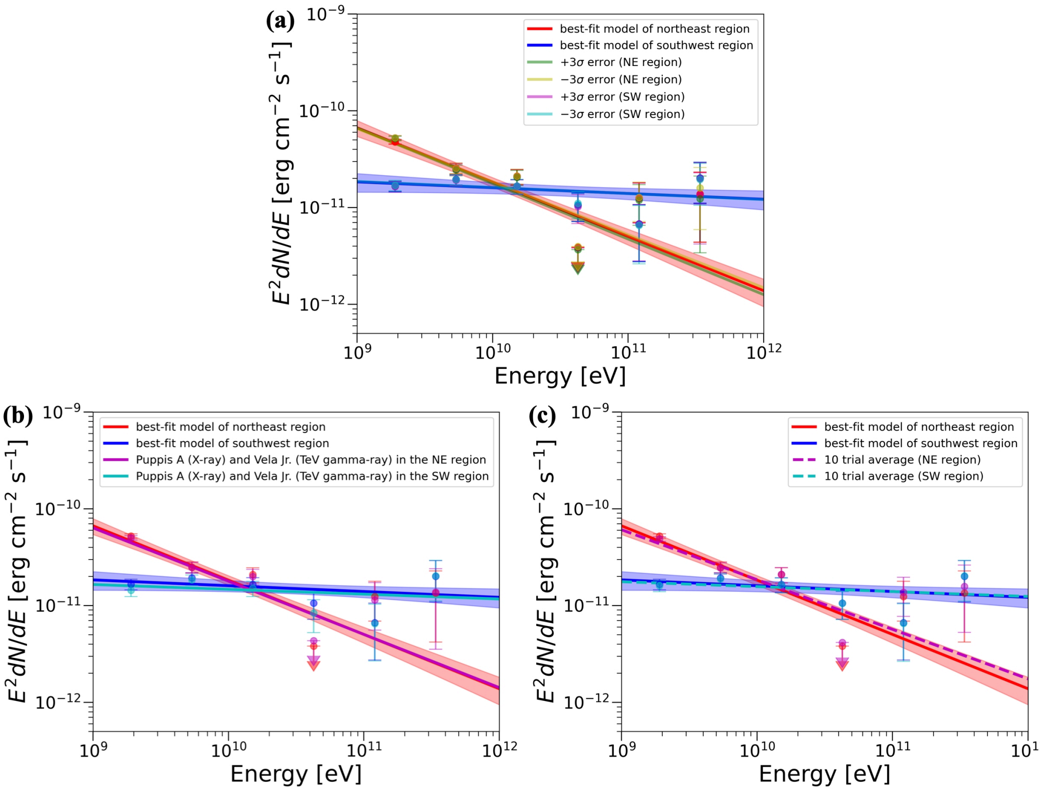

Figure 5.12. Best-fit spectrum and SED of the northeast and southwest regions compared with different models. (a) Impacts of the template size of Vela Jr. and Puppis A. Green (northeast) and magenta (southwest) lines represent the results of the models with template sizes of $+3\sigma$ errors. Yellow (northeast) and cyan (southwest) lines represent the results of the model with template sizes of -3σ errors. (b) impact of the template profile of Vela Jr. and Puppis A. Magenta (northeast) and cyan (southwest) lines represent the results of the model with their profile of X-ray and TeV gamma-ray distribution. (c) Impact of exclusion of all unassociated sources inside the Vela SNR region. Magenta (northeast) and cyan (southwest) lines represent the 10-trial average results of the models with some randomly chosen unassociated sources remained inside the Vela SNR region.

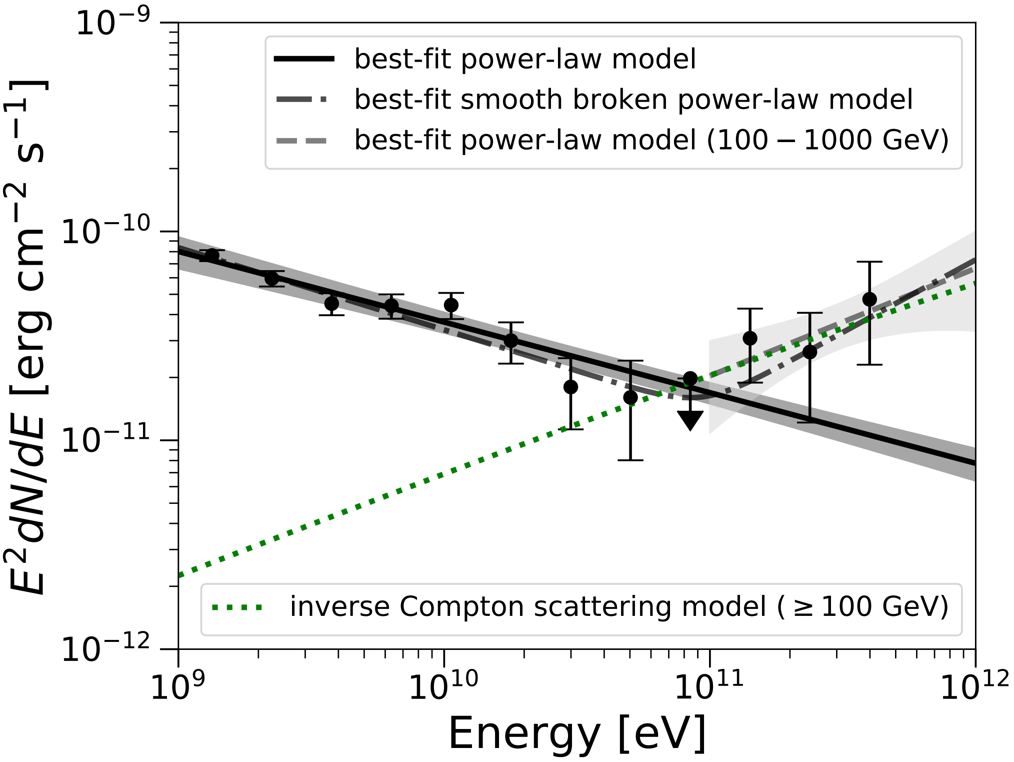

Figure 5.13. SED of the entire Vela SNR with 12 bins in the energy range of 1- − 500 GeV. Statistical uncertainty is indicated by error bars. Where the detection of each bin is not significant (TS<4), an upper limit is shown at the 95% confidence level. The Black line represents the best-fit power-law model of Vela SNR. The Light-gray line shows the best-fit power-law model of the entire Vela SNR with energy greater than 100GeV. The Dark-gray dash-dotted line represents the best-fit smoothly broken power-law model of Vela SNR. Hatched areas represent the statistical uncertainty of the best-fit models. The Green dotted line represents the result of modeling above 100 GeV with inverse Compton scattering.

results indicate that the hard spectrum does not originate from Vela Jr., and suggests that Vela SNR is a TeV gamma-ray source candidate.

The significance of the spectral break was derived by comparing the likelihoods between power-law and power-law with a break E_b spectra. We performed a binned maximum fit in the energy range of $1 - 1000$ GeV assuming a smoothly broken power-law spectrum in the form of

$$\frac{dN}{dE} \propto E^{-\Gamma_1} \left(1 + \left(\frac{E}{E_b} \right)^{\frac{\Gamma_1 - \Gamma_2}{\beta}} \right)^{\beta}, \tag{5.1}$$

where Γ_1 and Γ_2 are the indices below and above E_b, respectively. The parameter β, which determines the smoothness of the spectrum, was fixed to 0.2. The best-fit model with $\Gamma_1 = 2.39 \pm 0.04$, $\Gamma_2 = 1.31 \pm 0.36$, and $E_b = 92.9 \pm 35.9$ GeV is indicated by the dark-gray, dash-dotted curve in Figure 5.13. The spectral model with a break is preferred at 3.3σ corresponding to TS=13.8 for two additional degrees of freedom (E_b and Γ_2)[4]. This is consistent with the finding of the hard spectrum above 100 GeV in the spectral analysis in this section.

Since the gamma-ray spectrum in the LAT data analysis is almost determined by data below a few tens of GeV with good statistics, the presence of the break does not considerably affect the results of the northeast and southwest regions in Section 5.3.2. When we performed a spectral analysis of the northeast and southwest regions in the energy range of $1 - 30$ GeV, the results are consistent with those in Section 5.3.2. The photon indices of the northeast and southwest are 2.61 ± 0.07 and 2.03 ± 0.08, respectively. The best-fit spectra are within the uncertainties of spectra of the northeast and southwest, as shown in Figure 5.14. In addition, neither the northeast nor southwest regions showed a significant spectral break in the energy range of $1 - 1000$ GeV.

As in the spectral analysis of the northeast and southwest regions in Section 5.3.2, we performed the analysis with alternative assumptions about the templates of Vela Jr. and Puppis A, and inclusion of some unassociated sources in the background model. In all cases, we obtained similar results (see Figure 5.15). The results with the map cube template were also compared with a uniform template that has the same spatial size and only the profile was changed to uniform. We obtained consistent results when uniform templates were used to analyze the spectra of the northeast (photon index: 2.60 ± 0.07 and flux: $(2.8 \pm 0.1) \times 10^{-8}$ cm^{-2}s^{-1}) and southwest regions (photon index: 2.01 ± 0.06 and flux: $(0.9 \pm 0.1) \times 10^{-8}$ cm^{-2}s^{-1}). While the photon index of 2.29 ± 0.05 and flux of $(3.1 \pm 0.2) \times 10^{-8}$ cm^{-2}s^{-1} were obtained by using the uniform template for the entire SNR. The best-fit spectra and SED of the entire SNR is shown in the left panel of Figure 5.17. The relatively lower flux compared with the map cube template might be caused by the energy-dependent

---

[4] The value of β does not impact the significance of the spectral break. The significance of more than 3σ was also obtained when the value of β changed to 0.1 and 0.3.

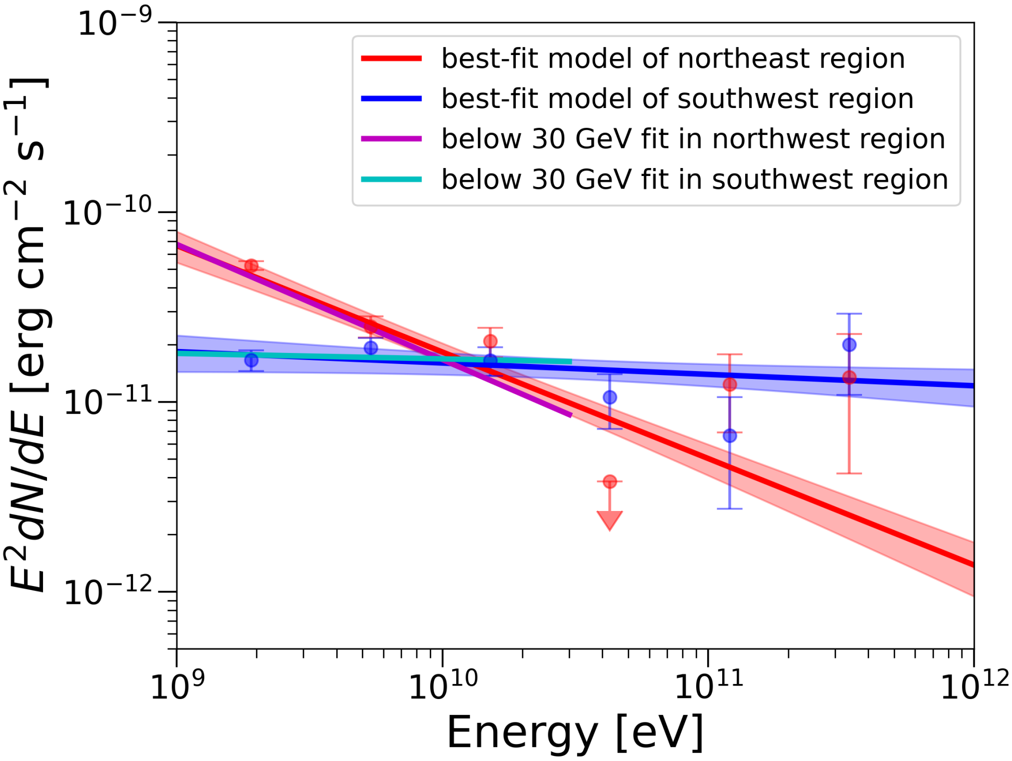

Figure 5.14. Best-fit gamma-ray spectra of the northeast (magenta) and southwest (cyan) regions in the energy range of $1 - 30$ GeV. Broad-band spectra and SEDs are same as those in Figure 5.11.

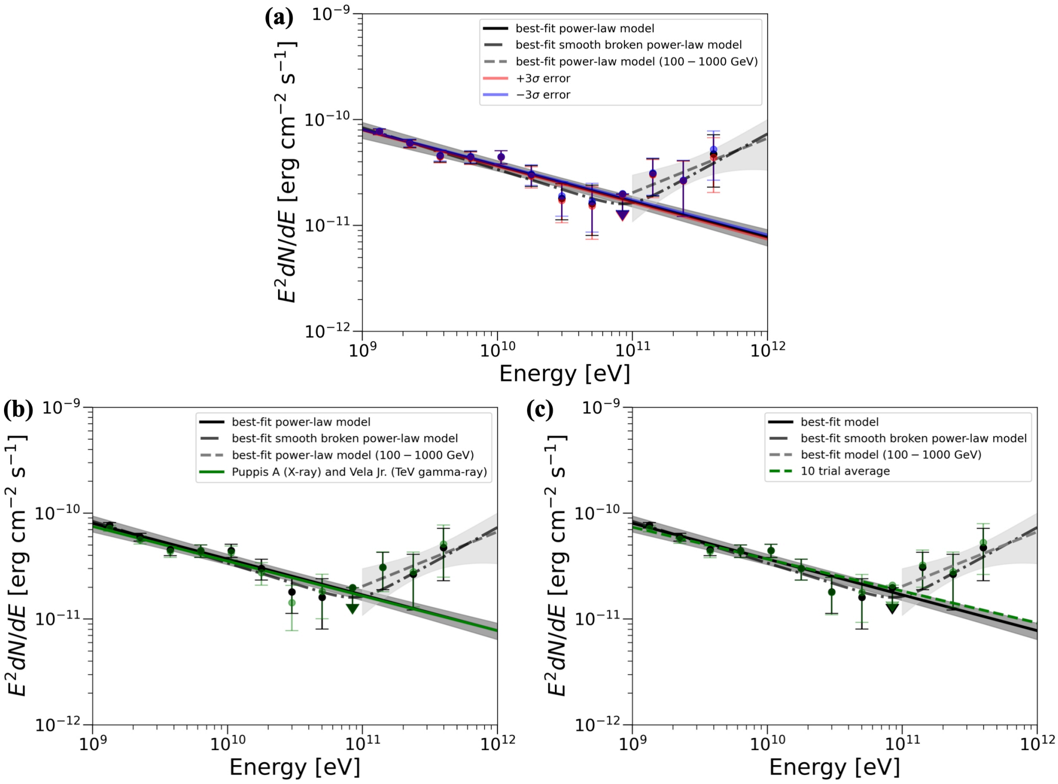

Figure 5.15. (a) Impacts of the template size of Vela Jr. and Puppis A. The red line represents the results of the models with template sizes of 3σ errors. The blue line represents the results of the model with template sizes of -3σ errors. (b) impact of the template profile of Vela Jr. and Puppis A. The green line represents the results of the model with their profile of X-ray and TeV gamma-ray distribution. (c) Impact of exclusion of all unassociated sources inside the Vela SNR region. The green lines represent the 10-trial average results of the models with some randomly chosen unassociated sources remained inside the Vela SNR region.

spatial distribution of brightness in the northeast and southwest regions.. As shown in Figure 5.11, the distribution has gradient in the low-energy band ($\lesssim$ 10 GeV), i.e., the northeast region is brighter than the southwest region. In high-energy brand ($\gtrsim$ 10 GeV), the distribution seems to be close to flat. The bright emission from the northeast region is difficult to assess with uniform template in the low-energy band. We considered that the energy-dependent distribution could be reproduced well with the map cube template.

5.3.4 Comparison with X-ray band

Our spatially resolved analysis revealed the brightness distribution inside Vela SNR in GeV gamma-ray band. Sushch, Hnatyk, and Neronov (2011) suggested the asymmetry of the gas density inside the SNR to explain the asymmetry of the brightness distribution in the X-ray band. The flux map in Figure 5.8 exhibits a similar asymmetry in the gamma-ray band.

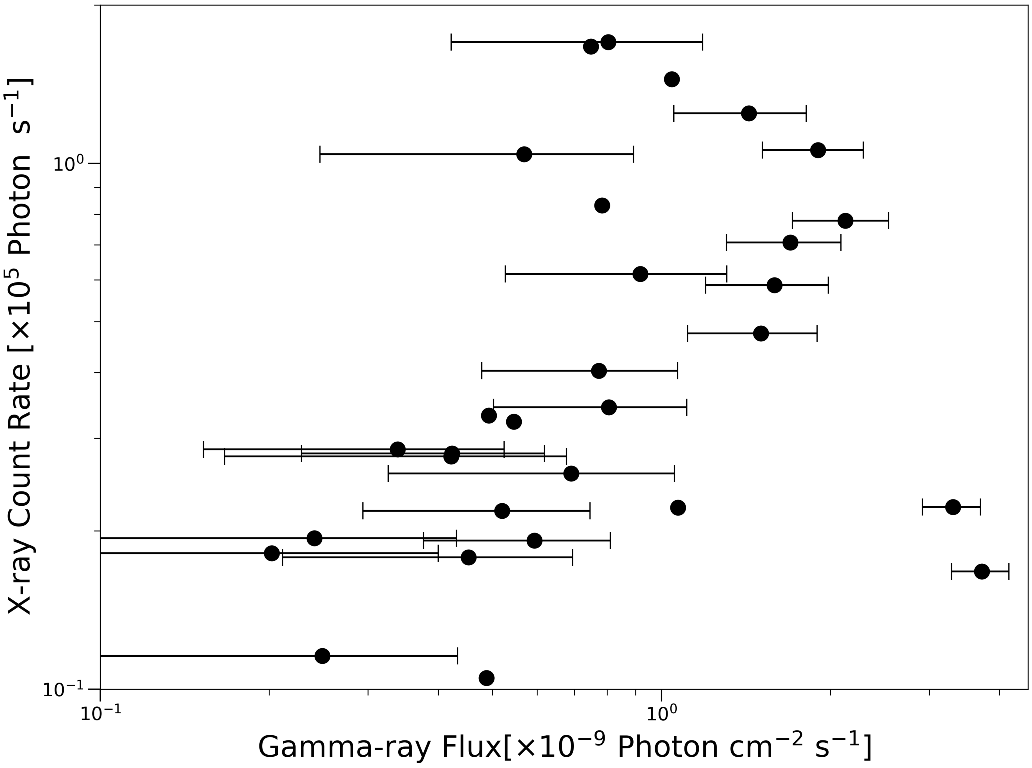

Figure 5.16. Relation between X-ray count rate and gamma-ray flux in the energy range of 1 − 500 GeV of each grid region. Grid regions overlapping other diffuse gamma-ray sources (Vela Jr., and Puppis A) are not shown. Plots without error bars represent the grid regions with the spectral parameters fixed to the results of all-phase data analysis.

The grid regions, which do not show significant gamma-ray emission, coincided with the dim region of Vela SNR in the X-ray band except for the regions overlapping with other gamma-ray sources (see white crosses in the maps of Figure 5.8). Figure 5.16 shows the scatter plot of the X-ray count rate and gamma-ray flux of each grid region. The grid regions with relatively low gamma-ray flux ($\sim 1 \times 10^{-9}$ cm^{-2}s^{-1}) and very high X-ray count rate is located on the north of Vela SNR (e.g., Grid reg 06, 07, and 08). The bright grid regions (Grid reg 04 and 18) in the gamma-ray band plotted at approximately 3.5×10^{-9} cm^{-2}s^{-1} are located at the northeast boundary of Vela SNR. Interaction between Vela SNR and the ISM have been reported in the northeast region (Dubner et al., 1998; Moriguchi et al., 2001). This indicates that the gamma-ray emission extends beyond the northeast boundary in the X-ray band or the contamination of the Galactic diffuse emission.

We performed the spectral analysis with a template created by X-ray emission (0.1 − 0.4 keV) observed by *ROSAT*. The soft X-ray is chosen by avoiding the emission of Vela Jr. and Puppis A. The spatial size of the template is the same as the map cube template and uniform template described in Section 5.3.3, but the profile in the analysis region instead follows the X-ray distribution. The map cube template and

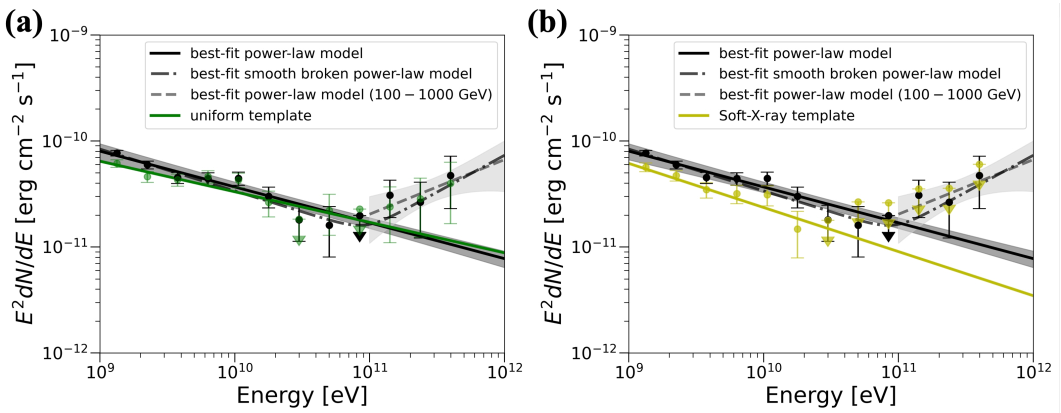

Figure 5.17. Best-fit spectra and SEDs of the uniform (a) and soft X-ray (b) templates. (a) The green line and plots represent the results of uniform template. (b) The yellow line and plots represent the results of soft X-ray template.

uniform template were preferred with TS of 426 and 125, respectively. In this case, we obtained a softer spectrum with a photon index of 2.42 ± 0.06 and lower flux $(2.7 \pm 0.2) \times 10^{-8}$ cm^{-2}s^{-1} in the energy range of $1 - 500$ GeV. The best-fit spectra and SED are shown in the right panel of Figure 5.17. The X-ray emission could not reproduce the energy-dependent spatial distribution well. The GeV gamma-ray distribution become flat in the energy $\gtrsim$ 10 GeV as shown in Figure 5.11. Figure 5.16 also shows that there are grid regions that are bright in the GeV gamma-ray band but dim in the X-ray band, and vice versa.

5.4 Discussion

SNRs are the important accelerators of Galactic cosmic rays. Observational evidence of the accelerated electrons at TeV energies was given by the discoveries of the synchrotron X-ray emission from young shell-type SNRs (e.g., Koyama et al., 1995; Koyama et al., 1997; Slane et al., 1999; Slane et al., 2001). The detection of the characteristic pion-decay feature in the gamma-ray spectra of middle-aged SNRs with the *Fermi*-LAT has provided evidence that cosmic-ray protons are accelerated in SNRs (e.g., Ackermann et al., 2013; Jogler and Funk, 2016; Abdollahi et al., 2022).

Current precise cosmic-ray observations revealed anomalies associated with electrons and positrons. The observed data show softening of the spectrum of electrons and positrons at $\sim$ 0.9 TeV (Aharonian et al., 2009; DAMPE Collaboration et al., 2017) and an excess of the cosmic-ray positrons (Adriani et al., 2009; Aguilar et al., 2013). A recent study by Ding et al. (2021) revealed that a model with a nearby PWN and a nearby SNR is the most favored to explain the anomalies of electrons and positrons. Because of its favored distance and age, the Vela SNR is one of the possible candidate SNRs, containing the PWN Vela X inside it. We found the spatially extended gamma-ray emission at the location of Vela SNR. We discuss how high total and maximum energies of electrons can be expected from our results, assuming the gamma-ray emission is radiated by the Vela SNR.

High-energy particle radiate gamma rays via several mechanisms. Accelerated protons produced gamma rays via neural pion (π^0) decay, which is a byproduct of the interaction of high-energy protons and the ambient medium. Accelerated electrons also generate gamma rays by the inverse-Compton (IC) scattering of low-energy photons. Interactions between the ISM and Vela SNR have been reported in the northeast region (Dubner et al., 1998; Moriguchi et al., 2001). Sushch, Hnatyk, and Neronov (2011) has also reported the density gradient inside Vela SNR base the asymmetry of brightness distribution in the X-ray band. The northeast region could be denser than the southwest region because of the stellar bubble created by the Wolf-Rayet star in the γ^2Velorum system. These previous results suggest that the dominant mechanism of gamma-ray radiation differs from region to region inside the Vela SNR. We found various spectra with photon indices of $1.5 - 3.0$ using spatially resolved analysis with the small grid regions. This indicates that the gamma-ray spectra were not uniform inside Vela SNR.

In the southwest region, some ($\sim 33\%$) grid regions represent hard spectra with photon indices of $1.5 - 2.0$. These hard gamma-ray spectra are consistent with the theoretically expected IC spectra ($\alpha_e = 2\Gamma - 1$) from an electron spectrum with a spectral index of $\alpha_e = 2.0 - 3.0$ in the current energy range. A proton spectrum with spectral index less than two is needed to reproduce the hard gamma-ray spectra with π^0-decay mechanism. It is difficult to obtained an index of less than two with the standard acceleration mechanism of DSA. The ISM density of the southwest region is predicted to be lower than that of the northeast region. This suggests that high-energy electrons emit gamma rays in these region via the IC mechanism, A recent study by Eagle et al. (2019) revealed the soft X-ray emission at the position of 2FHL J0826.1$-$4500, which is located in the west region of the Vela SNR and detected above 50 GeV with a hard spectrum (photon index $\Gamma \sim 1.6$). This gamma-ray source is located in Grid reg 24 in our work, and the consistent hard spectrum with a photon index of ~ 1.5 is obtained by the spatially resolved analysis. The possibility of the shock-cloud interaction is suggested using the multi-wavelength results in this region (Eagle et al., 2019).

As shown in Figure 5.8, the regions with hard spectra are dimmer compared with other regions. It is difficult to obtain particle spectra from each grid region. We revealed the different spatial distributions of the photon index and gamma-ray flux in the northeast and southwest regions. This allowed us to estimate the spectra of the accelerated particles using the gamma-ray spectra obtained from both the northeast and southwest regions.

We simply modeled the gamma-ray SEDs of the northeast and southwest regions, assuming a power-law particle spectrum:

$$\frac{dN_i}{dE} \propto E^{-\alpha_i}, \tag{5.2}$$

where $i = e$ or p denote the particle spectra of electrons and protons, respectively. α_i is the power-law index index of the particle distribution. We modeled the gamma-ray spectra with the IC and π^0-decay mechanisms assuming that each process is dominant. We used `anima`, which is a radiative code with Markov Chain Monte Carlo fitting routine (Zabalza, 2015) to derive the particle spectrum from the SEDs (Kafexhiu et al., 2014; Khangulyan, Aharonian, and Kelner, 2014). For seed target photons of the IC mechanism, we considered the cosmic microwave background, far-infrared (FIR) background with a temperature of 30 K and energy density of 0.2 eV cm^{-3}, and near-infrared (NIR) background with a temperature of 3000 K and energy density of 1 eV cm^{-3}, following H. E. S. S. Collaboration et al. (2019). The number density of the target matter is assumed to be 1 cm^{-3} in the π^0-decay mechanism. The results of the spectral index and total energy are summarized in Table 5.3, and the corresponding spectra are shown in Figure 5.11.

In the northeast region, the amount of total energy of electrons becomes quite high ($\sim 10^{49}$ erg) when the IC is assumed to be dominant. In addition, the photon index ($\Gamma_{\mathrm{NE}} = 2.56 \pm 0.06$) obtained in $1 - 1000$ GeV is inconsistent with the one expected from radio continuum emission from Vela Y and Vela Z, $\Gamma \sim 1.7$ (Alvarez et al., 2001). On the other hand, the modeling with π^0-decay mechanism requires particle index of 2.61 ± 0.07 in reasonable agreement with the radio spectral index for Vela Y and Z. Also, the total energy of accelerated protons less than 10^{50} erg can be accounted by assuming that 10% of the explosion kinetic energy is transferred to the accelerated protons. In addition, the radiation mechanism of π^0 decay is supported by the interactions with the ISM in the northeast region (Dubner et al., 1998; Moriguchi et al., 2001).

In the southwest region, the gamma-ray spectrum can be explained either the IC or π^0-decay mechanism in terms of energy. Given that there are several regions where the photon indices are <2 in the southwest region as shown in Figure 5.9, the IC mechanism can explain these hard components more reasonably than π^0-decay process. With more observational multi-wavelength data available, such as radio continuum, the radiation mechanism cab be estimated in more detail.

We obtained a hard gamma-ray spectrum with a photon index of 1.5 ± 0.4 for energies greater than 100 GeV. The hard gamma-ray spectrum is explained by the IC mechanism with a reasonable amount of the total energy listed in Table 5.3. In calculating the total energy, the index of electron spectrum is chosen to be 2.0 since the obtained index of the photon spectrum is ~ 1.5, which is close to a frequently-used value in the context of particle acceleration. As a result, in the IC mechanism , the maximum energy of the electrons can be at least a few TeV or higher. It would

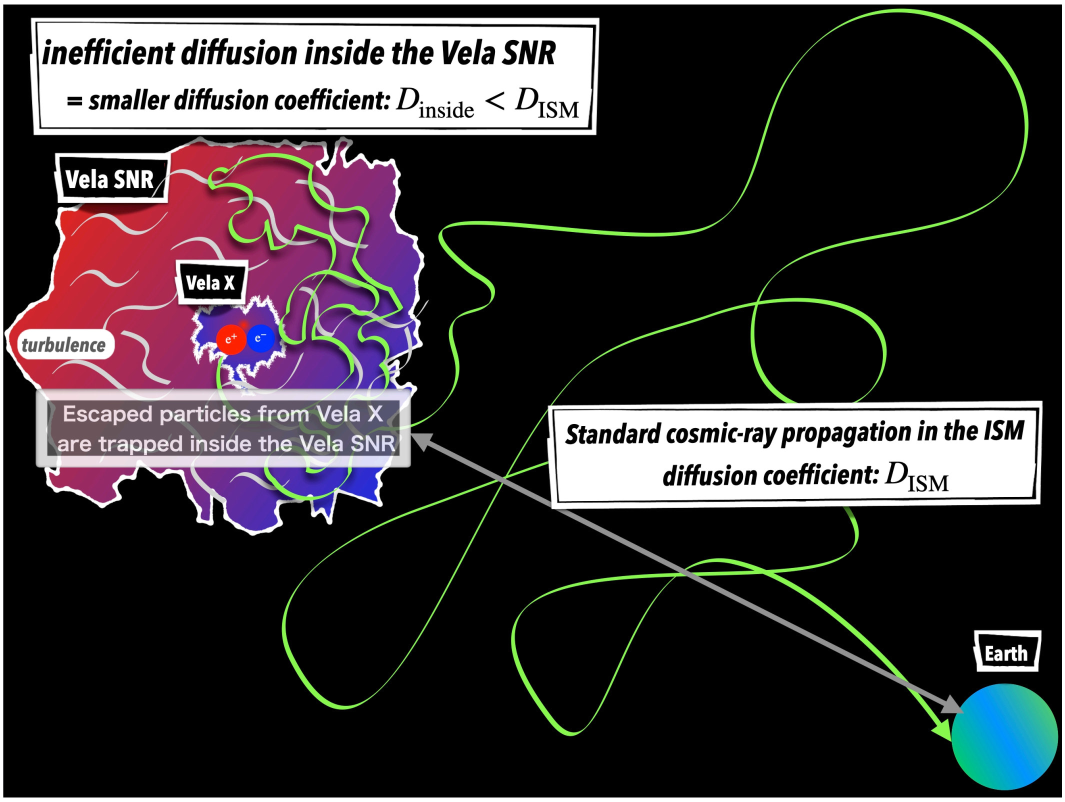

Figure 5.18. Schematic image of the origin of the high-energy electrons inside the Vela SNR.

be difficult to accelerate electrons up to such high energies at outer shock waves of a middle-aged SNR. It is plausible that the electrons and positrons from the PWN (i.e., Vela X) are trapped inside the Vela SNR (Huang et al., 2018), emitting gamma rays via the IC mechanism. A schematic image of this idea is shown in Figure 5.18. A more detailed analysis over multiple wavelength and future advanced missions could improve our understanding of the origin of the component.

Table 5.3: Results of gamma-ray radiation mechanism modeling of the Vela SNR

Region	Model	Particle Spectral Index $\alpha_{e,p}$	Total Energy (1 GeV − 10 TeV) $W_{e,p}$ (erg)	Total Energy (10 GeV − 10 TeV $W_{e,p}$ (erg)
northeast	Inverse Compton scattering	$3.68^{+0.35}_{-0.18}$	$\left(5.34^{+7.66}_{-2.04}\right) \times 10^{49}$	$(1.11 \pm 0.10) \times 10^{48}$
	π^0 decay	2.61 ± 0.07	$\left(2.89^{+0.39}_{-0.34}\right) \times 10^{49}$	$(6.91 \pm 0.48) \times 10^{48}$
southwest	Inverse Compton scattering	$2.96^{+0.09}_{-0.08}$	$\left(2.64^{+1.06}_{-0.75}\right) \times 10^{48}$	$\left(2.88^{+0.44}_{-0.43}\right) \times 10^{47}$
	π^0 decay	2.22 ± 0.06	$\left(7.41^{+0.86}_{-0.75}\right) \times 10^{48}$	$\left(3.98^{+0.37}_{-0.40}\right) \times 10^{48}$
whole (above 100 GeV)	Inverse Compton scattering	2.0 (fixed)	$\left(2.47^{+0.83}_{-0.92}\right) \times 10^{46}$	$\left(1.86^{+0.62}_{-0.69}\right) \times 10^{46}$

NOTE - The cosmic microwave background is assumed to be the seed photon of the inverse Compton scattering.
A number density of 1 cm^{-3} was also assumed as the density of the target matter.

Chapter 6

X-ray hotspots in the northwest region of RX J1713.7$-$3946

6.1 Overview

RX J1713.7$-$3946 is one of the best-studied accelerators of cosmic rays because of its strong non-thermal X-ray and gamma-ray radiation. We have analyzed accumulated *Chandra* observations with a total exposure time of $\sim$ 266 ks in the northwest rim of RX J1713.7$-$3946. We detected a substantially large number of point-like sources, referred to "hotspots", which are likely associated with the SNR. The spectra of the hotspots are well described by an absorbed power-law model. The spectral properties are different from diffuse X-ray emission in RX J1713.7$-$3946, and the harder hotspot tends to have the larger N_{H}. Yearly and monthly time variabilities are confirmed for some hotspots. We proposed that RX J1713.7$-$3946 is embedded in a complex surroundings where some dense molecular clumps and cores exists inside a wind-blown cavity, and that the hotspot traces synchrotron emission caused by an interaction of shock waves of the SNR and dense molecular cores with a number density of $10^5 - 10^7$ cm^{-3}. The X-ray radiation of the hotspots might be emitted both from primary electrons accelerated at the shocks and secondary electrons produced by the interaction of accelerated protons with the dense cores.

6.2 Observations and Data Reduction

The northwest region of RX J1713.7$-$3946 is observed with *Chandra* ACIS seven times from 2000 $-$ 2011 (Table 6.1). The total exposure time reached $\sim$ 266 ks, which allowed us to investigate relatively faint structures. Moreover, the seven-time observations over a span of 11 years, from 2000 $-$ 2011, enable us to explore year-scale variability. Taking advantage of the great angular resolution of *Chandra* and accumulated rich statistics, we performed a detailed analysis of small characteristic structures in the northwest rim of RX J1713.7$-$3946. All the data were reprocessed using `chandra_repro` with CALDB version 4.7.6 in Chandra Interactive Analysis of Observations (CIAO) version 4.9, provided by the Chandra X-Ray Center (CXC).

Table 6.1: Information of the *Chandra* observations.

Obs. ID	Target Name	Start Date (yyyy mm dd)	Pointing position ($\alpha[J2000], \delta[J2000]$)	(l, b)[b]	Exposure (ks)	A.D.[a] (arcmin)
736.	RX J1713.7−3946 NW	2000 Jul 25	$(17:11:49.9, -39:36:14.7)$	$(347.2660, -0.1121)$	29.6	···
5560	RX J1713.7−3946 NW	2005 Jul 9	$(17:11:45.5, -39:33:40.0)$	$(347.2923, -0.0752)$	29.0	···
6370	RX J1713.7−3946 NW	2006 May 3	$(17:11:46.3, -39:33:12.0)$	$(347.3001, -0.0728)$	29.8	···
10090	RX J1713.7−3946 NW	2009 Jan 30	$(17:11:44.4, -39:32:57.1)$	$(347.2999, -0.0654)$	28.4	···
10091	RX J1713.7−3946 NW	2009 May16	$(17:11:46.3, -39:32:55.7)$	$(347.3038, -0.0701)$	29.6	···
10092	RX J1713.7−3946 NW	2009 Sep 10	$(17:11:46.1, -39:33:51.6)$	$(347.3043, -0.0689)$	29.2	···
12671	RX J1713.7−3946 NW	2011 Jul 1	$(17:11:47.5, -39:33:41.2)$	$(347.2959, -0.0807)$	89.9	···
6721	CTB 37A	2006 Oct 7	$(17:14:35.8, -38:31:24.6)$	$(348.4558, +0.0879)$	19.9	70.3
14586	IC 4637	2014 Mar 7	$(17:05:10.5, -40:53:08.4)$	$(345.4794, +0.1403)$	29.6	109.8

[a] Angular distance from RX J1713.7−3946 NW with ObsID of 12671.

[b] Galactic coordinates (longitude l, latitude b) expressed in degrees.

6.3 Analysis and Results

6.3.1 Hotspots

A flux image at 0.5 − 7.0 keV of the northwest region of RX J1713.7−3946 is presented in Figure 6.1. The image was generated using `merge_obs` in CIAO, which combined all the observations of RX J1713.7−3946 listed in Table 6.1. We found many bright point-like sources, and conducted a detailed study to investigate the properties of these point-like structures.

65 sources were selected in the following procedure and defined them as "hotspots". First, point-like sources were systematically picked up using `wavdetect` in CIAO. In this process, we used a combined cont map in the range of 0.5 − 7.0 keV and a combined point-spread function (PSF) map that is weighted by an exposure time of each epoch. The `wavdetect` was ran with "wavelet scale" of 1 and 2, which is a parameter of a radius of the wavelet function (see Freeman et al., 2002, for details.). This results in the detection of 154 sources. Second, a criterion of the photon flux was set to be larger than 1.0×10^{-6} photon $\mathrm{cm}^{-2}\mathrm{s}^{-1}$, reducing the number of the detected sources to 65. The detection significance of these 65 sources was more than 4σ. Note that sources with photon fluxes smaller than the criterion value have limited statistics, causing large uncertainty in the spectral analysis. In this study, the detail properties of 65 hotspots were analyzed, hereafter labeled HS01−HS65. They are labeled in the order of their X-ray brightness. Their locations in the northwest rim of the SNR were shown in Figure 6.2, and the locations and properties (obtained below) are summarized in Table 6.2. Most of the hotspots were spatially consistent with the point-like sources, whereas some showed a slight spatial extension. Due to poor statistics, we could not confidently test their spatial extension.

Many hotspot were contained in the northwest shell of RX J1713.7−3946. Figure 6.3 illustrates the surface density of hotspot, i.e., summing the number of hotspot contained in "Shell reg", "Inner reg", and "Outer reg" shown in Figure 6.1, then divided by their areas. The radial widths of these regions are roughly $\sim 0.2^\circ$ (Shell reg), $\sim 0.1^\circ$ (Inner reg), and $\sim 0.1^\circ$ (Outer reg), assuming the center of the SNR being $(17^{\mathrm{h}}13^{\mathrm{m}}15^{\mathrm{s}}.2, -39^{\mathrm{d}}46^{\mathrm{m}}15^{\mathrm{s}}.6)$ (H.E.S.S. Collaboration et al., 2018b). The azimuthal

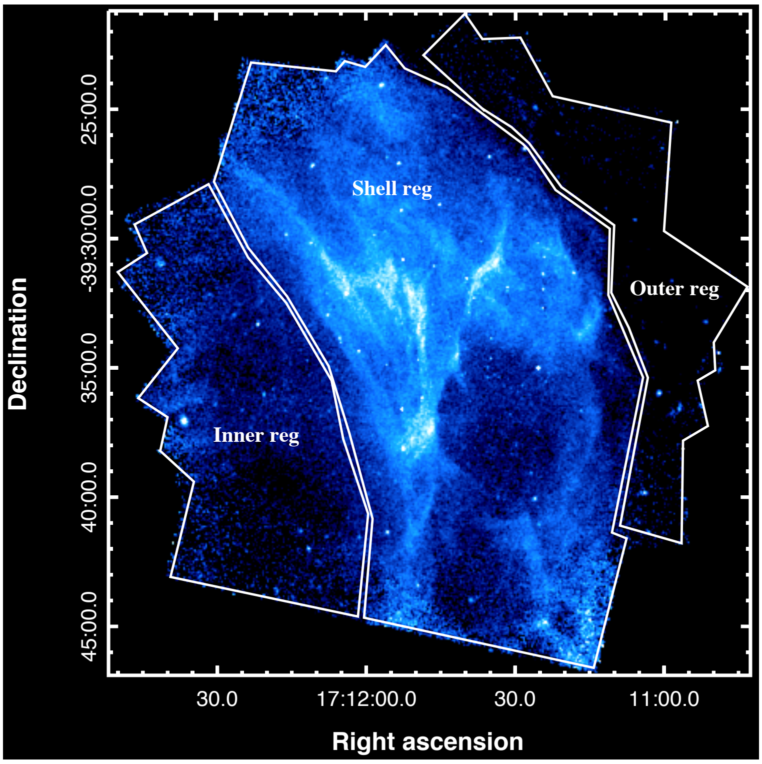

Figure 6.1. Combined flux image of the northwest region of RX J1713.7−3946 at 0.5−− 7.0 keV. Each pixel has a width of 1″. The three white regions indicate "Inner reg", "Shell reg", and " Outer reg".

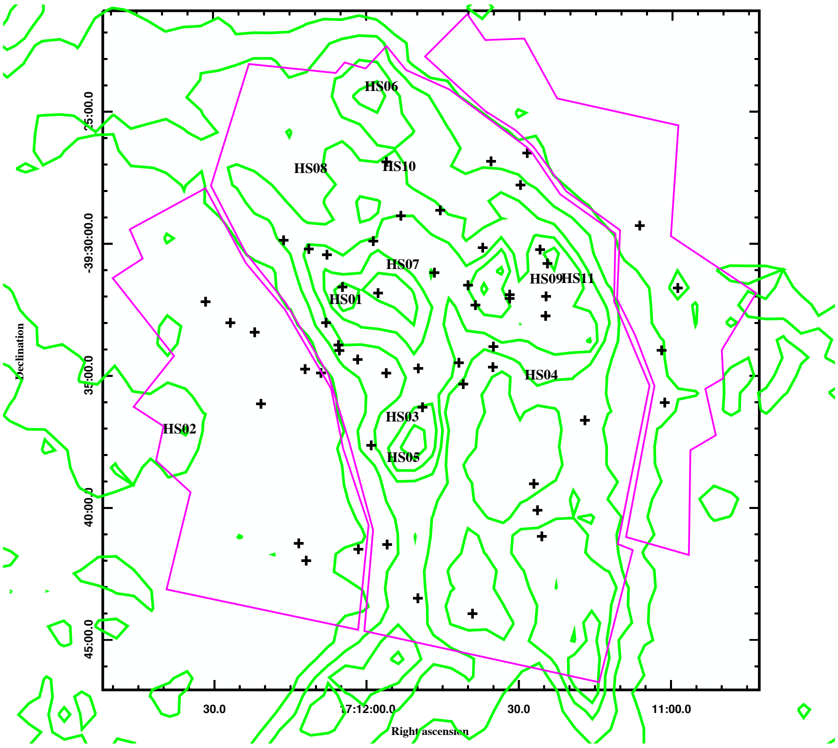

Figure 6.2. Location of HS01−HS65 in the northwest rim of RX J1713.7−3946. HS01−−HS11 (the top 11 brightest hotspot) are shown with their names, whereas the others are shown with black crosses. The contour is taken with XMM-Newton (0.5−8 keV), and the magenta regions are the same regions shown in Figure 6.1.

angle of these regions from the center is $\sim 60^\circ$. There is clearly an excess number of hotspots in the shell, which is one of the brightest regions in the whole SNR. Because the northwest part of RX J1713.7−3946 is located on the Galactic Plane, many X-ray sources likely exist both in the foreground and background. However we found that the number of hotspots is quite large in the northwest shell of RX J1713.7−3946, as follows. Same method of detecting hotspot was perform in other two regions in the vicinity of RX J1713.7−3946 observed with *Chandra*, namely SNR CTB 37A and the planetary nebula IC 4637[1]. They are $70.3'$and $109.8'$away from the northwest rim of RX J1713.7−3946 respectively, and located on the Galactic Plane as well (see Table 6.1). The surface density of the hotspots from these two observation are also shown in Figure 6.3, labeled as "CTB 37A" and "IC 4637". The population of the hotspots in the northwest shell of RX J1713.7−3946 suggests that the hotspots could be associated with the remnant.

We estimated the number of hotspots in the shell of the entire SNR. The average of the surface density obtained from CTB 37A and IC 4637 was $\sim$ 0.049 arcmin^{-2}, and used as background. Then the net surface density calculated from the two region of "Shell reg" and "Inner reg" was estimated to be 0.167 arcmin^{-2}. If the surface density is assumed to be uniform in the entire shell, simply described by an annulus with inner and outer radii of 0.2° and 0.5°, respectively, the number of hotspots in the entire shell of the SNR is estimated as $\sim$ 400.

---

[1] Note that the source-free region (i.e., outside the SNR CTB 37A) was extracted for the detection of point-like sources with the observation of CTB 37A.

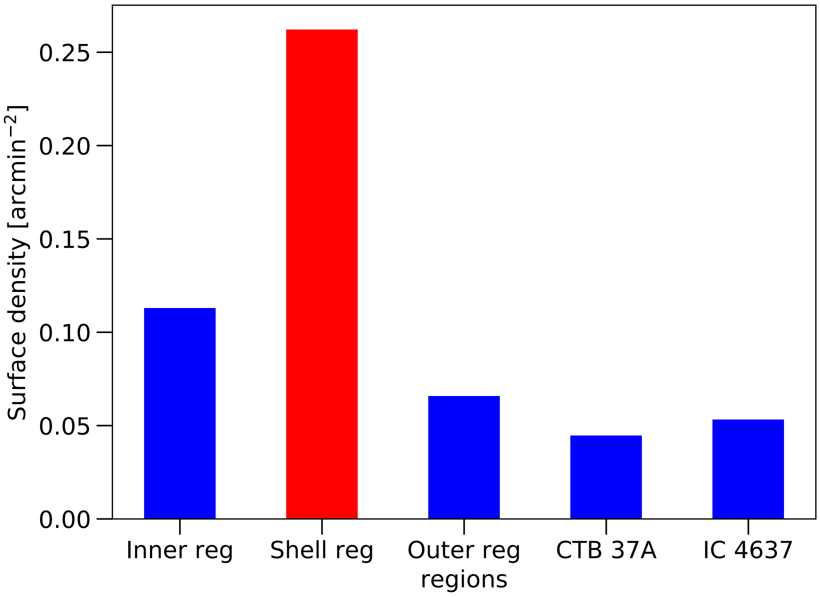

Figure 6.3. Surface density of hotspot in the northwest rim of RX J1713.7−3946 CTB 37A, and IC 4637. The northwest rim was divided into three regions, labeled Inner reg, Shell reg, and Outer reg, as shown in Figure 6.1.

Table 6.2: The summary of HS01−65.

HS ID	Position (α [J2000], δ [J2000])	Detection Significance (σ)	$N_{\rm H}$ (10^{22} cm^{-2})	Γ	Flux (min.) (10^{-14} erg cm^{-2} s^{-1})	Flux (max.) (10^{-14} erg cm^{-2} s^{-1})	χ^2/dof	Time Variability ($\geq 3\sigma$)
HS01	17:12:04.125, –39:32:10.859	73.4	$0.42^{+0.10}_{-0.08}$	$4.22^{+0.35}_{-0.30}$	$2.47^{+0.45}_{-0.91}$	$7.19^{+0.98}_{-0.94}$	315.1/289	Y
HS02	17:12:36.796, –39:37:05.230	19.5	$1.20^{+0.20}_{-0.18}$	$2.95^{+0.22}_{-0.20}$	$4.54^{+0.30}_{-0.60}$	$4.86^{+0.29}_{-0.43}$	76.4/92	N
HS03	17:11:52.997, –39:36:38.134	49.5	$0.33^{+0.16}_{-0.14}$	$3.84^{+0.53}_{-0.43}$	$1.17^{+0.33}_{-0.47}$	$3.59^{+0.23}_{-0.75}$	155.7/157	N
HS04	17:11:25.658, –39:35:02.662	58.5	$4.42^{+0.49}_{-0.45}$	$3.37^{+0.26}_{-0.24}$	$4.22^{+0.33}_{-1.01}$	$6.90^{+0.31}_{-1.10}$	188.8/186	YM
HS05	17:11:52.790, –39:38:09.992	26.9	$19.72^{+7.62}_{-5.94}$	$1.02^{+0.78}_{-0.67}$	$3.62^{+0.24}_{-1.43}$	$23.45^{+0.41}_{-7.85}$	145.2/172	Y
HS06	17:11:57.055, –39:24:07.441	14.1	$0.77^{+0.40}_{-0.29}$	$5.59^{+1.44}_{-1.03}$	$1.82^{+0.05}_{-0.89}$	$2.30^{+0.21}_{-1.10}$	67.3/79	N
HS07	17:11:52.863, –39:30:51.863	25.7	$0.38^{+0.27}_{-0.25}$	$2.57^{+0.48}_{-0.42}$	$0.52^{+0.16}_{-0.23}$	$1.83^{+0.31}_{-0.49}$	87.6/109	YM
HS08	17:12:10.965, –39:27:13.396	19.0	$0.72^{+0.30}_{-0.26}$	$1.91^{+0.28}_{-0.26}$	$0.85^{+0.23}_{-0.29}$	$3.39^{+0.28}_{-0.44}$	77.3/98	YM
HS09	17:11:24.721, –39:31:25.237	25.7	$28.41^{+10.38}_{-6.85}$	$2.30^{+1.27}_{-0.80}$	≤ 2.82	≤ 6.31	105.2/112	N
HS10	17:11:53.593, –39:27:09.311	17.6	$3.07^{+1.20}_{-0.97}$	$1.82^{+0.47}_{-0.43}$	$1.00^{+0.24}_{-0.53}$	$2.47^{+0.09}_{-0.78}$	68.6/77	Y
HS11	17:11:18.509, –39:31:23.079	15.6	≤ 0.56	$4.49^{+1.08}_{-0.84}$	$1.16^{+0.18}_{-0.99}$	$2.51^{+0.15}_{-1.72}$	71.7/96	Y
HS12	17:11:28.422, –39:26:34.798	16.6	$10.65^{+5.28}_{-4.30}$	$1.32^{+0.84}_{-0.77}$	$2.50^{+0.05}_{-1.48}$	$4.84^{+0.30}_{-2.73}$	46.2/56	N
HS13	17:12:21.943, –39:33:21.784	17.7	$1.31^{+0.57}_{-0.50}$	$2.17^{+0.45}_{-0.42}$	$0.67^{+0.25}_{-0.25}$	$2.90^{+0.44}_{-0.58}$	42.7/62	Y
HS14	17:11:40.029, –39:31:35.142	15.2	≤ 0.86	$3.41^{+1.42}_{-0.77}$	$0.38^{+0.15}_{-0.37}$	$1.06^{+0.26}_{-0.85}$	55.4/86	N
HS15	17:11:35.522, –39:26:53.704	15.2	≤ 0.73	$3.51^{+1.12}_{-0.70}$	$0.57^{+0.08}_{-0.41}$	$1.59^{+0.04}_{-0.88}$	50.8/52	N
HS16	17:12:07.920, –39:33:00.300	13.1	≤ 0.52	$2.29^{+0.66}_{-0.26}$	$0.43^{+0.29}_{-0.36}$	$2.73^{+0.08}_{-1.48}$	63.6/75	YM
HS17	17:11:53.219, –39:28:57.455	13.6	$3.61^{+2.53}_{-1.90}$	$1.36^{+0.82}_{-0.70}$	≤ 0.52	$2.92^{+0.46}_{-1.16}$	66.8/82	Y
HS18	17:12:11.875, –39:42:00.805	9.1	≤ 0.44	$1.39^{+0.42}_{-0.35}$	$0.42^{+0.25}_{-0.39}$	$2.09^{+0.04}_{-1.02}$	16.7/13	N
HS19	17:11:01.348, –39:36:01.349	11.6	$1.29^{+0.75}_{-0.59}$	$1.33^{+0.40}_{-0.37}$	$\cdots$	$8.13^{+0.42}_{-1.17}$	43.7/42	YM
HS20	17:11:45.483, –39:28:45.032	14.0	$6.16^{+7.70}_{-3.43}$	$0.56^{+1.17}_{-0.78}$	$0.94^{+0.54}_{-0.72}$	$2.90^{+0.27}_{-1.14}$	42.4/59	Y
HS21	17:11:24.699, –39:32:00.496	15.6	≤ 1.29	$1.87^{+0.69}_{-0.56}$	$0.67^{+0.32}_{-0.43}$	$1.60^{+0.29}_{-0.78}$	64.9/69	N
HS22	17:11:55.942, –39:41:24.307	14.0	$0.73^{+0.38}_{-0.32}$	$2.20^{+0.36}_{-0.32}$	≤ 0.27	$3.93^{+0.41}_{-0.59}$	42.1/50	Y
HS23	17:11:57.698, –39:31:53.047	9.0	≤ 1.01	$2.31^{+0.72}_{-0.59}$	≤ 0.38	$1.39^{+0.27}_{-0.60}$	87.6/104	Y
HS24	17:11:26.349, –39:40:06.366	11.6	$1.01^{+0.92}_{-0.81}$	$1.50^{+0.58}_{-0.54}$	$0.72^{+0.11}_{-0.24}$	$1.85^{+0.37}_{-0.63}$	34.2/52	N
HS25	17:12:01.715, –39:34:23.946	11.4	$7.78^{+7.79}_{-4.67}$	$1.16^{+1.31}_{-1.05}$	≤ 0.54	$3.34^{+0.62}_{-2.71}$	52.5/64	N
HS26	17:11:49.890, –39:43:26.415	7.1	≤ 3.02	$0.88^{+0.63}_{-0.57}$	≤ 0.47	$4.71^{+0.31}_{-1.23}$	26.8/29	N
HS27	17:11:31.848, –39:31:56.608	9.6	$1.89^{+1.95}_{-1.29}$	$1.59^{+0.95}_{-0.81}$	≤ 0.35	$1.51^{+0.12}_{-0.92}$	58.7/67	N
HS28	17:11:24.786, –39:32:44.837	10.9	≤ 1.21	$1.91^{+1.16}_{-0.61}$	≤ 0.20	$1.16^{+0.18}_{-0.70}$	34.0/49	N
HS29	17:11:39.132, –39:44:01.427	6.0	≤ 0.34	$2.30^{+0.86}_{-0.38}$	$0.74^{+0.03}_{-0.47}$	$0.78^{+0.01}_{-0.52}$	11.0/15	N

HS ID	Position (α [J2000], δ [J2000])	Detection Significance (σ)	$N_{\rm H}$ (10^{22} cm^{-2})	Γ	Flux (min.) (10^{-14} erg cm^{-2} s^{-1})	Flux (max.) (10^{-14} erg cm^{-2} s^{-1})	χ^2/dof	Time Variability ($\geq 3\sigma$)
HS30	17:12:20.736, –39:36:04.401	9.6	≤ 0.40	$2.84^{+1.13}_{-0.40}$	≤ 0.19	$1.39^{+0.60}_{-1.28}$	28.6/24	Y
HS31	17:11:48.976, –39:36:12.435	10.0	$13.65^{+10.55}_{-5.85}$	$2.22^{+1.66}_{-1.13}$	≤ 0.48	≤ 2.93	55.9/70	N
HS32	17:11:46.629, –39:31:06.732	9.3	…	…	…	…	−/−	N
HS33	17:12:16.244, –39:29:52.913	6.8	≤ 2.82	$2.43^{+1.78}_{-1.06}$	≤ 0.35	≤ 1.38	36.0/42	N
HS34	17:12:11.292, –39:30:12.754	6.9	≤ 0.43	$2.01^{+0.68}_{-0.30}$	≤ 0.12	$1.05^{+0.00}_{-0.47}$	63.2/72	Y
HS35	17:11:41.824, –39:34:31.392	8.8	≤ 1.05	$2.02^{+0.86}_{-0.56}$	≤ 0.25	$1.55^{+0.05}_{-0.83}$	43.6/50	N
HS36	17:11:35.140, –39:34:41.255	11.2	≤ 9.95	$-0.37^{+1.42}_{-1.19}$	$0.30^{+0.25}_{-0.28}$	$3.42^{+0.98}_{-1.79}$	29.0/31	N
HS37	17:12:01.602, –39:41:35.049	7.4	≤ 2.39	$2.66^{+1.25}_{-1.01}$	≤ 0.36	≤ 1.89	19.4/23	N
HS38	17:11:24.442, –39:30:45.768	7.8	$7.51^{+4.17}_{-6.19}$	≥ 3.01	≤ 0.02	≤ 0.73	44.7/53	N
HS39	17:12:05.302, –39:34:03.442	8.0	≤ 1.28	$2.59^{+2.15}_{-0.62}$	≤ 0.12	$0.52^{+0.01}_{-0.51}$	34.7/42	N
HS40	17:11:35.042, –39:33:54.616	9.3	$15.51^{+21.63}_{-14.96}$	$1.23^{+4.41}_{-2.53}$	≤ 0.55	≤ 1.63	31.8/39	N
HS41	17:11:25.888, –39:30:14.223	6.9	$2.90^{+4.80}_{-2.46}$	$4.26^{+3.90}_{-2.22}$	≤ 0.11	≤ 0.74	43.5/49	N
HS42	17:11:31.863, –39:32:05.315	7.4	≤ 1.99	≥ 2.88	≤ 0.06	≤ 0.10	51.2/50	N
HS43	17:11:06.326, –39:29:19.369	7.8	≤ 1.30	$1.10^{+0.84}_{-0.31}$	$0.97^{+0.04}_{-0.46}$	$1.34^{+0.13}_{-0.66}$	10.4/11	N
HS44	17:12:13.337, –39:41:21.576	4.9	≤ 6.98	$1.28^{+4.62}_{-0.79}$	…	≤ 1.10	2.8/2	N
HS45	17:12:04.689, –39:31:39.247	4.8	≤ 2.22	$0.58^{+2.78}_{-0.80}$	≤ 0.26	$0.99^{+0.48}_{-0.89}$	67.4/66	N
HS46	17:11:56.101, –39:34:54.946	7.8	…	…	…	…	−/−	N
HS47	17:11:56.054, –39:26:54.958	6.7	$2.59^{+3.47}_{-2.48}$	$2.48^{+1.93}_{-1.56}$	≤ 0.29	≤ 0.93	22.6/32	N
HS48	17:11:25.488, –39:41:05.711	5.6	$8.15^{+16.92}_{-7.02}$	$-0.01^{+2.21}_{-1.75}$	$0.60^{+0.05}_{-0.58}$	$1.98^{+0.20}_{-1.91}$	32.3/29	N
HS49	17:11:17.037, –39:36:41.864	7.9	≤ 4.56	$3.07^{+1.79}_{-1.35}$	≤ 0.35	≤ 1.72	10.8/24	NM[a]
HS50	17:12:31.583, –39:32:12.191	4.3	…	…	…	…	−/−	N
HS51	17:12:26.721, –39:33:00.127	5.9	≤ 0.47	$3.04^{+1.00}_{-0.54}$	≤ 0.33	≤ 0.71	13.3/20	N
HS52	17:11:27.062, –39:39:06.295	7.2	$11.99^{+16.59}_{-8.40}$	$2.70^{+3.06}_{-1.91}$	≤ 0.40	≤ 2.27	16.0/20	N
HS53	17:11:58.633, –39:29:54.987	5.2	$10.84^{+28.82}_{-8.51}$	≥ 0.16	≤ 0.45	≤ 8.29	38.3/49	N
HS54	17:12:05.491, –39:33:50.944	6.7	≤ 0.16	$1.86^{+0.59}_{-0.42}$	$0.37^{+0.11}_{-0.27}$	$0.79^{+0.18}_{-0.49}$	44.5/58	N
HS55	17:11:38.575, –39:32:20.384	5.7	…	…	…	…	−/−	YM
HS56	17:12:08.933, –39:34:54.495	7.3	…	…	…	…	−/−	N
HS57	17:11:37.148, –39:30:09.914	7.4	≤ 29.63	≥ -2.98	≤ 0.00	≤ 6.06	29.4/33	N
HS58	17:11:49.802, –39:34:44.236	9.0	…	…	…	…	−/−	N
HS59	17:11:59.065, –39:37:38.978	5.8	≤ 0.47	$1.60^{+0.75}_{-0.54}$	≤ 0.16	$0.50^{+0.04}_{-0.32}$	16.6/22	N
HS60	17:10:58.832, –39:31:40.962	6.6	…	…	…	…	−/−	N
HS61	17:11:29.741, –39:27:47.529	6.6	$3.14^{+2.86}_{-2.44}$	$4.77^{+4.44}_{-2.32}$	≤ 0.02	≤ 0.39	20.5/22	N
HS62	17:12:07.730, –39:30:25.835	5.5	≤ 16.01	≥ 4.47	≤ 0.22	≤ 1.15	39.7/46	N
HS63	17:12:12.049, –39:34:45.676	7.5	≤ 0.62	$2.40^{+1.81}_{-0.77}$	…	≤ 0.37	9.8/9	N

HS ID	Position (α [J2000], δ [J2000])	Detection Significance (σ)	N_{H} (10^{22} cm^{-2})	Γ	Flux (min.) (10^{-14} erg cm^{-2} s^{-1})	Flux (max.) (10^{-14} erg cm^{-2} s^{-1})	χ^2/dof	Time Variability ($\geq 3\sigma$)
HS64	17:11:40.961, –39:35:19.848	6.3	$10.29^{+10.36}_{-7.68}$	≥ 2.19	$\cdots$	≤ 0.23	12.3/15	YM
HS65	17:11:01.986, –39:34:02.649	6.5	≤ 3.21	$3.27^{+3.45}_{-1.53}$	$\cdots$	≤ 0.32	7.2/5	N

Note In the column density (N_{H}), photon index (Γ) and energy flux (min. and max.) columns, the errors and upper/lower limits indicate 1σ confidence. In the column of time variability, "1" represents time variability with more than 3σ and "0" with less than 3σ. In the time variability column, Y and M represent detection of time variation with more than 3σ on a year scale and a month scale, respectively, and N indicates non detection.

[a] Time variability of HS49 is not significant on a year scale, but is significant at more than 3σ on a month scale.

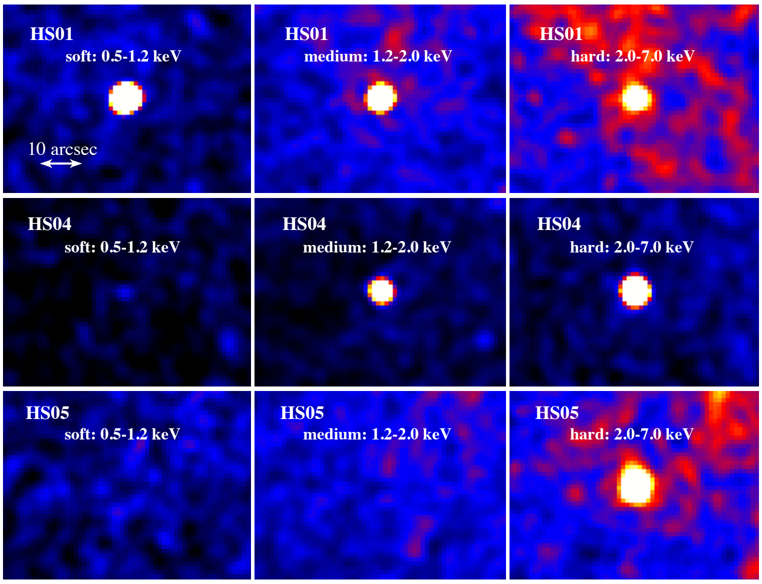

Figure 6.4. Flux images of the three hotspots (HS01, HS04, and HS05 from top to bottom), shown in the three energy bands of $0.5-1.2$, $1.2-2.0$, and $2.0-7.0$ keV from left to right.

6.3.2 Flux image

We produced flux images in three energy bands, $0.5-1.2$ keV (soft), $1.2-2.0$ keV (medium), and $2.0-7.0$ keV (hard). All seven epochs were combined with `merge_obs`, setting the bin size to 2 (i.e., one pixel corresponds to $1''$). The flux images of the three example hotspots (HS01, HS04, and HS05) are shown in Figure 6.4. As shown in the figure, various type of hotspot are observed: HS01 is bright in the broad band, whereas HS05 is dark in the soft and medium bands. This suggests that their spectra would also vary depending on the hotspots.

6.3.3 Spectral analysis

We performed spectral analysis of the hotspots. The spectrum of each hotspot was extracted from a circular region with a radius of $5''$ using `specextract` in CIAO. The background was extracted from an annulus region with inner and outer radii of $8''$ and $27''$, respectively. Both the source and background regions had the same central coordinate, which was detected by `wavdetect` in Section 6.3.1. XSPEC version 12.9.1 included in HEASoft version 6.21 was used in the following spectral analysis. The uncertainties in this section indicate 1σ.

An absorbed (TBabs in XSPEC; Wilms, Allen, and McCray (2000)) power-law model was used to fit the spectra. The spectra of the different epochs were jointly fitted: the parameters of the model (a photon index Γ and a column density of interstellar absorption N_{H}) were tied with the all spectra and left the normalization free for each epoch. Figure 6.5 presents the spectra of the three hotspots (HS01, HS04, and HS05), shown with the best-fit model. In Table 6.2, the results of each hotspot

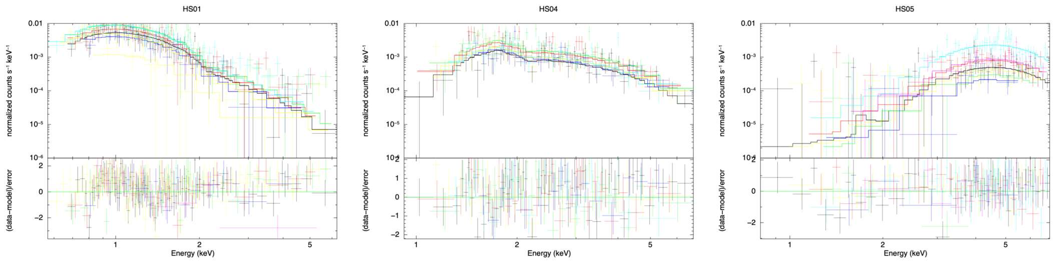

Figure 6.5. Spectrum of HS01, HS04, and HS05 from left to right, shown with the absorbed power-law model. The different colors represent the different epochs: the black, red, green, blue, cyan, magenta, and yellow spectra were taken in 2011, 2009 September, 2009 May, 2009 January, 2006, 2005, 2000, respectively.

are summarized. The upper and lower limits were set at a 1σ confidence level. The flux in the energy band of $0.5 - 7.0$ keV was calculated for each epoch, and the minimum and maximum values are shown in Table 6.2. Furthermore, because hotspots are dark at certain epochs, spectral fit could not be well performed using all the observation data. In this case, the fitting was performed using only epochs in which the hotspot was bright enough, thus only the maximum value of the energy flux is shown in Table 6.2. It should be noted that some hotspots with poor statistics were not well fitted, and their results are shown as "$\cdots$" in Table 6.2.

Figure 6.6 shows the $N_{\rm H} - \Gamma$ diagram, derived from the spectral fitting of each hotspot. Note that bright hotspots (HS01−HS11) are highlighted with red thick lines. Figure 6.6 does not include the results of hotspot whose spectral parameters were not well constrained and were obtained only with upper and lower limits. The typical values of $N_{\rm H}$ of $(0.7 - 1.0) \times 10^{22}$ cm^{-2} and Γ of $2.3 - 2.6$ in RX J1713.7−3946 are represented with cyan hatches. As shown in Figure 6.6, the spectral features of the hotspots substantially deviate from the typical values. There is a trend between $N_{\rm H}$ and Γ: the $N_{\rm H}$ of hotspots is larger where the Γ is smaller. It should be noted that we subtracted the spectral component of the SNR as background. Therefore, the spectrum of the hotspot has a pure X-ray emission from itself. We emphasize that the spectrum of the hotspot indicates a significantly different spectrum expected for the non-thermal radiation in RX J1713.7−3946. The origin of these spectra is discussed in Section 6.4.

We also fitted the spectra of HS01, HS04, and HS05 with thermal models, Bremsstrahlung and blackbody radiation. The column density was fixed to the best-fit values derived from using the power-law model. The results are presented in Table 6.3. The power-law model is favored, inferred from the chi-squared value, although the limited statistics do not confidently exclude the thermal origin. However, the featureless spectrum might support non-thermal radiation, namely the synchrotron emission from the accelerated electrons (see Section 6.4 for details).

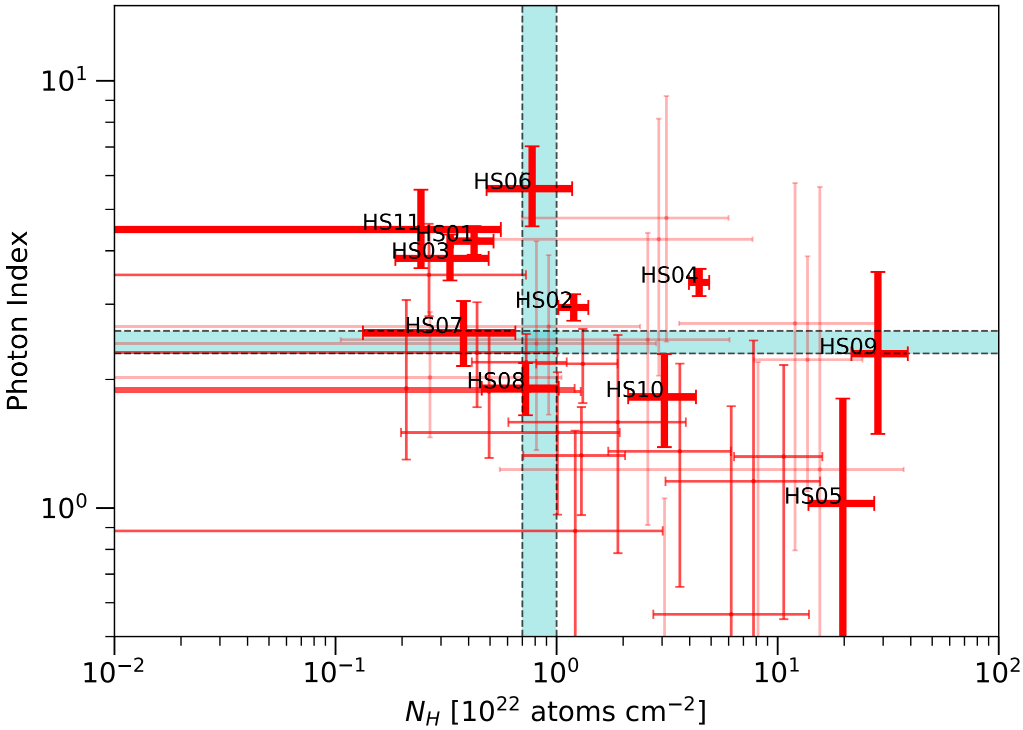

Figure 6.6. Diagram of the column density (N_H) and the photon index (Γ) derived from the spectral fitting of each hotspot. Typical N_H of $(0.7-1.0)\times10^{22}$ cm^{-2} and Γ of $2.3-2.6$ in the northwest shell of RX J1713.7−3946 are shown in the cyan hatches. The results of the bright hotspots are highlighted with the thick red lines.

Table 6.3: The Best-fit Parameters of HS01, HS04, and HS05.

HS	Model[a]	N_H (10^{22} cm^{-2})	$\Gamma/k_\mathrm{B}T$ (/keV)	Flux (minimum)[b] (10^{-14} erg cm^{-2}s^{-1})	Flux (maximum)[b] (10^{-14} erg cm^{-2}s^{-1})	χ/dof
HS01	PL	$0.423^{+0.095}_{-0.084}$	$4.22^{+0.35}_{-0.30}$	$2.47^{+0.45}_{-0.91}$	$7.19^{+0.98}_{-0.94}$	315.1/289
	Bremss	0.423 (fix)	$0.386^{+0.020}_{-0.019}$	$2.25^{+0.58}_{-0.47}$	$5.97^{+0.70}_{-0.63}$	344.8/290
	Bbody	0.423 (fix)	$0.176^{+0.005}_{-0.005}$	$2.11^{+0.52}_{-0.38}$	$5.41^{+0.61}_{-0.68}$	370.1/290
HS04	PL	$4.42^{+0.49}_{-0.45}$	$3.37^{+0.26}_{-0.24}$	$4.22^{+0.33}_{-1.01}$	$6.90^{+0.31}_{-1.10}$	188.8/186
	Bremss	4.42 (fix)	$1.41^{+0.10}_{-0.09}$	$3.92^{+0.54}_{-0.67}$	$6.40^{+0.58}_{-0.63}$	200.1/187
	Bbody	4.42 (fix)	$0.51^{+0.02}_{-0.02}$	$3.50^{+0.46}_{-0.51}$	$5.60^{+0.61}_{-0.50}$	239.4/187
HS05	PL	$19.72^{+7.62}_{-5.94}$	$1.02^{+0.78}_{-0.67}$	$3.62^{+0.24}_{-1.43}$	$23.45^{+0.41}_{-7.85}$	145.2/172
	Bremss[c]	19.72 (fix)	–	–	–	–
	Bbody	19.72 (fix)	$1.65^{+0.19}_{-0.15}$	$3.42^{+0.43}_{-0.64}$	$22.91^{+0.96}_{-2.41}$	145.74/173

[a] PL, Bremse, and Bbody represent the power-law, Bremsstrahlung, and black body models, respectively.
[b] Flux is calculated in the range of $0.5-7.0$ keV.
[c] Spectrum of HS05 is not able to fit with the Bremsstrahlung model.

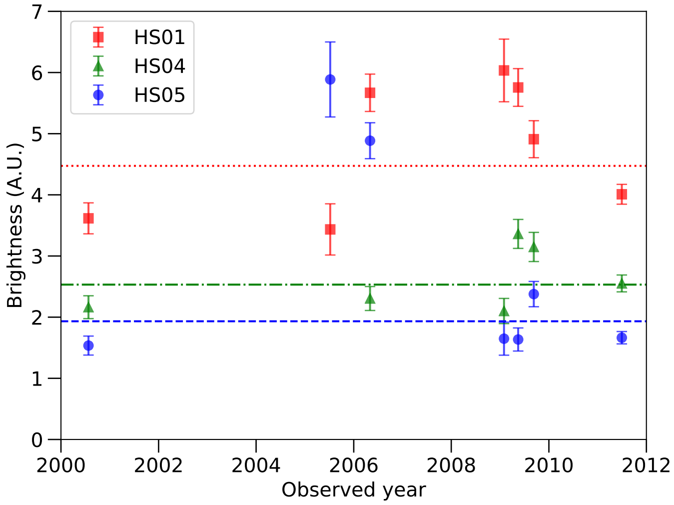

Figure 6.7. Light curves of HS01 (shown with red squares), HS04 (green triangles), and HS05 (blue circles). The horizontal lines represent the constant values that gives $\chi^2_{\rm min}$ in chi-square tests.

6.3.4 Time Variation

In this section, the time variation of the hotspots are discussed. Figure 6.7 presents light curves of the three hotspots, where the brightness was calculated by summing up the flux values inside a circular region with a radius of 5″. The three hotspots show varying brightness from time to time. The time variability was evaluated using a chi-square test. The chi-square value is given by

$$\chi^2 = \sum_I \frac{(f_i - f_c)^2}{\sigma_i^2}, \tag{6.1}$$

where i, f_i, f_c, and σ_i are subscript notating each observation, the brightness, the constant value, and the error of brightness, respectively. Once the minimum χ^2 value ($\chi^2_{\rm min}$) is found by changing f_c, the confidence to exclude the hypothesis of no time variation is derived from the value of $\chi^2_{\rm min}$. The constant value that gives $\chi^2_{\rm min}$ is also shown in Figure 6.7.

We found that 20 hotspots showed time variations at more than a 3σ confidence level, and 34 hotspots do so at more than 2σ (see Table 6.2). We noted that eight hotspots varied not only on a year scale but also on a month scale with more than 3σ, inferred from the same chi-squared test using the three data taken in 2009. The observed time variation may contain an important key for interpreting the origin of the hotspots: in fact a short time variation indicates a strong magnetic field of $\sim$ mG intensity, as discussed in Uchiyama et al. (2007).

6.4 Discussion

Our observations revealed the significantly large population of hotspots in the northwest shell of RX J1713.7−3946, the trend of the spectra (the larger the N_{H}, the smaller the Γ), and the yearly and monthly variabilities of the flux. We suggest that the hotspots are attributed to synchrotron radiation resulting in the interaction between a dense molecular core and the SNR shock. An inhomogeneous environment, where the dense cores and clumps have survived against the stellar wind from the massive progenitor star, is possible for RX J1713.7−3946. When the SNR shock interacts with the cores, synchrotron emission is expected due to an enhanced magnetic field surrounding the core (Inoue et al., 2012; Celli et al., 2019).

The timescales of synchrotron cooling and acceleration of electrons of energy E_e are given by

$$t_{\mathrm{synch}} \approx 12\left(\frac{B}{\mathrm{mG}}\right)^{-2}\left(\frac{E_e}{\mathrm{TeV}}\right)^{-1}\mathrm{yr}, \tag{6.2}$$

$$\approx 1.5\left(\frac{B}{\mathrm{mG}}\right)^{-3/2}\left(\frac{\varepsilon}{\mathrm{keV}}\right)^{-1/2}\mathrm{yr}, \tag{6.3}$$

and

$$t_{\mathrm{acc}} \approx 1\eta\left(\frac{\varepsilon}{\mathrm{keV}}\right)^{1/2}\left(\frac{B}{\mathrm{mG}}\right)^{-3/2}\left(\frac{v_{\mathrm{s}}}{3000\ \mathrm{km\ s^{-1}}}\right)^{-2}\mathrm{yr}, \tag{6.4}$$

respectively. Here B, η, and v_{s} are the strength of the magnetic field, the so-called Bohm factor which is defined as the mean free path of the particle divided by its gyro radius, and the shock speed, respectively[2]. The characteristic energy of a synchrotron photon (ε) is given by $\varepsilon \approx 0.016(B/\mathrm{mG})(E_e/\mathrm{TeV})^2$ keV.

Inoue et al. (2012) showed that the penetration depth of a particle into a dense clump due to its random walk is described with

$$\begin{aligned} l_{\mathrm{pd}} &\simeq (\kappa_{\mathrm{d}} t)^{1/2}, \\ &= 0.1\eta^{1/2}\left(\frac{E}{10\mathrm{TeV}}\right)^{1/2}\left(\frac{B}{100\ \mu\mathrm{G}}\right)^{-1/2}\left(\frac{t}{10^3\mathrm{yr}}\right)^{1/2}\mathrm{pc}, \end{aligned} \tag{6.5}$$

where t is denied as the time since the high-energy particles started penetrating into the clump. Here $\kappa_{\mathrm{d}} = 4\eta l_{\mathrm{g}} c/3\pi$ is the diffusion coefficient of a high-energy particle with a gyroradius of l_{g}.

We confirmed the thermal emission from the shock-core interaction is not dominant for the case of RX J1713.7−3946. The temperature of a proton in a shocked core, which corresponds to the upper limit of the temperature of electrons, is characterized by two parameters: the speed of the transmitted shock in the core and the number density ratio of the diffuse gas and the core. The shock speed in the core is given by $v_{\mathrm{sh,c}} \approx v_{\mathrm{sh,d}} \times (n_{\mathrm{d}}/n_{\mathrm{c}})^{1/2}$, where $v_{\mathrm{sh,d}}, n_{\mathrm{d}}$, and n_{c} are the shock speed in the diffuse gas, the number density of the diffuse gas, and the number density

---

[2] The case of $\eta = 1$ is the most efficient acceleration, known as Bohm limit.

of the core, respectively. The ambient density of RX J1713.7−3946 was estimated to be $n_{\mathrm{d}} \sim 0.01\ \mathrm{cm}^{-3}$ from X-ray observations (Slane et al., 1999; Cassam-Chenaï et al., 2004; Takahashi et al., 2008; Tanaka et al., 2008; Katsuda et al., 2015; Tsuji and Uchiyama, 2016). High-density objects such as cores and clumps are not heated enough to emit X rays by the transmitted shock because the shock speed in the core is roughly hundreds of meters per second. The timescale of plasma instability (Kelvin-Helmholtz instability) is the same order as the so-called "cloud-crushing time", t_{cc} (Klein, McKee, and Colella, 1994). Assuming a cloud with a size of L_{c}, the cloud-crushing time is given by $t_{\mathrm{cc}} = L_{\mathrm{c}}/v_{\mathrm{sh,c}}$. This results in tens of thousands of of years, consistent with the estimate in Celli et al. (2019)[3]. Thus the clump survives against the plasma instability because t_{cc} is much longer than the age of the SNR. Therefore, we presumed that the X-rays emitted from the hotspot are attributed to predominantly non-thermal (synchrotron) radiation. A non-thermal origin is also supported by the featureless spectra.

We proposed two scenario for the origin of the hotspot: the X-ray emission originated from "primary electrons" and/or from "secondary electrons". In this work, primary electrons indicates those accelerated by shocks (i.e., the forward shock of the SNR and/or the reflected shock induced by the interaction between the forward shock and the core). Secondary electrons are those produced by the decay of a charged pion, which is one of the products arising form the collision of very high-energy protons and mater in the core. Note that the secondary positrons are also taken into consideration. In the following analysis, we discuss the two scenarios, assuming $\eta = 1$ and $v_{\mathrm{s}} = 3900\ \mathrm{km\ s}^{-1}$ in the case of the northwest rim of RX J1713.7−3946 (Uchiyama et al., 2007; Tanaka et al., 2008; Tsuji and Uchiyama, 2016).

6.4.1 Hotspot originated from primary electrons.

When the SNR shock is interacting with the dense core, the magnetic field is enhanced, resulting in the strong synchrotron emission from the electrons accelerated at the SNR shock. As shown in Section 6.3.4, 20 hotspots are variable in the temporal interval of a few years, eight hotspots vary even in a few months, at more than 3σ confidence levels. The fast time variability of the synchrotron radiation might indicate the presence of an amplified magnetic field. Indeed, $B = 0.5 - 2.0$ mG could explain the observed year-scale and month-scale variations. Assuming $\varepsilon = 0.5$--10 keV and $B = 0.5 - 2$ mG, the cooling and acceleration timescales of $t_{\mathrm{synch}} = 0.2$-$- 6.0$ yr and $t_{\mathrm{acc}} = 0.1 - 5.3$ yr are obtained from Equations 6.3 and 6.4, respectively.

---

[3] In fact, Celli et al. (2019) used "clump-crossing time", which is calculated as $2L_{\mathrm{c}}/v_{\mathrm{sh,c}} \sim 1.4 \times 10^4$ yr

Substituting the synchrotron cooling time to Equation 6.5, the penetration depth of an electron is written as

$$l_{\mathrm{pd,e}} \approx 0.026 \left(\frac{B}{100\ \mu\mathrm{G}} \right)^{-3/2} \mathrm{pc} \tag{6.6}$$

(Fukui et al., 2012). Note that the penetration depth is independent of the energy of the electrons. It depends on the amplitude of the turbulent magnetic field with the scale of gyroradius of the electrons. Using Equation 6.6, $l_{\mathrm{pd,e}}$ is roughly estimated to be 2.3 mpc (milliparsec) for $B = 0.5$ mG, and 0.3 mpc for $B = 2.0$ mG.

The hotspot seems to be spatially comparable with the size of the PSF of *Chandra* which is approximately $1''$. This corresponds to a radius of $\sim$ 5 mpc, assuming the distance to the SNR of $\sim$ 1 kpc (Fukui et al., 2003). Therefore, the radius of the X-ray bright region in the core is expected to be smaller than 5 mpc.

The number density is tyically $\sim 10^5 - 10^6\ \mathrm{cm}^{-3}$ in the core of molecular clouds. The Atacama Large Millimeter/submillimeter Array (ALMA) found cores with number densities of $\sim 10^7\ \mathrm{cm}^{-3}$ in the regions such as Taurus and Orion A (e.g., Onishi et al., 2015; Ohashi et al., 2016; Ohashi et al., 2018). We therefore assumed $n = 10^5$-$- 10^7\ \mathrm{cm}^{-3}$ for the number density of the core.

The column density (N) could be described as

$$N = n \times l_{\mathrm{pd,e}} + N_{\mathrm{H,LOS}}, \tag{6.7}$$

where the first and second terms account for the column density of the core and the line-of-sight column density, respectively. Here, $N_{\mathrm{H,LOS}}$ is assumed to be the column density observed in the central region of the SNR, $0.4 \times 10^{22}\ \mathrm{cm}^{-2}$ (Cassam-Chenaï et al., 2004), because the central part is assumed to be less contaminated by the swept-up ISM than the shell region, and thus expected to have the information of the wind-blown cavity.

Figure 6.8 illustrates the relation between the estimated column density (N) and $l_{\mathrm{pd,e}}$, assuming n_{c} of 10^5, 10^6, and $10^7\ \mathrm{cm}^{-3}$. In Figure 6.8, the penetration depth of an electron into magnetic fields of 0.5, 1.0, and 2.0 mG are shown with the solid, dotted, and dashed vertical lines, respectively.

In the case of a strong magnetic field ($B = 0.5$ mG), $l_{\mathrm{pd,e}}$ was calculated to be $\sim$ 2.3 pc. This would result in a column density of $N \sim 1 \times 10^{23}\ \mathrm{cm}^{-2}$ for $n_c = 10^7\ \mathrm{cm}^{-3}$, which is roughly consistent with the observed values. Note that a lower column density, $N \lesssim 1 \times 10^{22}\ \mathrm{cm}^{-2}$, is obtained for $n_c = 10^5 - 10^6\ \mathrm{cm}^{-3}$.

In the case of a very strong magnetic field ($B = 2$ mG), $l_{\mathrm{pd,e}}$ becomes $\sim$ 0.3 mpc, which is much smaller than the size of the core. In this case, the electron cannot deeply penetrate to the core because it would quickly lose its energy in the skin of the core. This reduces the column density to $N \lesssim 1 \times 10^{22}\ \mathrm{cm}^{-2}$ in the case of $n_{\mathrm{c}} = 10^5 - 10^7\ \mathrm{cm}^{-3}$.

The spectral analysis shows that part of the hotspots are characterized by the

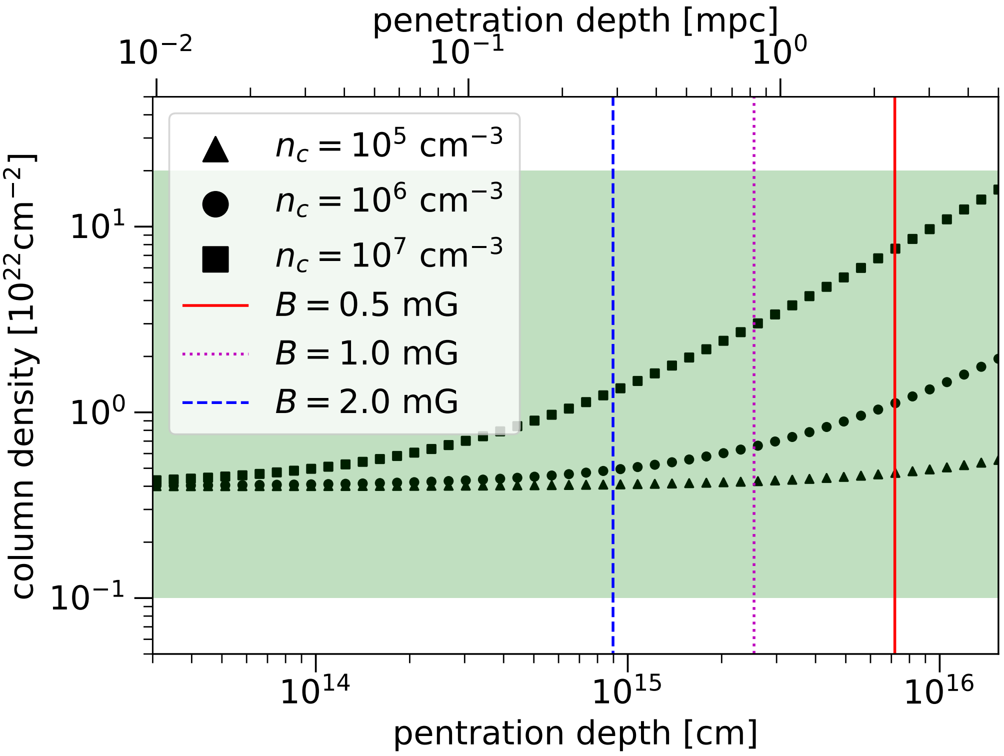

Figure 6.8. Estimated column density as a function of the penetration depth, assuming the number density of the core of 10^5, 10^6, and 10^7 cm^{-3}, and using Equation 6.7. The vertical red-solid, magenta-dotted, and blue-dashed lines represent the penetration depth of an electron in magnetic fields of 0.5, 1.0, and 2.0 mG, respectively, using Equation 6.6. The observed column density ($N_{\rm H} = (0.1 - 20) \times 10^{22}$ cm^{-2}) is shown in the green region.

low $N_{\rm H}$ and large Γ (see Figure 6.6) This can be interpreted as acceleration in the reflection shock caused by the interaction between the forward shock and the dense object (clumps and cores). The spectrum of electrons accelerated in the reflection shock becomes steeper due to low Mach number of the reflection shock (see Inoue et al., 2012, for details).

In summary, for the hotspot originating from primary electrons, the observed properties of the hotspots are interpreted as follows. The rapid flux variation is explained by the amplified magnetic field of $0.5-2$ mG. The larger $N_{\rm H}$ is interpreted as the deeper penetration depth in the $B = 0.5$ mG case, whereas the smaller $N_{\rm H}$ could be indicative of the shallower penetration depth in a very strong magnetic field of 2 mG. Furthermore, the observed large Γ might be caused by the reflection shock with lower Mach number.

6.4.2 Hotspot originated from secondary electrons.

The hotspots, the hard hotspots in particular, are likely attributed to the secondary electrons that are produced via the shock-cloud interaction. We assume the same penetration depth of the secondary electrons as that of protons. The hardest hotspot tends to have the largest column density, as shown in Figure 6.6. The spectrum of high-energy protons in the core is expected to be harder since low-energy protons do not penetrate the clump deeply, and only very high-energy protons are capable of reaching the core (Gabici and Aharonian, 2014; Celli et al., 2019). Therefore, one expects the harder spectrum of the secondary electrons produced via shock-clump interaction, and also harder spectrum of the synchrotron radiation from the secondary electrons, which is reconciled with the observed small Γ.

The timescale of pp interaction is characterized by $t_{\rm pp} \sim 6 \times 10^7 \left(n/1~{\rm cm}^{-3}\right)^{-1}$ yr with the number density of target matter of n. In the case of $n \sim 10^7~{\rm cm}^{-3}$, $t_{\rm pp}$ is ~ 6 yr, which is roughly consistent with the observed year-scale variability. Furthermore, the timescale of pp interaction is less than the age of RX J1713.7−3946 given $n = 10^5 - 10^7~{\rm cm}^{-3}$. Substituting the timescale of pp interaction to Equation 6.5, we derived the penetration depth of the proton,

$$l_{\rm pd,p} \sim 7.7 \left(\frac{E_{\rm p}}{10~{\rm TeV}}\right)^{1/2} \left(\frac{B}{100~\mu{\rm G}}\right)^{-1/2} \left(\frac{n}{10^7~{\rm cm}^{-3}}\right)^{-1/2} {\rm mpc}, \tag{6.8}$$

where $E_{\rm p}$ is the energy of the proton.

In the case of the core with $n = 10^7~{\rm cm}^{-3}$, protons with the energy of about 40 TeV are required to reach the vicinity of the center of the core, assuming $B = 1$ mG and $l_{\rm pd,p} \sim 5$ mpc in Equation 6.8. This results in a column density N of $\sim 10^{23}~{\rm cm}^{-2}$, which is roughly consistent with the observed larger $N_{\rm H}$. The energy of proton should be less than 200 TeV, otherwise the proton passed through the core without losing the energy by pp interaction, because of the longer penetration depth than the size of the X-ray emitting region (i.e., $l_{\rm pd,p} \geq 10$ mpc). Protons with the energy of ~ 40 TeV (≤ 200 TeV) can produce the secondary electron responsible for the synchrotron radiation in the X-ray energy band.

In the case of the core with $n = 10^5$ cm^{-3}, the proton energy of about 0.4 TeV is required to reach the vicinity of the center of the core, assuming $B = 1$ mG and $l_{\mathrm{pd,p}} \sim 5$ mpc in Equation 6.8. The energy of the proton should be less than 2 TeV in order to lose the energy by pp interaction within the X-ray emitting region. For protons with the energy of ~ 0.4 TeV (≤ 2 TeV), the energy is too low to produce the secondary electron responsible for the synchrotron radiation in the X-ray band. Therefore, the very large density of $n = 10^6 - 10^7$ cm^{-3} is preferred for the hard hotspot in the scenario of secondary electrons.

In the following, we estimate the synchrotron energy flux emitted from secondary electrons in order to verify the consistency with the observations. The observed flux of hard hotspot is $\sim 10^{-15} - 10^{-14}$ erg cm^{-2}s^{-1}, as derived in Section 6.3.3.

The energy density of protons in the SNR is described by

$$\begin{aligned} U_{\mathrm{p}} &= \frac{K_{\mathrm{p}}}{V}, &(6.9)\\ K_{\mathrm{p}} &= \xi E_{\mathrm{SN}} = \xi \times 10^{51} \text{ erg}. &(6.10)\end{aligned}$$

Here U_{p}, K_{p}, V, ξ, and E_{SN} are the energy density of protons, the total energy of proton filled in the volume of the SNR, the volume of the SNR, the fraction of the kinetic energy transferred from the SN explosion to protons with energy $10 - 1000$ TeV, and the typical kinetic energy of an SN explosion, respectively. Suppose that the protons have the power-law distribution of $N(E) \propto E^{-2}$, ξ is derived from the fraction ($\sim 33\%$) of energy occupied by the protons from 10 TeV to 1 PeV in the total energy from 1 GeV to 1PeV. This results in $\xi \approx 10\% \times 33\% \approx 0.033$. Note that we assumed the typical fraction of the kinetic energy transferred from the SN explosion to accelerated protons was 10%. The radius of the remnant is $\sim 30'$, which corresponds to ~ 9 pc, assuming $d = 1$ kpc (Fukui et al., 2003). If cosmic-ray protons are isotropically distributed inside the remnant, the total energy of protons contained in the X-ray emitting region is calculated by

$$W_{\mathrm{p}} = U_{\mathrm{p}} \times \frac{4}{3}\pi R^3, \tag{6.11}$$

where R is the radius of the X-ray emitting region, namely the core ($R = 5$ mpc). The synchrotron flux emitted by secondary electrons in the characteristic timescale τ is then given by

$$F_{\mathrm{X}} = \frac{\zeta W_{\mathrm{p}}}{4\pi d^2 \tau} \sim 8 \times 10^{-20} \left(\frac{\xi}{1}\right) \left(\frac{n}{1 \text{ cm}^3}\right) \text{erg cm}^{-2} \text{ s}^{-1}. \tag{6.12}$$

We assume that the fraction of the energy transferred from primary protons to secondary electrons (ζ) is 0.1, and the timescale (τ) is comparable with the timescale of pp interactions, $\tau \sim 6 \times 10^7 \left(n/1\,\mathrm{cm}^{-3}\right)^{-1}$ yr. We also assume that secondary electrons lose all their energy by synchrotron X-ray radiation in the amplified strong magnetic field.

In the case of $n = 10^6 - 10^7\,\mathrm{cm}^{-3}$ and $\xi = 0.033$, Equation 6.12 yields $F_X \sim 10^{-15}$-$- 10^{-14}\,\mathrm{erg\,cm^{-1}s^{-1}}$, which reproduces the observed flux level. In the case of $n = 10^5\,\mathrm{cm}^{-3}$, ξ should be ~ 0.33 to reach $\sim 10^{-15}\,\mathrm{erg\,cm^{-2}s^{-1}}$. $\xi \sim 0.33$, however, is unrealistically large since the typical fraction of the kinetic energy transferred from the SN explosion to accelerated protons is ~ 0.1. We also argued that $n = 10^5\,\mathrm{cm}^{-3}$ is not likely applicable because the expected energy of the proton inside the core is lower for producing the secondary electron responsible for the synchrotron X-ray.

If the hotspots originate from secondary electrons, one expects the hadronic gamma-ray radiation produced from the same protons. It is challenging but very interesting to observe the hadronic gamma-ray radiation from the hotspot and compare it with the X-ray properties. The current gamma-ray telescopes, with their limited angular resolution, make it unrealistic to detect the subarcsecond structures of the hotspots. CTA, however, will provide much better spatial resolution and sensitivity, and allow us to access the gamma-ray information of the hotspots. Neutrino observations may also contribute to this study of revealing the hadronic component.

6.4.3 ALMA CO observation and discoveries of shocked cloudlets at 0.01 pc scales

The hotspots are interpreted as the non-thermal X-ray emission as a result of shock-cloud interaction. Using the great spatial resolution of ALMA (Atacama Large Millimeter/submillimeter Array), Sano et al. (2020) observed the ^{12}CO lines in the direction of the northwest region of RX J1713.7−3946. Although the X-ray diffuse emission is radiated in the intercloud region, there are several dense molecular cloudlet with a size on order of 0.01 pc[4] in the vicinity of hotspots, as shown in bottom panel of Figure 6.9. The example cloudlets are shown as CL1−CL6. The separation between the hotspot and cloudlet are $\sim 0.05 - 0.15$ pc from CO peaks. Considering the cloudlet size and density contrast of cloudlet and diffuse region, Sano et al. (2020) expected that the enhanced magnetic field is $\sim 0.12 - 0.20$ pc away from the cloudlet. It is consistent with the observed separation between the hotspots and the cloudlets. Also, the closer separation is interpreted by the penetration into the cloudlets. These findings of dense and compact cloudlets in the vicinity of the hotspots supprot our understanding of the mechanism of the X-ray hotspots.

---

[4] In Sano et al. (2020), they referred the dense CO region as cloudlet. In this section, the dense regions are described as cloudlets.

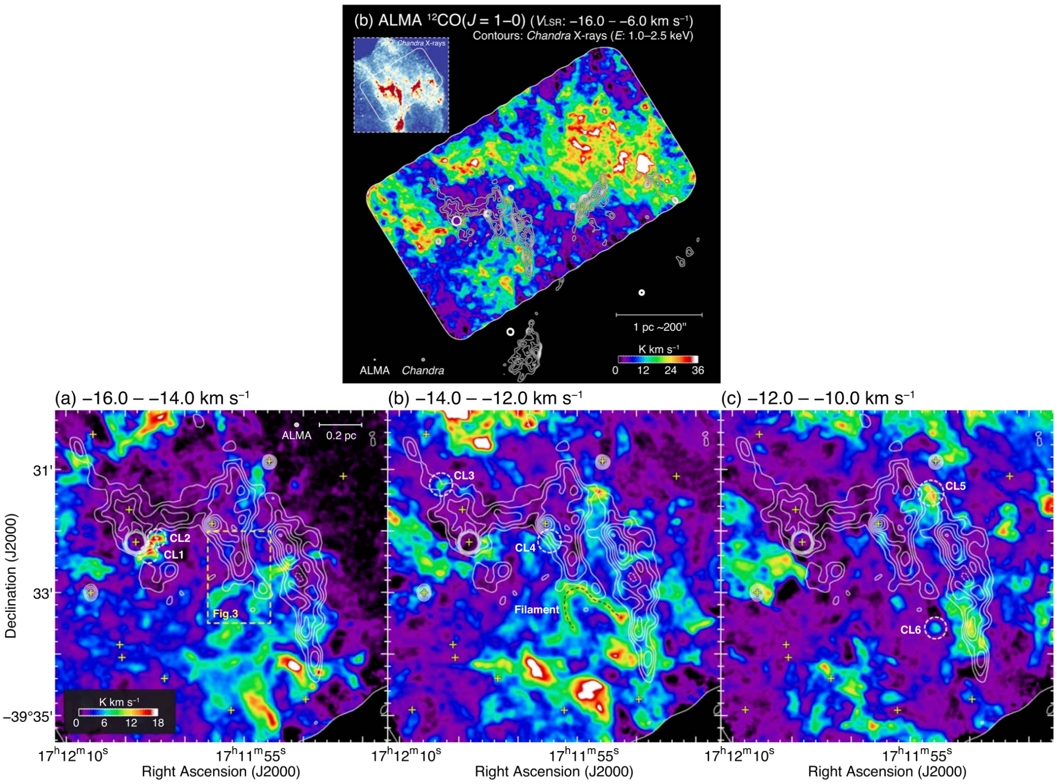

Figure 6.9. (Top) ALMA CO map in the northwest region of RX J1713.7−3946. X-ray image with *Chandra* is overlaid in the top left, the corresponding X-ray contour is represented by white curves. (Bottom) ALMA CO velocity channel map in the eastern part of the northwest limb. Same X-ray contour is overlaid by white curves and yellow crosses represent the position of X-ray hotspot identified by our study (Sano et al., 2020).

Chapter 7

Gamma-ray analysis of X-ray hotspots in the eastern ear of W50/SS 433 system with *Fermi*-LAT

7.1 Overview

We examined the X-ray and radio structure at the eastern ear of the W50/SS 433 system to clarify a characteristic feature of the termination region of the SS 433 jet, and found that hotspots ahead of the filament structure, which is considered to be a terminal shock of the SS 433 eastern jet, is clearly different from a single point source. Since there are no point sources nearby, the northern hotspot is likely a localized diffuse source. The northern hotspot corresponds to the peak of the radio emission. When a radiation model comparing synchrotron emission and inverse Compton emission is applied to the spectral energy distribution of the hotspot, the emission from this hotspot can be explained by the radiation from an electron population accelerated up to 30 TeV in a magnetic field strength of $B \leq 50\ \mu$G. This model also agrees with the radio and X-ray data, as well as the upper limit of gamma-ray emission obtained by the *Fermi*-LAT.

I contributed to the gamma-ray analysis of this work (Hayakawa et al., 2022) and derive the upper limits of gamma-ray emission from this hotspot with high precision, considering the results of current controversial and inconsistent gamma-ray analysis. The results of the other wavelength (X-ray and radio band) is presented in Hayakawa et al. (2022). The gamma-ray results are greatly contributed to constrain the electron spectrum and strength of magnetic field in this region.

7.2 Observations and Data Reduction

We analyzed about 12.5 year of the LAT data (from 2008 August 4 to 2021 February 22). The events were extracted within a $20^\circ \times 20^\circ$ region of interest (ROI) centered at the position of SS 433 with the energy of $0.5 - 300$ GeV. In Figure 7.1, a count map of the ROI is shown. The data were processed and analyzed through the standard analysis tool Fermitools version 2.0.8, which is available from the Fermi-LAT

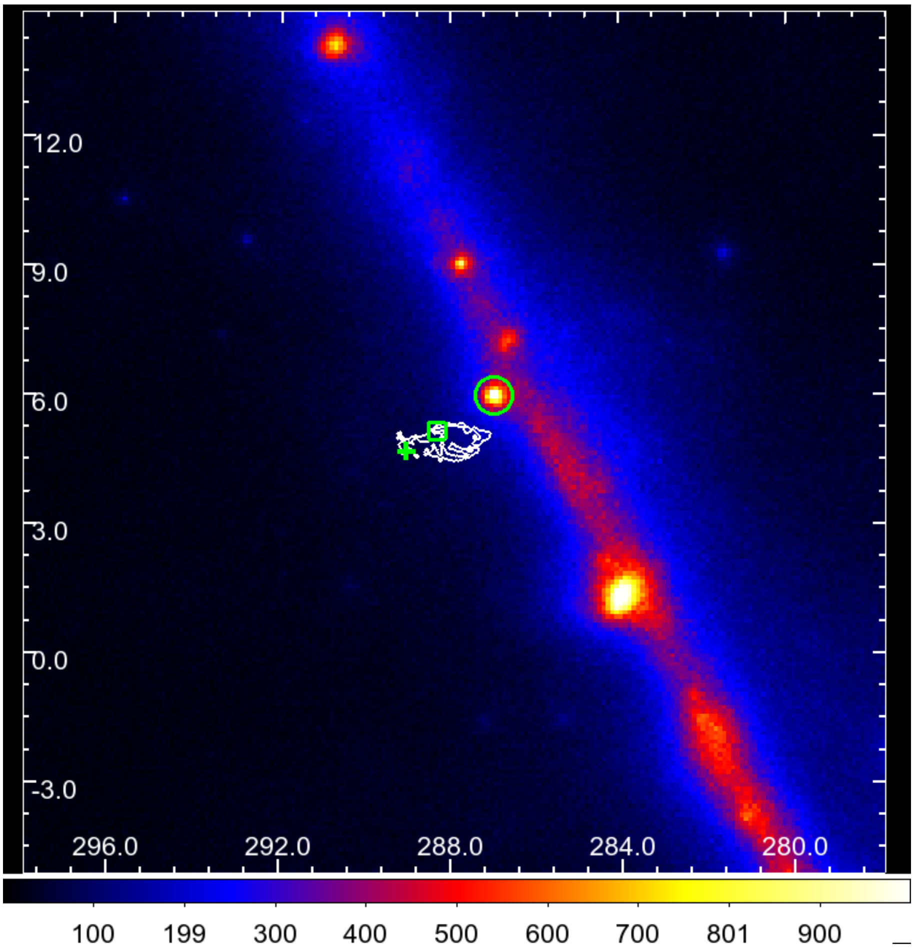

Figure 7.1. Count map of the ROI ($20° \times 20°$) in the energy range of $0.5 - 300$ GeV. The positions of the X-ray hotspot, Fermi j1913+0515, and pulsar PSR J1907+0602 are represented by green cross, box, and circle, respectively. White contour represents the distribution of radio continuum emission.

Science Support Center[1]. The events with "SOURCE" class and zenith angle less than 90° were used in the analysis, and the corresponding LAT instrument response function `P8R3_SOURCE_V3` were adopted. The latest fourth source catalog (4FGL-DR2 catalog; Ballet et al., 2020; Abdollahi et al., 2020) was used in the analysis, together with the Galactic diffuse model `gll_iem_v07.fits` and the isotropic diffuse emission model `iso_P8R3_SOURCE_V3_v1.txt`[2]. All sources listed in the 4FGL-DR2 catalog within a radius of 18° from the center of the ROI are included in the model.

The binned maximum likelihood method of `gtlike` implemented in Fermitools was used to extract the spectral information. In this optimization, we left the spectral parameters free for sources having a significance of $\geq 10\sigma$, and lying within 5° from the center of the ROI, while only the normalization was left free for sources with a significance $< 10\sigma$ and within 3° from the center. The spectral parameters for all

---

[1] https://fermi.gsfc.nasa.gov/ssc/

[2] https://fermi.gsfc.nasa.gov/ssc/data/access/lat/BackgroundModels.html

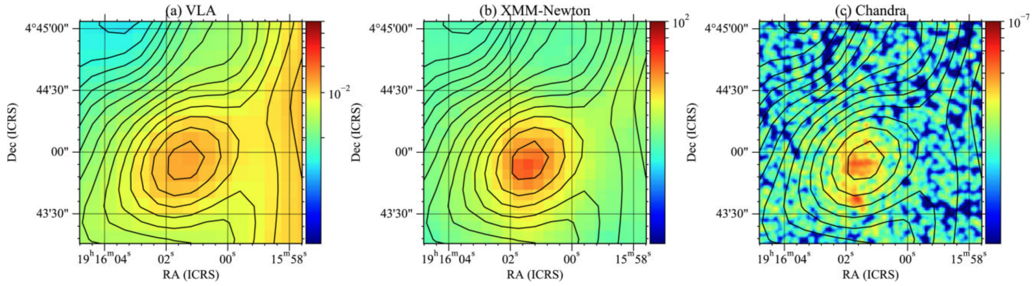

Figure 7.2. Comparison of the images around the hotspot of W50 with (a) VLA, (b) *XMM-Newton*, and (c) *Chandra* observations, respectively. The contour of VLA is overlaid with a black line, The X-ray hotspot are seen in both *XMM-Newton* and *Chandra*. The radio intensity is high at the X-ray hotspot. The northern hotspot which is resolved in the *Chandra* image seems closer to the peak of the radio flux.

other sources were fixed to the values of the source catalog. The normalizations of the Galactic and the isotropic diffuse models were left free.

7.3 Analysis and Results

At the eastern side of the W50/SS 433 system, we reveal the X-ray two hotspots as shown in right panel of Figure 7.2 (Hayakawa et al., 2022, including R.Higurashi). The position of the northern hotspots corresponds the bright area in the radio band. We tested whether significant GeV gamma-ray emission could be detected at the position of the X-ray hotspot, shown by green cross in Figure 7.1. As shown in Figure 2.22, the west excess is also confirmed in our analysis, owing to the excess is not included in the gamma-ray source catalog yet because it does not satisfy the criterion of the source catalog. There is no source in the gamma-ray source catalog at the position of X-ray hotspots. We added a test source at the position as a point source assuming a power-law type spectrum. By comparing the likelihoods with and without the test source in the model, TS ~ 3.6 was obtained. It means that significant GeV gamma-ray emission was not detected from the location of the hotspot. Figure 7.3 represents a TS map around SS 433/W50 system. In the west side (right hand), the west excess is seen like the previous GeV gamma-ray studies in (Xing et al., 2019; Li et al., 2020). At the position of the X-ray hotspot, the map shows low TS values, meaning the model sufficiently reproduce the gamma-ray emission. The normalization of the Galactic and isotropic diffuse model were found to be 0.942 ± 0.001 and 1.19 ± 0.02, respectively.

Since a significant gamma-ray emission is not detected from the hotspot, we derive upper limits of the gamma-ray emission at the hotspot position. The upper limits of the *Fermi* data are obtained by placing a point source at the position of the X-ray hotspot, and calculating the upper limits with 95% confidence level. Compared to previous work, such as the simultaneous fit with HAWC (Fang, Charles,

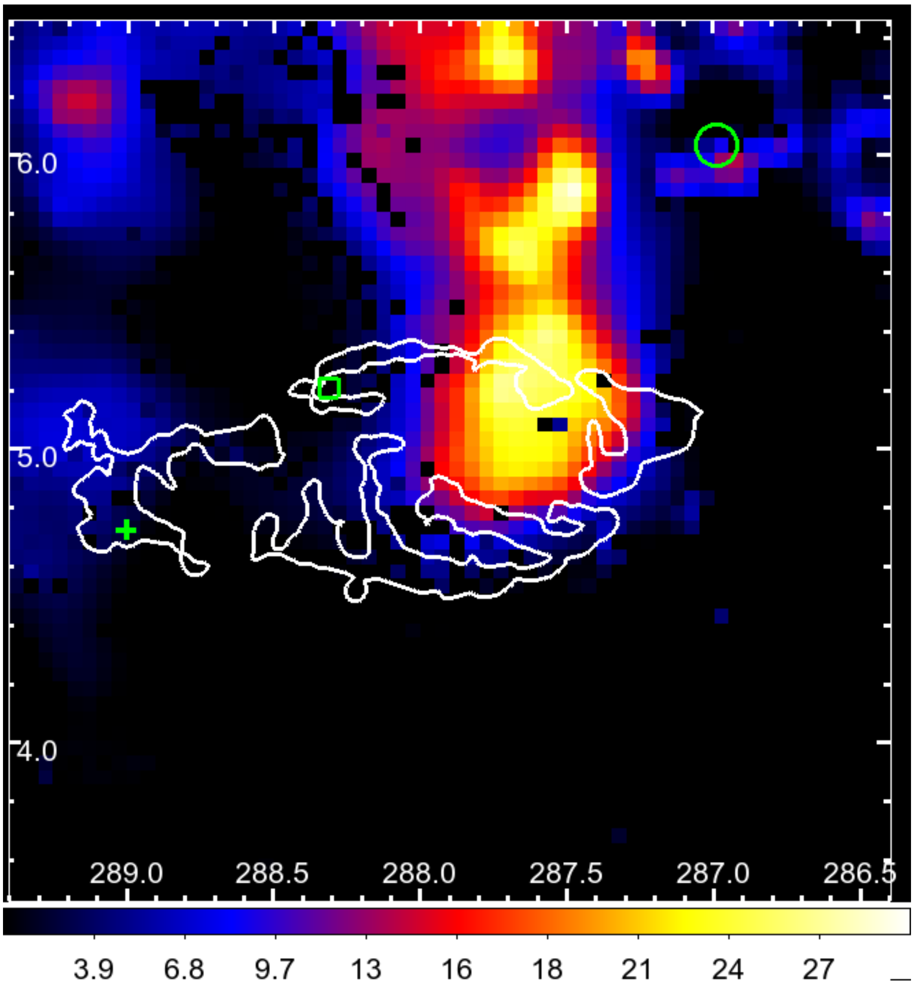

Figure 7.3. TS map of the region of W50/SS433 system in the energy range of $0.5 - 300$ GeV. The positions of the X-ray hotspot, Fermi j1913+0515, and pulsar PSR J1907+0602 are represented by the same markers in Figure 7.1. Distribution of radio continuum is shown by white contour.

and Blandford, 2020), we used only the *Fermi* data but for a longer time period than the one previously reported. The pulsar PSR J1907+0602 located in the vicinity of the SS 433 is not gated off, but included as a background source. It should be considered as a relatively conservative estimation of the flux at the hotspot. The upper limits obtained are plotted in Figure 7.6.

7.3.1 Uncertainties of gamma-ray upper limit

Table 7.1: Differences of setups on GeV gamma-ray studies.

Work	Energy range (GeV)	Source catalog[a]	Galactic diffuse emission model[b]	Fermi J1913[c]	PSR J1907[d]
Xing et al. (2019)	0.3 – 100	3FGL+FL8Y	gll_iem_v06.fits	Background	not concerned
Rasul et al. (2019)	0.1 – 1	3FGL	gll_iem_v06.fits	Background	not concerned
Sun et al. (2019)	0.1 – 10	4FGL	gll_iem_v06.fits	SS 433/W50	not concerned
Fang, Charles, and Blandford (2020)	0.1 – 300	4FGL	gll_iem_v07.fits	SS 433/W50	concerned
Li et al. (2020)	0.1 – 300	4FGL	gll_iem_v07.fits	SS 433/W50	concerned

[a] Gamma-ray source catalog used in the analysis. The latest catalog is the 4FGL, and the FL8Y is tentatively used catalog between 4FGL and 3FGL.

[b] Version of Galactic diffuse emission model. The model of gll_iem_v07.fits is released later than gll_iem_v06.fits.

[c] Treatment of the GeV gamma-ray source Fermi J1913 overlapping with the system in the line of sight. “Background” means that the source is not treated as the GeV gamma-ray emission from the system.

[d] Treatment of nearby bright pulsar PSR J1907. The impact of the pulsar is large because of the large PSF of LAT in the low energy band.

The uncertainties of GeV gamma-ray upper limits should be analyzed in detail because different setups affect the values of upper limits. In addition, the controversial results of the previous GeV gamma-ray studies (Xing et al., 2019; Sun et al., 2019; Rasul et al., 2019; Fang, Charles, and Blandford, 2020; Li et al., 2020) are considered to be caused by different setups. They differ in their treatment of gamma-ray source Fermi J1913+0515 and pulsar PSR J1907+0602. The differences of the setup on the previous GeV gamma-ray studies are summarized in Table 7.1. Fermi J1913+0515 is located inside the W50 (see green box region in Figure 7.1), and included in a background source in this work. Furthermore, the gamma-ray excess emission is reported in the west side of SS 433/W50 system (Xing et al., 2019; Li et al., 2020), which is not included in the background model in this work. Because of the large PSF of the *Fermi*-LAT the treatment of these nearby gamma-ray source affects the upper limits of the gamma-ray emission at the position of X-ray hotspot. Since the contribution of PSR J1907+0602 (see green circle region in Figure 7.1) to the SS 433 region is reported in Li et al. (2020), the effect of the pulsar should be checked. The insufficiency of the Galactic diffuse emission model is also caused the uncertainty of the upper limits because the SS 433/W50 system is near the Galactic plane.

Since the Fermi J1913+0515 is included in the background model, we analyzed the uncertainty of the upper limits of the hotspot when this gamma-ray source is removed from the model. Since the PSF of the LAT is larger at low energies and becomes smaller at higher energies, the upper limits of the hotspot changes by a factor of ~ 1.72 at low energies due to the entry of some photons from Fermi J1913+0515. At higher energies, above 10 GeV, the difference is only 0.5% at most. The estimated upper limits in this assumption are plotted in Figure 7.4 by blue plots.

The west excess reported in Li et al. (2020) is not a significant gamma-ray source, and is not included in the background model. Therefore, we added it to the model as a power-law spectrum at the position reported in Li et al. (2020) and analyzed the effect on the upper limit of the hotspot. As a results, the upper limit of the hotspot changed by $\sim 0.7\%$ at maximum. The estimated upper limits in this assumption are plotted in Figure 7.4 by yellow plots.

As repoted in Li et al. (2020), the region of SS 433 partly contains the radiation from the nearby pulsar PSR J1907+0602. A folded light curve of the pulsar is generated by using the photons within 1° from the pulsar, and shown in Figure 7.5. In contrast, the photons within $1\overset{\circ}{.}5$ from the hotspot are folded with the pulse phase of PSR J1907+0602, and shown in Figure 7.5. The figure represents that the region of the hotspot is affected by the pulsar emission. Therefore, we analyzed the off-pulse phase as the period of $0 - 0.136$ and $0.697 - 1.0$ of the pulse phase of PSR J1907+0602, following the analysis in Li et al. (2020). The corresponding off-pulse window is shown in Figure 7.5 by gray hatch. PSR J1907+0602 in the off-pulse phase was modeled with a power-law spectrum as in Li et al. (2020). The bottom panels of Figure 7.5 shows the all phase and off-pulse phase count maps around SS 433/W50 system. As a result, the upper limit of the hotspot became larger as the statistics became smaller,

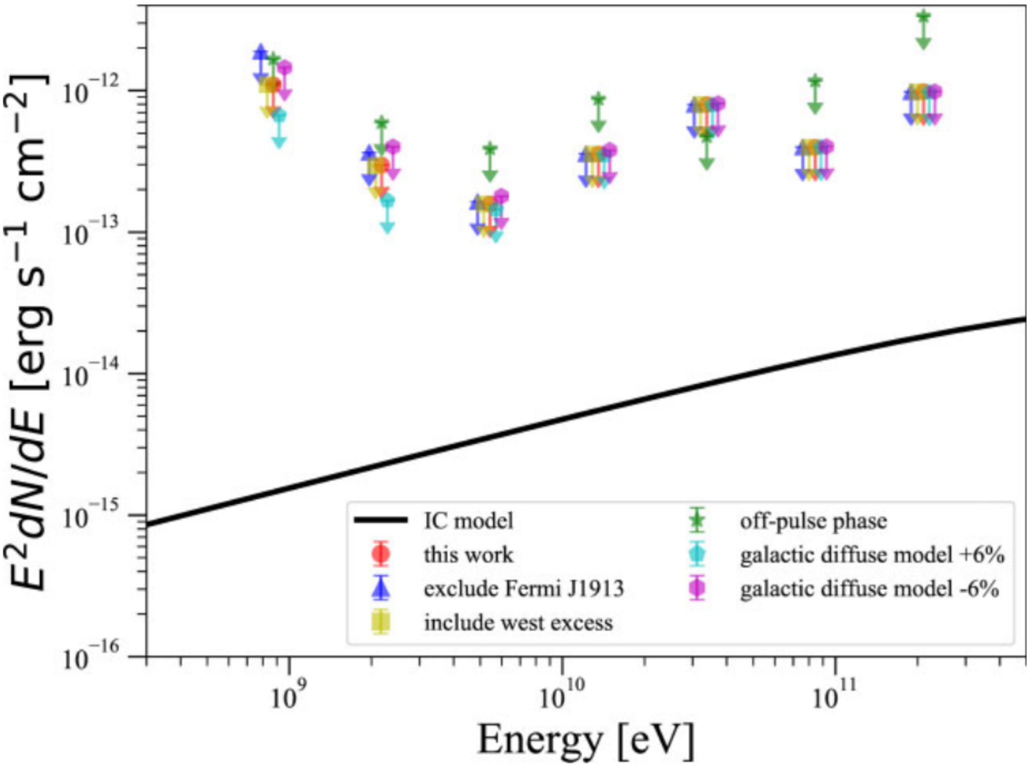

Figure 7.4. Estimation of uncertainties on the upper limit of the *Fermi* analysis. The red points are plotted at the actual energies, while the others are shifted horizontally for ease of viewing. The upper limit and total SED applied to Figure 7.6 are plotted in red and black solid curve, respectively. Each estimation is plotted in blue (exclude Fermi J1913+0515 from the background model), yellow (include the west excess detected in Li et al. (2020)), green (off-pulse phase analysis of PSR J1907+0602), cyan (+6% normalization of the Galactic diffuse model), and magenta (−6% normalization of the Galactic diffuse model).

and a change of a factor ~ 3.4 was obtained at maximum (shown in Figure 7.4).

In order to verify the uncertainty of the upper limit of the hotspot due to the insufficiency of the Galactic diffuse emission model. We intentionally varied the normalization of the Galactic diffuse emission model by $\pm 6\%$ (Abdo et al., 2013). As a result, a factor of about 0.56 (+6%) and 1.35 (-6%) was obtained at low energies where the Galactic diffuse emission is strong, and the change tend to be smaller at higher energies. The estimate upper limits in this assumption are plotted in Figure 7.4 by cyan and magenta.

7.4 Discussion

The best-fit X-ray and radio data, which is analyzed in Hayakawa et al. (2022), are plotted in Figure 7.6. Since the data are sparse, we overlaid a typical spectrum calculated by using a software package called `naima` (Zabalza, 2015). Using these multi-wavelength data, the radiation mechanism of the hotspot was estimated assuming the radiation model of synchrotron and inverse Compton scattering emission. The electron population is described by a cut-off power law with a cut-off energy of 30 TeV and a power-law index of 2. For the target seed photons of inverse Compton scattering, we considered the cosmic microwave background (CMB), near-infrared (NIR)/far-infrared (FIR) background , and photons from synchrotron self Compton (SSC). The temperature and energy density of the FIR background are assumed to be 20 K and 0.3 eV cm^{-3}, respectively, following the dust emission in solar neighborhood (Vernetto and Lipari, 2016). For the NIR background, they are set as 5000 K and 1 eVcm^{-3}.

When the total spectral energy distribution (SED) is computed varying the magnetic field from 1 to 100 μG, we find a solution of $B \lesssim 50\ \mu\mathrm{G}$. The magnetic field is constrained owing to the GeV gamma-ray upper limits and radio data point. The spectra of synchrotron and inverse Compton scattering assuming a magnetic field of 10 μG and a cut-off energy of 30 TeV are shown in Figure 7.6. The corresponding inverse Compton model does not exceed the GeV gamma-ray upper limits derived with different models (see Figure 7.4).

The scenario that the accelerated electrons dissipate their energy is further considered. Under the assumption of synchrotron radiation from relativistic electrons at the hotspot, the cooling time of an electron of energy E through synchrotron radiation is estimated to be $t_{\mathrm{synch}} \sim 4000(B/10\mu\mathrm{G})^{-2}(E/30\mathrm{TeV})^{-1}\mathrm{yr}$. In this case, the time variability of the hotspot is not expected in X-ray band. We note that a solution can be obtained for an electron index > 2 by allowing the cut-off energy to be larger than 30 TeV.

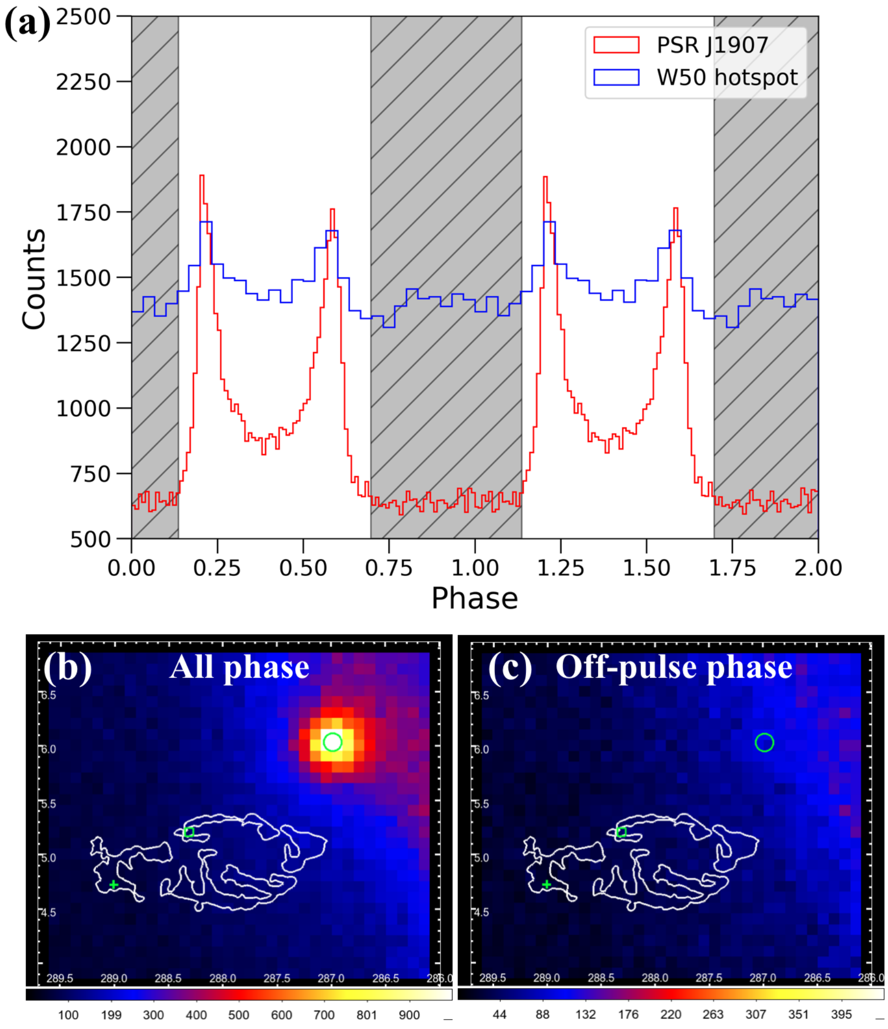

Figure 7.5. (a) Folded light curves of PSR J1907+0602 (red) within 1° from the pulsar and the region of hotspot (blue) within 1.°5 from the center of the hotspot generated by using the ephemeris of PSR J1907+0602. The gray hatched region is the off-pulse window used in the off-pulse phase analysis. (b) and (c) represent count maps around SS 433/W50 system and PSR J1907+0602 in all phase and off-pulse phase, respectively.

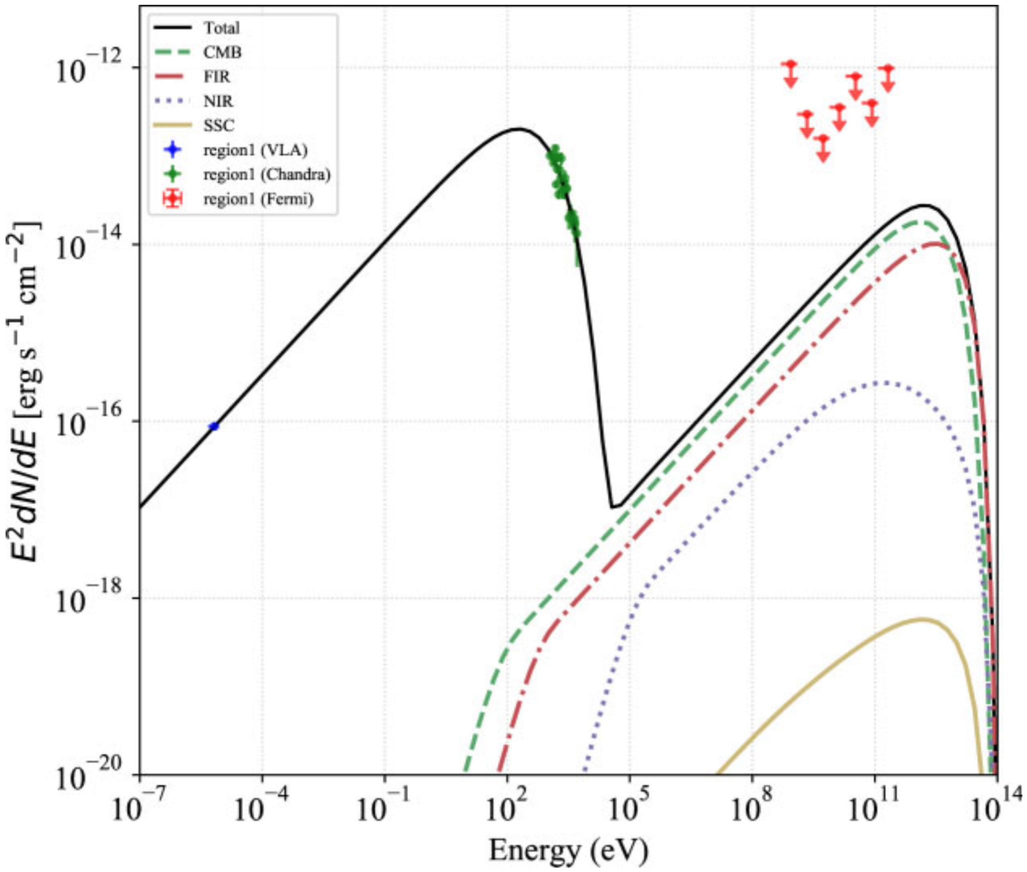

Figure 7.6. Spectral energy density (SED) of the hotspots. The inverse Compton emission from CMB, FIR, NIR, and SSC are shown in green, red, blue, and yellow, respectively. The total SED of the model with a cut-off energy $E_{\mathrm{cut}} = 30$ TeV, a power-law index of 2, and a magnetic field $B = 10\ \mu$G is shown using a black solid line. The flux of VLA is plotted in blue. The X-ray spectrum of Chandra of region 1 are shown in green and the upper limit of the Fermi are shown in red.

Chapter 8

Summary

The origin of cosmic rays is a still-lasting mystery in high-energy astronomy. SNRs are considered as the primary accelerators of the Galactic cosmic rays. To unveil the origin, we need to clear the cosmic-ray anomalies like positron excess, particle acceleration in astronomical objects, and transportation of the cosmic rays. In this thesis, gamma-ray and X-ray data analyses of the three cosmic-ray accelerators are conducted to understand the puzzling positron excess and particle acceleration in these targets.

Since the high-energy cosmic-ray electrons suffer energy loss during their propagation, they cannot travel long distances. Owing to the near distance, the Vela SNR is one of the most important sources of the cosmic-ray electron and positron. The cosmic-ray electrons from the Vela SNR are a candidate for the origin of the anomalous positron excess. The large apparent diameter of the Vela SNR has made it difficult to detect gamma-ray emission from the SNR due to the treatment of the Galactic diffuse background and overlapping sources in the line of sight. In Chapter 5, we succeed in claiming the detection of GeV gamma-ray emissions extending over the entire region of the Vela SNR with *Fermi*-LAT using $\sim$ 12 years of data for the first time. The size of the spatially extended gamma-ray emission was found to be comparable to that of X-rays. The large extended gamma-ray emission allows us to perform a spatially resolved analysis for 50 regions with a unit area of $1^\circ \times 1^\circ$. The photon flux of each region in the $1 - 500$ GeV band is in the range of $(0.2 - 3.5) \times 10^{-9}$ cm^{-2}s^{-1}. The photon index of each region differs widely from 1.5 to 3.0, and the spectra with harder indices ($\Gamma \lesssim 2.0$) are found in $\sim$ 33% of southwest regions. The northeast regions were found to be relatively brighter than the southwest region. This characteristic of the spatial distribution is reminiscent of the spatial pattern seen in the radio continuum emission and thermal X-ray emission. The total energy flux of the entire analysis region is $(2.07 \pm 0.12) \times 10^{-10}$ erg cm^{-2}s^{-1}, corresponding to the luminosity of $(2.04 \pm 0.12) \times 10^{33}$ erg s^{-1} (assumed the distance of 287 pc). The gamma-ray spectrum of the southwest region could be explained by the inverse Compton scattering. In this case, the maximum energy of the electrons is at least a few TeV. In contrast to the typical steep spectrum of middle-aged SNRs, the spectrum of the Vela SNR appears to extend into TeV energies. It is unlikely to accelerate the electrons up to such high energies at the outer shock waves of a middle-aged SNR. The Vela X, which is located inside the Vela SNR, is a plausible source of energetic electrons and also positrons.

We found the presence of very high-energy electrons in the nearby SNR. Accelerated electrons are observed as cosmic rays when they can travel from SNRs to Earth without significant energy loss. To study the energy dissipation inside SNRs due to radiation loss, interactions with the circumstellar medium, and so on, RX J1713.7$-$3946 is one of the best targets because of its strong synchrotron X-ray radiation emitted by very high-energy electrons and accumulated *Chandra* observations. In particular, the bright northwest rim is a characteristic region where several X-ray filaments are observed. In the northwest region, many point-like X-ray sources (hotspots) are apparent in the observed image, but have been ignored in previous X-ray analyses. In Chapter 6, we report, for the first time, a bunch of hotspots likely associated with the SNR. The spectra of the hotspots are well described by an absorbed power-law model with widely distributed parameters of $N_{\mathrm{H}} \sim 10^{21}$-$- 10^{23}$ cm^{-2} and $\Gamma \sim 0.5 - 6$. These parameters show the larger N_{H} for the smaller Γ, and are completely different from those in the remnant. We also found that X-ray intensities of about one-third of the 65 hotspots were variable on yearly scale, and eight hotspots showed monthly variabilities. We suggest that these hotspots are attributed to the synchrotron X-ray radiation resulting from the interaction between the SNR shock and the dense molecular cores. The synchrotron radiation in the shock-core interaction originates from the accelerated electrons interacting with the core (primary electron origin) and/or electrons produced via accelerated protons colliding with the core (secondary electron origin). Recently, dense molecular cloudlets are discovered in the vicinity of the hotspots with ALMA observations. Their findings reinforce our understanding of the mechanism of X-ray hotspots.

To study the acceleration of electrons in the different systems, the SS 433/W50 system is a distinctive target. This system has a microquasar SS 433, and its black hole jets interact with SNR W50 which is expanding around the jets. After the detection of TeV gamma-ray emission with HAWC, the system become one of the notable electron accelerators. X-ray hotspots are detected in the eastern ear where the radio continuum has also peak emission. In Chapter 7, using about 12.5 years of the *Fermi*-LAT data, we conduct a gamma-ray analysis at the position of the X-ray hotspots in the eastern terminal region of the system. Significant gamma-ray emission is not detected from the position of the hotspot. Considering the controversial previous studies in the GeV band, the accurate upper limits are derived for the first time. The electron spectrum is expected by the modeling of the multi-wavelength data of radio, X-ray, and gamma-ray upper limits. At the position of the hotspot, the electrons are accelerated to very high energy.

Throughout these results, what are clarified in this thesis is summarized as follows. First, the existence of the very high-energy electrons is indicated by the firm detection of the gamma-ray emission and its detailed analysis from the Vela SNR, suggesting that a nearby SNR can explain the positron excess. Second, the nature of the hotspots in RX J1713.7−3946 is uncovered by the detailed X-ray analysis, showing that they are created by the shock-cloud interaction. Lastly, the gamma-ray emission from the hotspot in the putative PeVatron source, SS 433/W50 system, is carefully constrained by using 12.5-year gamma-ray data, implying that the hotspot in such a complicated system can be one of the cosmic-ray accelerators. Our findings and future X-ray and TeV gamma-ray missions will help to estimate the contribution of the SNRs to the cosmic-ray electrons. It may leading to unveil the origin of the positron excess.

References

Abdo, A. A. et al. (May 2009a). “Fermi Large Area Telescope Observations of the Vela Pulsar”. In: *ApJ* 696.2, pp. 1084–1093. DOI: `10.1088/0004-637X/696/2/1084`. arXiv: `0812.2960 [astro-ph]`.

Abdo, A. A. et al. (Nov. 2009b). “Fermi LAT Discovery of Extended Gamma-Ray Emission in the Direction of Supernova Remnant W51C”. In: *ApJL* 706.1, pp. L1–L6. DOI: `10.1088/0004-637X/706/1/L1`. arXiv: `0910.0908 [astro-ph.HE]`.

Abdo, A. A. et al. (May 2009c). “Measurement of the Cosmic Ray $e^{+}+e^{-}$ Spectrum from 20GeV to 1TeV with the Fermi Large Area Telescope”. In: *Phys. Rev. Lett.* 102.18, 181101, p. 181101. DOI: `10.1103/PhysRevLett.102.181101`. arXiv: `0905.0025 [astro-ph.HE]`.

Abdo, A. A. et al. (Apr. 2010a). “Fermi Large Area Telescope Observations of the Vela-X Pulsar Wind Nebula”. In: *ApJ* 713.1, pp. 146–153. DOI: `10.1088/0004-637X/713/1/146`. arXiv: `1002.4383 [astro-ph.HE]`.

Abdo, A. A. et al. (Feb. 2010b). “Gamma-Ray Emission from the Shell of Supernova Remnant W44 Revealed by the Fermi LAT”. In: *Science* 327.5969, p. 1103. DOI: `10.1126/science.1182787`.

Abdo, A. A. et al. (Mar. 2010c). “Observation of Supernova Remnant IC 443 with the Fermi Large Area Telescope”. In: *ApJ* 712.1, pp. 459–468. DOI: `10.1088/0004-637X/712/1/459`. arXiv: `1002.2198 [astro-ph.HE]`.

Abdo, A. A. et al. (Apr. 2010d). “The Vela Pulsar: Results from the First Year of Fermi LAT Observations”. In: *ApJ* 713.1, pp. 154–165. DOI: `10.1088/0004-637X/713/1/154`. arXiv: `1002.4050 [astro-ph.HE]`.

Abdo, A. A. et al. (June 2011). “Observations of the Young Supernova Remnant RX J1713.7-3946 with the Fermi Large Area Telescope”. In: *ApJ* 734, 28, p. 28. DOI: `10.1088/0004-637X/734/1/28`. arXiv: `1103.5727 [astro-ph.HE]`.

Abdo, A. A. et al. (Oct. 2013). “The Second Fermi Large Area Telescope Catalog of Gamma-Ray Pulsars”. In: *ApJS* 208.2, 17, p. 17. DOI: `10.1088/0067-0049/208/2/17`. arXiv: `1305.4385 [astro-ph.HE]`.

Abdollahi, S. et al. (Apr. 2017). “Cosmic-ray electron-positron spectrum from 7 GeV to 2 TeV with the Fermi Large Area Telescope”. In: *Phys. Rev. D* 95.8, 082007, p. 082007. DOI: `10.1103/PhysRevD.95.082007`. arXiv: `1704.07195 [astro-ph.HE]`.

Abdollahi, S. et al. (Mar. 2020). “Fermi Large Area Telescope Fourth Source Catalog”. In: *ApJS* 247.1, 33, p. 33. DOI: `10.3847/1538-4365/ab6bcb`. arXiv: `1902.10045 [astro-ph.HE]`.

Abdollahi, S. et al. (July 2022). "Search for New Cosmic-Ray Acceleration Sites within the 4FGL Catalog Galactic Plane Sources". In: *ApJ* 933.2, 204, p. 204. DOI: 10.3847/1538-4357/ac704f. arXiv: 2205.03111 [astro-ph.HE].

Abeysekara, A. U. et al. (Nov. 2017). "Extended gamma-ray sources around pulsars constrain the origin of the positron flux at Earth". In: *Science* 358.6365, pp. 911–914. DOI: 10.1126/science.aan4880. arXiv: 1711.06223 [astro-ph.HE].

Abeysekara, A. U. et al. (Oct. 2018). "Very-high-energy particle acceleration powered by the jets of the microquasar SS 433". In: *Nature* 562.7725, pp. 82–85. DOI: 10.1038/s41586-018-0565-5.

Abeysekara, A. U. et al. (May 2020). "Evidence for Proton Acceleration up to TeV Energies Based on VERITAS and Fermi-LAT Observations of the Cas A SNR". In: *ApJ* 894.1, 51, p. 51. DOI: 10.3847/1538-4357/ab8310. arXiv: 2003.13615 [astro-ph.HE].

Abramowski, A. et al. (Dec. 2012). "Probing the extent of the non-thermal emission from the Vela X region at TeV energies with H.E.S.S." In: *A&A* 548, A38, A38. DOI: 10.1051/0004-6361/201219919. arXiv: 1210.1359 [astro-ph.HE].

Acciari, V. A. et al. (Sept. 2009). "Detection of Extended VHE Gamma Ray Emission from G106.3+2.7 with Veritas". In: *ApJL* 703.1, pp. L6–L9. DOI: 10.1088/0004-637X/703/1/L6. arXiv: 0911.4695 [astro-ph.HE].

Acero, F. et al. (Jan. 2017a). "Measurement of the X-ray proper motion in the south-east rim of RX J1713.7-3946". In: *A&A* 597, A106, A106. DOI: 10.1051/0004-6361/201629618. arXiv: 1610.01605 [astro-ph.HE].

Acero, F. et al. (May 2017b). "Prospects for Cherenkov Telescope Array Observations of the Young Supernova Remnant RX J1713.7-3946". In: *ApJ* 840, 74, p. 74. DOI: 10.3847/1538-4357/aa6d67. arXiv: 1704.04136 [astro-ph.HE].

Ackermann, M. et al. (Nov. 2010). "Fermi LAT observations of cosmic-ray electrons from 7 GeV to 1 TeV". In: *Phys. Rev. D* 82.9, 092004, p. 092004. DOI: 10.1103/PhysRevD.82.092004. arXiv: 1008.3999 [astro-ph.HE].

Ackermann, M. et al. (Jan. 2012). "Measurement of Separate Cosmic-Ray Electron and Positron Spectra with the Fermi Large Area Telescope". In: *Phys. Rev. Lett.* 108.1, 011103, p. 011103. DOI: 10.1103/PhysRevLett.108.011103. arXiv: 1109.0521 [astro-ph.HE].

Ackermann, M. et al. (2013). "Detection of the Characteristic Pion-Decay Signature in Supernova Remnants". In: *Science* 339.6121, pp. 807–811. DOI: 10.1126/science.1231160. arXiv: 1302.3307 [astro-ph.HE].

Ackermann, M. et al. (July 2017). "Search for Extended Sources in the Galactic Plane Using Six Years of Fermi-Large Area Telescope Pass 8 Data above 10 GeV". In: *ApJ* 843.2, 139, p. 139. DOI: 10.3847/1538-4357/aa775a. arXiv: 1702.00476 [astro-ph.HE].

Adriani, O. et al. (Apr. 2009). "An anomalous positron abundance in cosmic rays with energies 1.5-100GeV". In: *Nature* 458.7238, pp. 607–609. DOI: 10.1038/nature07942. arXiv: 0810.4995 [astro-ph].

Adriani, O. et al. (May 2011). “Cosmic-Ray Electron Flux Measured by the PAMELA Experiment between 1 and 625 GeV”. In: *Phys. Rev. Lett.* 106.20, 201101, p. 201101. DOI: `10.1103/PhysRevLett.106.201101`. arXiv: `1103.2880 [astro-ph.HE]`.

Adriani, O. et al. (Aug. 2013). “Cosmic-Ray Positron Energy Spectrum Measured by PAMELA”. In: *Phys. Rev. Lett.* 111.8, 081102, p. 081102. DOI: `10.1103/PhysRevLett.111.081102`. arXiv: `1308.0133 [astro-ph.HE]`.

Adriani, O. et al. (Nov. 2017). “Energy Spectrum of Cosmic-Ray Electron and Positron from 10 GeV to 3 TeV Observed with the Calorimetric Electron Telescope on the International Space Station”. In: *Phys. Rev. Lett.* 119.18, 181101, p. 181101. DOI: `10.1103/PhysRevLett.119.181101`. arXiv: `1712.01711 [astro-ph.HE]`.

Adriani, O. et al. (June 2018). “Extended Measurement of the Cosmic-Ray Electron and Positron Spectrum from 11 GeV to 4.8 TeV with the Calorimetric Electron Telescope on the International Space Station”. In: *Phys. Rev. Lett.* 120.26, 261102, p. 261102. DOI: `10.1103/PhysRevLett.120.261102`. arXiv: `1806.09728 [astro-ph.HE]`.

Aguilar, M. et al. (2013). “First Result from the Alpha Magnetic Spectrometer on the International Space Station: Precision Measurement of the Positron Fraction in Primary Cosmic Rays of 0.5-350 GeV”. In: *Phys. Rev. Lett.* 110.14, 141102, p. 141102. DOI: `10.1103/PhysRevLett.110.141102`.

Aguilar, M. et al. (Nov. 2014). “Precision Measurement of the (e^{+}+e^{-}) Flux in Primary Cosmic Rays from 0.5 GeV to 1 TeV with the Alpha Magnetic Spectrometer on the International Space Station”. In: *Phys. Rev. Lett.* 113.22, 221102, p. 221102. DOI: `10.1103/PhysRevLett.113.221102`.

Aguilar, M. et al. (2015). “Precision Measurement of the Proton Flux in Primary Cosmic Rays from Rigidity 1 GV to 1.8 TV with the Alpha Magnetic Spectrometer on the International Space Station”. In: *Phys. Rev. Lett.* 114.17, 171103, p. 171103. DOI: `10.1103/PhysRevLett.114.171103`.

Aguilar, M. et al. (2017). “Observation of the Identical Rigidity Dependence of He, C, and O Cosmic Rays at High Rigidities by the Alpha Magnetic Spectrometer on the International Space Station”. In: *Phys. Rev. Lett.* 119.25, 251101, p. 251101. DOI: `10.1103/PhysRevLett.119.251101`.

Aguilar, M. et al. (Mar. 2019a). “Towards Understanding the Origin of Cosmic-Ray Electrons”. In: *Phys. Rev. Lett.* 122.10, 101101, p. 101101. DOI: `10.1103/PhysRevLett.122.101101`.

Aguilar, M. et al. (Feb. 2019b). “Towards Understanding the Origin of Cosmic-Ray Positrons”. In: *Phys. Rev. Lett.* 122.4, 041102, p. 041102. DOI: `10.1103/PhysRevLett.122.041102`.

Aharonian, F. et al. (2005). “Detection of TeV γ-ray emission from the shell-type supernova remnant RX J0852.0-4622 with HESS”. In: *A&A* 437.1, pp. L7–L10. DOI: `10.1051/0004-6361:200500130`. arXiv: `astro-ph/0505380 [astro-ph]`.

Aharonian, F. et al. (Apr. 2006a). "A detailed spectral and morphological study of the gamma-ray supernova remnant RX J1713.7-3946 with HESS". In: *A&A* 449, pp. 223–242. DOI: `10.1051/0004-6361:20054279`. eprint: `astro-ph/0511678`.

Aharonian, F. et al. (Mar. 2006b). "First detection of a VHE gamma-ray spectral maximum from a cosmic source: HESS discovery of the Vela X nebula". In: *A&A* 448.2, pp. L43–L47. DOI: `10.1051/0004-6361:200600014`. arXiv: `astro-ph/0601575 [astro-ph]`.

Aharonian, F. et al. (2007a). "H.E.S.S. Observations of the Supernova Remnant RX J0852.0-4622: Shell-Type Morphology and Spectrum of a Widely Extended Very High Energy Gamma-Ray Source". In: *ApJ* 661.1, pp. 236–249. DOI: `10.1086/512603`. arXiv: `astro-ph/0612495 [astro-ph]`.

Aharonian, F. et al. (Mar. 2007b). "Primary particle acceleration above 100 TeV in the shell-type supernova remnant RX J1713.7-3946 with deep HESS observations". In: *A&A* 464, pp. 235–243. DOI: `10.1051/0004-6361:20066381`. eprint: `astro-ph/0611813`.

Aharonian, F. et al. (Apr. 2008a). "Discovery of very high energy gamma-ray emission coincident with molecular clouds in the W 28 (G6.4-0.1) field". In: *A&A* 481.2, pp. 401–410. DOI: `10.1051/0004-6361:20077765`. arXiv: `0801.3555 [astro-ph]`.

Aharonian, F. et al. (Dec. 2008b). "Energy Spectrum of Cosmic-Ray Electrons at TeV Energies". In: *Phys. Rev. Lett.* 101.26, 261104, p. 261104. DOI: `10.1103/PhysRevLett.101.261104`. arXiv: `0811.3894 [astro-ph]`.

Aharonian, F. et al. (Dec. 2009). "Probing the ATIC peak in the cosmic-ray electron spectrum with H.E.S.S." In: *A&A* 508.2, pp. 561–564. DOI: `10.1051/0004-6361/200913323`. arXiv: `0905.0105 [astro-ph.HE]`.

Aharonian, F. A. and A. M. Atoyan (Nov. 1991). "Cosmic ray positrons connected with galactic gamma radiation of high and very high energies". In: *Journal of Physics G Nuclear Physics* 17.11, pp. 1769–1778. DOI: `10.1088/0954-3899/17/11/021`.

Aharonian, F. A., A. M. Atoyan, and H. J. Voelk (Feb. 1995). "High energy electrons and positrons in cosmic rays as an indicator of the existence of a nearby cosmic tevatron". In: *A&A* 294, pp. L41–L44.

Aharonian, F. A. et al. (Nov. 2004). "High-energy particle acceleration in the shell of a supernova remnant". In: *Nature* 432, pp. 75–77. DOI: `10.1038/nature02960`. eprint: `astro-ph/0411533`.

Ahnen, M. L. et al. (2017). "A cut-off in the TeV gamma-ray spectrum of the SNR Cassiopeia A". In: *MNRAS* 472.3, pp. 2956–2962. DOI: `10.1093/mnras/stx2079`. arXiv: `1707.01583 [astro-ph.HE]`.

Albert, A. et al. (June 2020). "HAWC J2227+610 and Its Association with G106.3+2.7, a New Potential Galactic PeVatron". In: *ApJL* 896.2, L29, p. L29. DOI: `10.3847/2041-8213/ab96cc`. arXiv: `2005.13699 [astro-ph.HE]`.

Alvarez, H. et al. (June 2001). “The radio spectral index of the Vela supernova remnant”. In: *A&A* 372, pp. 636–643. DOI: 10.1051/0004-6361:20010509.

Ambrogi, L., S. Celli, and F. Aharonian (July 2018). “On the potential of Cherenkov Telescope Arrays and KM3 Neutrino Telescopes for the detection of extended sources”. In: *Astroparticle Physics* 100, pp. 69–79. DOI: 10.1016/j.astropartphys.2018.03.001. arXiv: 1803.03565 [astro-ph.HE].

Aschenbach, B., R. Egger, and J. Trümper (Feb. 1995). “Discovery of explosion fragments outside the Vela supernova remnant shock-wave boundary”. In: *Nature* 373.6515, pp. 587–590. DOI: 10.1038/373587a0.

Aschenbach, Bernd (1998). “Discovery of a young nearby supernova remnant”. In: *Nature* 396.6707, pp. 141–142. DOI: 10.1038/24103.

Atoyan, A. M., F. A. Aharonian, and H. J. Völk (Sept. 1995). “Electrons and positrons in the galactic cosmic rays”. In: *Phys. Rev. D* 52.6, pp. 3265–3275. DOI: 10.1103/PhysRevD.52.3265.

Atwood, W. B. et al. (June 2009). “The Large Area Telescope on the Fermi Gamma-Ray Space Telescope Mission”. In: *ApJ* 697.2, pp. 1071–1102. DOI: 10.1088/0004-637X/697/2/1071. arXiv: 0902.1089 [astro-ph.IM].

Axford, W. I., E. Leer, and G. Skadron (Jan. 1977). “The Acceleration of Cosmic Rays by Shock Waves”. In: *International Cosmic Ray Conference*. Vol. 11. International Cosmic Ray Conference, p. 132.

Baade, W. and F. Zwicky (July 1934). “Remarks on Super-Novae and Cosmic Rays”. In: *Physical Review* 46.1, pp. 76–77. DOI: 10.1103/PhysRev.46.76.2.

Bai, Yang, Joshua Berger, and Sida Lu (June 2018). “Supersymmetric resonant dark matter: A thermal model for the AMS-02 positron excess”. In: *Phys. Rev. D* 97.11, 115012, p. 115012. DOI: 10.1103/PhysRevD.97.115012. arXiv: 1706.09974 [hep-ph].

Ballet, J. et al. (May 2020). “Fermi Large Area Telescope Fourth Source Catalog Data Release 2”. In: *arXiv e-prints*, arXiv:2005.11208, arXiv:2005.11208. arXiv: 2005.11208 [astro-ph.HE].

Becker, Werner et al. (Aug. 2012). “The Proper Motion of the Central Compact Object RX J0822-4300 in the Supernova Remnant Puppis A”. In: *ApJ* 755.2, 141, p. 141. DOI: 10.1088/0004-637X/755/2/141. arXiv: 1204.3510 [astro-ph.HE].

Bell, A. R. (Feb. 1978). “The acceleration of cosmic rays in shock fronts. II”. In: *MNRAS* 182, pp. 443–455. DOI: 10.1093/mnras/182.3.443.

Blair, William P., Ravi Sankrit, and John C. Raymond (May 2005). “Hubble Space Telescope Imaging of the Primary Shock Front in the Cygnus Loop Supernova Remnant”. In: *AJ* 129.5, pp. 2268–2280. DOI: 10.1086/429381.

Blandford, R. D. and J. P. Ostriker (Apr. 1978). “Particle acceleration by astrophysical shocks”. In: *ApJL* 221, pp. L29–L32. DOI: 10.1086/182658.

Blum, Kfir, Boaz Katz, and Eli Waxman (Nov. 2013). “AMS-02 Results Support the Secondary Origin of Cosmic Ray Positrons”. In: *Phys. Rev. Lett.* 111.21, 211101, p. 211101. DOI: 10.1103/PhysRevLett.111.211101. arXiv: 1305.1324 [astro-ph.HE].

Blumenthal, George R. and Robert J. Gould (Jan. 1970). “Bremsstrahlung, Synchrotron Radiation, and Compton Scattering of High-Energy Electrons Traversing Dilute Gases”. In: *Reviews of Modern Physics* 42.2, pp. 237–271. DOI: `10.1103/RevModPhys.42.237`.

Blümer, Johannes, Ralph Engel, and Jörg R. Hörand el (2009). “Cosmic rays from the knee to the highest energies”. In: *Progress in Particle and Nuclear Physics* 63.2, pp. 293–338. DOI: `10.1016/j.ppnp.2009.05.002`. arXiv: `0904.0725 [astro-ph.HE]`.

Boezio, M. et al. (Mar. 2000). “The Cosmic-Ray Electron and Positron Spectra Measured at 1 AU during Solar Minimum Activity”. In: *ApJ* 532.1, pp. 653–669. DOI: `10.1086/308545`.

Bordas, Pol (Jan. 2020). “Gamma-ray echoes from SS 433”. In: *Nature Astronomy* 4, pp. 1132–1133. DOI: `10.1038/s41550-020-1186-0`. arXiv: `2008.12047 [astro-ph.HE]`.

Cao, Zhen et al. (June 2021). “Ultrahigh-energy photons up to 1.4 petaelectronvolts from 12 γ-ray Galactic sources”. In: *Nature* 594.7861, pp. 33–36. DOI: `10.1038/s41586-021-03498-z`.

Cassam-Chenaï, G. et al. (Nov. 2004). “XMM-Newton observations of the supernova remnant RX J1713.7-3946 and its central source”. In: *A&A* 427, pp. 199–216. DOI: `10.1051/0004-6361:20041154`. eprint: `astro-ph/0407333`.

Celli, S. et al. (2019). “Supernova remnants in clumpy media: particle propagation and gamma-ray emission”. In: *MNRAS* 487.3, pp. 3199–3213. DOI: `10.1093/mnras/stz1425`. arXiv: `1804.10579 [astro-ph.HE]`.

Chang, J. et al. (Nov. 2008). “An excess of cosmic ray electrons at energies of 300-800GeV”. In: *Nature* 456.7220, pp. 362–365. DOI: `10.1038/nature07477`.

Chen, Chuan-Hung, Cheng-Wei Chiang, and Takaaki Nomura (July 2015). “Dark matter for excess of AMS-02 positrons and antiprotons”. In: *Physics Letters B* 747, pp. 495–499. DOI: `10.1016/j.physletb.2015.06.035`. arXiv: `1504.07848 [hep-ph]`.

Cowsik, R., B. Burch, and T. Madziwa-Nussinov (May 2014). “The Origin of the Spectral Intensities of Cosmic-Ray Positrons”. In: *ApJ* 786.2, 124, p. 124. DOI: `10.1088/0004-637X/786/2/124`. arXiv: `1305.1242 [astro-ph.HE]`.

Dame, T. M., Dap Hartmann, and P. Thaddeus (Feb. 2001). “The Milky Way in Molecular Clouds: A New Complete CO Survey”. In: *ApJ* 547.2, pp. 792–813. DOI: `10.1086/318388`. arXiv: `astro-ph/0009217 [astro-ph]`.

DAMPE Collaboration et al. (Dec. 2017). “Direct detection of a break in the teraelectronvolt cosmic-ray spectrum of electrons and positrons”. In: *Nature* 552.7683, pp. 63–66. DOI: `10.1038/nature24475`. arXiv: `1711.10981 [astro-ph.HE]`.

Ding, Yu-Chen et al. (June 2021). “Implications of a possible TeV break in the cosmic-ray electron and positron flux”. In: *Phys. Rev. D* 103.11, 115010, p. 115010. DOI: `10.1103/PhysRevD.103.115010`. arXiv: `2007.00703 [astro-ph.HE]`.

Dodson, R. et al. (Oct. 2003). “The Vela Pulsar’s Proper Motion and Parallax Derived from VLBI Observations”. In: *ApJ* 596.2, pp. 1137–1141. DOI: `10.1086/378089`. arXiv: `astro-ph/0302374 [astro-ph]`.

Dubner, G. et al. (July 2013). “The most complete and detailed X-ray view of the SNR Puppis A”. In: *A&A* 555, A9, A9. DOI: 10.1051/0004-6361/201321401. arXiv: 1305.1275 [astro-ph.GA].

Dubner, G. M. and E. M. Arnal (Nov. 1988). “Neutral hydrogen and carbon monoxide observations towards the SNR Puppis A.” In: *A&AS* 75, pp. 363–369.

Dubner, G. M. et al. (Aug. 1998). “Neutral Hydrogen in the Direction of the VELA Supernova Remnant”. In: *AJ* 116.2, pp. 813–822. DOI: 10.1086/300466.

Eagle, J. et al. (Jan. 2019). “2FHL J0826.1-4500: Discovery of a Possible Shock-Cloud Interaction on the Western Edge of the Vela Supernova Remnant”. In: *ApJ* 870.1, 35, p. 35. DOI: 10.3847/1538-4357/aaf0ff. arXiv: 1811.05898 [astro-ph.HE].

Earl, James A. (Feb. 1961). “Cloud-Chamber Observations of Primary Cosmic-Ray Electrons”. In: *Phys. Rev. Lett.* 6.3, pp. 125–128. DOI: 10.1103/PhysRevLett.6.125.

Ellison, D. C. et al. (Mar. 2010). “Efficient Cosmic Ray Acceleration, Hydrodynamics, and Self-Consistent Thermal X-Ray Emission Applied to Supernova Remnant RX J1713.7-3946”. In: *ApJ* 712, pp. 287–293. DOI: 10.1088/0004-637X/712/1/287. arXiv: 1001.1932 [astro-ph.HE].

Fang, Ke, Eric Charles, and Roger D. Blandford (Jan. 2020). “GeV-TeV Counterparts of SS 433/W50 from Fermi-LAT and HAWC Observations”. In: *ApJL* 889.1, L5, p. L5. DOI: 10.3847/2041-8213/ab62b8. arXiv: 2001.03599 [astro-ph.HE].

Fang, Ke et al. (2022). “Evidence for PeV Proton Acceleration from Fermi-LAT Observations of SNR G106.3 + 2.7”. In: *Phys. Rev. Lett.* 129 (7), p. 071101. DOI: 10.1103/PhysRevLett.129.071101. URL: https://link.aps.org/doi/10.1103/PhysRevLett.129.071101.

FERMI-LAT Collaboration et al. (Apr. 2022). “A gamma-ray pulsar timing array constrains the nanohertz gravitational wave background”. In: *Science* 376.6592, pp. 521–523. DOI: 10.1126/science.abm3231. arXiv: 2204.05226 [astro-ph.HE].

Fesen, R. A. et al. (Feb. 2012). “The SN 393-SNR RX J1713.7-3946 (G347.3-0.5) Connection”. In: *AJ* 143, 27, p. 27. DOI: 10.1088/0004-6256/143/2/27. arXiv: 1112.0593 [astro-ph.HE].

Freeman, P. E. et al. (Jan. 2002). “A Wavelet-Based Algorithm for the Spatial Analysis of Poisson Data”. In: *ApJS* 138, pp. 185–218. DOI: 10.1086/324017. eprint: astro-ph/0108429.

Fukui, Y. et al. (Oct. 2003). “Discovery of Interacting Molecular Gas toward the TeV Gamma-Ray Peak of the SNR G 347.3–0.5”. In: *PASJ* 55, pp. L61–L64. DOI: 10.1093/pasj/55.5.L61.

Fukui, Y. et al. (Feb. 2012). “A Detailed Study of the Molecular and Atomic Gas toward the γ-Ray Supernova Remnant RX J1713.7-3946: Spatial TeV γ-Ray and Interstellar Medium Gas Correspondence”. In: *ApJ* 746, 82, p. 82. DOI: 10.1088/0004-637X/746/1/82. arXiv: 1107.0508.

Funk, Stefan (2015). “Ground- and Space-Based Gamma-Ray Astronomy”. In: *Annual Review of Nuclear and Particle Science* 65, pp. 245–277. DOI: 10.1146/annurev-nucl-102014-022036. arXiv: 1508.05190 [astro-ph.HE].

Gabici, S. and F. A. Aharonian (Nov. 2014). “Hadronic gamma-rays from RX J1713.7-3946?” In: *MNRAS* 445, pp. L70–L73. DOI: 10.1093/mnrasl/slu132. arXiv: 1406.2322 [astro-ph.HE].

Giacconi, Riccardo et al. (Dec. 1962). “Evidence for x Rays From Sources Outside the Solar System”. In: *Phys. Rev. Lett.* 9.11, pp. 439–443. DOI: 10.1103/PhysRevLett.9.439.

Ginzburg, V. L. and S. I. Syrovatsky (Jan. 1961). “Origin of Cosmic Rays”. In: *Progress of Theoretical Physics Supplement* 20, pp. 1–83. DOI: 10.1143/PTPS.20.1.

Golden, R. L. et al. (Dec. 1987). “Observation of cosmic ray positrons in the region from 5 to 50 GeV”. In: *A&A* 188.1, pp. 145–154.

Grondin, M. H. et al. (Sept. 2013). “The Vela-X Pulsar Wind Nebula Revisited with Four Years of Fermi Large Area Telescope Observations”. In: *ApJ* 774.2, 110, p. 110. DOI: 10.1088/0004-637X/774/2/110. arXiv: 1307.5480 [astro-ph.HE].

H. E. S. S. Collaboration et al. (Feb. 2015). “H.E.S.S. reveals a lack of TeV emission from the supernova remnant Puppis A”. In: *A&A* 575, A81, A81. DOI: 10.1051/0004-6361/201424805. arXiv: 1412.6997 [astro-ph.HE].

H. E. S. S. Collaboration et al. (July 2019). “H.E.S.S. and Suzaku observations of the Vela X pulsar wind nebula”. In: *A&A* 627, A100, A100. DOI: 10.1051/0004-6361/201935458. arXiv: 1905.07975 [astro-ph.HE].

Hanabata, Y. et al. (May 2014). “Detailed Investigation of the Gamma-Ray Emission in the Vicinity of SNR W28 with FERMI-LAT”. In: *ApJ* 786.2, 145, p. 145. DOI: 10.1088/0004-637X/786/2/145. arXiv: 1403.6878 [astro-ph.HE].

Hartman, R. C. et al. (July 1999). “The Third EGRET Catalog of High-Energy Gamma-Ray Sources”. In: *ApJS* 123.1, pp. 79–202. DOI: 10.1086/313231.

Hayakawa, Ryota et al. (June 2022). “X-ray hot spots in the eastern ear of the supernova remnant W 50 and the microquasar SS 433 system”. In: *PASJ* 74.3, pp. 510–520. DOI: 10.1093/pasj/psac011.

Hayakawa, S. (Nov. 1952). “Propagation of the Cosmic Radiation through Intersteller Space”. In: *Progress of Theoretical Physics* 8.5, pp. 571–572. DOI: 10.1143/ptp/8.5.571.

— (Feb. 1956). “Supernova Origin of Cosmic Rays”. In: *Progress of Theoretical Physics* 15.2, pp. 111–121. DOI: 10.1143/PTP.15.111.

H.E.S.S. Collaboration et al. (2018a). “Deeper H.E.S.S. observations of Vela Junior (RX J0852.0-4622): Morphology studies and resolved spectroscopy”. In: *A&A* 612, A7, A7. DOI: 10.1051/0004-6361/201630002. arXiv: 1611.01863 [astro-ph.HE].

H.E.S.S. Collaboration et al. (Apr. 2018b). “H.E.S.S. observations of RX J1713.7-3946 with improved angular and spectral resolution: Evidence for gamma-ray emission extending beyond the X-ray emitting shell”. In: *A&A* 612, A6, A6. DOI: 10.1051/0004-6361/201629790. arXiv: 1609.08671 [astro-ph.HE].

Hewitt, J. W. et al. (Nov. 2012). “Fermi-LAT and WMAP Observations of the Puppis A Supernova Remnant”. In: *ApJ* 759.2, 89, p. 89. DOI: `10.1088/0004-637X/759/2/89`.

HI4PI Collaboration et al. (Oct. 2016). “HI4PI: A full-sky H I survey based on EBHIS and GASS”. In: *A&A* 594, A116, A116. DOI: `10.1051/0004-6361/201629178`. arXiv: `1610.06175 [astro-ph.GA]`.

Hiraga, J. S. et al. (Mar. 2005). “Spectral properties of nonthermal X-ray emission from the shell-type SNR RX J1713.7 3946 as revealed by XMM-Newton”. In: *A&A* 431, pp. 953–961. DOI: `10.1051/0004-6361:20047015`. eprint: `astro-ph/0407401`.

Hobbs, G. B., R. T. Edwards, and R. N. Manchester (June 2006). “TEMPO2, a new pulsar-timing package - I. An overview”. In: *MNRAS* 369.2, pp. 655–672. DOI: `10.1111/j.1365-2966.2006.10302.x`. arXiv: `astro-ph/0603381 [astro-ph]`.

Hooper, Dan et al. (Nov. 2017). “HAWC observations strongly favor pulsar interpretations of the cosmic-ray positron excess”. In: *Phys. Rev. D* 96.10, 103013, p. 103013. DOI: `10.1103/PhysRevD.96.103013`. arXiv: `1702.08436 [astro-ph.HE]`.

Huang, Yan et al. (Mar. 2020). “Secondary-electron radiation accompanying hadronic GeV-TeV gamma-rays from supernova remnants”. In: *MNRAS* 492.3, pp. 4246–4253. DOI: `10.1093/mnras/staa019`.

Huang, Zhi-Qiu et al. (Oct. 2018). “Inefficient Cosmic-Ray Diffusion around Vela X: Constraints from H.E.S.S. Observations of Very High-energy Electrons”. In: *ApJ* 866.2, 143, p. 143. DOI: `10.3847/1538-4357/aadfed`. arXiv: `1807.04182 [astro-ph.HE]`.

Hwang, Una, Kathryn A. Flanagan, and Robert Petre (Dec. 2005). “Chandra X-Ray Observation of a Mature Cloud-Shock Interaction in the Bright Eastern Knot Region of Puppis A”. In: *ApJ* 635.1, pp. 355–364. DOI: `10.1086/497298`. arXiv: `astro-ph/0508243 [astro-ph]`.

Hwang, Una, Robert Petre, and Kathryn A. Flanagan (Mar. 2008). “X-Ray-emitting Ejecta in Puppis A Observed with Suzaku”. In: *ApJ* 676.1, pp. 378–389. DOI: `10.1086/528925`. arXiv: `0712.3208 [astro-ph]`.

Inoue, T. et al. (Jan. 2012). “Toward Understanding the Cosmic-Ray Acceleration at Young Supernova Remnants Interacting with Interstellar Clouds: Possible Applications to RX J1713.7-3946”. In: *ApJ* 744, 71, p. 71. DOI: `10.1088/0004-637X/744/1/71`. arXiv: `1106.3080 [astro-ph.HE]`.

Jogler, T. and S. Funk (2016). “Revealing W51C as a Cosmic Ray Source Using Fermi-LAT Data”. In: *ApJ* 816.2, 100, p. 100. DOI: `10.3847/0004-637X/816/2/100`.

Jones, Frank C. (Mar. 1968). “Calculated Spectrum of Inverse-Compton-Scattered Photons”. In: *Physical Review* 167.5, pp. 1159–1169. DOI: `10.1103/PhysRev.167.1159`.

Kachelrieß, M., A. Neronov, and D. V. Semikoz (Mar. 2018). “Cosmic ray signatures of a 2-3 Myr old local supernova”. In: *Phys. Rev. D* 97.6, 063011, p. 063011. DOI: `10.1103/PhysRevD.97.063011`. arXiv: `1710.02321 [astro-ph.HE]`.

Kafexhiu, Ervin et al. (Dec. 2014). “Parametrization of gamma-ray production cross sections for p p interactions in a broad proton energy range from the kinematic threshold to PeV energies”. In: *Phys. Rev. D* 90.12, 123014, p. 123014. DOI: `10.1103/PhysRevD.90.123014`. arXiv: `1406.7369 [astro-ph.HE]`.

Katagiri, H. et al. (Nov. 2011). “Fermi Large Area Telescope Observations of the Cygnus Loop Supernova Remnant”. In: *ApJ* 741.1, 44, p. 44. DOI: `10.1088/0004-637X/741/1/44`. arXiv: `1108.1833 [astro-ph.HE]`.

Katsuda, S. and H. Tsunemi (May 2006). “Spatially Resolved X-Ray Spectroscopy of Vela Shrapnel A”. In: *ApJ* 642.2, pp. 917–922. DOI: `10.1086/501434`. arXiv: `astro-ph/0603454 [astro-ph]`.

Katsuda, S. et al. (May 2008). “Discovery of Fast-Moving X-Ray-Emitting Ejecta Knots in the Oxygen-Rich Supernova Remnant Puppis A”. In: *ApJ* 678.1, pp. 297–302. DOI: `10.1086/586891`. arXiv: `0805.1369 [astro-ph]`.

Katsuda, S. et al. (Nov. 2015). “Evidence for Thermal X-Ray Line Emission from the Synchrotron-dominated Supernova Remnant RX J1713.7-3946”. In: *ApJ* 814, 29, p. 29. DOI: `10.1088/0004-637X/814/1/29`. arXiv: `1510.04025 [astro-ph.HE]`.

Katsuda, Satoru and Hiroshi Tsunemi (Aug. 2005). “Spatially Resolved Spectral Analysis of Vela Shrapnel D”. In: *PASJ* 57, pp. 621–628. DOI: `10.1093/pasj/57.4.621`. arXiv: `astro-ph/0507344 [astro-ph]`.

Katsuda, Satoru, Hiroshi Tsunemi, and Koji Mori (2008). “The Slow X-ray Expansion of the Northwestern Rim of RX J0852.0-4622”. In: *The X-ray Universe 2008*, p. 99.

Katsuda, Satoru et al. (May 2010). “Discovery of X-ray-emitting O-Ne-Mg-rich Ejecta in the Galactic Supernova Remnant Puppis A”. In: *ApJ* 714.2, pp. 1725–1732. DOI: `10.1088/0004-637X/714/2/1725`. arXiv: `1004.4132 [astro-ph.HE]`.

Kelner, S. R., F. A. Aharonian, and V. V. Bugayov (2006). “Energy spectra of gamma rays, electrons, and neutrinos produced at proton-proton interactions in the very high energy regime”. In: *Phys. Rev. D* 74.3, 034018, p. 034018. DOI: `10.1103/PhysRevD.74.034018`. arXiv: `astro-ph/0606058 [astro-ph]`.

Khangulyan, D., F. A. Aharonian, and S. R. Kelner (Mar. 2014). “Simple Analytical Approximations for Treatment of Inverse Compton Scattering of Relativistic Electrons in the Blackbody Radiation Field”. In: *ApJ* 783.2, 100, p. 100. DOI: `10.1088/0004-637X/783/2/100`. arXiv: `1310.7971 [astro-ph.HE]`.

Klein, Richard I., Christopher F. McKee, and Philip Colella (1994). “On the Hydrodynamic Interaction of Shock Waves with Interstellar Clouds. I. Nonradiative Shocks in Small Clouds”. In: *ApJ* 420, p. 213. DOI: `10.1086/173554`.

Kobayashi, T. et al. (Jan. 2004). “The Most Likely Sources of High-Energy Cosmic-Ray Electrons in Supernova Remnants”. In: *ApJ* 601.1, pp. 340–351. DOI: `10.1086/380431`. arXiv: `astro-ph/0308470 [astro-ph]`.

Kopp, Joachim (Oct. 2013). “Constraints on dark matter annihilation from AMS-02 results”. In: *Phys. Rev. D* 88.7, 076013, p. 076013. DOI: `10.1103/PhysRevD.88.076013`. arXiv: `1304.1184 [hep-ph]`.

Koyama, K. et al. (Nov. 1995). “Evidence for shock acceleration of high-energy electrons in the supernova remnant SN1006”. In: *Nature* 378, pp. 255–258. DOI: `10.1038/378255a0`.

Koyama, K. et al. (June 1997). “Discovery of Non-Thermal X-Rays from the Northwest Shell of the New SNR RX J1713.7-3946: The Second SN 1006?” In: *PASJ* 49, pp. L7–L11. DOI: `10.1093/pasj/49.3.L7`. eprint: `astro-ph/9704140`.

Kraushaar, W. L. et al. (Nov. 1972). “High-Energy Cosmic Gamma-Ray Observations from the OSO-3 Satellite”. In: *ApJ* 177, p. 341. DOI: `10.1086/151713`.

Krymskii, G. F. (June 1977). “A regular mechanism for the acceleration of charged particles on the front of a shock wave”. In: *Akademiia Nauk SSSR Doklady* 234, pp. 1306–1308.

Lazendic, J. S. et al. (Feb. 2004). “A High-Resolution Study of Nonthermal Radio and X-Ray Emission from Supernova Remnant G347.3-0.5”. In: *ApJ* 602, pp. 271–285. DOI: `10.1086/380956`. eprint: `astro-ph/0310696`.

Li, Jian et al. (Jan. 2020). “Gamma-ray heartbeat powered by the microquasar SS 433”. In: *Nature Astronomy* 4, pp. 1177–1184. DOI: `10.1038/s41550-020-1164-6`. arXiv: `2008.10523 [astro-ph.HE]`.

Linden, Tim and Stefano Profumo (July 2013). “Probing the Pulsar Origin of the Anomalous Positron Fraction with AMS-02 and Atmospheric Cherenkov Telescopes”. In: *ApJ* 772.1, 18, p. 18. DOI: `10.1088/0004-637X/772/1/18`. arXiv: `1304.1791 [astro-ph.HE]`.

Lipari, Paolo (Mar. 2017). “Interpretation of the cosmic ray positron and antiproton fluxes”. In: *Phys. Rev. D* 95.6, 063009, p. 063009. DOI: `10.1103/PhysRevD.95.063009`. arXiv: `1608.02018 [astro-ph.HE]`.

Liu, Wei et al. (2017). “Excesses of cosmic ray spectra from a single nearby source”. In: *Phys. Rev. D* 96 (2), p. 023006. DOI: `10.1103/PhysRevD.96.023006`. URL: `https://link.aps.org/doi/10.1103/PhysRevD.96.023006`.

Longair, Malcolm S. (2011). *High Energy Astrophysics*.

Lu, F. J. and B. Aschenbach (Oct. 2000). “Spatially resolved X-ray spectroscopy of the Vela supernova remnant”. In: *A&A* 362, pp. 1083–1092.

Mattox, J. R. et al. (1996). “The Likelihood Analysis of EGRET Data”. In: *ApJ* 461, p. 396. DOI: `10.1086/177068`.

Mertsch, Philipp and Subir Sarkar (Sept. 2014). “AMS-02 data confront acceleration of cosmic ray secondaries in nearby sources”. In: *Phys. Rev. D* 90.6, 061301, p. 061301. DOI: `10.1103/PhysRevD.90.061301`. arXiv: `1402.0855 [astro-ph.HE]`.

Meyer, Peter and Rochus Vogt (Feb. 1961). “Electrons in the Primary Cosmic Radiation”. In: *Phys. Rev. Lett.* 6.4, pp. 193–196. DOI: `10.1103/PhysRevLett.6.193`.

Miyamoto, S. et al. (Aug. 1971). “Measurement of the Location of the X-Ray Source Cygnus X-1”. In: *ApJL* 168, p. L11. DOI: `10.1086/180774`.

Miyata, Emi et al. (June 1994). “The Plasma Structure of the North-East Rim of the Cygnus Loop as Observed with ASCA”. In: *PASJ* 46, pp. L101–L104.

Miyata, Emi et al. (Sept. 2001). “Chandra X-Ray Observatory Study of Vela Shrapnel A”. In: *ApJL* 559.1, pp. L45–L48. DOI: 10.1086/323653.

Moriguchi, Y. et al. (Oct. 2005). “A Detailed Study of Molecular Clouds toward the TeV Gamma-Ray Supernova Remnant G347.3-0.5”. In: *ApJ* 631, pp. 947–963. DOI: 10.1086/432653. eprint: astro-ph/0506489.

Moriguchi, Yoshiaki et al. (Dec. 2001). “A ^{12}CO (J = 1 – 0) Survey of Molecular Clouds toward the Vela Supernova Remnant with NANTEN”. In: *PASJ* 53.6, pp. 1025–1036. DOI: 10.1093/pasj/53.6.1025.

Mueller, Dietrich and Kwork-Kwong Tang (Jan. 1987). “Cosmic-Ray Positrons from 10 to 20 GeV: A Balloon-borne Measurement Using the Geomagnetic East-West Asymmetry”. In: *ApJ* 312, p. 183. DOI: 10.1086/164859.

Nishimura, J. et al. (May 1980). “Emulsion chamber observations of primary cosmic-ray electrons in the energy range 30-1000 GeV”. In: *ApJ* 238, pp. 394–409. DOI: 10.1086/157997.

Nishina, Y., M. Takeuchi, and T. Ichimiya (Dec. 1937). “On the Nature of Cosmic-Ray Particles”. In: *Physical Review* 52.11, pp. 1198–1199. DOI: 10.1103/PhysRev.52.1198.

Ohashi, S. et al. (Dec. 2016). “Dense Core Properties in the Infrared Dark Cloud G14.225-0.506 Revealed by ALMA”. In: *ApJ* 833, 209, p. 209. DOI: 10.3847/1538-4357/833/2/209. arXiv: 1610.08581.

Ohashi, S. et al. (Apr. 2018). “Gravitationally Unstable Condensations Revealed by ALMA in the TUKH122 Prestellar Core in the Orion A Cloud”. In: *ApJ* 856, 147, p. 147. DOI: 10.3847/1538-4357/aab3d0. arXiv: 1803.03340.

Okuno, T. et al. (Aug. 2018). “Spatially resolved spectroscopy of non-thermal X-rays in RX J1713.7-3946 with Chandra”. In: *PASJ* 70, 77, p. 77. DOI: 10.1093/pasj/psy072. arXiv: 1805.06690 [astro-ph.HE].

Onishi, T. et al. (Dec. 2015). “ALMA Observations of a High-density Core in Taurus: Dynamical Gas Interaction at the Possible Site of a Multiple Star Formation”. In: *Revolution in Astronomy with ALMA: The Third Year*. Ed. by D. Iono et al. Vol. 499. Astronomical Society of the Pacific Conference Series, p. 211.

Pfeffermann, E. and B. Aschenbach (Feb. 1996). “ROSAT observation of a new supernova remnant in the constellation Scorpius.” In: *Roentgenstrahlung from the Universe*. Ed. by H. U. Zimmermann, J. Trümper, and H. Yorke, pp. 267–268.

Planck Collaboration et al. (Dec. 2016). “Planck intermediate results. XLVIII. Disentangling Galactic dust emission and cosmic infrared background anisotropies”. In: *A&A* 596, A109, A109. DOI: 10.1051/0004-6361/201629022. arXiv: 1605.09387 [astro-ph.CO].

Profumo, Stefano et al. (June 2018). “Lessons from HAWC pulsar wind nebulae observations: The diffusion constant is not a constant; pulsars remain the likeliest sources of the anomalous positron fraction; cosmic rays are trapped for long periods of time in pockets of inefficient diffusion”. In: *Phys. Rev. D* 97.12, 123008, p. 123008. DOI: 10.1103/PhysRevD.97.123008. arXiv: 1803.09731 [astro-ph.HE].

Rasul, Kajwan et al. (May 2019). "Gamma-rays from SS433: evidence for periodicity". In: *MNRAS* 485.2, pp. 2970–2975. DOI: 10.1093/mnras/stz559. arXiv: 1903.00299 [astro-ph.HE].

Ray, P. S. et al. (June 2011). "Precise γ-ray Timing and Radio Observations of 17 Fermi γ-ray Pulsars". In: *ApJS* 194.2, 17, p. 17. DOI: 10.1088/0067-0049/194/2/17. arXiv: 1011.2468 [astro-ph.HE].

Reynolds, S. P. (2008). "Supernova remnants at high energy." In: *ARA&A* 46, pp. 89–126. DOI: 10.1146/annurev.astro.46.060407.145237.

Reynoso, E. M. et al. (July 1995). "VLA Observations of Neutral Hydrogen in the Direction of Puppis A". In: *AJ* 110, p. 318. DOI: 10.1086/117522.

Reynoso, E. M. et al. (Oct. 2003). "Observations of the neutral hydrogen surrounding the radio-quiet neutron star RX J0822-4300 in Puppis A". In: *MNRAS* 345.2, pp. 671–677. DOI: 10.1046/j.1365-8711.2003.06978.x. arXiv: astro-ph/0307065 [astro-ph].

Rybicki, George B. and Alan P. Lightman (1986). *Radiative Processes in Astrophysics*.

Sakemi, Haruka et al. (June 2021). "Energy estimation of high-energy particles associated with the SS 433/W 50 system through radio observation at 1.4 GHz". In: *PASJ* 73.3, pp. 530–544. DOI: 10.1093/pasj/psab018. arXiv: 2103.05578 [astro-ph.HE].

Sano, H. et al. (Nov. 2010). "Star-forming Dense Cloud Cores in the TeV Gamma-ray SNR RX J1713.7-3946". In: *ApJ* 724, pp. 59–68. DOI: 10.1088/0004-637X/724/1/59. arXiv: 1005.3409.

Sano, H. et al. (Nov. 2013). "Non-thermal X-Rays and Interstellar Gas Toward the γ-Ray Supernova Remnant RX J1713.7-3946: Evidence for X-Ray Enhancement around CO and H I Clumps". In: *ApJ* 778, 59, p. 59. DOI: 10.1088/0004-637X/778/1/59. arXiv: 1304.7722.

Sano, H. et al. (Feb. 2015). "A Detailed Study of Non-thermal X-Ray Properties and Interstellar Gas toward the γ-Ray Supernova Remnant RX J1713.7-3946". In: *ApJ* 799, 175, p. 175. DOI: 10.1088/0004-637X/799/2/175. arXiv: 1401.7418 [astro-ph.HE].

Sano, H. et al. (Dec. 2020). "ALMA CO Observations of the Gamma-Ray Supernova Remnant RX J1713.7-3946: Discovery of Shocked Molecular Cloudlets and Filaments at 0.01 pc Scales". In: *ApJL* 904.2, L24, p. L24. DOI: 10.3847/2041-8213/abc884. arXiv: 2011.05018 [astro-ph.HE].

Shen, C. S. (Dec. 1970). "Pulsars and Very High-Energy Cosmic-Ray Electrons". In: *ApJL* 162, p. L181. DOI: 10.1086/180650.

Slane, P. et al. (Nov. 1999). "Nonthermal X-Ray Emission from the Shell-Type Supernova Remnant G347.3-0.5". In: *ApJ* 525, pp. 357–367. DOI: 10.1086/307893. eprint: astro-ph/9906364.

Slane, P. et al. (Oct. 2018). “Investigating the Structure of Vela X”. In: *ApJ* 865.2, 86, p. 86. DOI: 10.3847/1538-4357/aada12. arXiv: 1808.03878 [astro-ph.HE].

Slane, Patrick et al. (2001). “RX J0852.0-4622: Another Nonthermal Shell-Type Supernova Remnant (G266.2-1.2)”. In: *ApJ* 548.2, pp. 814–819. DOI: 10.1086/319033. arXiv: astro-ph/0010510 [astro-ph].

Sun, Xiao-Na et al. (June 2019). “Tentative evidence of spatially extended GeV emission from SS433/W50”. In: *A&A* 626, A113, A113. DOI: 10.1051/0004-6361/201935621. arXiv: 1904.05127 [astro-ph.HE].

Sushch, I., B. Hnatyk, and A. Neronov (Jan. 2011). “Modeling of the Vela complex including the Vela supernova remnant, the binary system γ^2 Velorum, and the Gum nebula”. In: *A&A* 525, A154, A154. DOI: 10.1051/0004-6361/201015346. arXiv: 1011.1177 [astro-ph.GA].

Takahashi, T. et al. (Jan. 2008). “Measuring the Broad-Band X-Ray Spectrum from 400eV to 40keV in the Southwest Part of the Supernova Remnant RXJ1713.7-3946”. In: *PASJ* 60, S131–S140. DOI: 10.1093/pasj/60.sp1.S131. arXiv: 0708.2002.

Tanaka, T. et al. (Oct. 2008). “Study of Nonthermal Emission from SNR RX J1713.7-3946 with Suzaku”. In: *ApJ* 685, 988-1004, pp. 988–1004. DOI: 10.1086/591020. arXiv: 0806.1490.

Tanaka, T. et al. (2011). “Gamma-Ray Observations of the Supernova Remnant RX J0852.0-4622 with the Fermi Large Area Telescope”. In: *ApJL* 740.2, L51, p. L51. DOI: 10.1088/2041-8205/740/2/L51. arXiv: 1109.4658 [astro-ph.HE].

Tang, Xiaping and Tsvi Piran (Apr. 2019). “Positron flux and γ-ray emission from Geminga pulsar and pulsar wind nebula”. In: *MNRAS* 484.3, pp. 3491–3501. DOI: 10.1093/mnras/stz268. arXiv: 1808.02445 [astro-ph.HE].

Tatischeff, Vincent and Stefano Gabici (2018). “Particle Acceleration by Supernova Shocks and Spallogenic Nucleosynthesis of Light Elements”. In: *Annual Review of Nuclear and Particle Science* 68.1, pp. 377–404. DOI: 10.1146/annurev-nucl-101917-021151. arXiv: 1803.01794 [astro-ph.HE].

Tibaldo, L. et al. (Sept. 2018). “Disentangling multiple high-energy emission components in the Vela X pulsar wind nebula with the Fermi Large Area Telescope”. In: *A&A* 617, A78, A78. DOI: 10.1051/0004-6361/201833356. arXiv: 1806.11499 [astro-ph.HE].

Tibet ASγ Collaboration et al. (Jan. 2021). “Potential PeVatron supernova remnant G106.3+2.7 seen in the highest-energy gamma rays”. In: *Nature Astronomy* 5, pp. 460–464. DOI: 10.1038/s41550-020-01294-9. arXiv: 2109.02898 [astro-ph.HE].

Tomassetti, Nicola and Fiorenza Donato (Apr. 2015). “The Connection between the Positron Fraction Anomaly and the Spectral Features in Galactic Cosmic-ray Hadrons”. In: *ApJL* 803.2, L15, p. L15. DOI: 10.1088/2041-8205/803/2/L15. arXiv: 1502.06150 [astro-ph.HE].

Treumann, R. A. and C. H. Jaroschek (2008). "Fundamentals of Non-relativistic Collisionless Shock Physics: V. Acceleration of Charged Particles". In: *arXiv e-prints*, arXiv:0806.4046, arXiv:0806.4046. arXiv: 0806.4046 [astro-ph].

Tsuji, N. and Y. Uchiyama (Dec. 2016). "Expansion measurements of supernova remnant RX J1713.7-3946". In: *PASJ* 68, 108, p. 108. DOI: 10.1093/pasj/psw102. arXiv: 1609.07886 [astro-ph.HE].

Tsuji, Naomi et al. (2019). "NuSTAR Observations of the Supernova Remnant RX J1713.73946". In: *ApJ* 877.2, 96, p. 96. DOI: 10.3847/1538-4357/ab1b29. arXiv: 1904.12436 [astro-ph.HE].

Tutone, A. et al. (Dec. 2021). "Multiple accelerated particle populations in the Cygnus Loop with Fermi-LAT". In: *A&A* 656, A139, A139. DOI: 10.1051/0004-6361/202141978. arXiv: 2109.15238 [astro-ph.HE].

Tylka, Allan J. (Aug. 1989). "Cosmic-ray positrons from annihilation of weakly interacting massive particles in the galaxy". In: *Phys. Rev. Lett.* 63.8, pp. 840–843. DOI: 10.1103/PhysRevLett.63.840.

Uchiyama, Y., F. A. Aharonian, and T. Takahashi (Mar. 2003). "Fine-structure in the nonthermal X-ray emission of SNR RX J1713.7-3946 revealed by Chandra". In: *A&A* 400, pp. 567–574. DOI: 10.1051/0004-6361:20021824. eprint: astro-ph/0209217.

Uchiyama, Y. et al. (Oct. 2007). "Extremely fast acceleration of cosmic rays in a supernova remnant". In: *Nature* 449, pp. 576–578. DOI: 10.1038/nature06210.

Uchiyama, Yasunobu et al. (Apr. 2012). "Fermi Large Area Telescope Discovery of GeV Gamma-Ray Emission from the Vicinity of SNR W44". In: *ApJL* 749.2, L35, p. L35. DOI: 10.1088/2041-8205/749/2/L35. arXiv: 1203.3234 [astro-ph.HE].

Vernetto, Silvia and Paolo Lipari (Sept. 2016). "Absorption of very high energy gamma rays in the Milky Way". In: *Phys. Rev. D* 94.6, 063009, p. 063009. DOI: 10.1103/PhysRevD.94.063009. arXiv: 1608.01587 [astro-ph.HE].

Vink, Jacco (2020). *Physics and Evolution of Supernova Remnants*. DOI: 10.1007/978-3-030-55231-2.

Wang, Z. R., Q.-Y. Qu, and Y. Chen (Feb. 1997). "Is RX J1713.7-3946 the remnant of the AD393 guest star?" In: *A&A* 318, pp. L59–L61.

Wilms, J., A. Allen, and R. McCray (2000). "On the Absorption of X-Rays in the Interstellar Medium". In: *ApJ* 542.2, pp. 914–924. DOI: 10.1086/317016. arXiv: astro-ph/0008425 [astro-ph].

Xin, Yu-Liang et al. (July 2017). "Revisiting SNR Puppis A with Seven Years of Fermi Large Area Telescope Observations". In: *ApJ* 843.2, 90, p. 90. DOI: 10.3847/1538-4357/aa74bb. arXiv: 1703.03911 [astro-ph.HE].

Xing, Yi et al. (Feb. 2019). "Fermi Observation of the Jets of the Microquasar SS 433". In: *ApJ* 872.1, 25, p. 25. DOI: 10.3847/1538-4357/aafc60. arXiv: 1811.09495 [astro-ph.HE].

Yamaguchi, H. and S. Katsuda (May 2009). “Suzaku Spectroscopy of Vela Shrapnel B”. In: *ApJ* 696.2, pp. 1548–1553. DOI: `10.1088/0004-637X/696/2/1548`. arXiv: `0902.3672 [astro-ph.HE]`.

Yamauchi, Shigeo, Nobuyuki Kawai, and Takashi Aoki (June 1994). “A Non-Thermal X-Ray Spectrum from the Supernova Remnant W 50”. In: *PASJ* 46, pp. L109–L113.

Zabalza, V. (July 2015). “Naima: a Python package for inference of particle distribution properties from nonthermal spectra”. In: *34th International Cosmic Ray Conference (ICRC2015)*. Vol. 34. International Cosmic Ray Conference, p. 922. arXiv: `1509.03319 [astro-ph.HE]`.

Zirakashvili, V. N. and F. A. Aharonian (Jan. 2010). “Nonthermal Radiation of Young Supernova Remnants: The Case of RX J1713.7-3946”. In: *ApJ* 708, pp. 965–980. DOI: `10.1088/0004-637X/708/2/965`. arXiv: `0909.2285 [astro-ph.HE]`.

Acknowledgements

First of all, I would like to thank my supervisors, Professor Yasunobu Uchiyama and Associate Professor Shinya Yamada, for their advice and encouragement. I would like to express my gratitude to Dr. Masaaki Hayashida for his technical supporst in gamma-ray analysis. I would like to express my gratitude to Dr. Naomi Tsuji for her technical supports and comments in X-ray analysis.

I am deeply grateful to the advisory Committee (Professor Shunji Kitamoto, Professor Tomohiro Harada, and Associate Professor Shinya Yamada) for their valuable advice on this paper, and to the professors in Astro and Solar-Terrestrial Physics Laboratories of Physics department in Rikkyo University for their comments at the weekly meetings. I am grateful to the members of the Fermi-LAT Collaboration for their helpful advice and comments. I would like to show my special thanks to the members of Uchiyama and Yamada groups. Your support and encouragement make my research life very fruitful.

I wish to thank my friends for their encouragements. Finally, I would like to express my deepest appreciation to my family for their daily support and encouragement.